

University of Southampton Research Repository

Copyright © and Moral Rights for this thesis and, where applicable, any accompanying data are retained by the author and/or other copyright owners. A copy can be downloaded for personal non-commercial research or study, without prior permission or charge. This thesis and the accompanying data cannot be reproduced or quoted extensively from without first obtaining permission in writing from the copyright holder/s. The content of the thesis and accompanying research data (where applicable) must not be changed in any way or sold commercially in any format or medium without the formal permission of the copyright holder/s.

When referring to this thesis and any accompanying data, full bibliographic details must be given, e.g.

Thesis: Author (Year of Submission) "Full thesis title", University of Southampton, name of the University Faculty or School or Department, PhD Thesis, pagination.

Data: Author (Year) Title. URI [dataset]

University of Southampton

Faculty of Engineering and Physical Sciences

Institute of Sound and Vibration Research

The influence of surrounding structures on ground-borne vibration from railways

by

Xiangyu Qu

ORCID ID: 0000-0002-6651-929X

Thesis for the degree of Doctor of Philosophy

April 2025

University of Southampton Abstract

Faculty of Engineering and Physical Sciences
Institute of Sound and Vibration Research

<u>Doctor of Philosophy</u>

The influence of surrounding structures on ground-borne vibration from railways

by

Xiangyu Qu

Railway transportation is widely recognised as an environmentally friendly and sustainable mode of transport, with extensive global development over recent decades. However, traininduced ground vibration has become a subject of increasing concern. To address this, various prediction methods, including empirical, analytical/semi-analytical, and numerical approaches, have rapidly evolved. Despite these advancements, most methods presume a free-field transmission path, disregarding the influence of buildings located between the excitation source and receiver points. This simplification highlights the need for more detailed investigations into the impact of surrounding structures on ground-borne vibration.

Ground vibration is fundamental to the vibration response of the target building. To improve computational efficiency and simplify the model, the ground vibration is investigated. The aim of this thesis is to explore and analyse the influence of surrounding structures located in the transmission path on ground vibration induced by railways. This investigation begins with a fundamental problem: the interaction between a single pile and the surrounding soil and its subsequent impact on ground response. To address this, a semi-analytical model has been developed to study the effects of a single pile on ground vibration. The finite element method is used to simulate a piled foundation structure. The surrounding soil is modelled by using the dynamic stiffness matrix method. The model's accuracy and reliability are examined across various conditions. Additionally, the ground velocity levels behind the pile and the corresponding insertion loss results are thoroughly investigated. The influence of the single pile on ground vibration is quantitatively analysed under varying conditions, including different soil wave velocities, frequencies, and layer parameters.

A semi-analytical model of a pile group embedded in soil is constructed by considering the transfer receptances between distinct piles, based on the single pile-soil dynamic interaction model. The model accuracy range is investigated. Then different pile configurations are investigated. These include two piles aligned transverse to the line from source point to the receiver point, two piles arranged axially to this line, and four piles arranged in a square 2×2 configuration. The ground response and the ground vibration mitigation effects are investigated and summarised.

Next, an analysis is conducted on the ground response behind a building structure with piled foundation. The ground velocity level response and the insertion loss results for a fixed unit load are presented. Furthermore, the excitation source is substituted with a railway train load operating within an embedded tunnel structure. The tunnel structure is simulated using the Pipein-Pipe method. The study summarises responses under varying train loads and distances

between the railway and the building, providing a comprehensive analysis of the impact of the structure located in the transmission path.

Finally, within the framework of a hybrid ground vibration prediction model, the impact of five different foundation types on ground response is explored. These are a raft foundation, strip foundations oriented both perpendicular and parallel to the direction of train movement, a pile foundation, and a box foundation. The excitation sources encompass both surface and underground railway force density levels. The line source transfer mobility for the different types of building foundation is computed using a set of incoherent point loads and combined with force densities to represent train excitation. The line source transfer mobility of the various foundation types is simulated using the finite element method. Leveraging high-performance computing and batch processing, the line source transfer mobility results are investigated. The findings reveal that deep foundations generally offer more significant ground vibration mitigation effects. However, when the train load is embedded below the surface, zones of amplified ground vibration may occur behind the building.

Overall, the presence of structures in the transmission path significantly influences ground vibration. When point loads or train loads are applied on the ground surface, the ground response is typically mitigated. However, when the loads are embedded in the ground, the vibration may be amplified in certain zones. Therefore, it is crucial to account for structures within the transmission path when predicting ground vibration impacts. Consequently, this approach is expected to yield more accurate predictions.

Table	e of C	Contentsi
Table	e of T	ablesvii
Table	e of F	iguresix
Rese	arch	Thesis: Declaration of Authorshipxxi
Ackr	owle	edgements xxiii
Defi	nitior	ns and Abbreviations xxv
Chap	oter 1	Introduction1
1.1	Bac	kground1
1.2	Aim	of the thesis3
1.3	Orig	ginal contributions4
1.4	Stru	ucture of the thesis5
Chap	oter 2	Literature review7
2.1	Gro	und-borne vibration prediction methods7
:	2.1.1	(Semi) analytical methods
:	2.1.2	Numerical methods
	2	.1.2.1 Time-domain numerical models 12
	2	.1.2.2 Frequency domain numerical models
:	2.1.3	Empirical models
:	2.1.4	Hybrid methods
2.2	Sing	gle pile-soil dynamic interaction17
2.3	Soil	-structure interaction20
:	2.3.1	Soil-structure interaction in analytical model
:	2.3.2	Soil-structure interaction in numerical model
:	2.3.3	Coupling loss in empirical models
2.4	Seis	smic soil-metamaterials in ground vibration24
2.5	Gap	os and summary26
Char		Single pile-soil dynamic interaction29
Jiia	JUGI J	, onigto pito-soit aynanno interaction23

3.1	Sen	ni-analytical model for single pile-soil interaction	29
3.2	. FE r	nodel for single pile and surrounding soil	34
	3.2.1	Axisymmetric model	35
	3.2.2	Three-dimensional model	36
3.3	Moo	del evaluation	37
	3.3.1	Free-field response	37
	3.3.2	The number of coupled nodes	39
	3.3.3	Ground response for load applied to the top of the pile	41
	3.3.4	Ground response for load applied adjacent to the pile	42
	3.3.5	Model accuracy under different shear wave velocities and frequencies	43
	3.3.6	Model comparison with other model	45
3.4	Gro	und vibration mitigation	49
	3.4.1	Ground vibration insertion loss on the centreline	49
	3.4.2	Insertion loss when load is further from the pile	51
	3.4.3	Frequency dependence of mitigation effects	52
3.5	Sing	gle pile coupled with layered soil	54
	3.5.1	Different shear wave velocity for subsoil	54
	3.5.2	Different upper soil depth	59
3.6	Sun	nmary	63
Cha	pter 4	Pile group-soil dynamic interaction	65
4.1	Sen	ni-analytical model for pile group	65
4.2	. Mod	del comparison	66
	4.2.1	Two piles aligned in the axial direction	67
	4.2.2	Two piles aligned in the transverse direction	70
	4.2.3	Four piles in square arrangement	73
4.3	В Мос	del limitations	76
4.4	Gro	und response	80
	4.4.1	Ground centreline response under different source load positions	80

4.4.2 Average insertion loss values
4.4.3 Insertion loss results on centreline behind the pile group
4.5 Summary93
Chapter 5 Ground vibration in the vicinity of a building due to a fixed unit load
95
5.1 Methodology95
5.2 Building finite element model98
5.3 Model verification
5.4 Ground response investigation102
5.4.1 Ground response in the vicinity of building102
5.4.2 The relationship between building modes and ground response105
5.4.3 Parametric study109
5.4.4 Overall ground response and comparison with pile group model114
5.4.4.1 Spectrum results for specific point114
5.4.4.2 Ground response on centreline behind the building115
5.4.4.3 Overall insertion loss contour115
5.4.4.4 Average insertion loss results116
5.5 Summary117
Chapter 6 Excitation by an underground railway119
6.1 Methodology 119
6.1.1 Sub-model description119
6.1.1.1 Train-track model119
6.1.1.2 Tunnel-ground model121
6.1.2 Calculation process
6.2 Model parameters130
6.3 Ground response results133
6.3.1 Ground vibration and mitigation effects under different train speeds134
6.3.1.1 Specific receiver points at specific frequencies

6.3.1.2 Ground response on the centreline behind the building136	
6.3.1.3 Overall insertion loss contour for underground railway case137	
6.3.1.4 Average results for different underground railway train speed cases	3
6.3.2 Ground vibration and mitigation effects for different distances between railway and building140	1
6.3.2.1 The results at 3.8 m away from the building on the centreline140	
6.3.2.2 Ground response on the centreline behind the building141	
6.3.2.3 Overall insertion loss contour for underground railway case142	
6.3.2.4 Average insertion loss results at different distances	
6.4 Summary144	
Chapter 7 Influence of various foundation types using a hybrid model. 147	
7.1 Line-source transfer mobility level: numerical model	
7.1.1 Model parameters148	
7.1.2 Foundation types	
7.1.3 Results	
7.2 Force density level: semi-analytical model	
7.3 Ground response under different foundation types160	
7.3.1 Surface railway case161	
7.3.1.1 The spectral results at a specific receiver point161	
7.3.1.2 The results at a specific frequency (50 Hz)162	
7.3.1.3 Results based on overall levels	
7.3.1.4 Overall results averaged over receiver points167	
7.3.2 Underground railway case168	
7.3.2.1 The spectral results at specific receiver point (5.6 m)168	
7.3.2.2 The results at specific frequency (50 Hz)169	
7.3.2.3 Results based on overall levels	
7.3.2.4 Overall results averaged over receiver points173	
7.3.3 Embedded load case 174	

7.4	Summary	177
Chap	pter 8 Conclusions and recommendations	179
8.1	Conclusions	179
8.2	Recommendations for future work	181
Appe	endix A The beam element matrices	183
Appe	endix B Dynamic stiffness matrix for the ground	187
Appe	endix CCoefficients for the elastic continuum	189
Appe	endix DMATLAB code for building model	193
List o	of References	195

Table of Tables

Table of Tables

Table 3-1	Material parameters of the soil and the pile.	35
Table 4-1	Material properties used in pile group model	67
Table 4-2	Receiver points location.	90
Table 5-1	Dimensions of the building.	100
Table 5-2	The materials parameters of the model in this case study	102
Table 6-1	The parameters of the train.	131
Table 6-2	The parameters of the track.	132
Table 6-3	The parameters of the tunnel structure.	132
Table 6-4	The parameters of the soil	133
Table 7-1	Material parameters used in FE model	148
Table 7-2	Track model parameters	159

Figure 1-1	Schematic view of how underground railway and surface railway induced ground-borne vibration affects the nearby building [1]	
Figure 1-2	Sketch of steps involved in predicting railway-induced vibration in buildings.	
Figure 1-3	Sketch of surrounding building and target building	3
Figure 2-1	Sketch of the model of a track on layered ground excited by a moving load [27]	
Figure 2-2	Sketch of the PiP model [35].	.11
Figure 2-3	Unit cell of the periodic finite element with PML [105]	.14
Figure 2-4	Determination of line source transfer mobility for excitation on the ground surface [117].	
Figure 2-5	Sketch of different types of loads in the single pile model [151]	.19
Figure 2-6	Sketch of meshless single pile model [163].	.20
Figure 2-7	Sketch of the coupled model used by Hussein et al. [168], showing a train of wheelsets running in a tunnel and a building coupled to the ground model at a series of nodes	;
Figure 2-8	Real part of the (a) vertical soil displacement and (b) vertical structural displacement at 50 Hz accounting for through-soil coupling of a group of surrounding buildings [178])
Figure 2-9	Sketch of source and receiver positions used in predicting railway vibration in buildings [6]	
Figure 3-1	Sketch of the semi-analytical model for single pile-soil interaction	.30
Figure 3-2	Sketch of equivalent foundation parameters.	.32
Figure 3-3	Receptance on the surface excited by point load and disc load (radius 0.5 m) at 40 Hz.	
Figure 3-4	The rotational displacement obtained from the displacements at the	34

Figure 3-5	Sketch of the FE model of the pile directly beneath the load36
Figure 3-6	The FE model for a load applied to the ground at some distance from the pile
Figure 3-7	Free-field response comparison when ground shear wave velocity is 250 m/s at (a) 10 Hz (b) 80 Hz, and when the shear wave velocity is 160 m/s at (c) 10 Hz and (d) 80 Hz.
Figure 3-8	Average level differences for model with different numbers of coupled nodes in (a) load above the pile and (b) load at 2.4 m from the pile 40
Figure 3-9	Magnitude of vibration response for a unit load applied to the top of the pile: comparison between FE model and semi-analytical model when the shear wave velocity is 250 m/s at (a) 40 Hz, (b) 80 Hz and when the shear wave velocity is 160 m/s at (c) 40 Hz, (d) 80 Hz
Figure 3-10	The magnitude of vibration induced by a load at 2.4 m from the pile obtained from FE model and semi-analytical model when the shear wave velocity is 250 m/s at (a) 40 Hz, (b) 80 Hz and when the shear wave velocity is 160 m/s at (c) 40 Hz, (d) 80 Hz
Figure 3-11	Average level differences under different values of dimensionless parameter
Figure 3-12	Comparison between different single pile-soil models at (a) the top of the pile and (b) on the ground 5 m away from the pile when the load is applied at the top of the pile
Figure 3-13	Comparison between different single pile-soil model at (a) the top of the pile and (b) on the ground 5 m away from the pile when the load is applied 2.4 m away from the pile
Figure 3-14	The free-field response and the response with pile when the shear wave velocity is 250 m/s at (a) 40 Hz, (b) 80 Hz and when the shear wave velocity is 160 m/s at (c) 40 Hz, (d) 80 Hz
Figure 3-15	IL of single pile model for two shear wave speeds and two frequencies. 51
Figure 3-16	The spectral IL results at the receiver points (a) 2 m and (b) 6 m behind the pile on the centreline under different shear wave velocities51

Figure 3-17	The IL for different distances between the pile centreline and the load
	(a) at 40 Hz and (b) at 80 Hz. Receiver points A, B, and C are 5 m, 10 m, 15 m away from the pile, respectively52
	15 III away II o III tile pite, respectively52
Figure 3-18	Contour plot of IL for load at 10 m from the pile and receiver 5 m behind
	the pile53
Figure 3-19	Insertion loss for different dimensionless value $\it a0$ when the distance
	between load and pile is 10 m, and the distance between receiver point
	and pile is 5 m54
Figure 3-20	Sketch of (a) the half-space model and (b) the layered soil model55
Figure 3-21	The spectral results of the IL at (a) 2 m and (b) 6 m behind the pile on the
	centreline for different subsoil shear wave velocity55
Figure 3-22	The overall IL contour from (a) half-space model (b) the model with
	subsoil shear wave velocity of 500 m/s (c) the model with subsoil shear
	wave velocity of 1000 m/s and (d) the model with subsoil shear wave
	velocity of 2000 m/s57
Figure 3-23	The spectral results of the IL average over ±10 m width at (a) 2 m and (b)
	6 m away from the pile for different subsoil shear wave velocity58
Figure 3-24	The average IL value of the receiver points with same distance behind
	the pile for different subsoil shear wave velocity models. (a) the results
	on the centreline and (b) the results average over ±10 m width59
Figure 3-25	Sketch of the layered soil model when the upper soil depth is (a) 2.5 m
	and (b) 7.5 m60
Figure 3-26	The spectral results about the IL on the centreline at (a) 2 m and (b) 6 m
	away from the pile for different upper soil layer depths
Figure 2, 27	The expectacl records about the Heavered ever 110 manifolds at (a) 2 mand
Figure 3-27	The spectral results about the IL average over ±10 m width at (a) 2 m and (b) 6 m away from the pile for different upper soil depth62
	(b) o m away from the pite for amoretic apper solit depth
Figure 3-28	The overall IL contour of the ground behind the single pile from the
	model when the upper soil depth is (a) 2.5 m and (b) 7.5 m62
Figure 3-29	The overall value of IL from one-third octave bands 10-80 Hz for
	different upper soil depth models: (a) the results on the centreline and
	(b) the results average over ±10 m width63

Figure 4-1	FE model of two piles aligned axially	.68
Figure 4-2	The magnitude of ground vibration influenced by two piles arranged behind one another: comparison between FE model and semi-analytical model (a) at 20 Hz, (b) at 40 Hz, (c) at 60 Hz, and (d) at 80 Hz.	-
Figure 4-3	The IL from two piles arranged behind one another: comparison between FE model and semi-analytical model (a) at 20 Hz, (b) at 40 Hz, (c) at 60 Hz, and (d) at 80 Hz.	,
Figure 4-4	Two piles arranged beside one another in the FE model	.71
Figure 4-5	The magnitude of ground vibration influenced by two piles arranged beside one another: comparison between FE model and semi-analytical model (a) at 20 Hz, (b) at 40 Hz, (c) at 60 Hz and (d) at 80 Hz.	-
Figure 4-6	The IL from two piles arranged beside one another: comparison between FE model and semi-analytical model (a) at 20 Hz, (b) at 40 Hz, (c) at 60 Hz and (d) at 80 Hz.	,
Figure 4-7	Four piles in two rows FE model.	.74
Figure 4-8	The magnitude of ground vibration influenced by four piles in two rows: comparison between FE model and semi-analytical model (a) at 20 Hz, (b) at 40 Hz, (c) at 60 Hz and (d) at 80 Hz.	,
Figure 4-9	The IL from four piles in two rows: comparison between FE model and semi-analytical model (a) at 20 Hz, (b) at 40 Hz, (c) at 60 Hz and (d) at 80 Hz.)
Figure 4-10	Different pile group arrangements for model limitation investigation with receivers on the centreline with (a) one pile (b) two piles arranged behind one another (c) three piles arranged behind one another (d) four piles arranged behind one another (e) three piles arranged beside one another and (f) five piles arranged beside one another.	
Figure 4-11	Summarised average ground displacement level differences on the centreline behind the pile group when the piles are arranged (a) behind one another, (b) beside one another.	I
Figure 4-12	Different pile group arrangements for model limitation investigation behind pile group with (a) one pile (b) two piles arranged behind one	

	another (c) three piles arranged benind one another (d) four piles arranged behind one another (e) three piles arranged beside one another and (f) five piles arranged beside one another.	
Figure 4-13	Summarised average ground displacement level differences for all the receiver points behind the pile group when the piles are arranged (a) behind one another, (b) beside one another.	
Figure 4-14	The IL averaged over ±10 m width on the ground which is 5 m, 10 m and 15 m behind the first pile and calculated from the difference in overall ground velocity level with/without piles evaluated over the range 10-80 Hz. under different load locations for two piles aligned in the axial direction with spacing (a) 2 m (b) 4 m, two piles aligned in the transverse direction with spacing (c) 2 m (d) 4 m, four piles in square arrangement with spacing (e) 2 m and (f) 4 m.	
Figure 4-15	The different load location IL for four piles in square arrangement when spacing is 4 m at (a) 20 Hz, (b) 40 Hz, (c) 60 Hz and (d) 80 Hz.	
Figure 4-16	Contour plot of IL (in dB) on ground surface (sum over one-third octave bands ranging from 10-80 Hz) when (a) two piles aligned in the axial direction with 2 m spacing (b) two piles aligned in the axial direction with 4 m spacing (c) two piles aligned in the transverse direction with 2 m spacing (d) two piles aligned in the transverse direction with 4 m spacing (e) four piles in square arrangement with 2 m spacing and (f) four piles in square arrangement with 4 m spacing.	
Figure 4-17	The overall IL results from one-third octave bands 10-80 Hz and average over ±10 m width on the ground with different distance away from the pile group.	
Figure 4-18	The average IL for the receiver points with same distance behind the pile group in one-third octave bands at (a) 4 m and (b) 8 m away from the pile group.	:
Figure 4-19	The IL for different pile group configurations with 2 m spacing when receiver points are located on the centreline behind the pile groups at (a) 20 Hz, (b) 40 Hz, (c) 60 Hz and (d) 80 Hz.	

Figure 4-20	The IL for different pile group configuration with 4 m spacing when receiver points are located in the centreline behind pile groups at (a) 20 Hz, (b) 40 Hz, (c) 60 Hz and (d) 80 Hz.					
Figure 4-21	Sketch of the receiver points behind the piles90					
Figure 4-22	The spectrum of IL for different pile group configurations at (a) point R1, (b) point R2, (c) point R3, (d) point R4, (e) point R5 and (f) point R6 on the centreline behind the pile group.					
Figure 4-23	The IL results on the centreline calculated from the difference in overall velocity response level with/without pile evaluated over the range 10-80 Hz. 93					
Figure 5-1	Overview of the modelling approach for the building, ground and interaction					
Figure 5-2	Building model sketch					
Figure 5-3	The 3D finite element model used for verification					
Figure 5-4	Ground response comparison between semi-analytical model and finite element model at (a) 40 Hz and (b) 80 Hz					
Figure 5-5	The semi-analytical model information including the model dimension, position and receiver point position					
Figure 5-6	Insertion loss contour plot and profile along the lines indicated for a unit fixed load (a) at 40 Hz and (b) at 80 Hz					
Figure 5-7	The insertion loss in one-third octave bands at positions A and B indicated in Figure 5-6					
Figure 5-8	Mode shapes of the building with constrained foundation when shell Young's Modulus is 3×10 ¹⁰ N/m²					
Figure 5-9	Displacement level of ground in vertical direction (dB ref=10 ⁻¹² m/N) at (a) point A and (b) point B					
Figure 5-10	Displacement level and insertion loss at mode frequencies (dB ref=10 ⁻¹² m/N) at (a) point A and (b) point B					
Figure 5-11	Mode shapes of the building with constrained foundation when shell Young's Modulus is increased to 5×10 ¹⁰ N/m ²					

Figure 5-12	Displacement level and insertion loss at mode frequencies (dB ref=10 ⁻¹² m/N) at (a) point A and (b) point B when shell Young's Modulus is increased to 5×10 ¹⁰ N/m ²
Figure 5-13	Result of parametric study for different span length and the number storeys (a) Insertion loss at point A (b) insertion loss at point B110
Figure 5-14	The spectral results for the ground response behind the (a) one-storey building and the (b) six-storey building at point A and (c) one-storey building and the (d) six-storey building at point B
Figure 5-15	Spectral IL values for different number of storeys at point A and point B112
Figure 5-16	Contours of the ground IL calculated from the difference in overall ground velocity level with/without building evaluated over the range 1-80 Hz behind a building with varying storeys: (a) one storey, (b) two storeys, (c) three storeys, (d) four storeys, (e) five storeys, and (f) six storeys
Figure 5-17	The spectrum results at specific point on the centreline which is 28 m away from the load (a) the ground velocity level and (b) IL results114
Figure 5-18	The overall results from all frequencies on the centreline receiver points (a) the ground velocity level (reference value is 1×10 ⁻⁹ m/s) and (b) IL results
Figure 5-19	The overall IL contour for the (a) pile foundation building and (b) pile group with same dimensions located between the load and receiver points
Figure 5-20	The average results from all the receiver points at the same distance away from the load (a) the ground velocity level and (b) IL results117
Figure 6-1	(a) A unit load acting on the infinitely long tunnel invert can be construed as (b) the uniform normal stress acting on the unit rectangular area [35].
Figure 6-2	(a) Boundary conditions and (b) equivalent forces in PiP model127
Figure 6-3	Sketch of the track model in MOTIV: coupling of wheel, track and invert.

Figure 6-4	The track roughness spectrum133
Figure 6-5	The location of the railway, building and receiver points
Figure 6-6	The ground response spectrum at 28 m away from the railway on the building centreline for an underground railway with different train speeds: (a) the free field ground response and (b) the ground response in the presence of the building
Figure 6-7	The IL result at (a) 28 m away from the railway (3.8 m from near of the building) and (b) 35 m away from the railway (10.8 m from near of the building) on the building centreline for an underground railway at different train speeds.
Figure 6-8	The results from overall velocity levels include (a) free field response and (b) total ground response on the centreline receiver points located behind the building
Figure 6-9	The IL results on the centreline behind the building derived from overall velocity levels
Figure 6-10	The overall IL contour on the ground behind the piled building when the excitation underground train speed is (a) 60 km/h (b) 80 km/h (c) 100 km/h (d) 120 km/h and (e) 140 km/h
Figure 6-11	The average (a) free field ground response level and (b) ground response level with the building under different underground train speeds, average calculated over ±10 m width
Figure 6-12	The average IL calculated from overall velocity levels averaged over ±10 m width under different underground train speeds
Figure 6-13	The spectrum results on the centreline which is 3.8 m away from the building for (a) the ground velocity level response in the presence of the building and (b) IL results
Figure 6-14	The overall (a) ground velocity level in the presence of the building and (b) IL results from all frequencies for receiver points on the centreline, for cases with different distances between the railway and the building, train speed 100 km/h

Figure 6-15	The IL results contour for cases with different distances between the
	railway and the building. (a) 10 m (b) 15 m (c) 20 m (d) 25 m and (e) 30 m.
	143
Figure 6-16	(a) Ground velocity level in the presence of the building and (b) IL results
	average from all receiver points at the same distance from the building,
	for cases with different distance between the railway and the building,
	train speed 100 km/h144
Figure 7-1	Sketch of underground railway FE model in ABAQUS147
Figure 7-2	Sketch of surface railway FE model in ABAQUS148
Figure 7-3	The boundary conditions, load and receiver points in the FE model for
	surface railway149
Figure 7-4	The sketch of incoherent load for (a) underground railway case and (b)
J	surface railway case
Figure 7-5	Common foundation types of buildings [232]
rigule 7-5	Common foundation types of buildings [202].
Figure 7-6	The profile of structure with different foundation types including (a) raft
	foundation (b) strip foundation (c) pile foundation and (d) box
	foundation
Figure 7-7	The average LSTM level from all the receivers 5.6 m away from the rear
	of the building excited by the (a) surface railway and (b) underground
	railway153
Figure 7-8	The overall LSTM level on the centreline on the ground for different
	foundation types when the excitation is (a) surface railway and (b)
	underground railway154
Figure 7-9	The overall IL on the centreline on the ground for different foundation
	types when the excitation is (a) surface railway and (b) underground
	railway154
Figure 7-10	The contour plots of IL on the ground behind different types of building
	in the surface railway case (a) raft foundation (b) strip foundation in
	normal direction (c) strip foundation in tangential direction (d) pile
	foundation and (e) box foundation

Figure 7-11	The contour plots of IL on the ground behind different types of building foundation in the underground railway case (a) raft foundation (b) strip foundation in normal direction (c) strip foundation in tangential direction (d) pile foundation and (e) box foundation
Figure 7-12	The overall LSTM level averaged over ±9 m width plotted against distance when the excitation is from (a) surface railway and (b) underground railway
Figure 7-13	The overall IL averaged over ±9 m width plotted against distance when the excitation is from (a) surface railway and (b) underground railway. 157
Figure 7-14	Force density levels
Figure 7-15	The results on the centreline at 5.6 m away from the building (a) the ground velocity response level and (b) IL value
Figure 7-16	The average insertion loss results from all receivers 5.6 m away from the building excited by the surface railway
Figure 7-17	The results on the centreline behind the building at 50 Hz: (a) the ground velocity response level and (b) IL value
Figure 7-18	The average insertion loss from all receivers at same distance away from the surface railway at 50 Hz
Figure 7-19	The overall results at different distances away from surface railway on the centreline. (a) The overall ground velocity response level and (b) corresponding IL value
Figure 7-20	Contour plots of IL on the ground behind different types of building foundation for surface railway excitation: (a) raft foundation (b) strip foundation in normal direction (c) strip foundation in tangential direction (d) pile foundation and (e) box foundation
Figure 7-21	The (a) ground velocity level and (b) average over ±9 m width plotted against distance (surface railway case)
Figure 7-22	The results on the centreline at 5.6 m away from the building excited by the underground railway (a) the ground velocity response level and (b) IL value

Figure 7-23	The average insertion loss results from all the receivers 5.6 m away
	from the rear of the building excited by underground railway169
Figure 7-24	The results on the centreline behind the building at 50 Hz including (a)
	the ground velocity response level and (b) IL value170
Figure 7-25	The average insertion loss from all receivers at the same distance away
	from the underground railway at 50 Hz
Figure 7-26	The overall results at different distances away from underground
	railway on the centreline. (a) The overall ground velocity response level
	and (b) corresponding IL value
Figure 7-27	Contour plots of IL on the ground behind different types of building
	foundation for underground railway excitation: (a) raft foundation (b)
	strip foundation in normal direction (stripN) (c) strip foundation in
	tangential direction (stripT) (d) pile foundation and (e) box foundation. 173
Figure 7-28	The average (a) ground velocity level and (b) IL at different distances
	average over ±9 m width plotted against distance from the building
	(underground railway case)174
Figure 7-29	Contour plot of IL for embedded load at depth of 10 m and pile
	foundation with (a) pile length 5 m, (b) pile length 10 m, and (c) pile
	length 15 m
Figure 7-30	The average IL for the influence of various length of pile foundation 176
Figure 7-31	Contour plot of IL for building with pile foundation with pile depth 10 m
	when (a) load depth is 0 m (b) load depth is 5 m, (c) load depth is 10 m,
	and (d) load depth is 15 m176
Figure 7-32	The average IL for pile foundation building under different load depth. 177

Research Thesis: Declaration of Authorship

Research Thesis: Declaration of Authorship

Print name: Xiangyu Qu

Title of thesis: The influence of surrounding structures on ground-borne vibration from railways

I declare that this thesis and the work presented in it are my own and has been generated by me

as the result of my own original research.

I confirm that:

1. This work was done wholly or mainly while in candidature for a research degree at this

University;

2. Where any part of this thesis has previously been submitted for a degree or any other

qualification at this University or any other institution, this has been clearly stated;

3. Where I have consulted the published work of others, this is always clearly attributed;

4. Where I have quoted from the work of others, the source is always given. With the exception

of such quotations, this thesis is entirely my own work;

5. I have acknowledged all main sources of help;

6. Where the thesis is based on work done by myself jointly with others, I have made clear

exactly what was done by others and what I have contributed myself;

7. Parts of this work have been published as:

Qu, X., Thompson, D., Ntotsios, E., Squicciarini, G. (2024). The Influence of a Building on the

Ground-Borne Vibration from Railways in Its Vicinity. In: Sheng, X., et al. Noise and Vibration

Mitigation for Rail Transportation Systems (pp. 595-603). IWRN 2022. Lecture Notes in

Mechanical Engineering. Springer, Singapore. https://doi.org/10.1007/978-981-99-7852-6_56

Qu, X., Thompson, D., Ntotsios, E. and Squicciarini, G. (2023). The influence of the modes of

surrounding buildings on the ground vibration from railways. In: INTER-NOISE and NOISE-CON

Congress and Conference Proceedings (Vol. 265, No. 7, pp. 216-223). Institute of Noise Control

Engineering.

C: +	Date:
Nonatilita.	11910'
oignature.	

Acknowledgements

Pursuing my PhD has been an extraordinary journey that has profoundly deepened my understanding of the world. Along the way, I've had the privilege of interacting with people from diverse cultures. Every challenge I've faced has helped me grow and pushed me to progress, greatly enriching my life. I am deeply grateful to the many individuals who have supported, guided, and inspired me throughout this journey.

I am deeply grateful to my supervisors, Prof. David Thompson and Dr. Evangelos Ntotsios, for their steadfast support and guidance. Despite the challenges posed by the pandemic that limited our in-person interactions at the beginning of my PhD, they ensured we stayed connected through weekly online meetings. Their guidance has been invaluable, not only helping me develop important academic skills but also encouraging me to approach all my work with care and dedication. I deeply value the time spent under their guidance. Also, I am thankful to my other supervisor, Dr. Giacomo Squicciarini, whose insightful advice and guidance have been very helpful in advancing my PhD project.

I also appreciate the assistance of Dr. Wenjing Sun, Dr. Yuan He, and Dr. Dong Zhao with my research project. I would like to thank my colleagues Christopher Knuth, Pablo Miranda Valiente, Kubra Kumrular, Nara Hahn, and all my other colleagues at ISVR for making this journey a rewarding experience.

My heartfelt thanks go to my wonderful family, particularly my father and mother, for their endless support and love. I must also extend my sincerest gratitude to my wife, Jing Wan. Without their support, completing this thesis would not have been possible.

Lastly, I am grateful to the China Scholarship Council for their financial support.

Symbols

A	. A matrix determined by the train type
A	. Magnitude of ground vibration
a	. Radius of the tunnel
<i>a</i> ₀	. Dimensionless frequency
В	. Construction matrix for the train
Č	. Vector of boundary conditions
<i>C</i> _g	. Vibration level attenuation in the ground
<i>C</i> _{gb}	. Coupling loss between the ground and the building
<i>C</i> _b	. Vibration level attenuation in the building
<i>c</i> _p	. Compressional wave velocity
<i>c</i> _s	. Shear wave velocity
<i>c</i> _B	. Bending wave speed in the pile structure
D	. Bending stiffness
$d_{ m pr}$. Distance between pile and receiver point
d_0	. Distance between adjacent source positions considered on a line
E	. Equivalent Young's Modulus
<i>E</i> _p	. Young's Modulus of the pile
<i>E</i> _R	. Young's Modulus of the rail
<i>E</i> _S	. Young's Modulus of the slab
<i>E</i> _s	. Young's Modulus of the soil
f	. Frequency
<i>f</i> _{max}	. Maximum frequency
$\widehat{\boldsymbol{F}}_f$. Vector of external forces at the coupled nodes
$\boldsymbol{\hat{F}_p}$. Equivalent force at pile coupled nodes
$\hat{\mathbf{f}}_s$. Equivalent force at soil

G Green's function of soil
$\widetilde{\widetilde{\mathbf{H}}}$
$\widehat{\mathbf{H}}_{s}$ Transfer receptances from coupled nodes to receivers
H_{s} Soil's receptance matrix
$\widehat{\mathbf{H}}^{G}_{Pile}$ Transfer function between coupled nodes in one pile
$\widehat{H}^G_{Pile\ group}$ Transfer function between coupled nodes in pile group
IIdentity matrix at coupled nodes
I_n Modified Bessel function of the first kind
$I_{ m R}$ Rail moment of inertia
$I_{ m S}$
K Stiffness matrix of the train
\mathbf{K}_0 Global stiffness matrix for building
$\widetilde{\mathbf{K}}^e$ Element dynamic stiffness matrix of the e-th layer
$\widehat{\mathbf{K}}_{ extsf{b}}$ Dynamic stiffness matrix of the building
K_n Modified Bessel function of the second kind
$\widehat{\mathbf{K}}_{\mathtt{p}}$ Dynamic stiffness matrix of the pile
$\widehat{\mathbf{K}}_{\mathrm{p},n}$ Dynamic stiffness of the n -th pile in the pile group
K_z Surrounding soil stiffness matrix for single pile
$k_{\mathbb{C}}$
$k_{ m P}$ Stiffness of the rail fastener
k_x
k_y Wavenumber in y direction
$L_{ m a,room}$ Vibration acceleration level in the room
$L_{ m tunnelwall}$ Vibration acceleration level at tunnel wall
$L_{ m FD}$ Force density level
$L_{ m G}^{ m pile}$ Ground velocity level behind the pile
$L_{ m G}^{ m free}$ Free-field ground velocity level
$L_{ m LSTM}$ Line source transfer mobility level

L _D	Point source transfer mobility level
<i>L</i> _V	
Δl	
M	Mass matrix for train
M ₀	Global mass matrix for building
<i>m'</i>	Mass per unit length of pile
<i>N</i>	The number of axles in the train
$N_j(\theta)$	Shape function of the tunnel
n	The number of receivers
<i>n</i>	Circumferential mode number
p	Vertical force between wheelset and rail
$\widetilde{\mathbf{p}}^e$	Traction at the layered soil interface
P	Transmission path in empirical model
$\widetilde{\mathbf{p}}^i$	Load at layered soil interface
	Load in Pipe-in-Pipe model
$\widetilde{R}_{\text{H}} \dots \dots$	Receptance of the linearised wheel-rail contact spring
R_R	Rail receptance matrix
\widetilde{R}_{T}	Receptance matrix of the wheel-rail contact
R _W	Wheelset receptance matrix
R	Receiver term in empirical model
r	Pile radius
<i>r</i> ₀	Radius of the tunnel
s	Trigonometric functions matrix
<i>S</i>	Source term in empirical model
<i>s</i> _{max}	Maximum coupled node spacing
Ť	Stress coefficient matrix
$\widetilde{\widetilde{\mathbf{T}}}_{j}$	Equivalent load induced by a unit load applied in the tunnel
Û	Total response on the ground

Ŭ Displacement coefficient matrix
$\widetilde{\mathbf{U}}^e$ Displacement at the layered soil interface
$\widehat{f U}_f$ Displacement at the coupled nodes in foundation
$\widehat{\boldsymbol{U}}_i$ Vector of the displacement at the internal nodes
$\widehat{f U}_p$ Displacement at coupled nodes
$\widehat{f U}_{s0}$ Free-field ground response at coupled nodes
$\widehat{f U}_0$ Free-field ground response at receiver points
ŭDisplacement decomposed in the circumferential direction
$\widetilde{\mathbf{u}}^i$ Displacement at layered soil interface
$u_{ m G}$ Displacement of the ground
u_{ref} Reference displacement amplitude
$\widetilde{\mathbf{u}}_{R}$ Displacement of the rail
$\widetilde{\mathbf{u}}_{T}$ Displacement of the train
$\widetilde{\mathbf{u}}_{W}$ Wheelset displacement
$u_{ m s}$ Displacement at soil-foundation interface
$u_{\mathrm{s}0}$ Free-field soil displacement at the coupled nodes
u_1 Displacement at left edge of pile section
u_2 Displacement at right edge of pile section
X Excitation position
$y_{ m gr}$ Ground response receiver point
y
Y_i Transfer mobility from each point
Y_L Line source transfer mobility
z_1 The location of the receiver point
$z_{ m p}$ The location of the unit force
$ ilde{z}$
etaWavenumber in tunnel model
$eta_{ extsf{s}}$

δ	Dirac function
η	Loss factor
θ	Rotational angle
λ	Wavelength
μ	Lamé constant
ν	Poisson's ratio
ξ	Wavenumber in pile model
ρ	Equivalent density
$ ho_{ m p}$	Density of the pile
$ ho_{ ext{s}}$	Density of the soil
σ_{NN}^{W}	Wheelset receptance
τ	Traction at tunnel wall and full space
ω	Circular frequency
Superscript	
<i>Ŷ</i>	In spatial-frequency domain
	In spatial-frequency domain In frequency-wavenumber domain
<i>X</i>	
$ ilde{ ilde{X}}$ $ ilde{ ilde{X}}$	In frequency-wavenumber domain
$ ilde{ ilde{X}}$ $ ilde{ ilde{X}}$	In frequency-wavenumber domain In frequency-wavenumber domain in two directions
$ ilde{X}$ $ ilde{X}$ $ ilde{X}$	In frequency-wavenumber domain In frequency-wavenumber domain in two directions Decompose in circumferential direction
$ ilde{X}$ $ ilde{Z}$ $ ilde$	In frequency-wavenumber domain In frequency-wavenumber domain in two directions Decompose in circumferential direction
$ ilde{X}$ $ ilde{Z}$ $ ilde$	In frequency-wavenumber domain In frequency-wavenumber domain in two directions Decompose in circumferential direction Two dimensional Wavenumber domain finite element method
$ ilde{X}$ $ ilde{X}$ Abbreviations 2D 2.5D	In frequency-wavenumber domain In frequency-wavenumber domain in two directions Decompose in circumferential direction Two dimensional Wavenumber domain finite element method Three dimensional
$ ilde{X}$	In frequency-wavenumber domain In frequency-wavenumber domain in two directions Decompose in circumferential direction Two dimensional Wavenumber domain finite element method Three dimensional Boundary element
$ ilde{X}$	In frequency-wavenumber domain In frequency-wavenumber domain in two directions Decompose in circumferential direction Two dimensional Wavenumber domain finite element method Three dimensional Boundary element Degrees of freedom
\tilde{X}	In frequency-wavenumber domain In frequency-wavenumber domain in two directions Decompose in circumferential direction Two dimensional Wavenumber domain finite element method Three dimensional Boundary element Degrees of freedom Dynamic stiffness matrix
$ ilde{X}$	In frequency-wavenumber domain In frequency-wavenumber domain in two directions Decompose in circumferential direction Two dimensional Wavenumber domain finite element method Three dimensional Boundary element Degrees of freedom Dynamic stiffness matrix Decibel

FE Finite element
FEM Finite element method
FFT Fast Fourier transform
FRAFederal Railroad Administration
FTA Federal Transit Administration
ILInsertion loss
LSTMLine source transfer mobility
MFS Method of Fundamental Solutions
MOTIV Modelling of train induced vibration software
PDE Partial differential equation
PiPPipe-in-Pipe
PML Perfectly matched layer
PSPIPile-soil-pile interaction
SSISoil-structure interaction
SBMSingular boundary method
SSM Seismic-soil metamaterials
StripT The strip foundation whose orientation is tangent to the train's moving
StripN The strip foundation whose orientation is normal to the train's moving
Stabil A MATLAB toolbox for finite element structural mechanics
TLMThin-layer method

Chapter 1 Introduction

1.1 Background

In recent years, railway transportation has generally been seen as an environmentally friendly and sustainable form of transport as it alleviates traffic congestion and air pollution problems [1]. Despite the railway having positive environmental benefits for transporting both passengers and freight, the problems of train-induced ground vibration caused by railways have also garnered progressively more attention. Figure 1-1 illustrates the influence of ground vibration induced by surface railways and underground railways. The vibration spreads through the soil and affects the near-by building. Railway vibration has potential impacts on the residents who live near the railway line [2], may cause damage to neighbouring historic buildings [3, 4], and may interfere with sensitive precision instruments [5]. Therefore, an accurate and efficient prediction model for railway vibration is required for investigations of ground-borne vibration, which could provide evidence to support appropriate mitigation design.

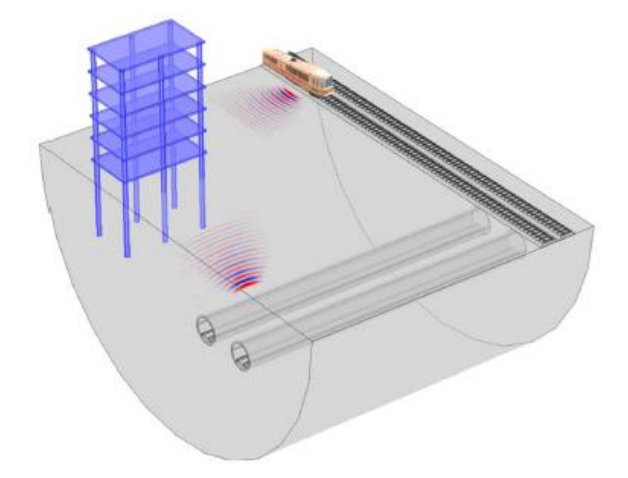


Figure 1-1 Schematic view of how underground railway and surface railway induced ground-borne vibration affects the nearby building [1].

The prediction of railway-induced vibration in buildings is a complicated problem. As shown in Figure 1-2, it can be divided into three subproblems: the source, the transmission path, and the receiver. The first subproblem is the simulation of the source. This part includes modelling the train and the track, including the rail, fasteners, track bed, etc. Vibration is generated at the wheel/rail interface [1], due to the wheel and rail roughness. This excitation is the source of vibration for both surface railways and underground railways. The second subproblem is the transmission path through the soil. Vibration transmitted through the soil is usually calculated assuming a free-field ground. It is usual to choose an elastic horizontally layered half-space to represent the soil. Because the soil condition is very complex in actual situations, it is difficult to

find a suitable model to simulate the soil comprehensively. Thus, to simulate the ground, many assumptions and simplifications are required. The third subproblem is the receiver building. For this, a dynamic soil-structure interaction (SSI) model is usually considered to simulate the attenuation that occurs when the vibration is transmitted into the foundation, represented for example as a coupling loss [6]. Usually, the surface ground vibration at receiver point's location forms the basis for the target building's vibration. In some cases of railway-induced vibration, the primary concern is not with the buildings acting as receivers but rather with the vibrations transmitted through the ground. Consequently, the third sub-problem can be omitted and the response is identified solely as that of the receiver point.

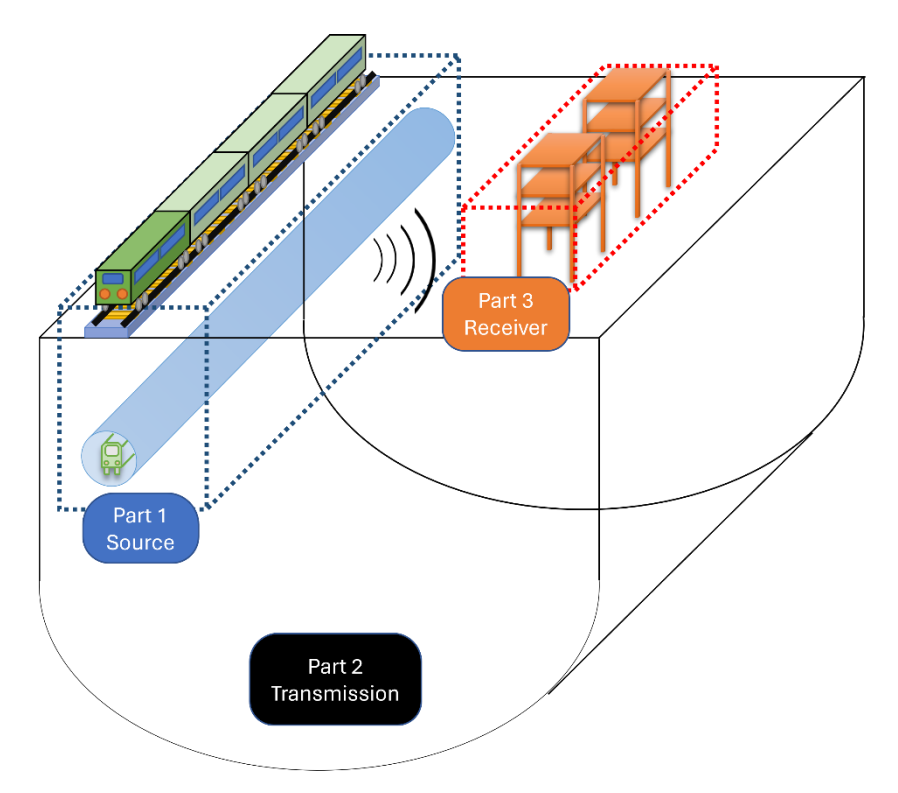


Figure 1-2 Sketch of steps involved in predicting railway-induced vibration in buildings.

Researchers have developed various methods and models to predict railway-induced ground vibration. However, in order to obtain the calculation results more conveniently and quickly, many assumptions are made. Focusing on the second subproblem, the transmission path, the ground is usually considered as a free field, which means the impact of the presence of surrounding structures between the vibration source (track) and the receiver position is neglected. This is one of the most important assumptions for the vibration transmission path. But in fact, as seen in Figure 1-3, between the vibration source and the target buildings (the buildings that are considered to assess whether the railway vibration meets the criteria), or around the target building, there may be many other surrounding structures located in the transmission path. When the SSI is considered, these surrounding structures can be seen to affect the free-field vibration and will then have an impact on the vibration response of the target building. To investigate the response of the target building, it is essential first to understand the ground surface response at

the location of the building. Thus, it is necessary to investigate the influence of surrounding structures on ground-borne vibration from railways, and the effects of the foundations of these surrounding buildings on the ground vibration.

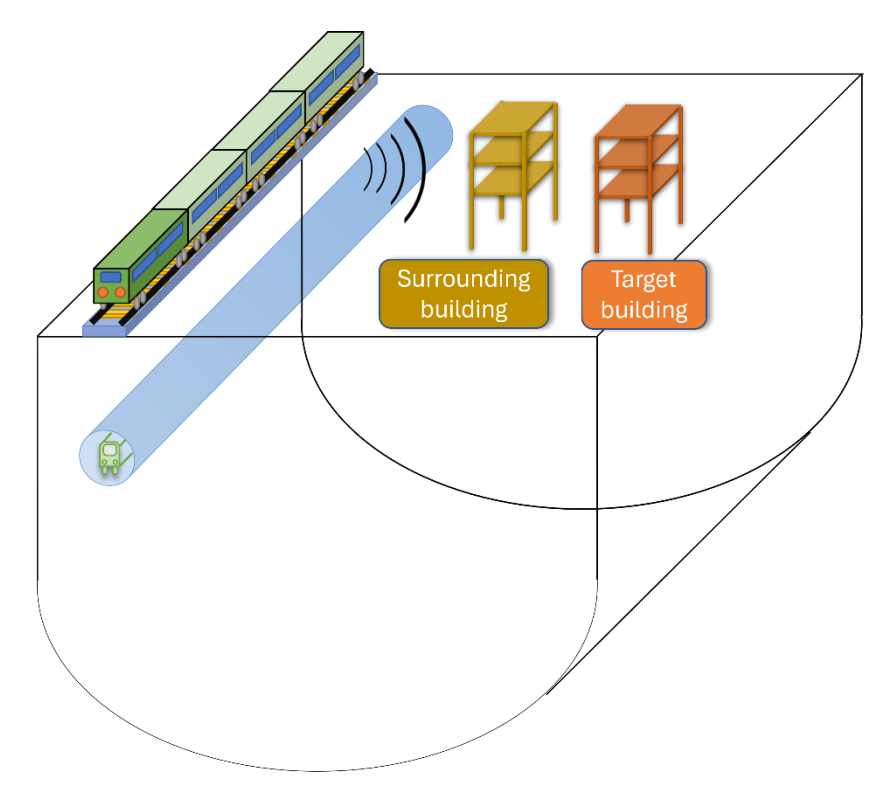


Figure 1-3 Sketch of surrounding building and target building.

Certain surrounding structures located in the transmission path near the target building may affect the transmission path of ground vibration, leading to inaccuracies in the results of ground vibration prediction. Addressing this question of relevance, this thesis concentrates on analysing the influence of structures situated in the vicinity of the railway and within the transmission path to assess their impact on ground vibration.

1.2 Aim of the thesis

The ground vibration is key to how the target building responds to vibrations. To make the model simpler and faster to compute, the study focuses only on the ground vibration, without explicitly including the target building. The aim of this thesis is to investigate and analyse the influence on the ground vibration induced by unit loads and railways from surrounding structures located in the transmission path. The single pile, pile group, piled foundation building, and a surrounding building with various types of foundation located in the transmission path are investigated.

The main objectives of this work are:

1. To explore the effects on ground vibration caused by a single pile situated in the transmission path, for a fixed harmonic unit load external to the pile. To assess the

- accuracy of the model including the effects of the rotational degrees of freedom (DOFs) at coupled nodes.
- 2. To assess how the configuration of a pile group influences the mitigation and amplification of ground vibration. To assess the accuracy of the model with different numbers of piles.
- 3. To investigate the influence of a building with pile foundations on ground vibration, examining the modes of the building and their relationship with ground response, and exploring how variations in the number of storeys and span length affect the ground vibration.
- 4. To develop a comprehensive model including the train, track, tunnel, soil, and building which could predict the ground vibration. This model will enable the investigation of ground vibration under a broad range of conditions.
- 5. To examine the impact of various foundation types on ground vibration in the vicinity of the building. To assess the ground vibration effects under different foundation types when the excitation is a surface railway or an underground railway.

1.3 Original contributions

The main original contributions of this thesis are outlined as follows.

- A semi-analytical pile-soil model is developed to analyse the influence of a single pile on
 its surrounding soil. The range of frequencies within which the model has the capability to
 predict the ground response reliably is established under different conditions.
- 2. A semi-analytical model has been constructed to examine the impact of a pile foundation on the reduction of ground vibration.
- 3. The relationship between the building modes and the ground vibration is revealed using this model.
- 4. An enhanced comprehensive model, building upon the semi-analytical framework, is developed to calculate ground vibration induced by underground railways. Compared with the MOTIV (Modelling Of Train Induced Vibration software) model [7, 8], the inclusion of the building using a finite element (FE) model contributes to a more extensive model, enabling the consideration of more complex cases, for example, where surrounding buildings are located within the transmission path.
- 5. Based on a hybrid modelling approach, the influence of five different kinds of building foundation on the ground response is investigated. This study systematically summarises the impacts of the various building foundations on the surface ground vibration.

1.4 Structure of the thesis

The structure of this thesis is outlined in this section. Following the introduction in this first chapter, a literature review is presented in Chapter 2 focusing on ground vibration prediction methods, and soil-structure interaction.

Chapter 3 introduces a semi-analytical approach for single pile-soil interaction and the ground vibration in the presence of a single pile when there is a fixed harmonic unit load applied either on the pile or on the ground near the pile. The model accuracy is evaluated by comparing this semi-analytical single pile-soil model with an FE numerical model. Then the single pile located in a layered surrounding soil is investigated under different soil parameters. The ground response and ground vibration mitigation effects are studied.

Based on the single pile-soil interaction model, Chapter 4 introduces a model of the influence of a pile group on the ground vibration. The model accuracy range is investigated by comparison with an FE model. Then different pile group configurations are investigated: two piles located in a line perpendicular or parallel with respect to the point load-receiver line, and four piles in a square arrangement. The ground vibration behind the pile group is also calculated.

In Chapter 5, the semi-analytical model is extended to analyse the mitigation effects of ground vibration caused by a building with a pile foundation. Additionally, this chapter investigates the relationship between the building's modes and the mitigation effects of ground vibration. Subsequently, a comparison between the building and a similarly dimensioned pile group is conducted to examine the influence of the upper structure on the ground behind the building.

In Chapter 6, a comprehensive model is developed including the train, track, tunnel, soil, and a building structure. The building is modelled by using an FE model. The other components are built by using a semi-analytical model, MOTIV. The influence of a building with a pile foundation on the ground vibration can be calculated when the excitation is from an underground railway. The results, including the ground response at a specific receiver point behind the building, the overall response from the full frequency range, and the average results from all receiver points at the same distance behind the building, are presented.

In Chapter 7, a hybrid model is developed to investigate the ground vibration caused by trains and this is used to consider the impact of different kinds of building foundations. This hybrid model consists of two subcomponents: a semi-analytical model to determine the force density level and a 3D FE model for the line source transfer mobility (LSTM) level in the presence of the building. Then the final ground response and the insertion loss results are summarised.

Finally, the conclusions and recommendations for future work are summarised in Chapter 8.

Chapter 2 Literature review

To study ground vibration from railways, it is crucial to employ effective prediction techniques. In addition to the vibration prediction method, soil-structure dynamic interaction also significantly influences the vibration. In the literature review, the prediction methods for the railway-induced ground-borne vibration are summarised. Then different types of dynamic models for the pile (structure)-soil interaction are reviewed.

2.1 Ground-borne vibration prediction methods

Several researchers have published review papers to summarize the mechanisms and methods for predicting ground vibration. Gutowski and Dym [9] provided an early review of the propagation of ground vibration in soil. Thompson, Kouroussis and Ntotsios [1] provided a comprehensive review of the ground vibration problem including the ground vibration criteria and mechanisms. Yang and Hsu [10], and Sheng [11] focused on the ground vibration induced by underground railways. Kouroussis, Connolly and Verlinden [12] focused on the influence of different train parameters.

Generally, based on the stage of train-induced ground vibration prediction, models can be categorised into scoping models in the initial process, environmental assessment models during the planning process, and detailed design models throughout the construction and design process [13]. The prediction methods can be divided into three categories, namely analytical methods, numerical methods, and empirical methods. In recent years, hybrid models combining empirical methods with other prediction techniques have also been utilised to predict train-induced ground-borne vibration [14]. The approach used will vary depending on whether the interest is in the vibration of existing or new sensitive target buildings due to new or existing railways. Additionally, with recent advances in machine learning models and the availability of large datasets, predicting train-induced ground vibrations using machine learning has become increasingly popular [15-18].

2.1.1 (Semi) analytical methods

Analytical models (or semi-analytical models) are used to describe a problem mathematically. When predicting ground-borne vibration, the elastodynamic partial differential equations (PDE) of the soil must be solved using appropriate boundary conditions and initial conditions. Typically, integral transforms, particularly the Fourier transform, are applied to solve the system of equations employed to represent the physical problem. The fast Fourier transform (FFT) is a

widely used numerical method for obtaining results. Thus, this method is often referred to as a semi-analytical method. Analytical models contain many assumptions and simplifications. The physical concept of the analytical models is clear, and the calculation efficiency is high. Compared to numerical models, which typically yield approximate numerical solutions, analytical models directly derive from fundamental theoretical equations and involve simplified assumptions, allowing them to directly obtain exact solutions. They are helpful to analyse the nature of vibration generation and propagation and can obtain reliable results with appropriate assumptions. The (semi) analytical models are commonly separated into sub-models representing the train, track, and ground.

When investigating railway induced ground-borne vibration, one of the key issues is to simulate the response of the soil by using a homogeneous or layered elastic half-space model. For a fixed harmonic load excitation on the half space, researchers such as Pak and Guzina [19], Liu et al. [20], He et al. [21] have explored ground responses using Green's function approaches for both layered and poroelastic half-spaces. Regarding the moving load excitation on a half space, Eason [22] derived analytical results. Sheng et al. [23] developed the moving Green's function in a free field. Initially, the half-space free field was modelled in cylindrical coordinates and then transformed into Cartesian coordinates. Addressing more complicated situations, Jones et al. [24] investigated the ground vibration excited by a moving rectangular load. Hu et al. [25] investigated the saturated soil response under a moving load. Additionally, Sheng et al. investigated the ground response induced by a railway based on a fixed load [26] and a moving load [27] applied on the track. Figure 2-1 shows the moving load applied on the track.

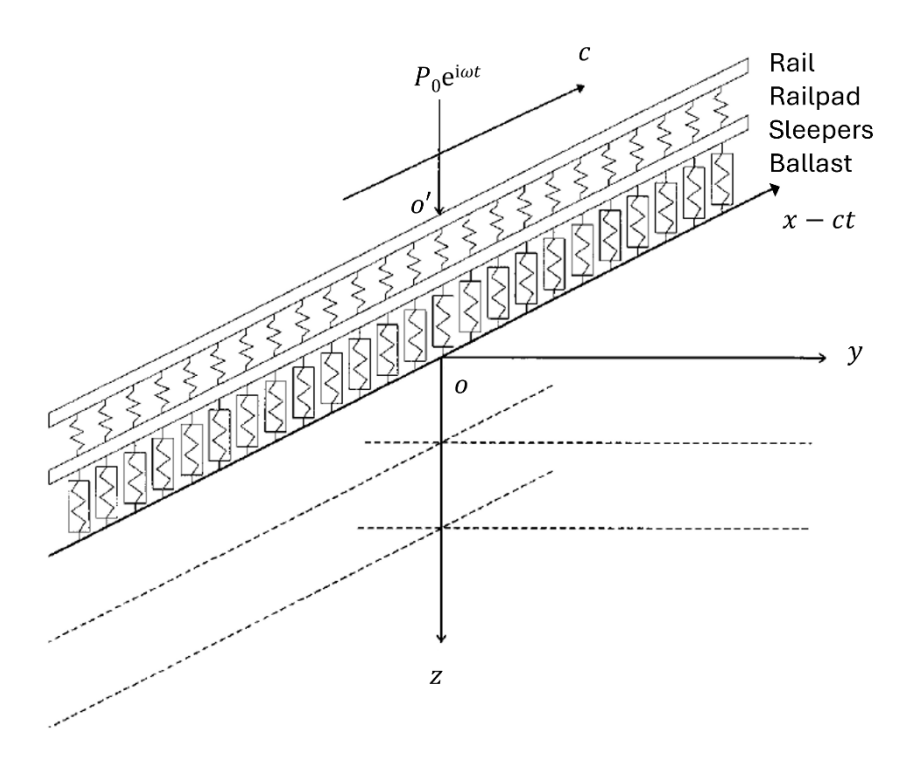


Figure 2-1 Sketch of the model of a track on layered ground excited by a moving load [27].

It is often assumed that the ground consists of parallel layers with homogeneous material properties within each layer. Under these assumptions, the dynamic stiffness matrix (DSM) method can be used to simulate the ground response for a homogeneous half-space or a layered half-space [7, 28, 29]. In this method, the stiffness matrix of the soil can be obtained conveniently and directly, and the soil is represented by linear materials. The model response is calculated in the frequency-wavenumber domain. The soil model can also be coupled with other models such as a train-track theoretical model to simulate the ground-borne vibration induced by the train.

Additionally, some classical semi-analytical models are also used to simulate the ground in the research field of railway vibration. The thin-layer method (TLM) is a semi-analytical method for the analysis of elastic wave propagation in a layered soil which can also be used in the railway vibration field [30, 31]. The basic principle of this method is to discretise the ground in the vertical direction and divide the soil into multiple thin layers. Then the boundary conditions of the soil foundation are introduced to establish the global stiffness matrix which is solved to determine the dynamic response of the layered medium. Although the TLM employs the finite element concept for different layers using shape functions, the stiffness matrix for each layer can be derived analytically. Therefore, it can be classified as a semi-analytical model. As in the DSM method it is formulated in the frequency-wavenumber domain.

Due to the dominance of vertical vibration and considerations regarding calculation efficiency and model simplicity, two-dimensional analytical models have been developed for predicting ground vibration. In underground railway cases, embedded beam models prove to be useful for

investigating ground vibration induced by the railway in a tunnel. Metrikine and Vrouwenvelder [32] investigated ground vibration by employing an embedded infinitely long Euler-Bernoulli beam model to represent the tunnel. The soil rests on a rigid base, indicating that the layered soil is finite in depth and supported by a rigid foundation. The model of a beam embedded in soil has become a popular framework for investigating ground vibration induced by underground railways, with several researchers exploring this further. Koziol et al. [33] investigated the ground response when an infinite beam is embedded in a half space. Based on this method Yuan et al. [34] investigated the saturated poroelastic soil dynamic response. Hu et al. [25] investigated the saturated soil based on this method. However, when using the beam model to simulate an embedded tunnel, it fails to simulate high frequency responses accurately because the beam does not account for wave transmission in the circumferential direction.

The Pipe-in-Pipe (PiP) model is also a widely used semi-analytical model to simulate underground railways in tunnels [35-37]. The inner pipe is based on shell theory, and represents the tunnel wall. The outer 'pipe' is based on continuum theory, and is used to simulate the surrounding soil which is considered to be infinite. A sketch of the PiP model is shown in Figure 2-2. It can produce more accurate results than the embedded beam model. Gupta et al. [38] validated this model and analysed its advantages especially in terms of computation efficiency. Then, based on the PiP model, the dynamic response in more complicated situations has been investigated, including twin tunnels [39], floating-slab track in tunnels [37], a double-deck circular tunnel [40], and periodic jointed tunnels [41]. For the ground response, Hussein et al. [42] investigated the ground response by employing fictitious forces and 2.5D Green's functions in a full space [43]. They further extended their analysis to a layered half-space using the dynamic stiffness matrix [44].

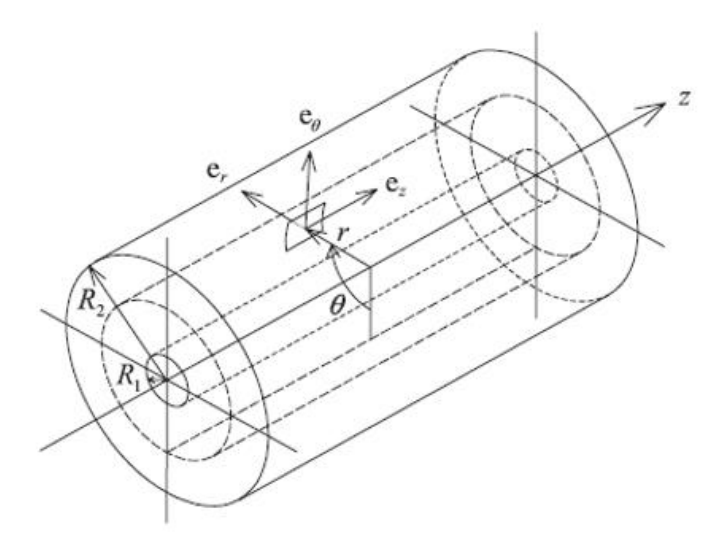


Figure 2-2 Sketch of the PiP model [35].

Recently, Yuan et al. [45] provided a semi-analytical model for ground vibration. The total wave field in a half-space containing a cylindrical hole is characterised by outgoing cylindrical waves and downward-propagating plane waves. The tunnel was located in a homogeneous half space. He et al. [46] investigated a tunnel located in a layered soil based on this method combined with the transfer function method, which was first developed by Thomson [47] and Haskell [48]. Yuan and He [49-52] expanded the applications of this semi-analytical model to cases involving shallowly buried tunnels and existing buildings.

In summary, the homogeneous or horizontally layered half-space analytical models are used for the ground vibration in railway ground vibration research. There are various methods to compute the response in the framework of these models and, especially, there are multiple models to consider the response of track-soil or tunnel-soil systems. The concepts and assumptions of these ground analytical models are clear. However, few studies considered the foundation of the building in the ground model and its influence on the ground-borne vibration propagating to a target building.

2.1.2 Numerical methods

Numerical methods can be used to investigate the effects of more complex geometry and materials. In these, the ground is usually discretised using finite elements or boundary elements. The challenge is that the number of elements becomes large as the scale of the problem increases, especially at higher frequency. In order to represent wave propagation, at least six elements per wavelength are commonly required [53]. Therefore, the number of elements in a large model can become huge, resulting in very large computation times. Fortunately, with the development of computer science, numerical methods which require high computational power

are capable of simulating the whole system of the railway, ground, and buildings with more details in an acceptable efficiency. The numerical methods can be categorised into time-domain and frequency-domain approaches.

2.1.2.1 Time-domain numerical models

With the continuous improvement of computing power, the use of the finite element method (FEM) has developed rapidly in the field of ground-borne vibration. Initially, two dimensional (2D) methods were utilised due to the limitations of computer power [54]. However, the environmental vibration caused by trains is a complicated three-dimensional coupled problem, including the effects of train load motion and soil-structure dynamic interaction. 2D models are capable of describing dynamic responses within the plane of the model only and cannot account for variations in the third dimension. Consequently, 2D models cannot achieve accurate predictions. A common approach is a 3D two-stage time-domain model based on the 'weak coupling' method. Connolly et al. [55] and Kouroussis et al. [56, 57] built a two-stage time-domain model to investigate the influence of vehicle and track parameters on the environmental vibration. The first stage of such an approach usually consists of a sub-model consisting of a multibody train model on a flexible beam track model where the embankment is considered to be rigid or represented by an equivalent stiffness. In the second stage the support forces beneath the track obtained from the first model are applied to the soil sub-models. That represents a 'weak coupling' assumption in which the details of the ground are assumed not to influence the vehicle-track interaction.

When an FE model is used to represent the ground, the boundary of this model plays an important role as it is important to prevent spurious reflections from the edge of the domain. Specific boundary conditions used with the finite element method to investigate environmental vibration problems include viscoelastic boundaries [58-61], scaled boundary finite elements [62], infinite elements [63-68], perfectly matched layer (PML) boundaries [69], and absorbing boundary conditions [70, 71]. Additionally, the FE method can account for soil anisotropy and complex layering, offering advantages over traditional analytical models.

When a BE model is used to represent the ground, the finite element formulation is applied for the track structure while the boundary element time-domain formulation is applied for the infinite ground [72, 73].

Unlike with the frequency-domain method discussed below, the time-domain method can also consider the non-linear response of the soil [74-76]. When applied to investigations of environmental vibration, the 3D time-domain method allows for the consideration of details such as non-linear material properties, which are not feasible in frequency domain models. The time-domain method can handle many complex situations with fewer limitations especially for the soil

compared with analytical methods. However, some complicated time-domain models have the drawback: they usually require a long calculation time. Additionally, in many situations, it is difficult to obtain the input data to describe the nonlinear or inhomogeneous properties of the soil.

2.1.2.2 Frequency domain numerical models

A 3D numerical model can calculate specific cases and yield accurate results. However, computational efficiency remains a significant challenge. Upon comparing the 2D and 3D models, Xu et al. [77] and Real et al. [61] discovered that the 3D model yields more accurate results but its computational time was 600 times greater than that of the 2D model. Due to the large calculation time required for full 3D models, the prediction model can be simplified to reduce the calculation cost by making use of the characteristics of the railway structure. A common assumption is that the track and the soil layers are uniform in the direction of train travel. Therefore, a 2D finite element mesh or 1D boundary element mesh is used for the cross-section, with the third dimension defined in the wavenumber domain. An inverse Fourier transform over wavenumber is used to obtain the calculated results in the spatial domain. This kind of model is known as the 2.5D approach, which is the main branch of the frequency-domain models. By assuming all the materials in the system are linear, the response of the ground or the building can be calculated in the frequency-wavenumber domain by applying a Fourier transform.

Some 2.5D finite element prediction models have been used with artificial boundaries [78-81], infinite elements [82-84], boundary elements [85-90], or PML [91-95] to simulate the infinite ground efficiently. Also, some new types of boundary conditions have been investigated. Yang et al. [96] combined the PML and infinite elements as the boundary condition to simulate the wave propagation in the soil. In [97], the finite elements were coupled with the scaled boundary finite element method (FEM-SBFEM).

The 2.5D models can widely investigate environmental vibration problems caused by surface railways and underground railways. However, such a 2.5D model does not consider the characteristics of the periodic support of the track structure and the resulting parametric excitation. In order to solve this problem, the periodic finite element method has been used, in which the Floquet transform is employed to represent the periodic geometry of the soil and tunnel. This method is less efficient than 2.5D track-ground models, but it can improve the computational efficiency compared with 3D models. Additionally, the periodic FE model does not need to account for the wave-field originating from outside the domain in the longitudinal direction, making it simpler than fully 3D models. Based on this method, different boundary conditions applied to the soil have been investigated including the fixed boundary [98], artificial boundary conditions [99], boundary element conditions [5, 100-103], infinite element boundary

conditions, and PML [104, 105]. One example of a unit cell of the periodic FE model with PML boundary is shown in Figure 2-3.

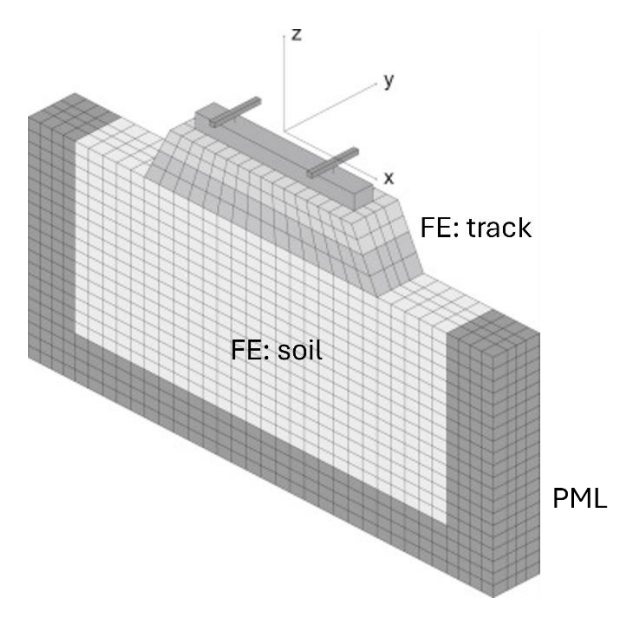


Figure 2-3 Unit cell of the periodic finite element with PML [105].

The BE method includes the radiation condition implicitly, and can be used to simulate an infinite ground. In some early FE-BE models in 2D or 2.5D, the BE was based on full-space Green's functions [106, 107]. Consequently, the ground surface and interfaces between different soil layers need to be discretised, which increases the number of elements. Alternatively, Green's functions based on a half space or a layered soil can be applied in BE equations, thereby requiring fewer mesh elements [108, 109].

The singular boundary method (SBM) is a meshless method. The SBM eliminates the computationally expensive integration procedure in the BE method. It serves as an alternative to mesh-based approaches to investigate the wave propagation problems and railway ground vibration problems [110-112]. This method eliminates the need to consider connectivity between elements and nodes, thereby simplifying the model and enhancing computational efficiency.

Additionally, sometimes to improve the calculation efficiency a time-domain FE vehicle-track model is coupled with the ground that is modelled in the frequency and wavenumber domain beneath the sleepers. Such models are hybrid time-domain and frequency-domain models [113, 114].

Overall, there are many types of numerical model, which are convenient for modelling and calculation. Due to the different assumptions made in different approaches, there are differences in the accuracy and efficiency of the calculation results.

2.1.3 Empirical models

Empirical models, which may be based on measured data, theoretical or numerical predicted results, are relatively simple. Empirical methods are usually used in the preliminary stage of environmental impact assessment and prediction, i.e. the initial feasibility study stage of the construction of a new railway line or building. Empirical methods have high prediction efficiency and low computational cost, but the prediction accuracy is relatively low if it is used for a situation other than the one where the measurements are taken. According to ISO 14837-1 [13], predicting vibration levels can be divided into three subproblems: the vibration source, the transmission path, and the receivers. The magnitude of ground-borne vibration at receivers can be represented as

$$A(f) = S(f)P(f)R(f)$$
(2-1)

where S(f) is the source term, P(f) represents the transmission path, R(f) is the receiver term and f is frequency.

A commonly used empirical method is based on the procedures developed by the Federal Railroad Administration (FRA) and the Federal Transit Administration (FTA) in the USA [115, 116]. This chain formula considers the three factors mentioned above that affect the vibration but is expressed in decibels. The vibration velocity level at receiver point i is written as

$$L_{V,i} = L_{FD} + L_{LSTM,i} + C_{gb}$$
 (2-2)

where $L_{\rm FD}$ is the force density level (FDL), $C_{\rm gb}$ is an adjustment to account for ground-building foundation interaction and attenuation of vibration amplitude as vibration propagates through the building, and $L_{\rm LSTM,}i$ is the line source transfer mobility (LSTM) level. It can be calculated by

$$L_{\text{LSTM},i} = 10 \log_{10} \left(d_0 \sum_{j=1}^{l} |L_{\text{P}i,j}|^2 \right)$$
 (2-3)

where d_0 is the distance between adjacent source positions considered on a line. $L_{\mathrm{P}i,j}$ is one of l point source transfer mobilities between excitation point j and receiver point i. The result $L_{\mathrm{P}i,j}$ is expressed in decibels. A sketch of the method used to determine the LSTM for excitation on the ground surface is shown in Figure 2-4.

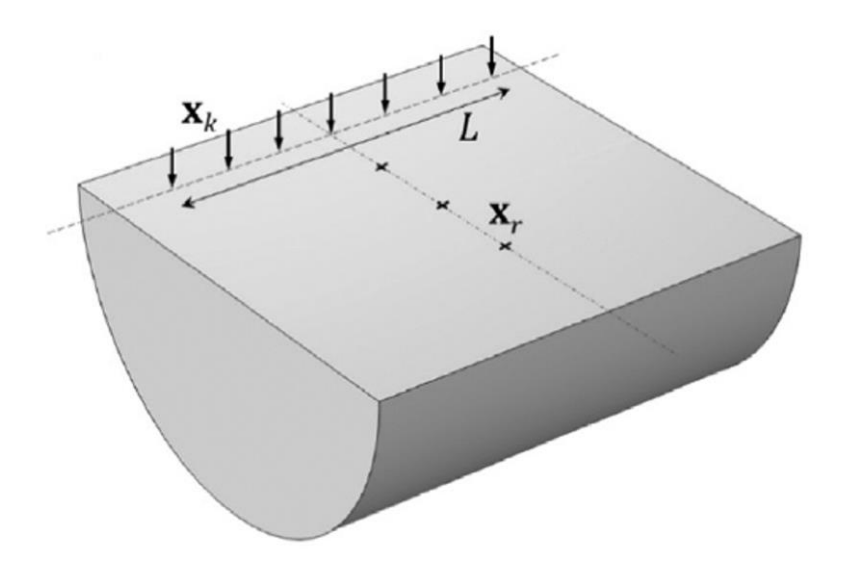


Figure 2-4 Determination of line source transfer mobility for excitation on the ground surface [117].

There are also some other empirical methods based on measured data. Kurzweil [118] presented a chain formula for estimating vibration spectra due to ground-transmitted vibration in buildings near subways. The vibration acceleration level in the room is given by

$$L_{\rm a, room} = L_{\rm tunnel \, wall} - C_{\rm g} - C_{\rm gb} - C_{\rm b}$$
 (2-4)

where $L_{\rm tunnel\ wall}$ is the vibration acceleration level at the tunnel wall, $C_{\rm g}$ is the vibration level attenuation in the ground, $C_{\rm gb}$ is the vibration level attenuation when the vibration is transmitted through the building foundation, also known as coupling loss between the ground and the building, and $C_{\rm b}$ is the vibration level attenuation within the building. All terms are in decibels.

Melke [119] also investigated the chain of transmission losses within the source-path-receiver system. Madshus et al. [120] focused on the chain of transmission based on a large number of vibration measurements in Norway and Sweden. Also some empirical methods based on measured data have been applied in the UK [121] and Switzerland [122]. Rossi and Nicolini [123] propose a simple empirical prediction model for train-induced vibration; the maximum differences between the model results and measured data were 5.8 dB. With et al. [124] presented a validation of an empirical model to predict train-induced ground vibration in a preliminary design phase. Gjelstrup et al. [125] built a novel empirical model for predicting railway-induced vibration nuisance and structure-borne noise in nearby dwellings exposed to railway traffic. Auersch [126] developed a simple and fast prediction model based on the three components from Eq. (2-1).

2.1.4 Hybrid methods

Hybrid methods, also called semi-empirical methods, have attracted increasing attention. The chain formula is too simplified for accurate prediction, whereas the reliability of numerical models and the accuracy of their prediction results depend on the accuracy of the input parameters. It is sometimes very difficult to obtain the physical parameters of the whole system with sufficient accuracy. Therefore, hybrid prediction models based on empirical methods combined with numerical methods are becoming popular.

Verbraken et al. [127] and Kuo et al. [14] used such a hybrid empirical-numerical methodology to predict the ground vibration. This hybrid approach can use a combination of measured data, from train passages or from hammer excitation, and numerical models. Three cases can be considered, where both railway and building are present, where the railway is present but there is no building at the site, and where the building is present but there is no track at the site.

Kouroussis et al. [128, 129] predicted the ground vibration by combining the numerical and experimental prediction methods based on the FRA approach framework [115]. Colaço et al. [130] predicted the vibration level in a building by combining numerical results and experimental measurements. The SILVARSTAR European project [131] investigated the combination of empirical and numerical models for the source term and transmission path term in Eq. (2-2).

Regardless of whether (semi) analytical methods, numerical methods, or empirical methods are used, it is necessary to simplify the vehicle, tunnel, and soil systems. This simplification can affect the accuracy of vibration predictions. To improve the precision of vibration prediction results in the detailed design process, more accurate input parameters for the soil layers can be obtained through on-site measurement. Due to its consideration of the specific conditions of the tunnel and layered soil, the hybrid approach based on measured transfer functions is able to give more precise prediction findings. Lai et al. [132] assessed the vibrational impact of underground railway traffic on two buildings in Rome by combining experimental measurements with numerical simulations. Liu et al. [133] predicted the ground-borne vibration using the hybrid approach framework that includes an analytical train model for the source term and an in-situ measured transfer function for the transmission path term.

2.2 Single pile-soil dynamic interaction

In the previous section, some prediction models for railway-induced ground vibration have been introduced. It is also important to predict the response of buildings based on the ground response. Therefore, soil-structure interaction (SSI) serves as the fundamental basis for this analysis.

An important element in SSI is the interaction between a single pile and the soil, the modelling of which has developed rapidly through theoretical research. Kuo and Hunt [134] presented a thorough review of modelling methods for the dynamic behaviour of single piles and pile groups. They summarised linear single-pile-soil dynamic models into four broad groups.

The first and simplest approach represents the soil interacting with the pile as a group of equivalent springs, based on dynamic Winkler foundation theory. In this method it is assumed that outward propagating waves in the soil are in plane-strain conditions [135]. In Novak's theory [136, 137], the soil is simulated by a set of infinite elastic layers, which are applied to the pile as equivalent springs. The pile can be modelled by using the equations of motion of a beam or elastic column. Some experimental results support Novak's theory [138]. Recently, this model has also been extended through the use of nonlinear springs [139], viscoelastic effects [140, 141] and the variable section impedance of the pile [142]. Additionally, using this method, the dynamics of pile groups have been investigated [143, 144]. However, Novak's model is a 2D model and cannot accurately capture the effects of the third dimension on the pile and surrounding soil.

The second approach involves representing the soil as an elastic continuum, such as a cylinder, which is coupled to a beam or column model of the pile to overcome the limitations from the Winkler foundation theory. The interaction between the pile and soil is represented by using equivalent loads. Novak and Nogami [145, 146] used an analytical model to investigate pile-soil interaction vibration problems when the motion is limited to one plane. Kuo and Hunt [147] have utilised elastic-continuum formulations in the wavenumber domain to assess the dynamic response of piles. The pile was represented as a rod in axial vibration and as an Euler-Bernoulli beam in bending. The fictitious pile method [148-150], which represents the pile as a beam with a series of uniform patch loads along its length, could be categorised as one of the elastic continuum approaches. Based on such single-pile models, pile group models have also been developed and widely applied. Kaynia and Kausel [151] developed a semi-analytical model for the dynamic response of a single pile and a pile group in layered soil. Different types of loads are introduced corresponding to the pile-soil traction. The sketch of the single pile model from Kaynia and Kausel is shown in Figure 2-5.

Chapter 2

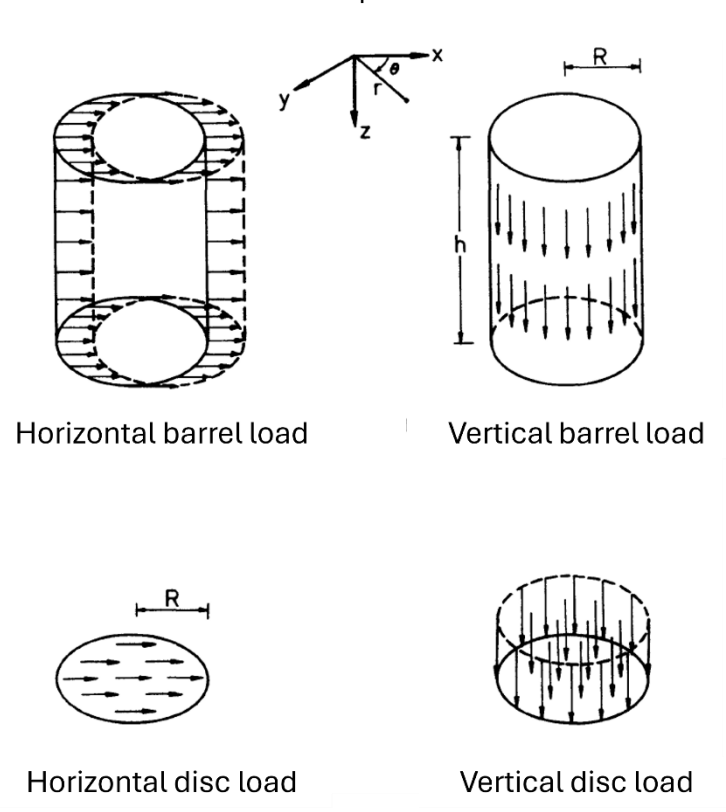


Figure 2-5 Sketch of different types of loads in the single pile model [151].

A third modelling technique makes use of the boundary element (BE) method to represent the soil. The pile can be represented using an analytical model, a FE model, or a BE model. In this approach, if the full-space Green's function is used, the ground surface boundary and the soilpile interaction surface are discretised and represented by boundary elements. Kattis et al. [152] have used this method to evaluate the pile-soil dynamic behaviour. If the half-space Green's function is used, only the pile surface has to be discretised. Kaynia [153] used the BE method based on half-space Green's functions to solve the dynamic response of pile foundations, and based his analysis on the static interaction factor principle proposed by Poulos et al. [154], applied to the dynamic case. Masoumi and Degrande [155] used a subdomain formulation to predict the free-field vibration due to pile driving. Auersch [156], Sen et al. [157], Maseo et al. [158] and Talbot and Hunt [159] investigated the dynamic behaviour of piles and pile groups by use of a half-space BE formulation. More recently, Edirisinghe and Talbot [160] investigated the dynamic behaviour of a pile near an underground railway tunnel based on the half-space BE method. However, the calculation efficiency is a limitation of some BE models. To address this, Edirisinghe and Talbot [161, 162] investigated the pile-group interaction through the soil by using the BE method with an iterative wave-scattering approach, which could improve the computational time. Conto et al. [163] investigated the single pile-soil interaction using a meshless singular boundary method in an effort to reduce computational time. A sketch of this single pile model is shown in Figure 2-6.

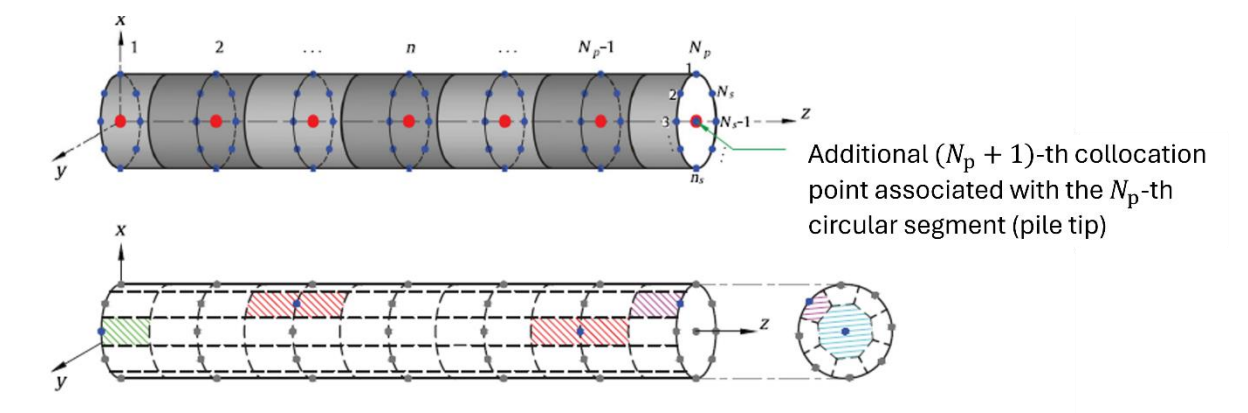


Figure 2-6 Sketch of meshless single pile model [163].

The application of the FE method for the soil constitutes the fourth method. In this case a suitable boundary condition is required to prevent wave reflection at the edges of the domain as discussed in Section 2.1.2. To represent the pile-soil interaction, either an axisymmetric model [148] or a three-dimensional (3D) solid element model [164] can be adopted. Kuhlemeyer [165, 166] used the FE method to investigate the dynamic response of a pile in the lateral and vertical directions when a force is applied on the pile cap. A comparison with Novak's model [135] was also presented, indicating good agreement at very low frequency.

2.3 Soil-structure interaction

To achieve more accurate predictions of train-induced vibrations in buildings, it is necessary to consider building coupling loss. In analytical and numerical models, this coupling loss is related to soil-structure interaction (SSI), whereas in empirical models, it is typically based on specific coefficients.

2.3.1 Soil-structure interaction in analytical model

The analytical model is a rigorously formulated framework for ground vibration. Within this model, the building coupling loss is generally characterised through SSI. More recently, the study of SSI has not only been limited to theoretical research and application in seismic engineering, but has also been applied in research into train-induced ground vibration. SSI is an important part of submodelling approaches. In some research a fast and convenient method has been presented for evaluating the influence of foundations. Kuo et al. [167] built semi-analytical models to evaluate the effects of piled and raft foundations on the vibration level transmitted into buildings near railways. From Hussein et al. [168], based on the dynamic stiffness matrix of the soil, a transmission matrix H could be calculated, which represents the soil-pile interaction at different

coupled nodes between the soil and the foundation on the piles. A sketch of the model used by Hussein et al. [168] is shown in Figure 2-7.

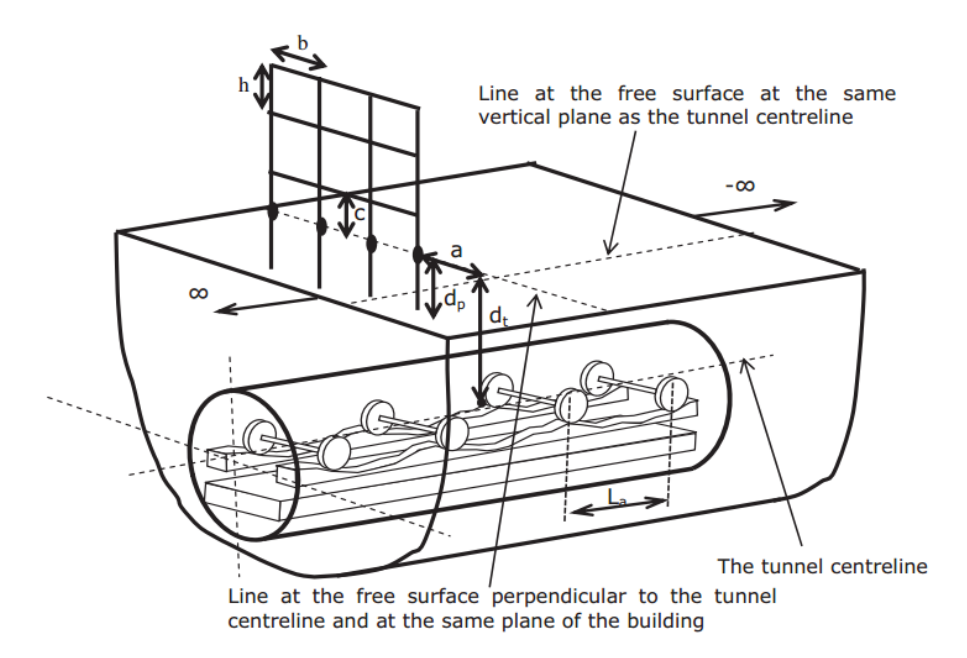


Figure 2-7 Sketch of the coupled model used by Hussein et al. [168], showing a train of wheelsets running in a tunnel and a building coupled to the ground model at a series of nodes.

The response at the soil-foundation interface u_s is given by

$$u_{\rm s} = (I + H_{\rm s}K_{\rm h})^{-1}u_{\rm s0} \tag{2-5}$$

where $H_{\rm s}$ is the soil's receptance matrix, $K_{\rm b}$ is the dynamic stiffness matrix of the building, I is the identity matrix with the number of rows and columns equal to the number of DOFs at the coupled nodes, and $u_{\rm s0}$ represents the free-field soil displacement at the coupled node positions. This equation represents the interaction between the soil and the foundation.

Additionally, the transfer matrix model [126] is widely applied in the analytical approach for describing the SSI. For the traditional impedance-based analytical model [169-171], it can be extended to form a hybrid approach to simulate the SSI for predicting the train-induced vibration in the building [172]. In addition to these methods, one DOF models [173], 2D framed models [168], and 3D analytical models [52, 174] are used to calculate building vibration induced by railways. Bucinskas et al. [175] used a mixed-frame-of-reference approach to create a receptance matrix to simulate the structures interacting with the soil. The excitation and the soil part were modelled by using semi-analytical model, but the structure was simulated by a 3D FE model.

2.3.2 Soil-structure interaction in numerical model

The numerical approach has developed rapidly in recent years alongside advances in computer science. For higher accuracy in predicting railway-induced vibration and noise in buildings, it is essential to consider soil-structure interaction (SSI) and coupling loss. The foundation plays a crucial role in the dynamic interaction between the ground and the building. Compared with studies that neglect SSI when determining displacement at the ground-building interface, including SSI in numerical or analytical models, or incorporating coupling loss in empirical models, leads to more accurate results.

SSI is an important aspect of environmental vibration induced by railways and should be taken into account to simulate the attenuation at the foundation, especially in numerical or analytical models. The SSI is classified according to the analysis method, which can be divided into numerical methods and simplified methods. In view of the wide applicability of the numerical methods, the boundary element method, the finite element method, or a combination of these two methods can be applied to the analysis of the SSI. Some numerical models can be used to calculate the vibration transmitted to the buildings directly. These models contain the numerical building model directly coupled to the ground model. Ropars et al. [176] built a numerical model to investigate the vibration response in a complex building neighbouring the railway. The building had a pile foundation and was located above a tunnel and coupled with a four-layered soil model. Villot et al. [177] use a 2D FE-BE ground-structure interaction model (MEFISSTO software) to estimate the influence of building modifications on the vibration response in the building. Yang et al. [2] investigated the building vibration induced by the underground railway using a full 3D FE model. The boundary element method has been applied by Coulier et al to investigate the effects of a group of buildings on ground vibration [178]. The displacement results of the building and the surrounding soil are shown in Figure 2-8. However, this approach is generally computationally expensive, so sub-modelling approaches are commonly used.

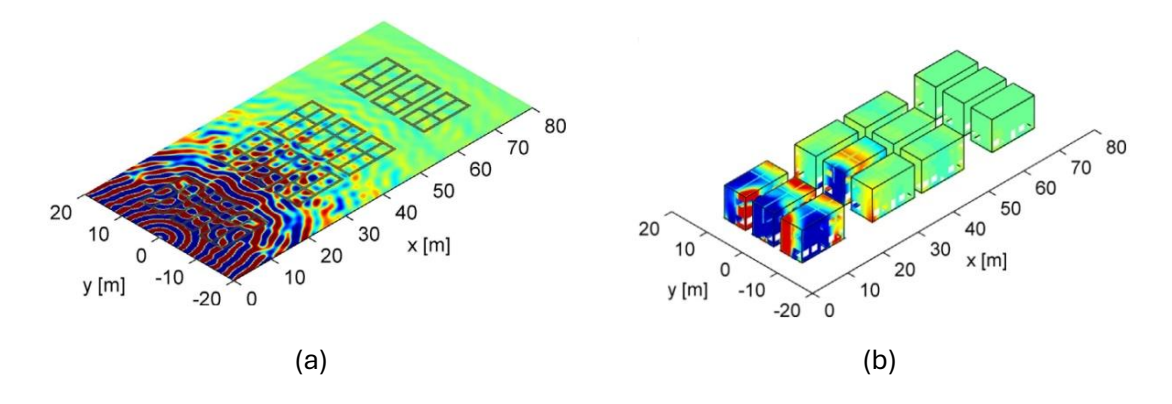


Figure 2-8 Real part of the (a) vertical soil displacement and (b) vertical structural displacement at 50 Hz accounting for through-soil coupling of a group of surrounding buildings [178].

Fiala et al. [179] used a sub-modelling technique to calculate the vibration in a building. They considered the SSI when investigating the structure-borne vibration and noise by using a transmission matrix approach. Celebi et al. [180] determined the impedance function for different foundation types. The results were obtained by using a substructure approach which was formulated on basis of the boundary element method. Lopez-Mendoza et al. [181] built a scoping numerical model to predict vibration in buildings induced by railway traffic considering SSI. Edirisinghe and Talbot [162] discussed the interaction between a tunnel and a building's piled foundation in the spatial-frequency domain by using the Pipe-in-Pipe and boundary element models. Peng et al. [182] used thin-layer elements to simulate the contact interface between the pile and soil. They found the tunnel-pile interaction is greatest when the piles are installed parallel to the tunnel and extend below it. For improving the calculation efficiency, López-Mendoza et al. [183] built a simplified building-soil coupled model in the time domain by using spring elements to represent the soil. They also compared several different simplified spring models for considering SSI. Additionally, the 2.5D model is more efficient compared with the 3D numerical model. Lopes et al. [92, 184] combined a 2.5D finite element method (FEM) - perfectly matched layer (PML) model of the ground with a 3D FE model of a building to predict the vibration induced in buildings considering the SSI. Colaço et al. [185] used a simplified SSI method based on 2.5D FEM- Method of Fundamental Solutions (MFS) to model the infinite ground, which could predict the vibration induced by railway traffic. This simplified SSI approach is efficient for the prediction of building vibration induced by railways, and validated by the experimental results [186]. Additionally, combining experimental and numerical methods into a hybrid model can be a practical way to assess the building's dynamic response accurately [187, 188].

2.3.3 Coupling loss in empirical models

The coupling loss in the empirical model refers to \mathcal{C}_{gb} in Eq. (2-2). In the FTA report [116], the coupling loss and its relation with the foundation types are introduced. The coupling loss is used to describe the foundation response to incident ground vibration in empirical or semi-empirical models based on in-situ measurement data. It represents the reduction in vibration at the soil-structure interface due to the presence of the foundation structures. The general rule-of-thumb is that the heavier the building foundation, the greater the coupling loss as the vibration propagates from the ground into the building. Nelson and Saurenman [189] discussed the ground-borne vibration influenced by the building foundation response. They found that shallow slab-on-grade floors have little coupling loss whereas deep piles may exhibit a substantial coupling loss.

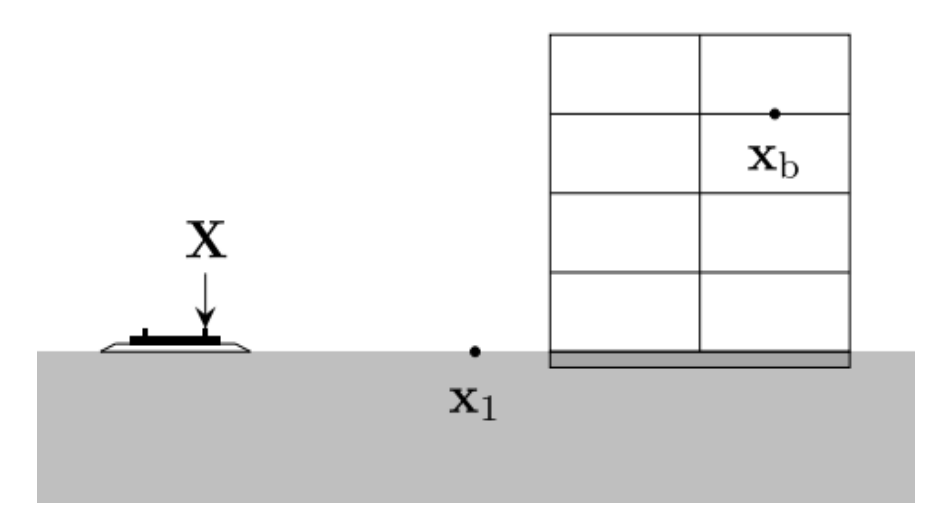


Figure 2-9 Sketch of source and receiver positions used in predicting railway vibration in buildings [6].

On the basis of the hybrid empirical-numerical prediction method proposed by Kuo et al. [6, 190], and FRA approach [115], the vertical vibration level at a point \mathbf{X}_b in a building as shown in Figure 2-9 is given by

$$L_{v}(\mathbf{X}_{b}) = L_{FD}(\mathbf{X}, \mathbf{x}_{1}) + L_{LSTM}(\mathbf{X}, \mathbf{x}_{1}) + C_{gb}(\mathbf{X}, \mathbf{x}_{b})$$
 (2-6)

where $L_{\rm FD}$ is the equivalent force density level (FDL), $L_{\rm LSTM}$ is the line source transfer mobility, the $C_{\rm gb}$ is the coupling loss or building correction factor. ${\bf X}$ is the excitation position. The coupling loss values can be evaluated in two different configurations: (a) excitation by a nearby railway; and (b) excitation by impulses on the soil's surface. In both cases $C_{\rm gb}$ is evaluated as the level difference between ${\bf x}_{\rm b}$ and ${\bf x}_{\rm 1}$. A parametric study was presented in reference [6] of the influence of soil properties, foundation type, floor thickness, building layout, and number of storeys on the coupling loss based on the hybrid method.

The coupling loss concept is well-adapted for use with empirical methods when evaluating the environmental vibration induced by railways. In the same way as for the empirical model, the coupling loss concept is clear, and the calculation procedure is simple, allowing results in the building to be obtained easily. However, it is oversimplified, and the uncertainty is quite large and cannot meet the requirement when more accurate prediction results are required. The SSI in analytical and numerical models can be used to obtain more accurate results.

2.4 Seismic soil-metamaterials in ground vibration

Seismic soil-metamaterials (SSM) consist of structured soils composed of cylindrical voids or rigid inclusions. They are one of the most commonly used types of seismic metamaterials.

Examples of such inclusions are concrete cylinders or rubber layers, which are embedded in the ground in a periodic pattern. An elastic SSM-based barrier is effective not only in mitigating seismic vibrations but also in reducing railway-induced ground vibrations.

The periodic pile group stands out as a prominent SSM structure for ground vibration mitigation. A group of piles can effectively provide a screening effect against plane wave vibration. Richart et al. [191] were the first to propose that a row of piles could act as a wave barrier and mitigate vibration. A row of rigid piles was investigated for its effectiveness in screening surface waves using a 2D semi-analytical model [192], and subsequently expanded to a 3D semi-analytical model [193]. The 3D BE method has also been employed to assess the effectiveness of screening surface waves and isolating vibration using a row of piles [152]. Additionally, the wave screening and vibration isolation effects of a row of hollow piles were investigated using a 3D BE model [194]. Combining this with Biot's theory [195], the plane wave screening effect of a row of piles embedded in homogeneous poroelastic soil was investigated [196, 197]. Recently, multiple rows of piles have attracted more attention as wave barriers compared with single-row configurations due to their increased efficiency in vibration isolation. Gao et al. [198] employed an analytical model based on the half-space Green's function to assess the vibration mitigation effects of multiple rows of piles. Lu et al. [199-202] investigated the various types of wave isolation effects provided by multiple rows of piles in the frequency domain. Huang and Shi [203-205] investigated the ground vibration reduction and attenuation influenced by a pile group. Pu and Shi [206-208] investigated the influence of periodic piles on ground vibration and demonstrated the presence of attenuation zones. Ma et al. [209] investigated the attenuation zone of ground vibration through experimental research. Li et al. [210] considered concrete piles with circular sections as inclusions to investigate how the SSM influences railway ground vibration. The soil-structure interaction is governed by the principles of displacement compatibility. According to these principles, the displacement of the structure at the interface must be compatible with the displacement of the adjacent soil, ensuring continuity and deformation consistency across the boundary.

Apart from pile groups, other buried periodic inclusions (usually called phononic crystals) have also been investigated. Continuous buried periodic inclusions have been selected to investigate the mitigation effects on vibration induced by traffic by using a 2.5D FE model [211]. Other types of periodic structures such as periodic underground barriers [212], wave impeding blocks [213], prefabricated periodic composite rubber-concrete barriers [214], periodic geofoam-filled trenches [215], periodic hollow steel trenches [216], and periodic composite in-filled trenches [217] have also been investigated for ground vibration mitigation.

There are several other categories of seismic metamaterials [218]. In addition to SSM, these include buried mass resonators, above-surface resonators, and auxetic materials, which are characterised by a negative Poisson's ratio.

2.5 Gaps and summary

The three main methods of predicting environmental vibration induced by railways have been introduced: semi-analytical models, numerical models, and empirical models. In order to improve the computational efficiency, all vibration prediction models adopt many assumptions and simplifications. If the ground-borne vibration caused by train passages needs to be predicted, a building model can be coupled with the free-field ground by using a sub-modelling technique. It is usually assumed that the free-field vibration of the ground is seen as the soil dynamic response and the vibration is not affected by other structures, which is reasonable if the prediction accuracy is not required to be very high. But the presence of the building will influence the free-field vibration, which should not be ignored if more accurate prediction results are required.

The SSI or coupling loss at the building foundation should be considered in the prediction of environmental vibration induced by the railway. This is because when the train-induced vibration is transmitted to the building foundation, there is attenuation due to structure-soil interaction. When the SSI influences the building, the building will also have an effect on the ground. Thus, the ground vibration response, which is the basis of the target building vibration prediction, would be influenced by the surrounding structures located between the vibration source and receiver point. Behind a building, there may be shielding of vibration or amplification at the receiver position. The impact of the surrounding structures should be taken into account, but the relevant research is lacking.

The existing research on pile dynamic behaviour and pile-soil interaction using various approaches mainly focuses on investigating the response to excitation on the pile, predominantly for vertical excitation, or equivalently the response of the pile head to vibration transmitted through the ground. When focusing on the periodic pile arrays the primary focus is on their impact on band gaps based on periodic theory. There is a strong need for investigation into the effect of one pile in modifying the response of the surrounding ground when the excitation is applied remotely from the pile. Moreover, the reliable range of the models in such a case needs to be investigated.

Furthermore, the urban environment is quite a complex system. There are many surrounding structures affecting the transmission of train-induced vibration to the target buildings. Thus, it is

Chapter 2

essential to consider the impact of the surrounding structures on the ground vibration to get more accurate results of railway-induced noise and vibration in buildings in order to guide the engineering design. However, most research has considered the influence of SSI on the target building but ignored its effect on the free-field vibration, which should be improved when higher accuracy is required. When considering the dynamic SSI and coupling loss of the surrounding buildings, the ground vibration response would be more accurate, and the target building vibration response will be closer to reality.

In summary, current prediction models for the railway-induced vibration in a target building contain the vibration source (train and track), transmission path (free-field ground), and the target building. It has almost always been assumed that the nearby surrounding structures will not influence the ground vibration at the target building, so all other buildings (apart from the target building) are ignored. However, the influence of surrounding structures cannot be ignored when focusing on the vibration response of the target building with higher accuracy. The influence of surrounding structures on ground-borne vibration from railways should therefore be investigated clearly. The pile-soil interaction, forming the foundation of the entire study, is appropriately selected as the fundamental research problem from which to begin this investigation.

Chapter 3 Single pile-soil dynamic interaction

The single pile-soil interaction model, characterised by its ease of construction and efficient calculations, is an important case to consider in relation to railway vibration mitigation, and forms the basis for studying pile foundations and SSI more generally. The existing research on single pile dynamic behaviour and pile-soil interaction using various approaches mainly focuses on investigating the response to excitation on the pile, predominantly for vertical excitation. There is a strong need for investigation into the effect of a pile in modifying the ground response when excitation is applied remotely from the pile. Moreover, the reliable frequency range of the model in such a case needs to be investigated due to the simplifying assumptions made.

This chapter begins by establishing a coupled pile-soil semi-analytical model. The pile is modelled by beam finite elements, and the soil, assumed homogeneous, is simulated by the semi-analytical DSM method [44] in the frequency-wavenumber domain. The pile model is an FE model embedded within a semi-analytical surrounding model. For simplicity, it is still referred to as a semi-analytical model. For comparison, FE models of the whole problem are built. Two cases are investigated: an axisymmetric model for loads applied at the top of the pile and a 3D model for scenarios where the load is applied at a distance from the pile. The first case is introduced as it is more common in the literature. For train loads, the vertical load is significantly larger than the horizontal load. Therefore, the ground response induced by vertical loads is investigated. To ensure consistency, only vertical loads are considered in the single-pile model. The results from the semi-analytical model and the FE models are compared, from which the accuracy of the semi-analytical model is evaluated. Finally, the vibration of the ground surface in the presence of a pile is investigated, and the vibration mitigation effects are determined for different frequencies and shear wave velocities of the ground.

3.1 Semi-analytical model for single pile-soil interaction

Two situations are considered in this study. In the first, the pile is positioned directly beneath the load, which is included as a reference because it has been the focus in much previous research [148]. In the second, a point load is applied to the ground surface at some distance away from the pile. For each case, a semi-analytical model is developed, and comparisons are made with results from the respective FE model.

In the semi-analytical model, the ground is modelled using the DSM method [44] in the frequency-wavenumber domain. The details of this method can be found in Appendix B. The pile is represented by a Timoshenko beam. Although an Euler-Bernoulli beam would be sufficient in

most cases for the frequency range 1-80 Hz, a Timoshenko beam model is used because it takes account of shear deformation and rotational inertia effects, making it more suitable for large-section piles. For convenience, an FE approach is used for the pile, although analytical beam models could also be used. A sketch of the semi-analytical model is given in Figure 3-1, which indicates that the pile and the ground are coupled at a set of node points on the beam centreline. At each node point, coupling can be considered in three translational DOFs and optionally in three rotational DOFs.

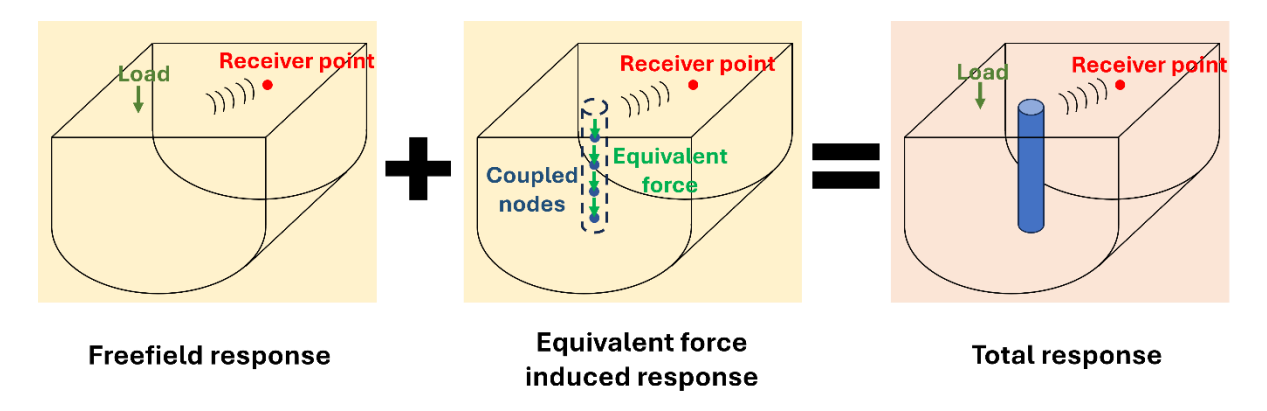


Figure 3-1 Sketch of the semi-analytical model for single pile-soil interaction.

As shown in Figure 3-1, the displacement response at a receiver point in the vicinity of the embedded pile can be separated into two parts: the response in the free field induced by the load, and the response induced by the equivalent reaction forces at the coupled nodes between the pile and the ground [168]. Based on this assumption, the displacement $\widehat{\bf U}$ at the receiver point at circular frequency ω can be expressed as

$$\widehat{\mathbf{U}} = \widehat{\mathbf{U}}_0 + \widehat{\mathbf{H}}_{\mathrm{s}} \widehat{\mathbf{F}}_{\mathrm{s}} \tag{3-1}$$

where $\widehat{\mathbf{U}}_0$ represents the ground vibration at the receiver point induced by the load in the absence of the pile. $\widehat{\mathbf{H}}_s$ signifies a matrix of transfer receptances of the soil between the coupled nodes and the receiver point, which are also known as Green's functions. The transfer receptance is assumed to be based on an equivalent disc load at each coupled nodes, the diameter of which is equal to the pile's diameter. $\widehat{\mathbf{F}}_s$ signifies a vector of equivalent reaction forces (also assumed to be disc loads) at the coupled nodes. They can be calculated based on coupling the ground with the finite element model of the pile, as described below. When the load is applied at some distance from the pile, it is treated as a point load applied to the ground surface.

To calculate the ground displacement, it is necessary to determine the equivalent forces $\hat{\mathbf{F}}_s$ at the coupled node positions. These equivalent forces account for the interaction between the pile and the surrounding soil and play a crucial role in determining the response of the system. To avoid singularity, the equivalent force is modelled as a disc load rather than a point load. Additionally,

for computational efficiency, the disc load is applied as the equivalent force at each coupled node instead of using a discretised ring load. The forces at the coupled nodes can be denoted as a vector $\hat{\mathbf{F}}_s(\omega)$, which includes up to 6 DOFs at each coupled node point:

$$\hat{\mathbf{f}}_{s}(\omega) = \begin{bmatrix} \hat{\mathbf{f}}_{s1}(x_{c,1}, y_{c,1}, z_{c,1}, \omega) \\ \hat{\mathbf{f}}_{s2}(x_{c,2}, y_{c,2}, z_{c,2}, \omega) \\ \vdots \\ \hat{\mathbf{f}}_{sk}(x_{c,k}, y_{c,k}, z_{c,k}, \omega) \end{bmatrix}$$
(3-2)

The force vector at coupled node k acting on the pile foundation is equal to the force vector acting on the soil at the same position, but opposite in direction.

$$\hat{\mathbf{f}}_{p}(\omega) = -\hat{\mathbf{f}}_{s}(\omega) \tag{3-3}$$

where subscript p denotes the nodes of the FE pile model and subscript s indicates the corresponding nodes belonging to the soil.

The relationship between the dynamic forces $\hat{\mathbf{F}}_p(\omega)$ and displacements $\hat{\mathbf{U}}_p(\omega)$ at the coupled nodes in the pile is given by

$$\widehat{\mathbf{F}}_{\mathbf{p}}(\omega) = \widehat{\mathbf{K}}_{\mathbf{p}}(\omega)\widehat{\mathbf{U}}_{\mathbf{p}}(\omega) \tag{3-4}$$

where $\widehat{\mathbf{K}}_{\mathrm{p}}(\omega)$ is the dynamic stiffness matrix of the pile, which can be calculated using the conventional FE method. In the current model, a 3D beam element including axial and transverse displacements is used to simulate the pile structure. The stiffness matrix and mass matrix can be found in Appendix A.

When calculating the dynamic stiffness matrix of the pile, $\widehat{\mathbf{K}}_p(\omega)$, equivalent parameters are applied to allow for the soil volume replaced by the pile. The pile-soil system can be seen as a combination of the free-field ground and an equivalent system consisting of the pile from which the excavated soil is subtracted. This is indicated in the sketch in Figure 3-2.

Chapter 3

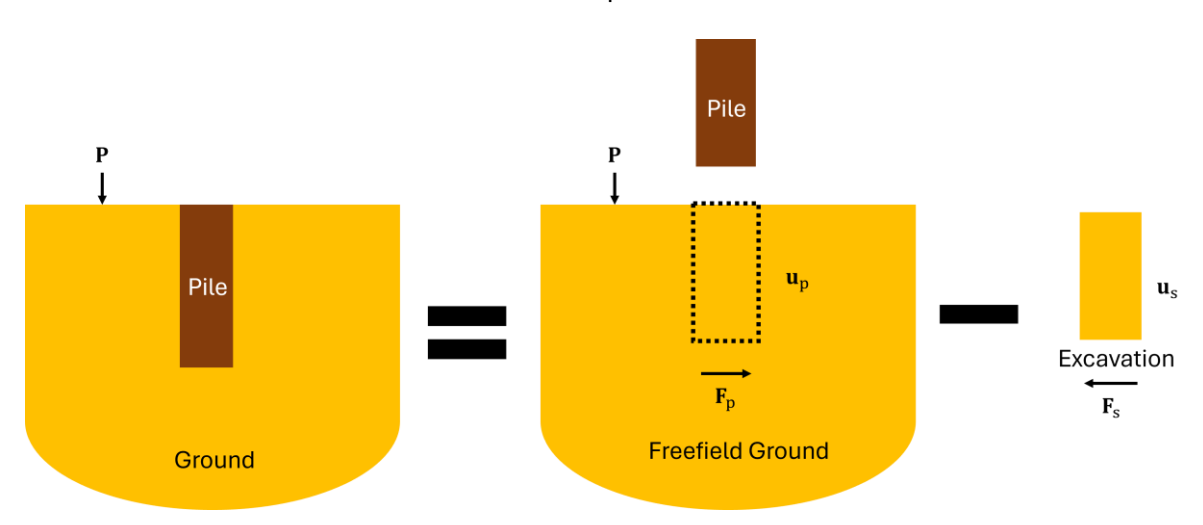


Figure 3-2 Sketch of equivalent foundation parameters.

The principles for selecting equivalent parameters are discussed in [151]. The equivalent density and Young's modulus of the pile located in the soil are

$$\rho = \rho_{\rm p} - \rho_{\rm s} \tag{3-5}$$

$$E = E_{\rm p} - E_{\rm s} \tag{3-6}$$

It is assumed that the displacements of the coupled nodes located within the pile are equal to the displacements of the corresponding nodes situated within the soil:

$$\widehat{\mathbf{U}}_{\mathbf{D}}(\omega) = \widehat{\mathbf{U}}_{\mathbf{S}}(\omega) \tag{3-7}$$

To calculate the displacements at the coupled nodes, it is assumed, similar to Eq. (3-1), that the displacement at the position of these nodes is given by

$$\widehat{\mathbf{U}}_{s}(\omega) = \widehat{\mathbf{U}}_{s0}(\omega) + \widehat{\mathbf{H}}_{pile}^{G}(\omega)\widehat{\mathbf{F}}_{s}(\omega)$$
(3-8)

where $\widehat{\mathbf{U}}_{s0}(\omega)$ means the displacement at the coupled nodes induced by a unit load in the absence of the pile. It is denoted as

$$\widehat{\mathbf{U}}_{s0}(\omega) = \begin{bmatrix} \widehat{\mathbf{u}}_{s0,1}(x_{c,1}, y_{c,1}, z_{c,1}, \omega) \\ \widehat{\mathbf{u}}_{s0,2}(x_{c,2}, y_{c,2}, z_{c,2}, \omega) \\ \vdots \\ \widehat{\mathbf{u}}_{s0,k}(x_{c,k}, y_{c,k}, z_{c,k}, \omega) \end{bmatrix}$$
(3-9)

The matrix $\widehat{\mathbf{H}}_G^{\mathrm{pile}}(\omega)$ consists of the soil point and transfer receptances between the coupled nodes, which can be denoted as

$$\widehat{\mathbf{H}}_{\mathsf{G}}^{\mathsf{pile}}(\omega) = \begin{bmatrix} \widehat{\mathbf{H}}_{11}(\omega) & \widehat{\mathbf{H}}_{12}(\omega) & \cdots & \widehat{\mathbf{H}}_{1k}(\omega) \\ \widehat{\mathbf{H}}_{21}(\omega) & \widehat{\mathbf{H}}_{22}(\omega) & \cdots & \widehat{\mathbf{H}}_{2k}(\omega) \\ \vdots & \vdots & \ddots & \vdots \\ \widehat{\mathbf{H}}_{l1}(\omega) & \widehat{\mathbf{H}}_{l2}(\omega) & \cdots & \widehat{\mathbf{H}}_{lk}(\omega) \end{bmatrix}$$
(3-10)

where

$$\widehat{\mathbf{H}}_{lk}(\omega) = \widehat{\mathbf{H}}(x_{c,l} - x_{c,k}, y_{c,l} - y_{c,k}, z_{c,l} - z_{c,k}, \omega)$$
(3-11)

means the Green's function of the soil from a force at coupled node k to the displacement at coupled node l. Figure 3-3 presents the transfer receptance on the ground surface calculated at 40 Hz using the DSM model under both point load and disc load excitations. The shear wave velocity in this case is 250 m/s, and the soil is considered a half-space free field. The radius of the disc load is 0.5 m. An evident observation is the exceptionally high receptance at the point of force application under point load excitation. Conversely, under disc load excitation, a plateau-like pattern emerges, indicating stable receptance values within the radius range of the load. Due to the use of a logarithmic Fourier transform, it is not possible to calculate results at r=0, and no results are obtained at the centre point of the disc load. Thus, in the single pile model, when calculating the receptance at the driving points, a distance of 0.2 times the pile section radius is maintained from the load centre to avoid singularity. This value effectively represents the receptance at the driving points.

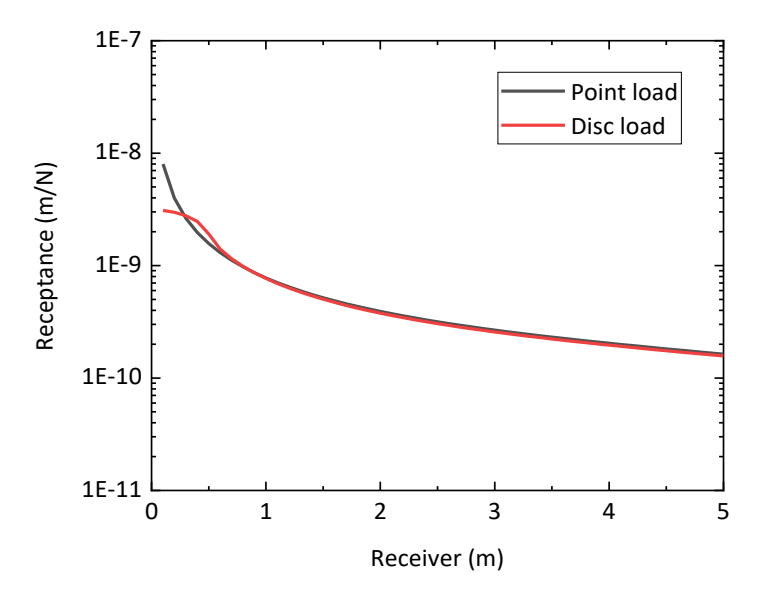


Figure 3-3 Receptance on the surface excited by point load and disc load (radius 0.5 m) at 40 Hz.

Combining Eqs (3-4)-(3-8), the displacement of the pile can be written as

$$\widehat{\mathbf{U}}_{p}(\omega) = \left(\mathbf{I} + \widehat{\mathbf{H}}_{G}^{pile}(\omega)\widehat{\mathbf{K}}_{p}(\omega)\right)^{-1}\widehat{\mathbf{U}}_{s0}(\omega)$$
(3-12)

Based on the Betti-Rayleigh reciprocal theorem (dynamic reciprocal theorem) applied to the soil [219], the Green's function in the frequency domain satisfies

$$G_{ij}(\mathbf{r}_2, \mathbf{r}_1, \omega) = G_{ii}(\mathbf{r}_1, \mathbf{r}_2, \omega)$$
 (3-13)

where G is the Green's function of soil. i, j=1, 2, 3, 4, 5, 6 indicate displacement in x, y, z directions and rotation in x, y, z directions. \mathbf{r}_1 and \mathbf{r}_2 are two position vectors denoting the location of receiver points of the soil. Eq. (3-13) means the response at \mathbf{r}_1 in the j direction induced by a force at \mathbf{r}_2 in the i direction is equal to the response at \mathbf{r}_2 in the i direction induced by a force at \mathbf{r}_1 in the j direction. Thus, the displacement at a receiver point induced by a moment, is equal to the rotation response at the position of the moment induced by a force at receiver point position.

To calculate the rotational responses, the rotational displacements are approximated by evaluating the displacements at opposite edges of the disc, with radius equal to the pile radius, as indicated in the sketch in Figure 3-4. For example, the rotational displacement θ about the y direction is determined as follows

$$\theta = \frac{u_1 - u_2}{2r} \tag{3-14}$$

where u_1 and u_2 are the displacements at the edge of pile section area induced by the external load, and r is the radius of the pile.

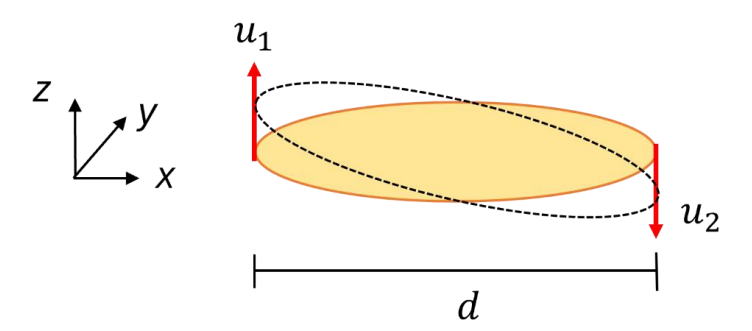


Figure 3-4 The rotational displacement obtained from the displacements at the edges of the pile cross-section.

It is assumed that the amplitude of the equivalent force (moment) is the same as the amplitude of the interaction force (moment) between the pile and the surrounding soil. Based on the dynamic reciprocity theorem, the displacement induced by the moment at receiver point is equal to the rotational angle induced by the traction at the coupled nodes.

3.2 FE model for single pile and surrounding soil

Two finite element models are introduced that are used for comparison with the semi-analytical model. The material parameters used for the soil and pile in these comparisons are summarised

in Table 3-1. Two types of soil with different shear wave velocities are chosen, representing a typical soft-to-medium soil and a stiffer one. For simplicity, the soil is modelled as a homogeneous half space for the purpose of the validation study and ground vibration investigation. The frequency range considered in this section is from 10 Hz to 80 Hz. In this chapter, the single pile model serves as the foundational model for train-induced vibrations. Consequently, the frequency range of this model aligns with the feelable vibration frequency limits of 1-80 Hz in railway vibration problems. Additionally, the pile has negligible effect at low frequencies between 1 and 10 Hz. Therefore, the frequency range of interest is 10-80 Hz in this section.

Table 3-1 Material parameters of the soil and the pile.

Name	Density (kg/m³)	Young's modulus (MPa)	Poisson's ratio	Loss factor	P-wave speed (m/s)	S-wave speed (m/s)
Softer soil	2100	143	0.333	0.1	320	160
Stiffer soil	2100	350	0.333	0.1	500	250
Pile	2500	30000	0.2	0.1	3652	2236

3.2.1 Axisymmetric model

When a vertical load is applied at the top of a circular pile, the configuration is axisymmetric. The FE model built in ABAQUS can take advantage of this by using an axisymmetric formulation in which only the two-dimensional cross-section is meshed. A sketch of the model is shown in Figure 3-5. The pile is situated directly beneath the load, and the receiver points are positioned on the ground surface close to the pile, from 0.1 m to 15 m away from the model symmetry axis, with a spacing of 0.1 m.

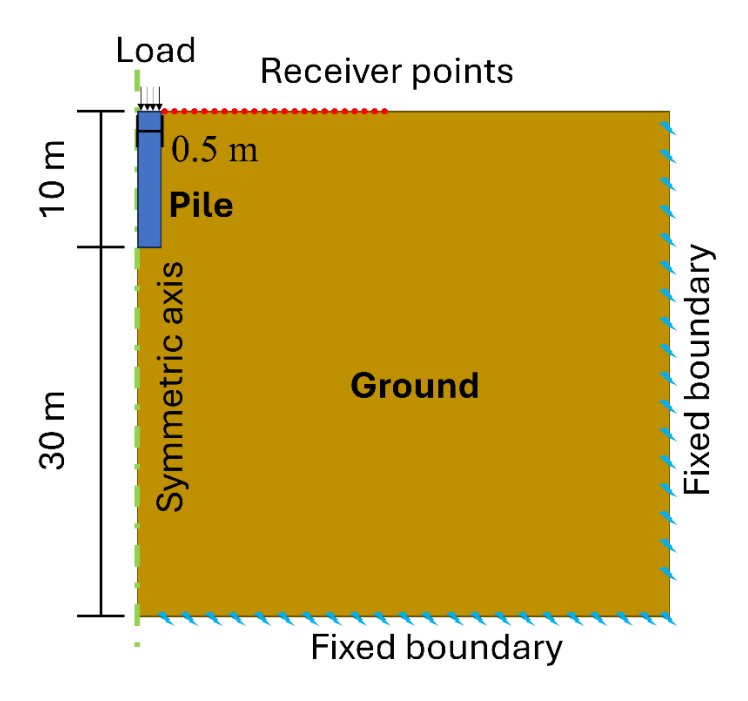


Figure 3-5 Sketch of the FE model of the pile directly beneath the load.

Both the pile radius and the disc load radius are specified as 0.5 m in the FE model. The pile length is 10 m. The boundaries at the right-hand side and the bottom of the domain are fixed. The domain size is chosen to ensure the shear waves are correctly captured; the shortest wavelength considered is 2 m (shear wave velocity of c_s =160 m/s at 80 Hz) and the longest wavelength is 25 m (shear wave velocity of c_s =250 m/s at 10 Hz). The size of model is 40 m×40 m. Although some wave reflections can occur at the fixed boundaries, with the current value of damping the model size is sufficient for this not to be significant, as will be seen in the results in Section 3.3. To allow a fine spacing of receiver points to be used, the element size is set to 0.05 m, which is more than sufficient to meet the requirement of at least six elements in one wavelength. Thus, a total of 640,000 elements are employed. Evaluation of the model accuracy will be discussed in Section 3.3. The FE model employs an axisymmetric four-noded element type for both the soil and the pile in the commercial FE software ABAQUS.

3.2.2 Three-dimensional model

When the load is positioned at a certain distance away from the pile, the problem is no longer axisymmetric, necessitating the establishment of a 3D FE model. A sketch of the model is shown in Figure 3-6. The load, pile and receivers are aligned in the y direction.

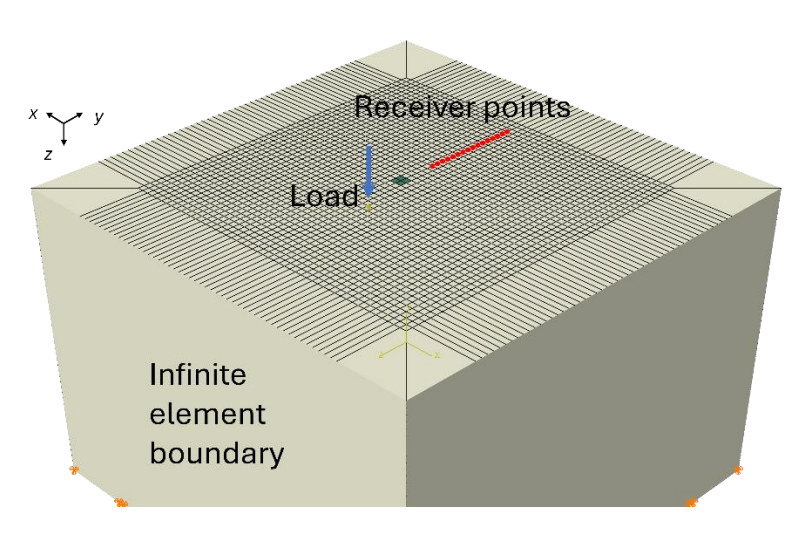


Figure 3-6 The FE model for a load applied to the ground at some distance from the pile.

Different meshes are used for the two different sets of soil properties considered. In each case the pile is located at the centre of the model and has length of 10 m. For convenience it has a square cross-section with a width of 0.8 m. For the stiffer soil, the overall size of the model is $30\times30\times20$ m. The width and length of this model are chosen to ensure that the longest shear wavelength considered (c_s =25 m at 10 Hz) could be included in the model. The element size is 0.4 m, which ensures that there are more than six nodes within one shear wavelength at the highest frequency of f=80 Hz. The model consists of 135,000 elements. For the softer soil condition, the model size is $20\times20\times20$ m and the element size is set to 0.2 m, which is more suitable for the shorter shear wavelengths in this case (minimum value 1.25 m). Similar to the previous case, this ensures that there are at least six nodes within one shear wavelength for frequencies up to 80 Hz. In this case the model includes a total of 592,500 elements.

Due to limitations of the model size, the point load is positioned at a distance of only 2.4 m away from the centroid of the pile. Moreover, the receiver points are only selected between 4.8 m and 10.8 m away from the load location. The interval between the receiver points is 0.4 m, which is corresponding to the brick finite element size. To prevent wave reflections from the boundaries, infinite elements are applied at the sides of the domain, although the bottom of the domain is fixed. The element type used for the ground and the pile is an 8-node brick element. The infinite elements are 8-node linear, one-way infinite brick elements. The model is established in ABAQUS.

3.3 Model evaluation

3.3.1 Free-field response

Before considering the pile, the validity of the FE models is first verified. For this, a comparison between the semi-analytical DSM for a half space and the FE models is shown in Figure 3-7 for a

homogeneous ground in the absence of the pile. The dynamic stiffness matrix method is extensively used in ground simulation, and can be considered as a reference solution [44].

The results are shown in Figure 3-7 for the two sets of soil properties and for two frequencies, 10 Hz and 80 Hz, in the form of the displacement amplitude for a unit force (transfer receptance). The results from the semi-analytical model are shown both for a point load and for a disc load. The results from the axisymmetric FE model are compared with the semi-analytical model for the case of a disc load with unit amplitude; the 3D FE model is compared with the semi-analytical model for the case of a point load with unit amplitude. The results from the point load and disc load are similar at low frequency where the wavelength is large compared with the disc dimensions, but at higher frequency the disc load produces a different response compared to the point load. This occurs because at high frequencies, the corresponding wavelength becomes small, and the wavelength is of the same order as the pile diameter, allowing the pile's diameter to influence the response. The displacement in the disc load area is no longer consistent at different radii. The assumption of the semi-analytical model is inconsistent with the realistic situation. For both values of shear wave velocity and for both frequencies, there is a good agreement between the results obtained from the semi-analytical model with disc load and the axisymmetric FE model, especially at the higher frequency. At low frequency the results from the FE model contain some oscillations due to reflections from the boundary, but these are small. A reasonable level of agreement is found between the semi-analytical model with point load and the 3D FE model. However, more significant differences exist compared to the disc load models because the fully 3D FE model does not correspond precisely to the axisymmetric semi-analytical model.

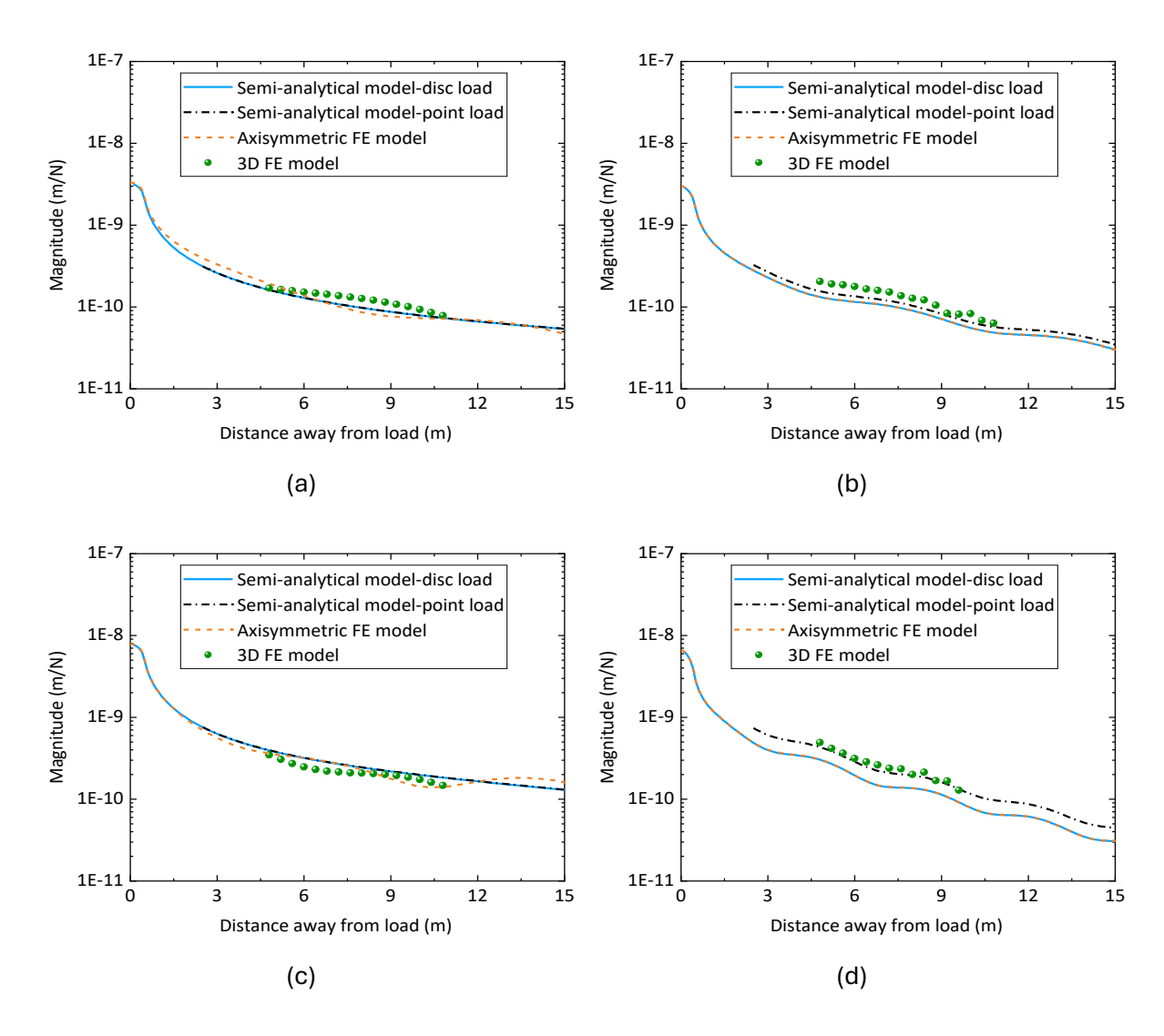


Figure 3-7 Free-field response comparison when ground shear wave velocity is 250 m/s at (a) 10 Hz (b) 80 Hz, and when the shear wave velocity is 160 m/s at (c) 10 Hz and (d) 80 Hz.

3.3.2 The number of coupled nodes

The accuracy of the prediction results in the presence of the pile could be affected by the number of coupled nodes used in the semi-analytical model. Here, results are compared for different numbers of coupled nodes. To evaluate the model accuracy, the average level difference is employed as an evaluation metric. It can be calculated by

$$D = \frac{\sum_{i=1}^{n} 10 \log_{10} \left(\frac{u_i}{u_{\text{ref}}}\right)^2}{n}$$
 (3-15)

where u_i is the magnitude of the displacement response, n is the number of receivers, and $u_{\rm ref}$ is the reference displacement amplitude which is calculated from the semi-analytical model when the smallest value of coupled node distance is used, 0.125 m.

The average level differences obtained with different numbers of coupled nodes are shown in Figure 3-8 for the two cases, load above the pile and load at 2.4 m from the pile; in each case the

pile length is 10 m, and the frequency is 80 Hz. The rotation DOFs are considered at coupled nodes from the pile.

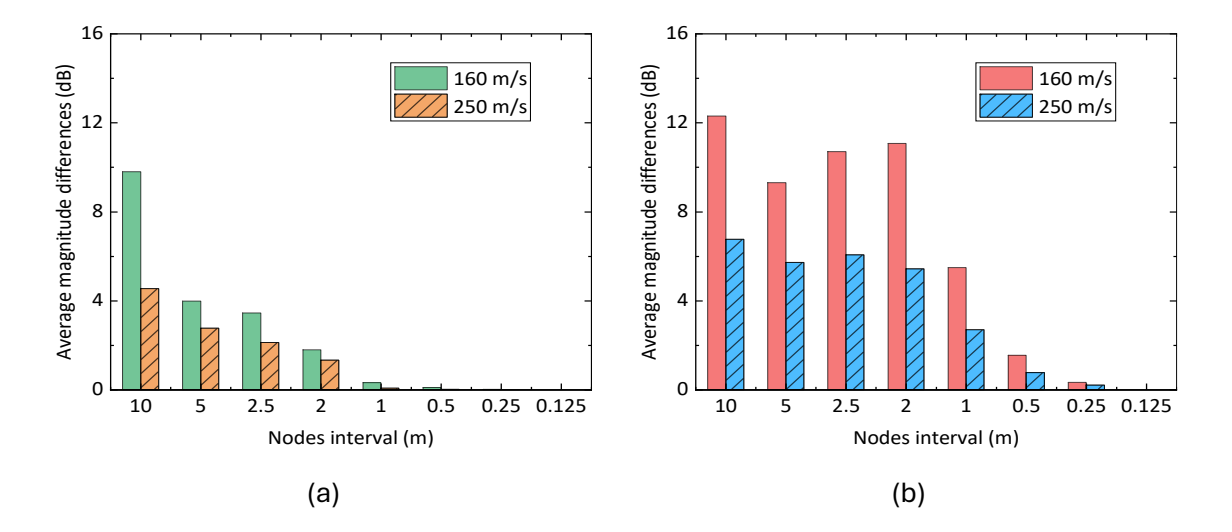


Figure 3-8 Average level differences for model with different numbers of coupled nodes in (a) load above the pile and (b) load at 2.4 m from the pile.

When the load is positioned at the top of the pile, and considering a shear wave velocity of 250 m/s, convergence is achieved when the interval between coupled nodes is less than 1 m. In this case, the average level difference approaches zero, confirming the model has converged. However, in the case of a shear wave velocity of 160 m/s, a coupled node interval of less than 0.5 m is required for the model to converge.

When an external load is considered (2.4 m away from the pile), the model's accuracy is not as high as in the case of the load above the pile. However, in this case the results obtained are not significantly affected by the shear wave speed, and the model can still achieve convergence provided that the distance between coupled nodes remains less than 0.5 m. Thus, in both models, the interval between coupled nodes is selected as 0.25 m, which is sufficient to converge and get accurate results.

The coupled node spacing can also be expressed in terms of the bending wavelength, which can be represented as

$$\lambda_{\rm B} = \frac{c_{\rm B}}{f} \tag{3-16}$$

where f is the frequency, $c_{\rm B}$ is the bending wave speed in the pile structure. For an Euler-Bernoulli beam, it can be calculated from

$$c_{\rm B} = \left(\frac{D\omega^2}{m'}\right)^{1/4} \tag{3-17}$$

where m' is the mass per unit length of pile, ω is the angular frequency, and D is the bending stiffness. For a rectangular beam it can be calculated by

$$D = \frac{Eh^3b}{12(1-v^2)} \tag{3-18}$$

For a circular beam it can be calculated by

$$D = \frac{E\pi r^4}{4(1-\nu^2)} \tag{3-19}$$

where E is the Young's modulus of the pile. h is the height of the rectangular pile section, b is the width of the rectangular pile section, r is the radius of the circular pile section, equal to the disc load radius of 0.5 m, and ν is Poisson's ratio.

In this section, the parameters of the pile are from Table 3-1. At 80 Hz, the coupling node interval is 0.25 m, which is much less than one-sixth of the bending wavelength. (For the circular beam the wavelength is 111.16 m, while for the rectangular beam it is 106.6 m).

3.3.3 Ground response for load applied to the top of the pile

In this subsection, a comparison is made between the finite element model and the semianalytical model at various frequencies for the case in which the pile is directly beneath the load.

The magnitude of the response for a unit load, obtained from both the FE model and the semi-analytical model, is shown in Figure 3-9. Results are shown for frequencies of 40 Hz and 80 Hz and shear wave velocities of $c_{\rm s}$ =250 m/s and $c_{\rm s}$ =160 m/s. At both frequencies and both wavespeeds, the magnitudes of the ground response from the FE model and the semi-analytical model exhibit a high level of agreement. The constant value near the pile centre in the finite element model results from the disc load. The radius of the constant value region shown in this figure matches the radius of the pile.

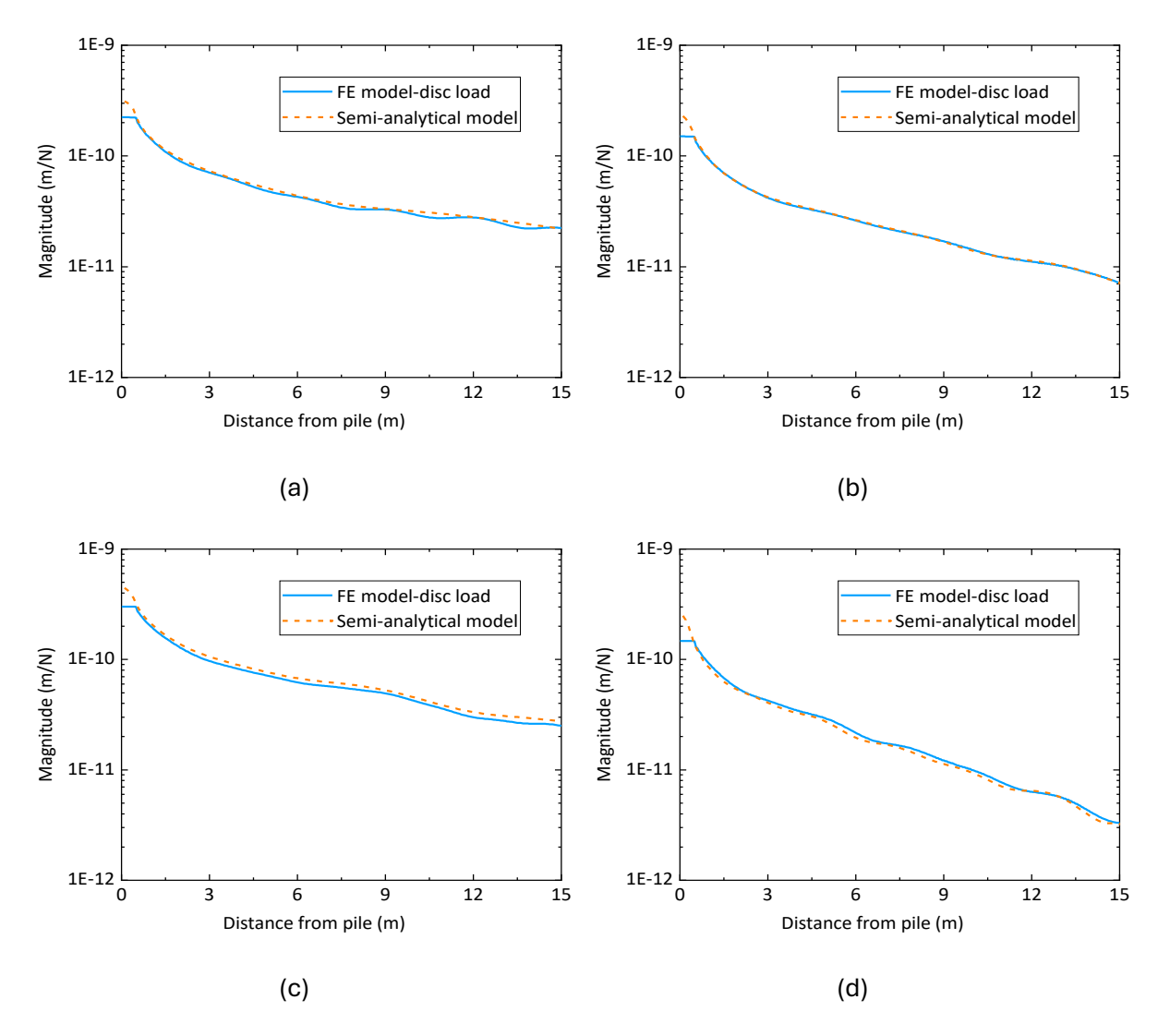


Figure 3-9 Magnitude of vibration response for a unit load applied to the top of the pile: comparison between FE model and semi-analytical model when the shear wave velocity is 250 m/s at (a) 40 Hz, (b) 80 Hz and when the shear wave velocity is 160 m/s at (c) 40 Hz, (d) 80 Hz.

3.3.4 Ground response for load applied adjacent to the pile

In this subsection the ground response results obtained from the FE model and the semi-analytical model are compared for the situation in which an external point load is applied 2.4 m away from the centre of the embedded pile. In the semi-analytical model, two cases are considered: one in which the rotational DOFs at the coupled nodes are included, and the other in which they are neglected.

The magnitudes of the responses for a unit load are shown in Figure 3-10 for two frequencies and the two sets of soil properties. Here, the pile section is square with a side length of 0.8 m. If the shear wavelength is much larger than the pile section side length (e.g., the shear wavelength is 6.25 m, when c_s =250 m/s, f=40 Hz), the results are similar from the FE model and the semi-analytical model both with/without considering rotation DOFs. If the shear wavelength is closer

to the pile section side length (e.g., the shear wavelength is 3.125 m, when $c_{\rm S}$ =250 m/s, f=80 Hz, or shear wavelength is 4 m, when $c_{\rm S}$ =160 m/s, f=40 Hz), the ground response from the model without considering rotation DOFs shows significant differences, whereas the model with rotation DOFs exhibits only minor discrepancies with the FE model. When the shear wavelength approaches closer to the pile section side length (e.g. when the shear wavelength is 2 m, i.e. $c_{\rm S}$ =160 m/s and f=80 Hz), these differences are enhanced but the model with rotation DOFs still has similar trends to the FE model. Therefore, it is clear that considering the rotational DOFs of the coupling points on the embedded pile can improve the accuracy of the model.

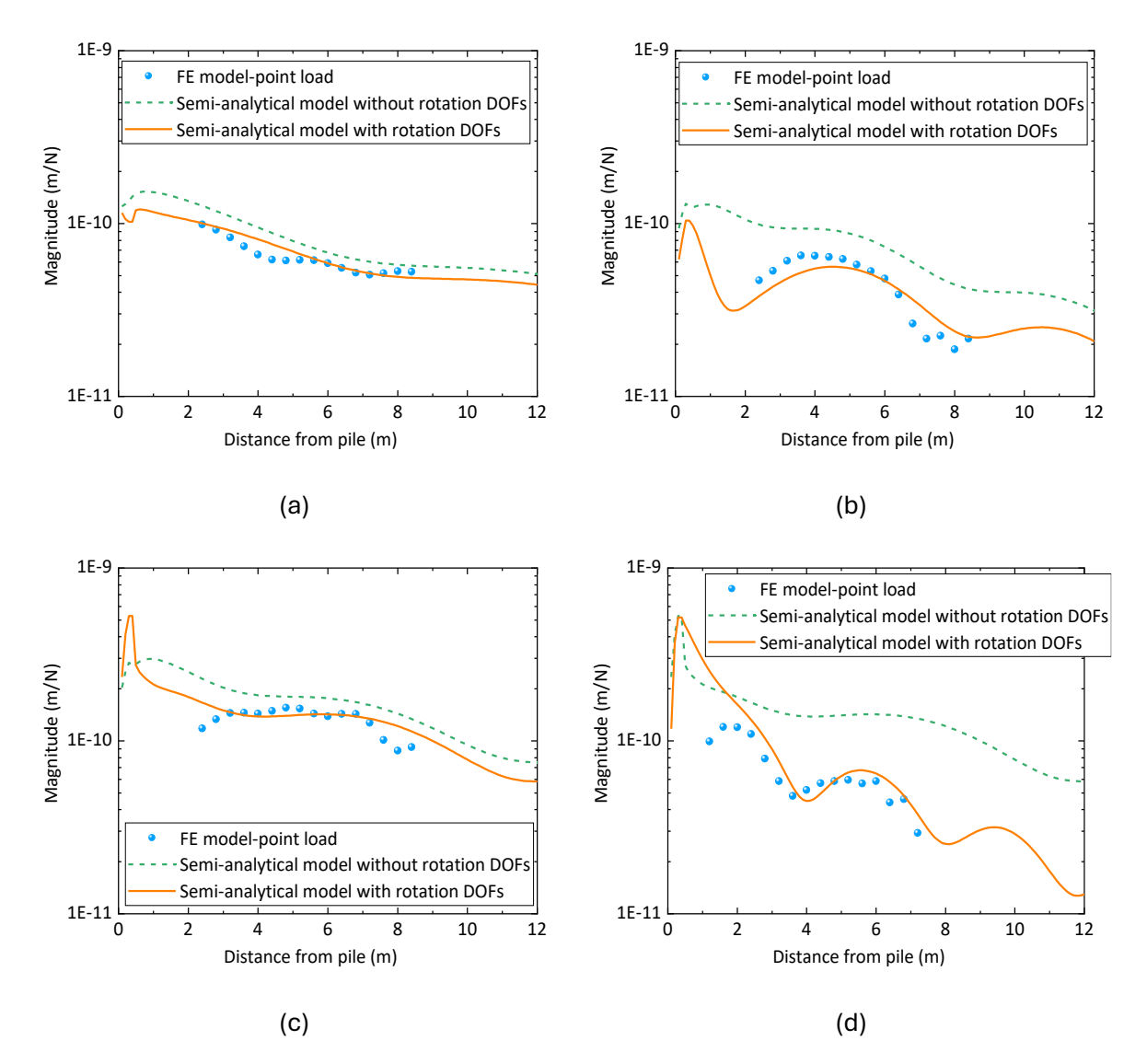


Figure 3-10 The magnitude of vibration induced by a load at 2.4 m from the pile obtained from FE model and semi-analytical model when the shear wave velocity is 250 m/s at (a) 40 Hz, (b) 80 Hz and when the shear wave velocity is 160 m/s at (c) 40 Hz, (d) 80 Hz.

3.3.5 Model accuracy under different shear wave velocities and frequencies

After discussing the magnitude of the ground response from the semi-analytical model and FE model, a summary of the model accuracy is provided for a wider range of frequencies and shear

wave velocities. The frequencies considered in this subsection range from 10 Hz to 80 Hz in intervals of 10 Hz, while the shear wave velocities are 100 m/s, 160 m/s, 200 m/s and 250 m/s. The first natural frequency of the pile is 10.8 Hz, and the second, third, and fourth modal frequencies are 23.9 Hz, 45.8 Hz, and 73.6 Hz, respectively, all of which fall within the considered frequency range. The average level difference from Eq. (3-15) is used for evaluating the model accuracy. The value of $u_{\rm ref}$ in Eq. (3-15) is taken here as the displacement amplitude that is calculated from the FE model.

To describe the relationship between shear wavelengths, frequencies and embedded pile radius, a dimensionless parameter a_0 [135] is introduced:

$$a_0 = \frac{\omega \cdot r}{c_{\rm S}} \tag{3-20}$$

where r is the radius of the pile; if the pile section is square, it represents half the width. If the value of a_0 is small, it corresponds to a larger shear wave velocity (which indicates that the soil possesses a higher stiffness) or a lower frequency.

Figure 3-11 depicts the average level differences for the cases of the load above the pile and the load at 2.4 m from the pile, corresponding to various values of a_0 . The receiver points are positioned directly behind the pile, extending up to 15 m away, with each point spaced at intervals of 0.1 m. In total, there are 150 receiver points. Each point in Figure 3-11 corresponds to the average level differences under a distinct combination of shear wave velocity and frequency. The results demonstrate that, within the range of values considered, a smaller value of a_0 corresponds to a smaller average level difference value. For the model with the load at 2.4 m from the pile including rotational DOFs, the average level difference is less than 3 dB for most cases with a_0 less than 1. This corresponds to a shear wavelength that is greater than 3 times the pile diameter. At larger values of a_0 the difference increases as the beam model of the pile does not account for the influence of the size of the pile in shielding the vibration transmission.

In the case where the load is applied directly above the pile, the inclusion of rotation DOFs has no effect. This is due to the symmetry of the model, which prevents any rotation. However, when the load is applied on the ground surface away from the pile, the cases with and without rotation DOFs at the coupled nodes are considered. It can be seen that the semi-analytical model that accounts for rotational DOFs yields lower average level differences than when rotational DOFs are not accounted for. These results confirm that incorporating rotational DOFs into the semi-analytical model is necessary to yield more accurate results.

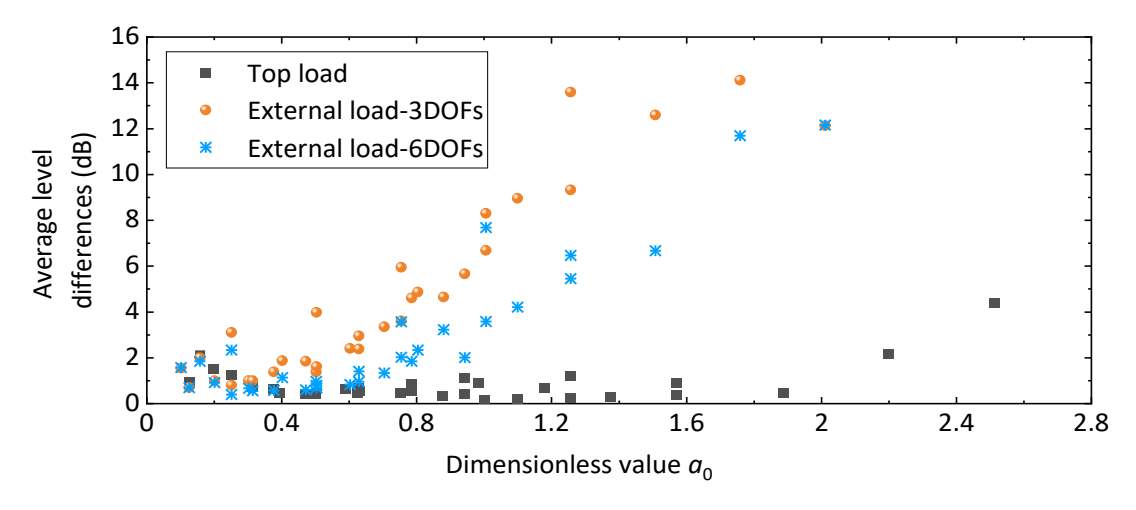


Figure 3-11 Average level differences under different values of dimensionless parameter.

3.3.6 Model comparison with other model

For the single pile dynamic model coupled with the surrounding soil, several classical models exist, such as Novak's model [135], and Kuo's model [147]. In this section, a comparison is made between these classical models from the literature, the semi-analytical model presented in this chapter, and the numerical FE model.

The calculation in Novak's model is efficient due to the assumption of plane-strain conditions. Novak's model assumes the soil consists of an infinite number of infinitesimally thin, independent, horizontal elastic layers extending infinitely in all directions. When a unit vertical load is applied to the surface directly above the pile, the vertical displacement of the pile is [135]

$$u_z(z) = \frac{-\cos(\alpha z)}{EA\alpha \tan(\alpha L)} - \frac{\sin(\alpha z)}{EA\alpha}$$
 (3-21)

where E is the Young's modulus of the pile, A is the sectional area of the pile, L is the pile length, and

$$\alpha = \sqrt{\frac{m'\omega^2 - GS_z}{EA}} \tag{3-22}$$

where G is the soil shear modulus. m' is the mass per unit length of the pile, and

$$S_z = 2\pi a_0 \frac{J_1(a_0)J_0(a_0) + Y_1(a_0)Y_0(a_0)}{J_0(a_0) + Y_0(a_0)} + \frac{4i}{J_0^2(a_0) + Y_0^2(a_0)}$$
(3-23)

where J_0 and J_1 are Bessel functions of the first kind of order zero and one respectively. Y_0 and Y_1 are Bessel functions of the second kind of order zero and one respectively. a_0 is the dimensionless value, calculated by Eq. (3-20).

Based on the assumption from Novak's method, the displacement of the ground can be calculated from the displacement at the pile at the corresponding depth

$$u_{\rm g}(d_{\rm pr}, z_1) = u(z_1) \sqrt{\frac{r}{d_{\rm pr}}} e^{-\beta_{\rm S} \omega \frac{d_{\rm pr}}{c_{\rm S}}} e^{-i\omega \frac{d_{\rm pr}}{c_{\rm S}}}$$
(3-24)

where $d_{\rm pr}$ is the distance between the pile and the receiver point on the ground, r is the radius of the pile, z_1 is the location of the receiver point, and $\beta_{\rm S}$ is the damping ratio of the soil.

In Kuo's method, a novel 3D single pile model was developed. The motion of the pile can be conceptualised as an infinite rod undergoing axial vibration and an Euler-Bernoulli beam experiencing lateral vibration. The vertical displacement of the pile can be represented as

$$u_z(z) = \frac{1}{2\pi} \int_{-\infty}^{\infty} \widetilde{U}_z(\xi) e^{i\xi z_1} d\xi$$
 (3-25)

where ξ is the longitudinal wavenumber.

The vertical displacement of the infinite pile in the wavenumber domain is

$$\widetilde{U}_{z}(\xi) = \frac{1}{EA\xi^{2} + \widetilde{K}_{z}(\xi) - m'\omega^{2}}$$
(3-26)

where

$$\widetilde{K}_{z}(\xi) = 2\pi r \begin{bmatrix} 0 & 0 & 1 \end{bmatrix} \begin{bmatrix} \mathbf{T}_{\infty} \end{bmatrix}_{r=r} \begin{bmatrix} \mathbf{U}_{\infty} \end{bmatrix}_{r=r}^{-1} \begin{bmatrix} 0 \\ 0 \\ 1 \end{bmatrix}$$
(3-27)

where $[\breve{\mathbf{T}}_{\infty}]$ and $[\breve{\mathbf{U}}_{\infty}]$ are the stress and displacement factor matrix. The details can be seen in Appendix B in which terms are related to Bessel function of the second kind $K_n(r)$.

Based on the mirror-image method, the free-end boundary condition at the top of the pile can be generated. The mirror-image method is used by Wolf [220] and Rikse [221] as a kind of boundary in the system. Kuo [222] applied this method for the single pile dynamic investigation. Then the displacement on the ground based on the pile displacement can be calculated by:

$$\begin{bmatrix} \widetilde{U}_r \\ \widetilde{U}_\theta \\ \widetilde{U}_z \end{bmatrix}_{r=d} = \begin{bmatrix} \mathbf{\breve{U}}_\infty \end{bmatrix}_{r=d} \begin{bmatrix} \mathbf{\breve{U}}_\infty \end{bmatrix}_{r=r}^{-1} \begin{bmatrix} 0 \\ 0 \\ \widetilde{U}_z \end{bmatrix}_{r=r}$$
(3-28)

where d is the distance of the receiver point away from the pile. $[\widetilde{U}_r \quad \widetilde{U}_\theta \quad \widetilde{U}_z]_{r=d}^T$ means the response of the receiver point in the ground.

Finally, based on the inverse Fourier transform, the ground response in the spatial-time domain is

$$\begin{bmatrix} u_r(z,t) \\ u_{\theta}(z,t) \\ u_z(z,t) \end{bmatrix} = \frac{1}{2\pi} \int_{-\infty}^{\infty} \begin{bmatrix} \widetilde{U}_r \\ 0 \\ \widetilde{U}_z \end{bmatrix}_{r=d} e^{\mathrm{i}\xi z} d\xi e^{\mathrm{i}\omega t}$$
(3-29)

A comparison between Novak's method, Kuo's method, the semi-analytical method and the full FE model is shown in Figure 3-12. The pile is 10 m long, and embedded in a half space. The parameters of both the pile and the surrounding soil are the same as those previously mentioned, listed in Table 3-1. The radius of the pile is 0.5 m. It can be seen that when focusing on the displacement at the top of the pile, the results from Novak's method and Kuo's method are similar to those from the semi-analytical model and the FE model under different dimensionless values a_0 . When focusing on the ground response 5 m away from the pile, Novak's method and Kuo's method differ from the other methods when the dimensionless value a_0 is larger than 0.9. This discrepancy arises because Novak's method assumes a plane-strain condition to calculate soil displacement in the far field.

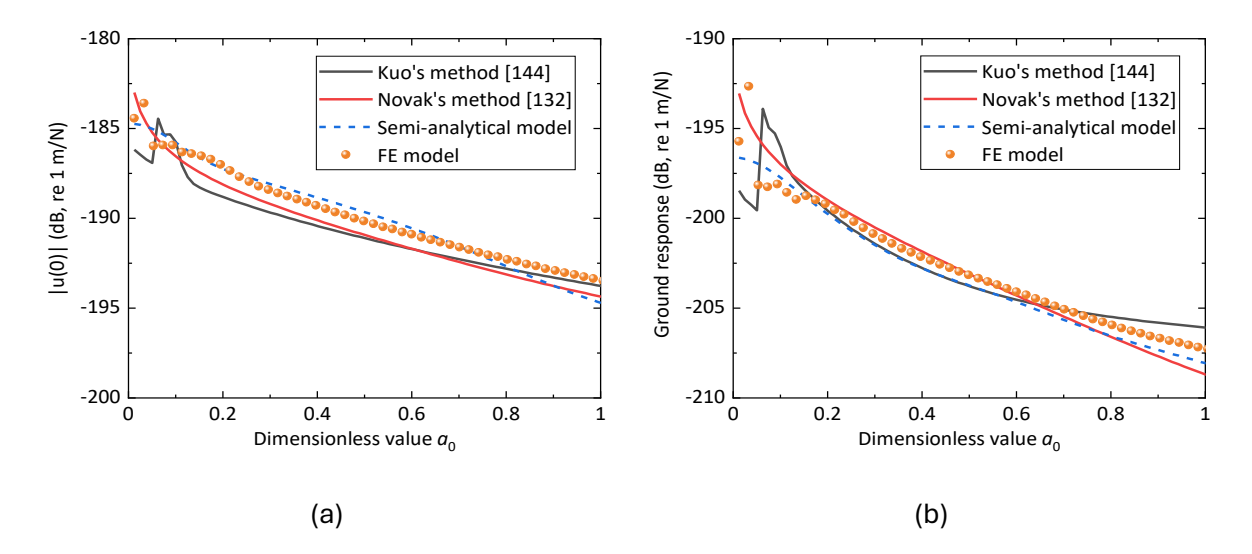


Figure 3-12 Comparison between different single pile-soil models at (a) the top of the pile and (b) on the ground 5 m away from the pile when the load is applied at the top of the pile.

If the load is applied near the pile, the models need an improvement. Based on the coupled subsystem method introduced in [222] and [223], the piles located in the surrounding soil should be discretised. When the load is applied on the ground near the pile, the displacement of the pile is related to:

$$\mathbf{U}(\omega) = \left[\mathbf{I} + \mathbf{A}_{33} \mathbf{B}_{33}^{-1}\right]^{-1} \mathbf{U}_0(\omega) \tag{3-30}$$

where ${\bf A}_{33}$ is the frequency response function matrix related to the displacement of the soil to the forces acting on the soil. ${\bf B}_{33}$ is the frequency function matrix related to the displacement on the pile to the force acting on the pile. They are receptance matrices. ${\bf U}_0(\omega)$ means the incident wave displacement, i.e. the freefield response at pile location.

For Novak's method, the diagonal element A_{33} of matrix ${f A}_{33}$ can be calculated by

$$A_{33} = \frac{1}{GS_z L/N} \tag{3-31}$$

where N represents the number of segments into which the single pile is divided.

The matrix \mathbf{B}_{33} is related to the force applied on the pile and displacement of receiver points on the pile. The displacement on the pile under different unit force locations is

$$u(z) = \begin{cases} \frac{(-\cos{(\alpha z_1)} - \sin{(\alpha z_1)} \tan{(\alpha L)})\cos{(\alpha z_p)}}{EA\alpha \tan{(\alpha L)}} & 0 \le z_p \le z_1\\ \frac{-\cos{(\alpha z_1)}\cos{(\alpha z_p)}}{EA\alpha \tan{(\alpha L)}} - \frac{\cos{(\alpha z_1)}\sin{(\alpha z_p)}}{EA\alpha} & z_1 \le z_p \le L, \end{cases}$$
(3-32)

where z_1 is the location of the receiver point, z_p is the location of the unit force, and

$$\alpha = \sqrt{\frac{m'\omega^2}{EA}} \tag{3-33}$$

For Kuo's method, the calculation is in the frequency-wavenumber domain. The terms in the frequency response matrices in Eq. (3-30) can be calculated by

$$\widetilde{\mathbf{A}}_{33}(\xi) = \frac{1}{\widetilde{K}_z(\xi)} \tag{3-34}$$

where $\widetilde{K}_{z}(\xi)$ can be calculated from Eq. (3-27), and

$$\widetilde{\mathbf{B}}_{33}(\xi) = \frac{1}{EA\xi^2 - m'\omega^2} \tag{3-35}$$

Since $\widetilde{\mathbf{U}}_0(\omega)$ in Eq. (3-30) should also be calculated in the wavenumber domain, the free-field response at the pile location can be initially computed in the spatial domain and then first and then transformed into the wavenumber domain using Fourier transform. The number of receiver points in the spatial domain at the pile location should be sufficient. In this case, 1,000 receiver points were selected. The distance between the pile and the load is 2.4 m. The pile has a length of 10 m and a radius of 0.4 m. The comparison between the different methods is summarised in Figure 3-13 under different dimensionless values. The "3DOF" means the coupled nodes from the semi-analytical model without rotational DOFs. The "6DOF" means the coupled nodes from the semi-analytical model with rotational DOFs.

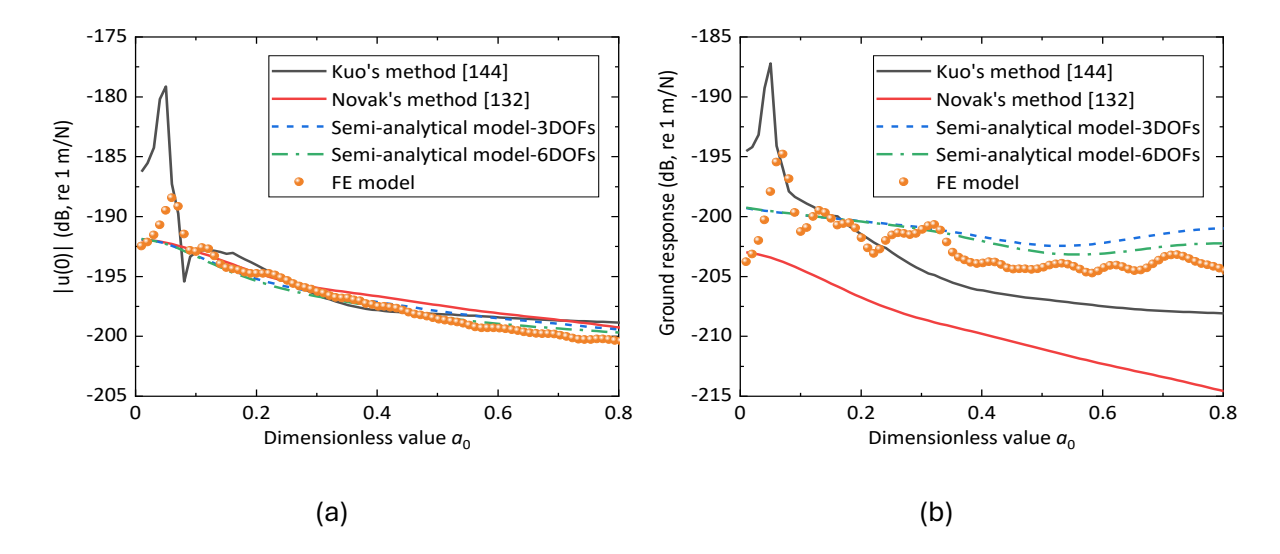


Figure 3-13 Comparison between different single pile-soil model at (a) the top of the pile and (b) on the ground 5 m away from the pile when the load is applied 2.4 m away from the pile.

It can be observed that the response of the pile at the surface point is similar regardless of the model used. All the models are not very accurate when the dimensionless value is smaller than 0.1, but it becomes accurate within the range of 0.1 to 0.8. However, when focusing on the ground receiver point 5 m behind the pile location, different models exhibit varying levels of accuracy. Novak's model is not accurate because it is overly simplified, treating the problem as occurring in a single plane. Kuo's method is more accurate at lower dimensionless values, but as the dimensionless value increases—corresponding to higher frequencies—the model's accuracy diminishes. The present semi-analytical model produces more accurate results, especially when accounting for the rotational degrees of freedom (DOFs) of the beam elements.

3.4 Ground vibration mitigation

3.4.1 Ground vibration insertion loss on the centreline

In this section, the effects of the pile in mitigating the ground response are discussed and analysed for the case in which the load is 2.4 m from the pile based on the semi-analytical model. Figure 3-14 depicts the magnitude of the free-field response and the response in the presence of the pile. The results correspond to frequencies of 40 Hz and 80 Hz and shear wave velocities in the ground of c_s =250 m/s and c_s =160 m/s. The receiver points are positioned on the ground surface directly behind the pile, at distances from the pile centreline extending from 0.1 m to 15 m, with a spacing of 0.1 m. These figures provide an overview of the ground response characteristics. Based on the observations from Figure 3-14, the magnitude of the response with the pile is smaller than that of the free-field response, indicating that the presence of the pile leads to a suppression of the ground vibration response. When the shear wavelength is short, oscillatory

ground responses are observed behind the pile (Figure 3-14 (b) and (d)). This phenomenon occurs because, when a pile is embedded in the soil, it could enhance the interference between surface waves and body waves, resulting in oscillations in ground vibration.

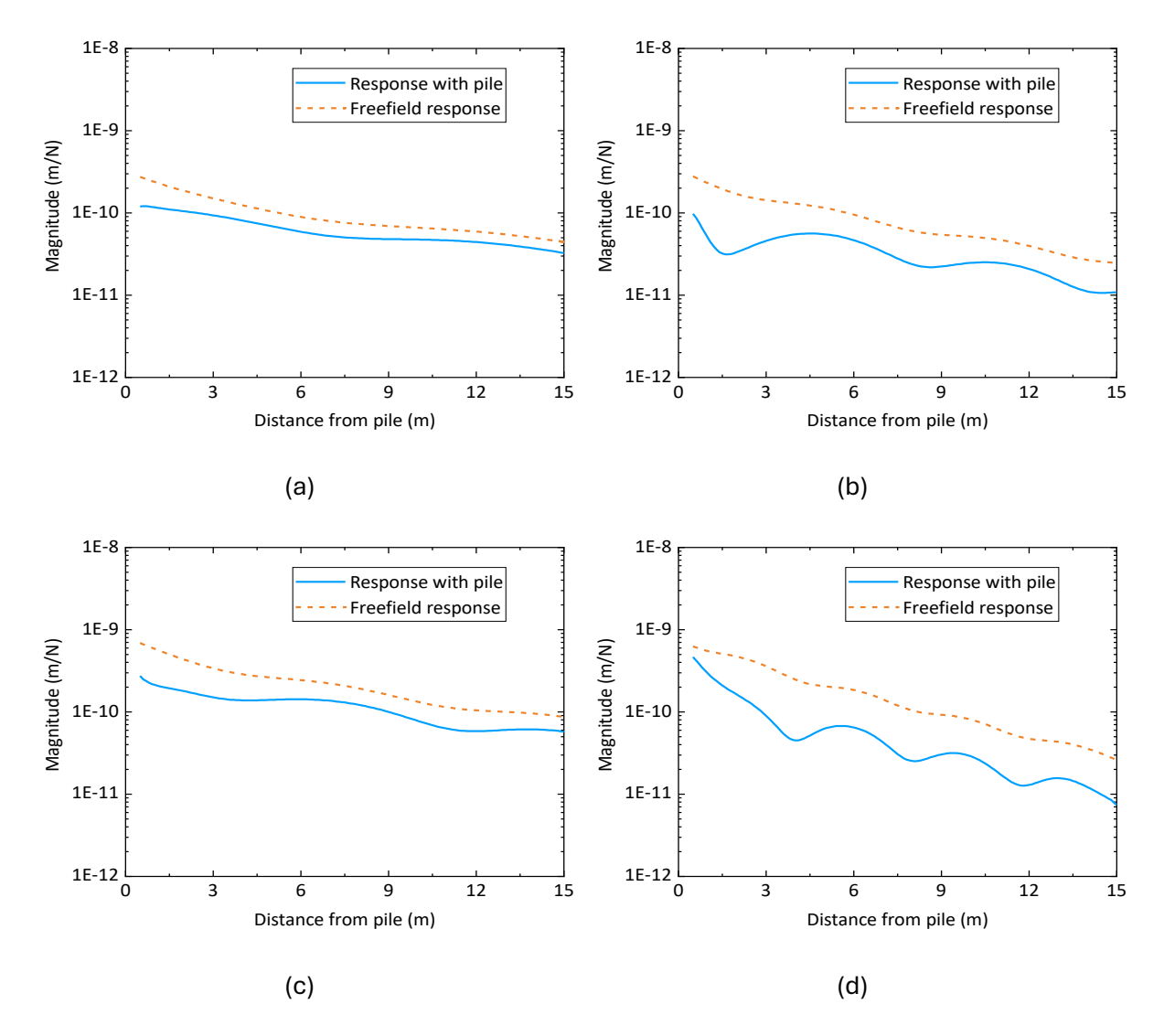


Figure 3-14 The free-field response and the response with pile when the shear wave velocity is 250 m/s at (a) 40 Hz, (b) 80 Hz and when the shear wave velocity is 160 m/s at (c) 40 Hz, (d) 80 Hz.

Figure 3-15 depicts the insertion loss (IL) at each ground vibration receiver point obtained from the results in Figure 3-14. As above, the load was at 2.4 m from the pile. The results are for frequencies of 40 Hz and 80 Hz, and for shear wave velocities of $c_{\rm s}$ =250 m/s and $c_{\rm s}$ =160 m/s. If the IL value is positive, it means the vibration on the ground is reduced by the presence of the pile. The results indicate that the vibration mitigation effects are more significant at 80 Hz than at 40 Hz and generally greater for the softer soil.

Chapter 3

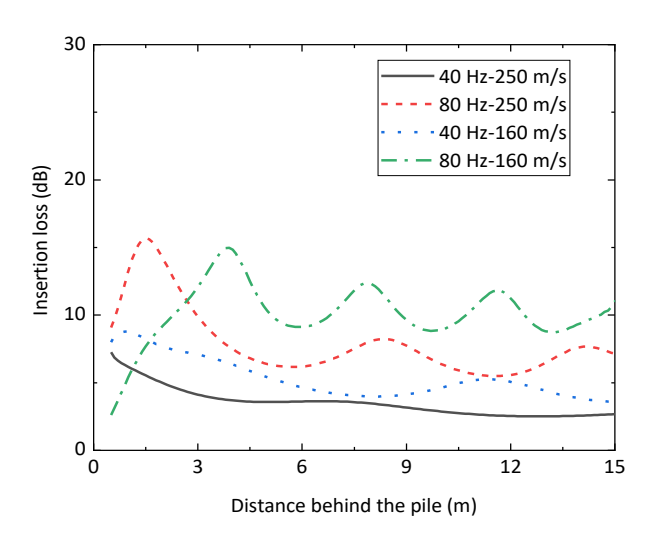


Figure 3-15 IL of single pile model for two shear wave speeds and two frequencies.

Figure 3-16 shows the spectral IL results for two different shear wave velocities at locations 2 m and 6 m behind the pile on the centreline. In the frequency region 1-100 Hz, the value of IL is positive, indicating that ground vibration is mitigated when a pile is located in the transmission path. The results show that at lower frequencies, IL is close to zero, indicating that the presence of the pile does not influence the ground response. As the frequency increases, the value of IL also increases. When the shear wave velocity is 160 m/s, the IL is larger compared to when the shear wave velocity is 250 m/s. Also, the IL value from the ground receiver points 2 m away from the piles is slightly larger than the IL value from all receiver points 6 m away from the piles.

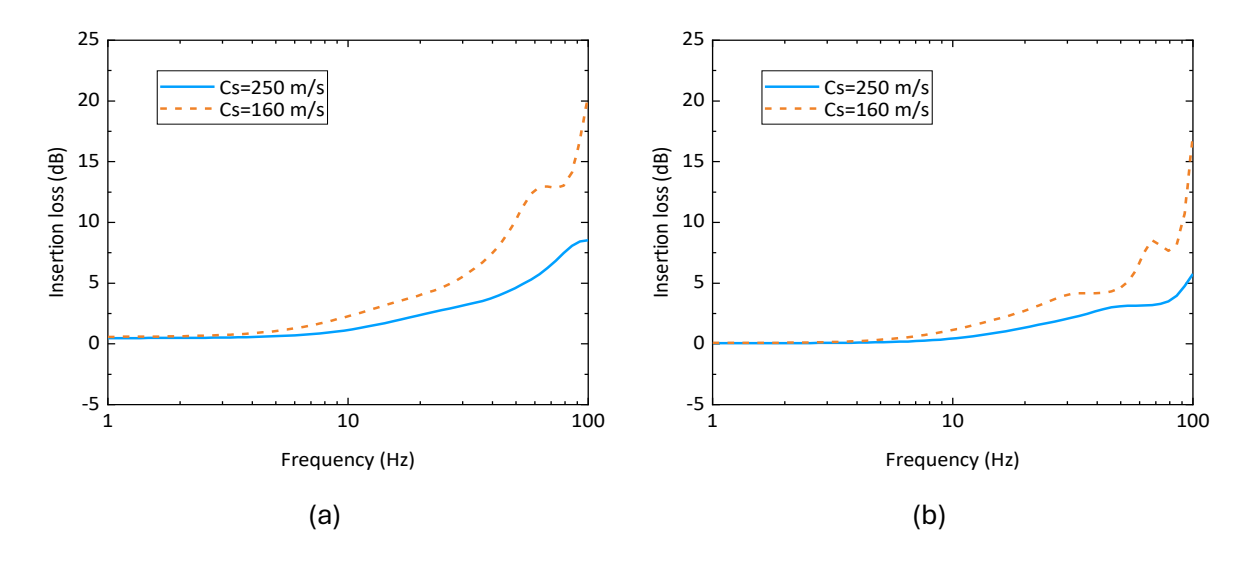


Figure 3-16 The spectral IL results at the receiver points (a) 2 m and (b) 6 m behind the pile on the centreline under different shear wave velocities.

3.4.2 Insertion loss when load is further from the pile

Using the semi-analytical model, the IL at selected receiver points is investigated for different distances between the pile and the load. In the results in Figure 3-17, there are three receiver

points behind the pile: points A, B, and C are 5 m, 10 m, 15 m away from the pile, respectively. When the load is between 1 and 10 m from the pile, the IL experiences a significant reduction as this distance is increased. For loads beyond 10 m, the IL stabilises at a consistent low level. Hence when the load is positioned at a considerable distance from the pile, the vibration mitigation effect is diminished and not significantly influenced by the distance from the load.

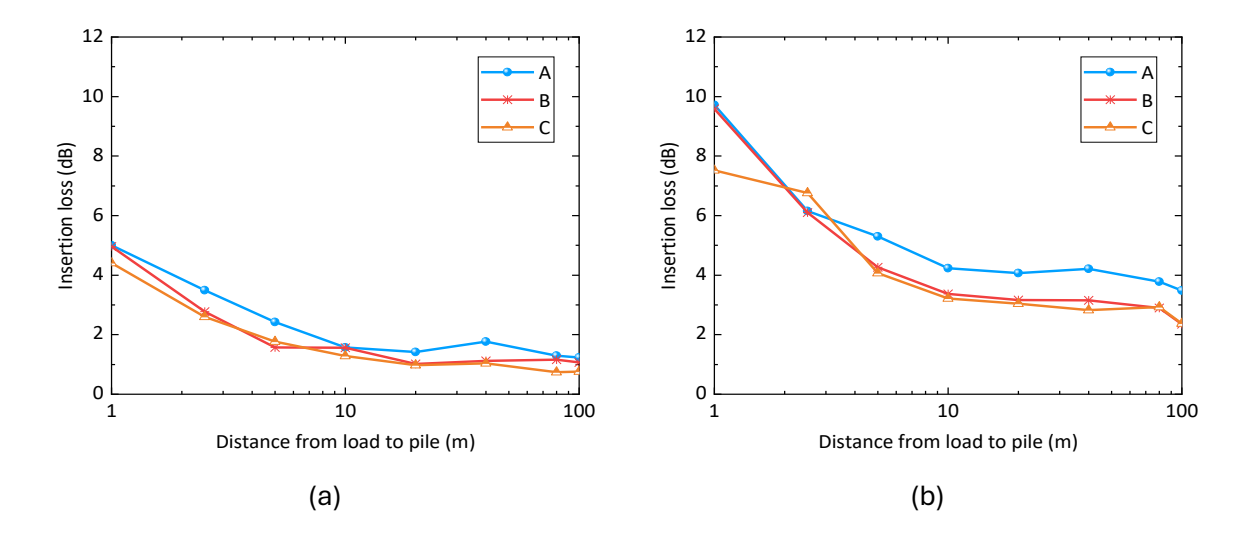


Figure 3-17 The IL for different distances between the pile centreline and the load (a) at 40 Hz and (b) at 80 Hz. Receiver points A, B, and C are 5 m, 10 m, 15 m away from the pile, respectively.

3.4.3 Frequency dependence of mitigation effects

To study the frequency dependence of the mitigation effect, a receiver point 5 m behind the pile is selected, with the load positioned 10 m in front of the pile (so the distance between load and receiver point is 15 m). The IL is computed for different frequencies and shear wave velocities. The range of shear wave velocities spans from 150 m/s to 500 m/s, with an interval of 50 m/s. The frequency range is from 10 Hz to 80 Hz, with a spacing of 10 Hz. The results are shown in the form of a contour plot of IL in Figure 3-18.

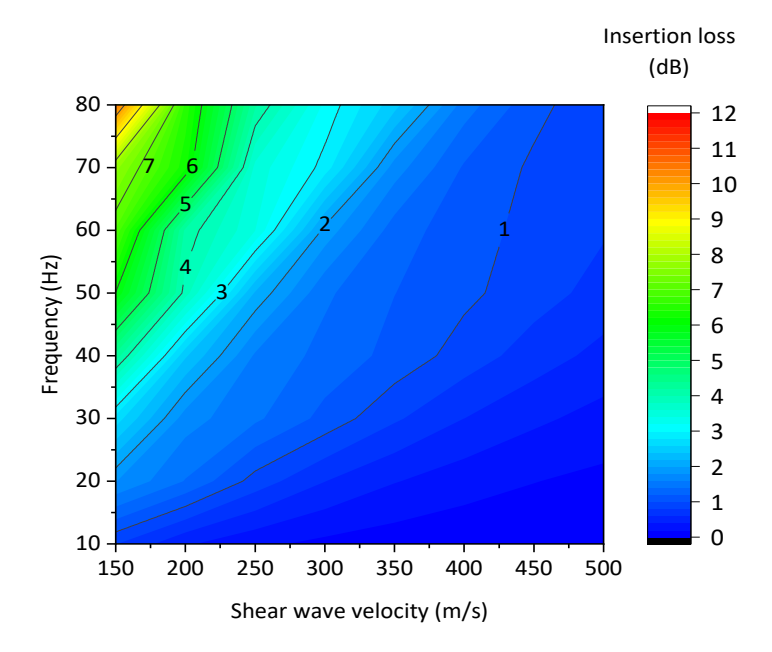


Figure 3-18 Contour plot of IL for load at 10 m from the pile and receiver 5 m behind the pile.

The value of IL is shown to increase when the frequency is increased, or the shear wave velocity is decreased. Therefore, the pile will have greater vibration attenuation effects at higher frequencies and lower shear wave velocity.

The value of IL is summarised in Figure 3-19 for different values of the dimensionless parameter a_0 , which was introduced in Eq. (3-20). Based on the validation results shown in Figure 3-11, the range for a_0 is constrained to be below 1. In general, the value of IL is larger when the value of a_0 increases. This means the mitigating effects are greater when the frequency increases or the shear wave velocity decreases.



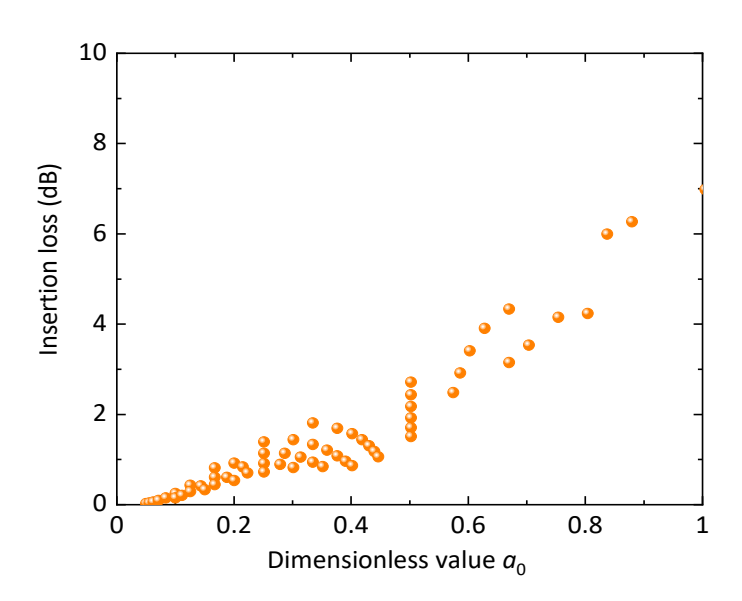


Figure 3-19 Insertion loss for different dimensionless value a_0 when the distance between load and pile is 10 m, and the distance between receiver point and pile is 5 m.

3.5 Single pile coupled with layered soil

The semi-analytical method described in the previous sections can also be applied for the case of a layered ground, which is modelled using the DSM from Appendix B.

The ground response behind the pile is investigated. To examine the influence of different layered soils on the ground response, two main types of cases are studied. The first involves an upper soil layer with a depth of 5 m and a shear wave velocity of 250 m/s, overlying subsoil layers with varying shear wave velocities of 250 m/s (which is the same as half-space case), 500 m/s, 1000 m/s, and 2000 m/s. The second involves an upper soil layer with depths of 2.5 m, 5 m, or 7.5 m, all with an identical shear wave velocity of 250 m/s, overlying a subsoil with a shear wave velocity of 2000 m/s.

3.5.1 Different shear wave velocity for subsoil

Four different cases are modelled in this section, with the only difference being the subsoil shear wave velocity. For all the cases, the upper soil shear wave velocity is 250 m/s. When the subsoil shear wave velocity is also 250 m/s, it represents a half-space soil model. The shear wave velocity is then increased to 500 m/s, 1000 m/s, and 2000 m/s. The upper soil depth is 5 m in all cases, while the subsoil is infinite in depth. The width of the pile section is 0.8 m, and the length of the pile is 10 m, which are consistent with the model dimensions used in Section 3.4. Figure 3-20 shows a sketch of the model with different shear wave velocities; it includes the distance between the point load and pile centreline, the length of the pile, and the shear wave velocities for each layered soil.

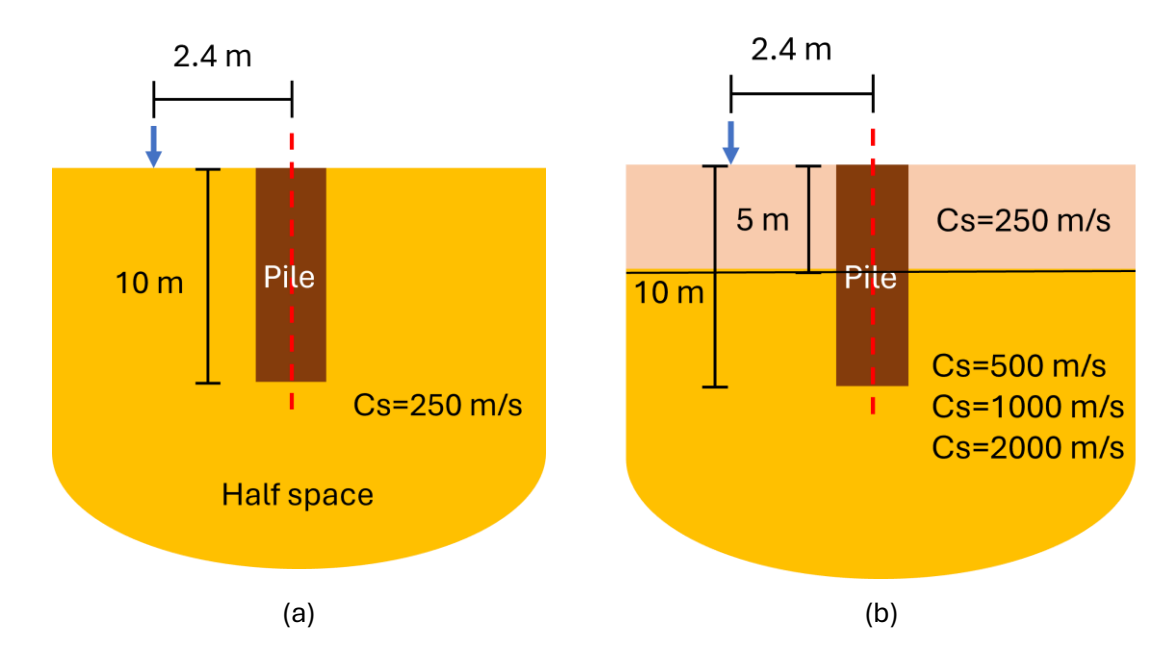


Figure 3-20 Sketch of (a) the half-space model and (b) the layered soil model.

The spectral results of the IL at 2 m and 6 m behind the pile on the centreline are summarised in Figure 3-21, which shows a peak at 25 Hz. From the spectra, the IL below 10 Hz is close to zero. Additionally, when the subsoil shear wave velocity increases, the peak value of IL also becomes greater. For layered soil, an increase in the difference in shear wave velocity between different soil layers enhances wave reflection at the interfaces. This reflected wave interferes with the surface wave generated at the pile–soil interface, reducing vibration amplification. Consequently, a larger IL peak is observed in Figure 3-21.

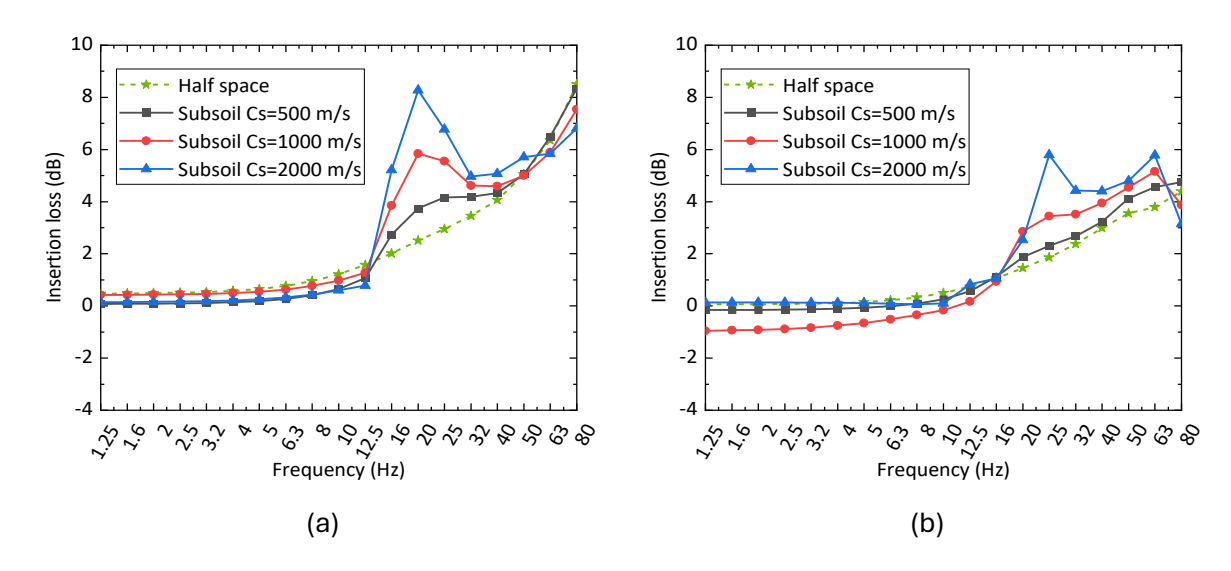


Figure 3-21 The spectral results of the IL at (a) 2 m and (b) 6 m behind the pile on the centreline for different subsoil shear wave velocity.

The overall ground velocity level behind the pile is calculated by a sum over one-third octave bands.

$$L_{\text{G,overall}}^{\text{pile}}(y_{\text{gr}}) = 10 \log_{10} \left(\sum_{i=1}^{n} 10^{\frac{L_{\text{G},i}^{\text{pile}}(y_{\text{gr}})}{10}} \right)$$
(3-36)

where $L_{\mathrm{G},i}^{\mathrm{pile}}(y_{\mathrm{gr}})$ means the ground response velocity level from the single pile model in the i-th one-third octave band. The frequency range covers bands from 1 Hz to 80 Hz.

The overall ground response velocity level in the free field is similarly calculated by

$$L_{G,\text{overall}}^{\text{free}}(y_{\text{gr}}) = 10 \log_{10} \left(\sum_{i=1}^{n} 10^{\frac{L_{G,i}^{\text{free}}(y_{\text{gr}})}{10}} \right)$$
 (3-37)

where $L_{G,i}^{free}(x_{gr})$ represents the ground response velocity level from the free-field model in the i-th one-third octave band. The frequency range covers bands from 1 Hz to 80 Hz.

An overall value of IL at receiver point $y_{
m gr}$ can be calculated by

$$IL_{\text{overall}}(y_{gr}) = L_{\text{G,overall}}^{\text{free}}(y_{gr}) - L_{\text{G,overall}}^{\text{pile}}(y_{gr})$$
 (3-38)

A contour plot of the overall IL is plotted for different shear wave velocities of the subsoil. The results are shown in Figure 3-22. It can be seen that the pattern of the IL value is similar for each value of the subsoil shear wave velocity. Overall, as the distance between the receiver and the pile increases, the value of IL decreases, indicating that the suppression of ground surface vibration becomes less significant. Surface vibration suppression is most pronounced directly behind the pile no matter what the shear wave velocity of the subsoil is. When the shear wave velocity of the subsoil increases, the IL value becomes larger, indicating that ground vibration is more effectively mitigated. When the wave velocity of the subsoil is high, it indicates that the subsoil is very stiff. For the pile, this means the constraint at the bottom part is more fixed, leading to a more significant vibration mitigation effects on the surface ground, which is consistent with the calculation results.

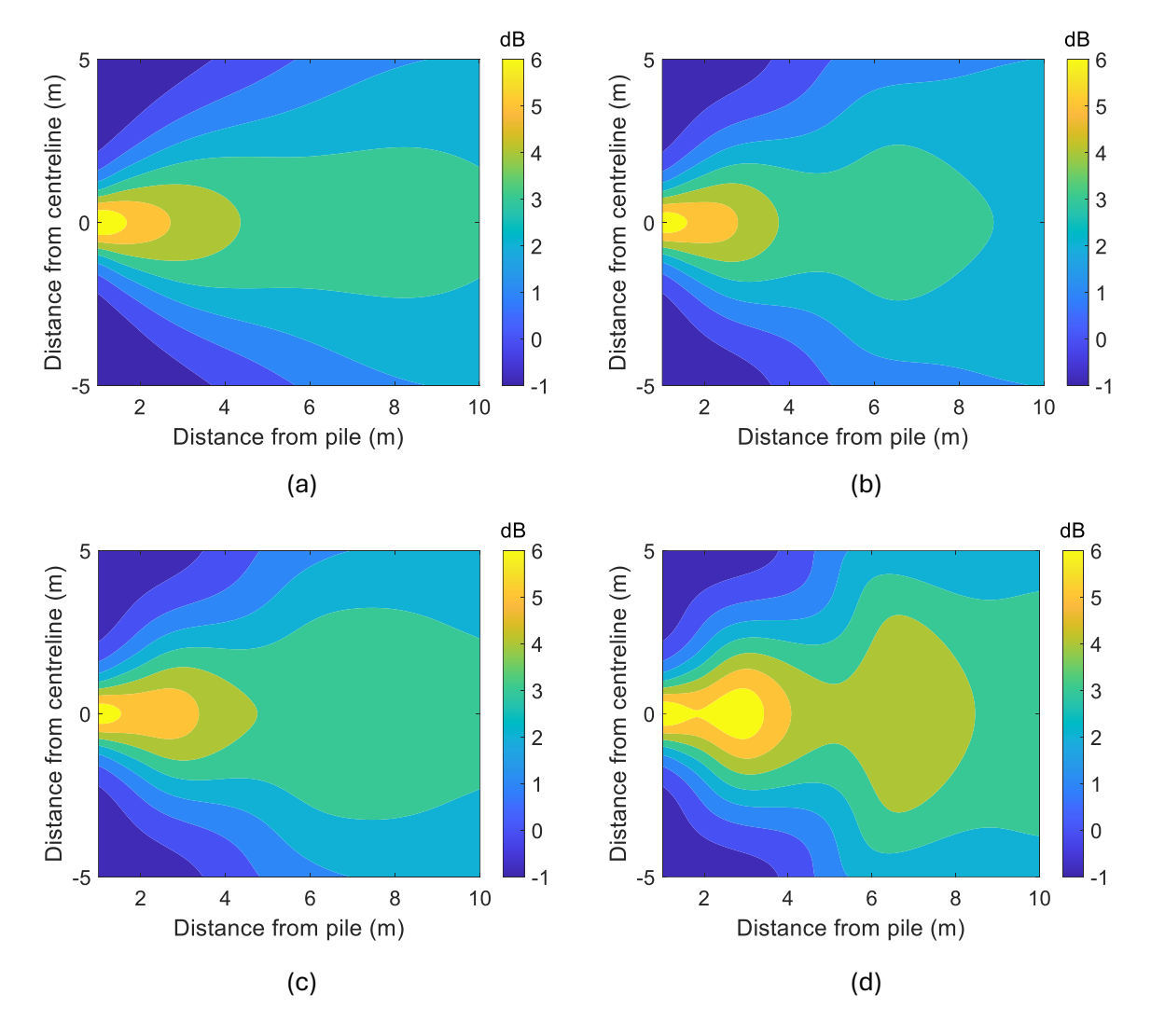


Figure 3-22 The overall IL contour from (a) half-space model (b) the model with subsoil shear wave velocity of 500 m/s (c) the model with subsoil shear wave velocity of 1000 m/s and (d) the model with subsoil shear wave velocity of 2000 m/s.

The average IL value from all the receiver points at the same distance behind the pile is calculated. The average ground velocity value level behind the pile is next calculated by

$$L_{\text{G,average}}^{\text{pile}}(y) = 10 \log_{10} \left(\frac{\sum_{i=1}^{k} 10^{\frac{L_{\text{G,overall}}^{\text{pile}}(y_{\text{gr}}^{k})}{10}}}{k} \right)$$
(3-39)

where $L_{\rm G, overall}^{\rm pile}(y_{\rm gr}^k)$ means the overall ground response velocity level (i.e. the sum over frequency bands) from the single pile model at the k-th receiver point at distance y. The value can be calculated by using Eq. (3-36).

The average ground response velocity level in the free field is calculated by

$$L_{\text{G,average}}^{\text{free}}(y) = 10 \log_{10} \left(\frac{\sum_{i=1}^{k} \frac{L_{\text{G,overall}}^{\text{free}}(y_r^k)}{10}}{k} \right)$$
(3-40)

where $L_{G, \text{overall}}^{\text{free}}(y_r^k)$ represents the ground response velocity level from free-field model at the k-th receiver point at distance x. The value can be calculated by using Eq. (3-37).

An average value of IL at a distance y behind the pile can be calculated by

$$IL_{\text{average}}(y) = L_{\text{G,average}}^{\text{free}}(y) - L_{\text{G,average}}^{\text{pile}}(y)$$
 (3-41)

The spectral IL results for different subsoil shear wave velocities are shown in Figure 3-23. The results are from all the receiver points over ± 10 m width at the same distance behind the pile. If the subsoil shear wave velocity is 250 m/s, which is the same as the upper soil, the layered soil can be seen as the half space. At frequencies lower than 10 Hz, the IL value is close to zero regardless of the situation. It can be observed that when focusing on the average IL spectrum from all receiver points, there is a significant peak at approximately 20 Hz for the 2-metre distance and at 25 Hz for the 6-metre distance. If the subsoil shear wavelength is larger, the peak value in the IL spectrum results is also larger. Similar to the peak shown in Figure 3-21, the layered soil causes increased wave reflection, which amplifies the impact of the pile on the surface vibration, resulting in a higher IL peak.

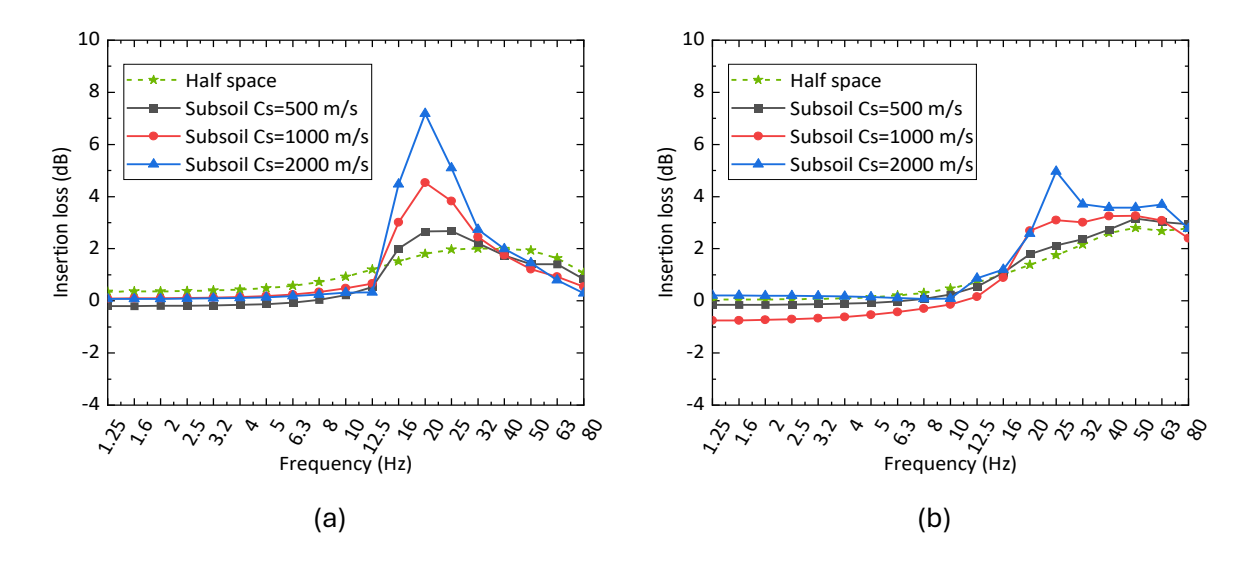


Figure 3-23 The spectral results of the IL average over ±10 m width at (a) 2 m and (b) 6 m away from the pile for different subsoil shear wave velocity.

The IL results at different distances behind the pile are shown in Figure 3-24. The average IL results are from all the receiver points on the centreline and over \pm 10 m width at the same distance behind the pile. As the distance from the pile increases, for positions along the centreline the IL generally decreases. Furthermore, higher subsoil shear wave velocities result in more effective

ground vibration mitigation along the centreline. For the value of IL averaged over ± 10 m width, the average value is minimal for small y because it approaches zero as x becomes large as can be seen from the contour in Figure 3-22. It can be seen that if the subsoil shear wave velocity is larger, the ground vibration is mitigated more.

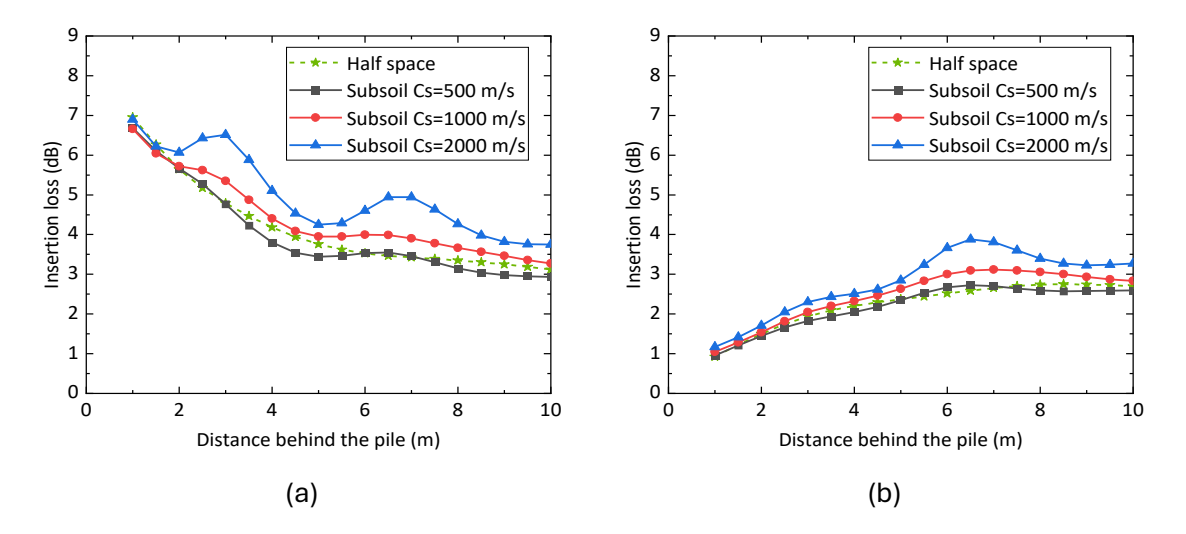


Figure 3-24 The average IL value of the receiver points with same distance behind the pile for different subsoil shear wave velocity models. (a) the results on the centreline and (b) the results average over ± 10 m width.

3.5.2 Different upper soil depth

Different depths of the upper soil layer may also influence the ground vibration mitigation effects of the single pile. In this section, the depth of the upper soil layer is investigated. For all the cases, the subsoil shear wave velocity is 2000 m/s. The depth of the upper soil layer is 2.5 m, 5 m or 7.5 m. When the upper soil layer is 5 m, the results have already been shown in section 3.5.1. A sketch of the two new cases in which the upper soil depth is 2.5 m and 7.5 m is shown in Figure 3-25.

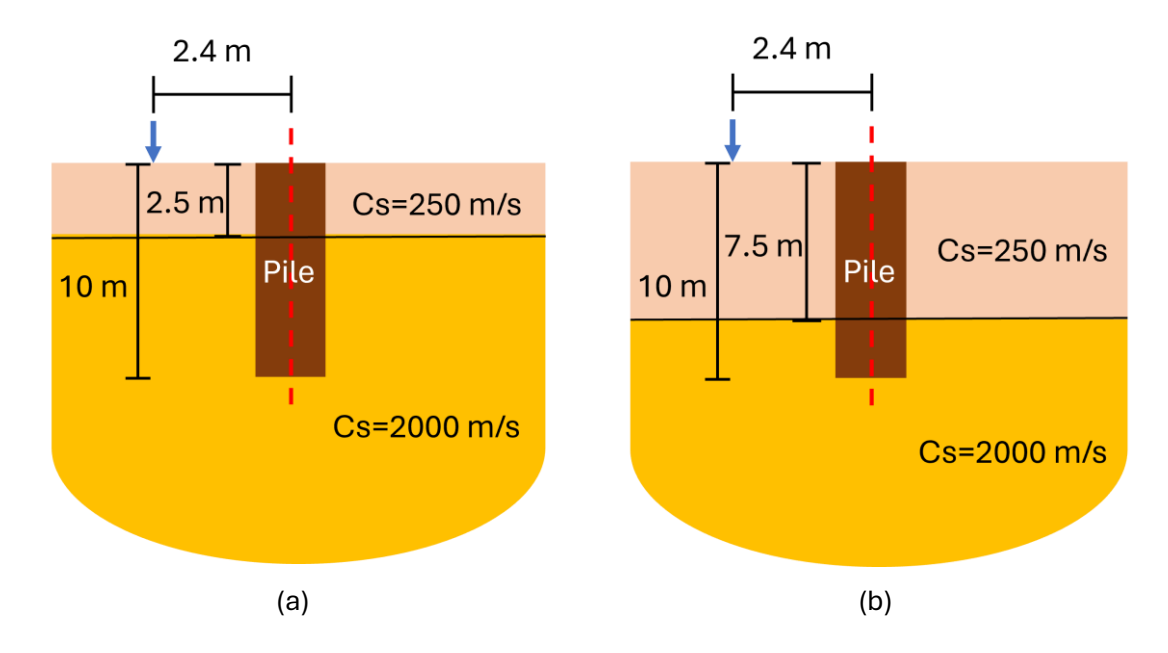


Figure 3-25 Sketch of the layered soil model when the upper soil depth is (a) 2.5 m and (b) 7.5 m.

The spectral results for the IL on the centreline, at 2 m and 6 m behind the pile, are presented in Figure 3-26 for varying upper soil depths. It can be observed that at frequencies below 10 Hz, the IL values are close to zero. Furthermore, the peak IL values occur at higher frequencies when the upper soil depth is shallower. The presence of the layered soil induces wave reflection at the interface, causing the IL peak to occur at different frequencies depending on the depth of the upper soil layer. Taking the IL at the 6 m receiver point as an example, when the upper soil depth is 2.5 m, 5 m, and 7.5 m, the corresponding IL peaks occur at 40 Hz, 20 Hz, and 10 Hz, respectively. Notably, the shear wavelengths in the upper soil at these frequencies are 6.25 m, 12.5 m, and 25 m, which correspond to approximately three times the upper soil depth.

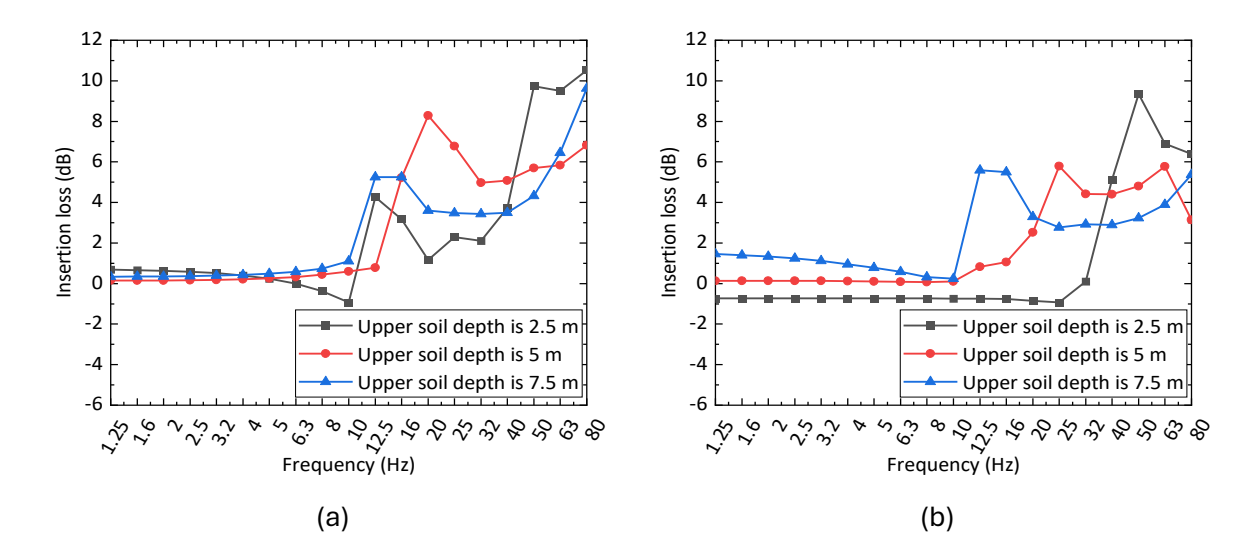


Figure 3-26 The spectral results about the IL on the centreline at (a) 2 m and (b) 6 m away from the pile for different upper soil layer depths.

Figure 3-27 shows the IL spectrum averaged over all the receiver points at distances of 2 m and 6 m behind the pile. The results are from all the receiver points over \pm 10 m width at the same distance behind the pile. Three cases are considered, with the upper soil depths being 2.5 m, 5 m, and 7.5 m, respectively. It can be observed that there is a significant peak in all cases for frequencies above 10 Hz. However, the peak value shifts depending on the location and upper soil depth. For the average IL spectrum from all receiver points 6 m away from the pile, the peak frequency decreases as the upper soil depth increases. However, for the average IL spectrum over all receiver points 2 m away from the pile, when the upper soil depth is 5 m, the peak frequency is the highest of the three cases.

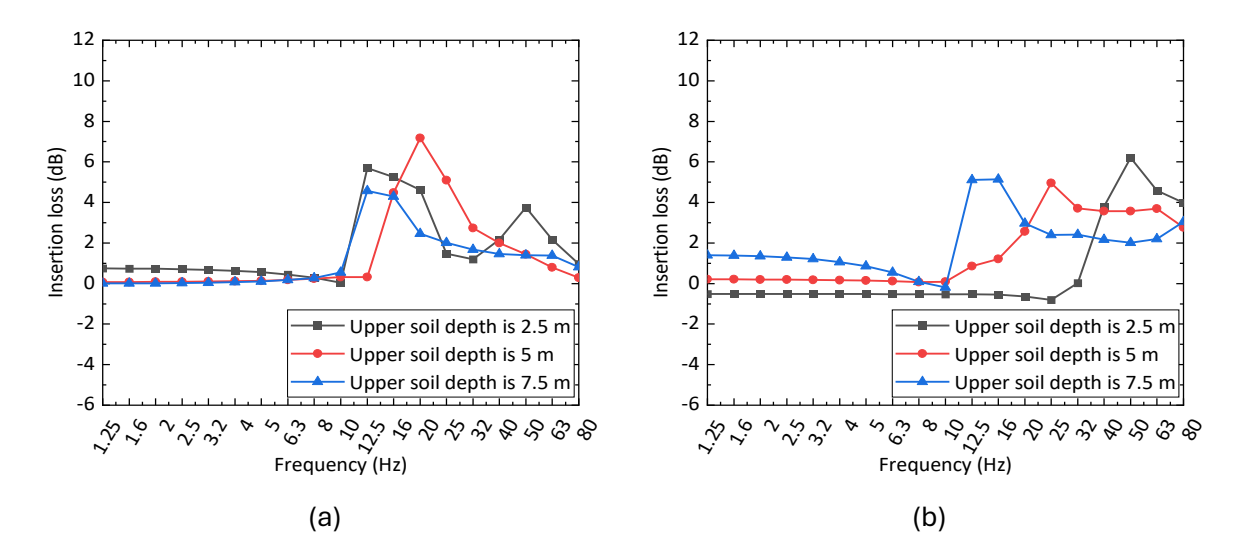


Figure 3-27 The spectral results about the IL average over ±10 m width at (a) 2 m and (b) 6 m away from the pile for different upper soil depth.

The contour plot of the overall IL on the ground behind the single pile is summarised in Figure 3-28. It can be observed that there is a ground vibration mitigation zone behind the pile no matter how deep the upper soil layer is. When the upper soil layer depth is only 2.5 m, the IL value is larger compared to the case where the upper soil layer depth is 7.5 m. The IL results from the case where the upper soil layer depth is 5 m, shown in Figure 3-22 (d), fall between these two IL values.

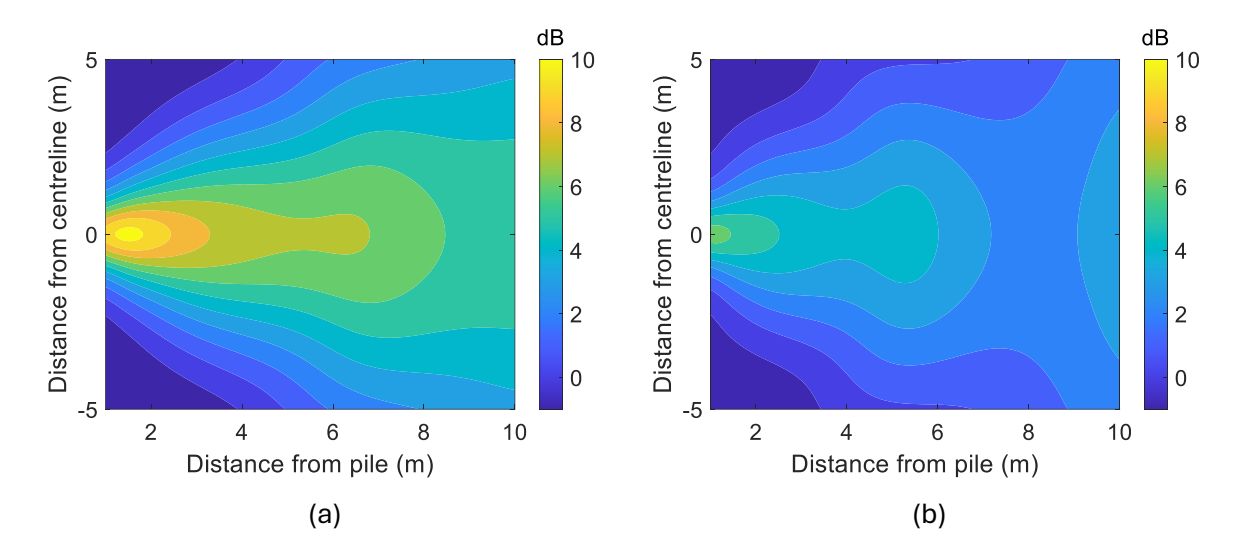


Figure 3-28 The overall IL contour of the ground behind the single pile from the model when the upper soil depth is (a) 2.5 m and (b) 7.5 m.

The overall IL is summarised in Figure 3-29, which includes the overall IL results from one-third octave bands ranging from 10 Hz to 80 Hz. Additionally, the figure presents the value of IL averaged over all the receiver points over \pm 10 m width at the same distance behind the pile. Generally, as the upper soil depth increases, the IL value decreases, indicating that the ground vibration mitigation effects are reduced. Especially when the distance away from the pile is over

6 m, different upper soil depths would cause significantly different ground vibration mitigation effects.

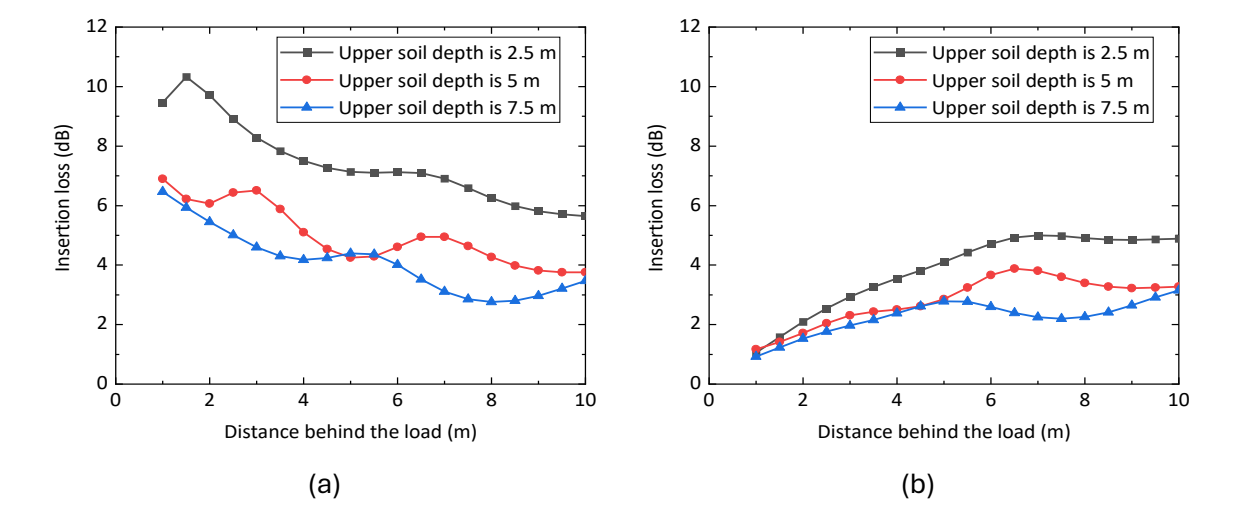


Figure 3-29 The overall value of IL from one-third octave bands 10-80 Hz for different upper soil depth models: (a) the results on the centreline and (b) the results average over ±10 m width.

3.6 Summary

A semi-analytical model is developed for simulating pile-soil interaction and calculating the ground response in the presence of a pile. This semi-analytical model is based on coupling a free field DSM model of the soil with a model of the pile based on beam finite elements. Results are compared with FE models for the full coupled pile-soil problem to evaluate the model accuracy for different frequencies and soil shear wave speeds. For this comparison, cases are considered in which the load is applied at the top of the pile and where the load is located on the ground surface at some distance from the pile.

The semi-analytical model demonstrates reliable results, particularly at lower frequencies and higher shear wave velocities, although for the case in which the load is at some distance from the pile, reliable results are obtained for a narrower range of parameters. It is found that a spacing of 0.25 m is required between the coupled nodes used in the semi-analytical model for convergence up to 80 Hz. This spacing ensures that the distance is less than one-sixth of the bending wavelength in the single pile. It is shown to be important to include rotational DOFs in the pile-soil interaction for shear wavelengths shorter than 2 m (for a pile width of 0.8 m). Compared with the classical models from the literature, the semi-analytical model considering rotational DOFs yields more accurate results. For the model including rotational DOFs, with the load at 2.4 m from the pile, the average level difference between the semi-analytical model and the FE model is less than 3 dB if the shear wavelength in the soil is greater than 3 times the pile diameter. When the dimensionless value a_0 exceeds 1.0, the average difference level is significant. This indicates that

Chapter 3

the results from the FE model, which considers the pile section size, differ greatly from those of the semi-analytical model, which is based on a single beam pile model. Thus, for shorter shear wavelengths, the difference increases as the beam model used for the pile does not account for the influence of its radius in shielding the vibration transmission.

The presence of the pile leads to a reduction in the ground response behind it. The mitigation effects become more significant as the frequency is increased, or the shear wave velocity is decreased. As the load point is moved further from the pile, the mitigation effect reduces until it converges to a roughly constant value for distances greater than 10 m.

If a pile is embedded in a layered soil, and the subsoil shear wave velocity is higher, greater mitigation of ground vibration is observed, reflecting the stabilising effects of the stiffer subsoil. Generally, when the subsoil is stiff, a decrease in the depth of the upper soil layer correlates with an increase in the IL value, indicating more ground vibration mitigation effects.

Chapter 4 Pile group-soil dynamic interaction

To study the influence on the ground response of a building situated within the transmission path between the excitation source and the receiver point, it is important to consider the complex foundations of the surrounding structures. Among these, the pile group foundation serves as a significant case. Therefore, it is valuable as a first step to study a pile group located in the transmission path without an overlying building. This investigation represents a progressive step beyond the single pile model. Based on the theory from single pile-soil interaction, the interaction of a pile group with the surrounding soil is investigated in this chapter. To simplify the model, the cap of the pile group is omitted.

4.1 Semi-analytical model for pile group

To develop a semi-analytical model, similar to the single pile-soil model, the piles are modelled by beam finite elements, and the surrounding soil is modelled using the dynamic stiffness matrix (DSM) approach. The details for the DSM method are shown in Appendix B. The main difference between single pile-soil interaction and pile group-soil interaction is the soil transfer function matrix. In the single pile model, the transfer function matrix contains only the receptances associated with one pile. However, in the pile group model, the transfer receptances between different piles are also considered.

Similar to Eq. (3-1), the ground response in the frequency domain in the presence of the pile group structure can be represented as

$$\widehat{\mathbf{U}} = \widehat{\mathbf{U}}_0 + \widehat{\mathbf{H}}_{\mathrm{S}} \widehat{\mathbf{f}}_{\mathrm{S}} \tag{4-1}$$

where $\widehat{\mathbf{H}}_s$ contains the transfer receptances between different positions on the piles and receiver points on the ground, $\widehat{\mathbf{F}}_s$ is the vector of equivalent forces acting at all the piles' coupled nodes, and $\widehat{\mathbf{U}}_0$ is the free-field response at the receiver points. When calculating the equivalent forces at all the coupled nodes, it is essential to consider the interaction between the different piles through the ground. Similar to the displacement in the single pile model described in Eq. (3-12), the displacement at the coupled nodes in the frequency domain is given by

$$\widehat{\mathbf{U}}_{p}(\omega) = \left(\mathbf{I} + \widehat{\mathbf{H}}_{Pile group}^{G}(\omega) \widehat{\mathbf{K}}_{p}(\omega)\right)^{-1} \widehat{\mathbf{U}}_{s0}(\omega)$$
(4-2)

If there are n piles in the pile group structure, the vector $\hat{\mathbf{U}}_{\mathrm{g}}(\omega)$ describes the displacement for these n piles:

$$\widehat{\mathbf{U}}_{p}(\omega) = \begin{bmatrix} \widehat{\mathbf{U}}_{p,l}(\omega) & \widehat{\mathbf{U}}_{p,2}(\omega) & \cdots & \widehat{\mathbf{U}}_{p,n}(\omega) \end{bmatrix}^{T}$$
(4-3)

where $\widehat{\mathbf{U}}_{p,n}(\omega)$ means the displacement of the n-th pile. The size of this matrix is based on the number of coupled nodes in each pile. The dynamic stiffness matrix of the pile group can be written as

$$\widehat{\mathbf{K}}_{\mathbf{p}}(\omega) = \begin{bmatrix} \widehat{\mathbf{K}}_{\mathbf{p},1}(\omega) & & \\ & \ddots & \\ & & \widehat{\mathbf{K}}_{\mathbf{p},n}(\omega) \end{bmatrix}$$
(4-4)

where $\widehat{\mathbf{K}}_{\mathrm{p},n}(\omega)$ is the dynamic stiffness of the n-th pile in the pile group. It is assumed that there is no mechanical coupling between the piles except through the ground. As in Chapter 3, equivalent properties are used for the pile to allow for the excavated soil, see Eq. (3-5) and Eq. (3-6). The ground transfer receptance between the different piles is written as

$$\widehat{\mathbf{H}}_{\text{Pile group}}^{G}(\omega) = \begin{bmatrix} \widehat{\mathbf{H}}_{11}^{G}(\omega) & \widehat{\mathbf{H}}_{12}^{G}(\omega) & \cdots & \widehat{\mathbf{H}}_{1n}^{G}(\omega) \\ \widehat{\mathbf{H}}_{21}^{G}(\omega) & \widehat{\mathbf{H}}_{22}^{G}(\omega) & \cdots & \widehat{\mathbf{H}}_{2n}^{G}(\omega) \\ \vdots & \vdots & \ddots & \vdots \\ \widehat{\mathbf{H}}_{n1}^{G}(\omega) & \widehat{\mathbf{H}}_{n2}^{G}(\omega) & \cdots & \widehat{\mathbf{H}}_{nn}^{G}(\omega) \end{bmatrix}$$
(4-5)

where $\widehat{\mathbf{H}}_{ij}^{\mathrm{G}}(\omega)$ means the receptance at j-th pile when the unit load applied on i-th pile. Each component of the transfer receptance matrix is a matrix similar to that given in Eq. (3-10).

4.2 Model comparison

Several different pile group configurations are considered that are located between the applied unit load and the receiver points. These consist of two piles aligned transverse to the line from source to receiver, two piles aligned axially to this line, and four piles arranged in a square 2×2 configuration.

For comparison with the results from the semi-analytical model, a corresponding 3D numerical FE model is established. The size of 3D FE numerical model is the same as that introduced above in Section 3.2.2. Each pile has a length of 10 m and features a square cross-section with a width of 0.8 m for simplicity. Considering the balance between computational efficiency and accuracy, the model's overall dimensions are 30×30×20 m, and the size of each element is set at 0.4 m. In ABAQUS, the element type specified is C3D8, indicating three-dimensional, eight-node brick elements. Infinite elements are used along all sides of the model to minimise the wave reflection effects occurring at the model's edge, but the bottom of the model is fixed.

The material properties are summarised in Table 4-1. The soil parameters are the same as the stiff soil parameters in the single pile model. The calculation frequency range is 10-80 Hz.

Table 4-1 Material properties used in pile group model.

Name	Density (kg/m³)	Young's modulus (MPa)	Poisson's ratio	Loss factor	P-wave speed (m/s)	S-wave speed (m/s)
Soil	2100	350	0.333	0.1	500	250
Pile	2500	30000	0.2	0.1	3652	2236

4.2.1 Two piles aligned in the axial direction

In the first configuration, two piles are located behind one another between the unit load excitation and the receiver points, i.e. two piles aligned in the axial direction (y direction). Results are compared between the 3D finite element model and the semi-analytical model. The FE model built in ABAQUS is shown in Figure 4-1. The boundary conditions, model dimensions, element sizes, material properties remain similar to the single pile 3D FE model introduced in Chapter 3. The distance between the two piles is 4 m. The distance between the point load and first pile is 2.4 m. A line of receiver points is selected behind the second pile, shown by the red markers in Figure 4-1.

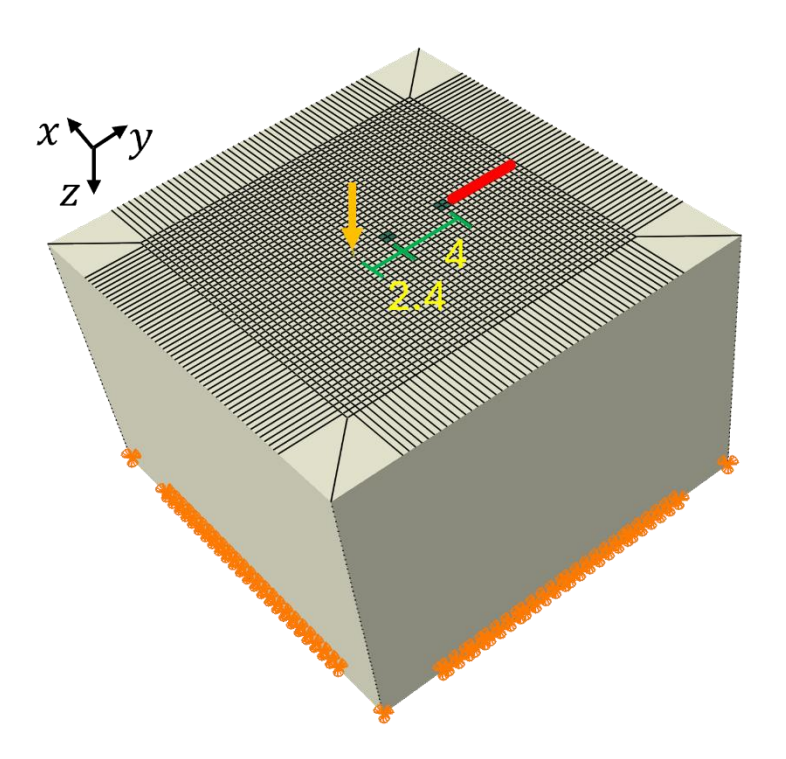


Figure 4-1 FE model of two piles aligned axially.

The magnitude of the ground displacement at the receiver points is shown in Figure 4-2. In this figure, the ground response calculated from the 3D FE model and from the semi-analytical model are compared. Additionally, the free-field response from both models is also shown. The outside edges of the piles are marked as the red dashed lines in these figures. The results from FE model and semi-analytical model are in general agreement although the match at high frequencies is not as good as at low frequencies. The receiver points behind the pile extend up to the edge of the 3D model, resulting in more significant differences between the 3D FE model and the semi-analytical model at greater distances from the load location. As mentioned in Chapter 3, the accuracy of model is related to the shear wavelength. For the pile group model, the more piles there are in the model, the more the errors accumulate and the smaller is the available range of the model.

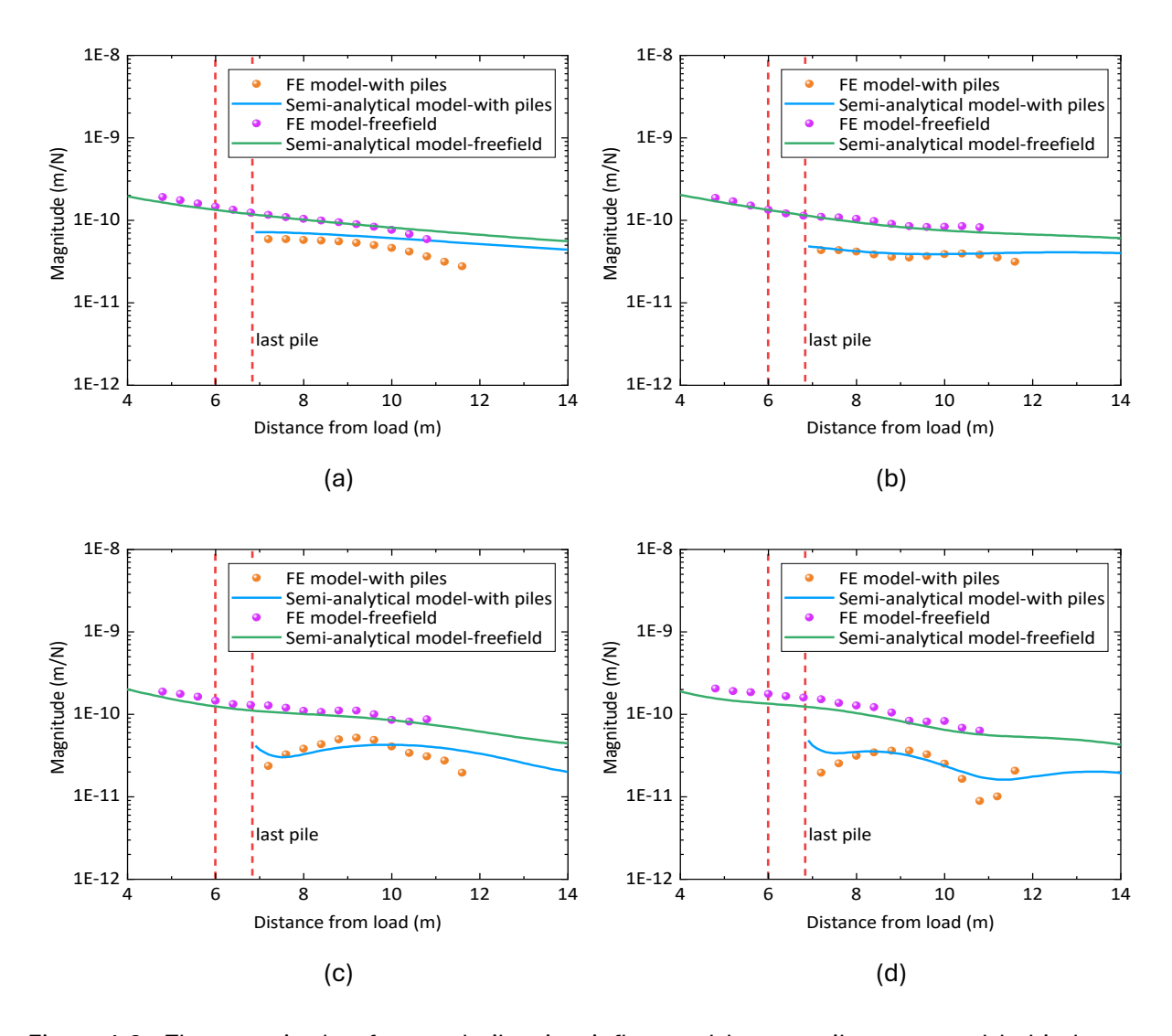


Figure 4-2 The magnitude of ground vibration influenced by two piles arranged behind one another: comparison between FE model and semi-analytical model (a) at 20 Hz, (b) at 40 Hz, (c) at 60 Hz, and (d) at 80 Hz.

The insertion loss at the frequencies of 20 Hz, 40 Hz, 60 Hz, and 80 Hz is represented in Figure 4-3. The IL results were calculated using both the semi-analytical model and the FE model. The positive IL values across all frequencies indicate that the presence of the piles effectively mitigates ground vibration at these positions.

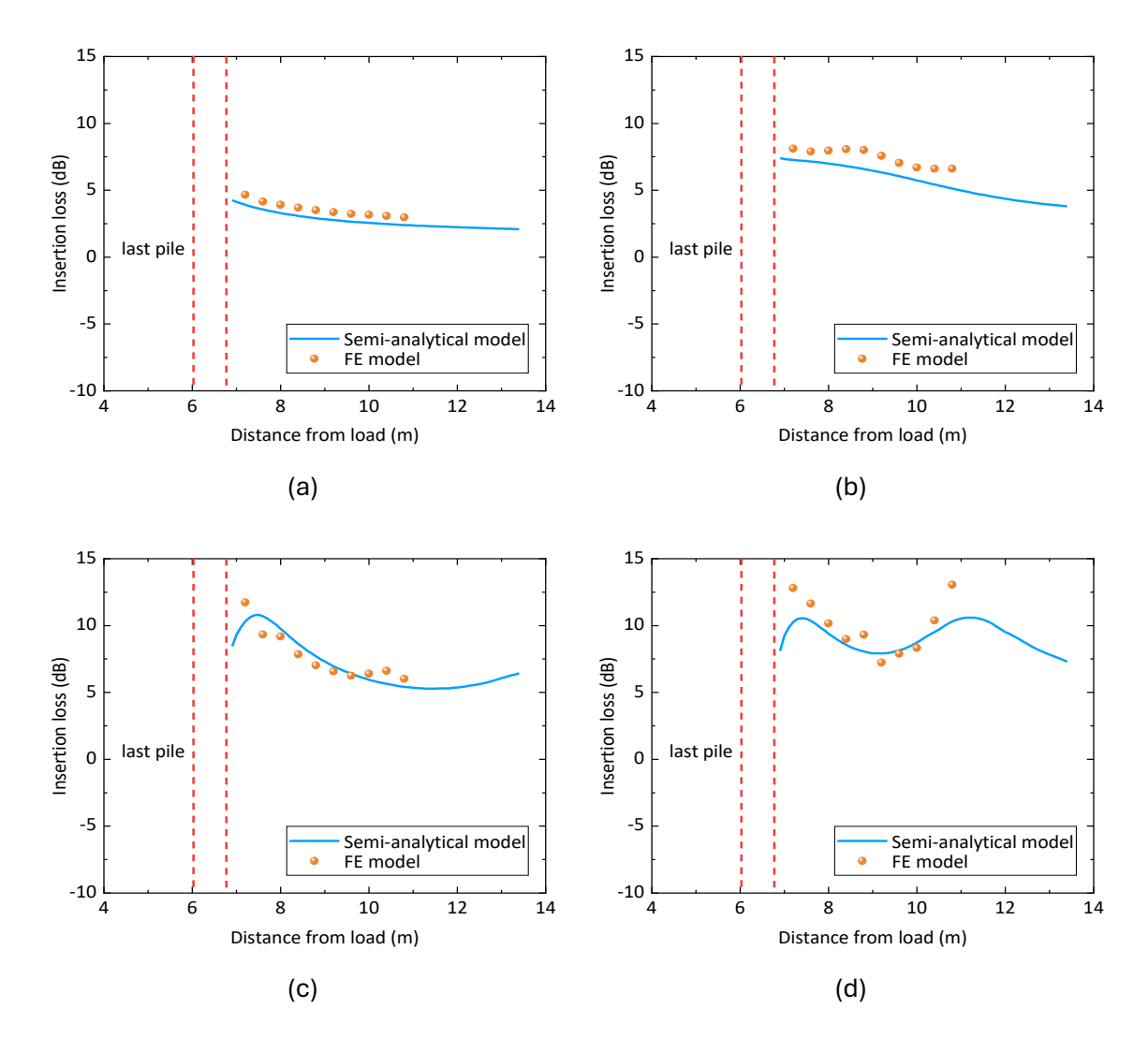


Figure 4-3 The IL from two piles arranged behind one another: comparison between FE model and semi-analytical model (a) at 20 Hz, (b) at 40 Hz, (c) at 60 Hz, and (d) at 80 Hz.

4.2.2 Two piles aligned in the transverse direction

In this second arrangement, the identical pair of piles is aligned perpendicular to the line between excitation point load and receiver points, i.e. two piles aligned in the transverse direction (x direction). All the other parameters are the same as the previous model. A sketch of FE model including the point load position (yellow) and receiver points position (red) is shown in Figure 4-4.

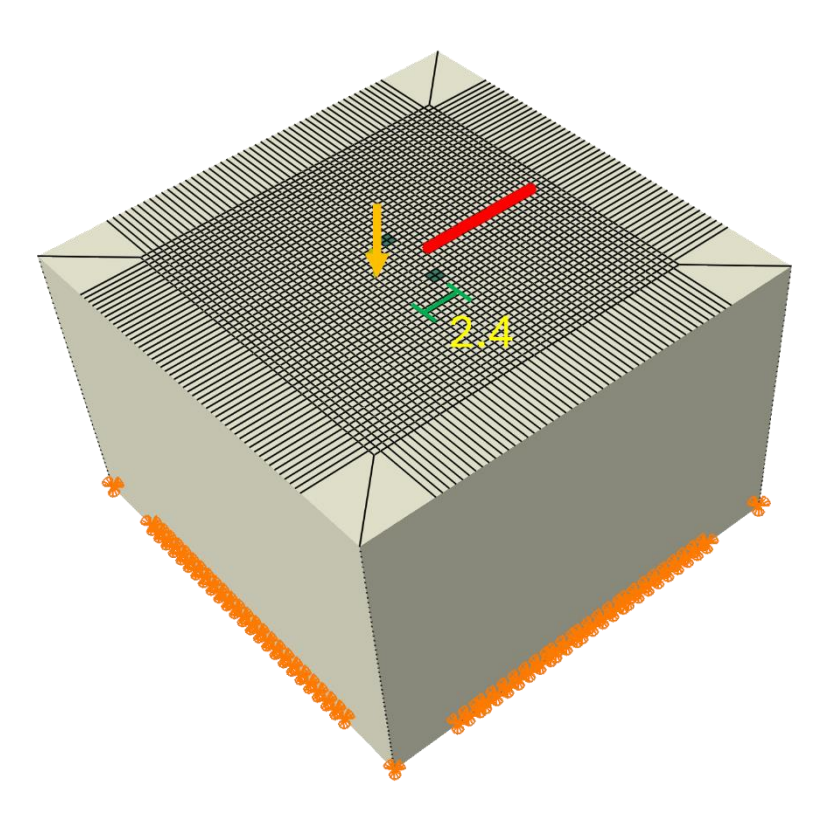


Figure 4-4 Two piles arranged beside one another in the FE model.

The magnitude of the ground displacement from the two models is shown in Figure 4-5. It can be concluded that there is a good agreement between the FE model and the semi-analytical model. In this configuration, the results obtained from the semi-analytical model exhibit a better agreement with the FE model than for the case of the two piles aligned in the axial direction. When two piles are arranged beside one another, the free-field ground response and the ground response with the piles are similar to each other on this centreline.

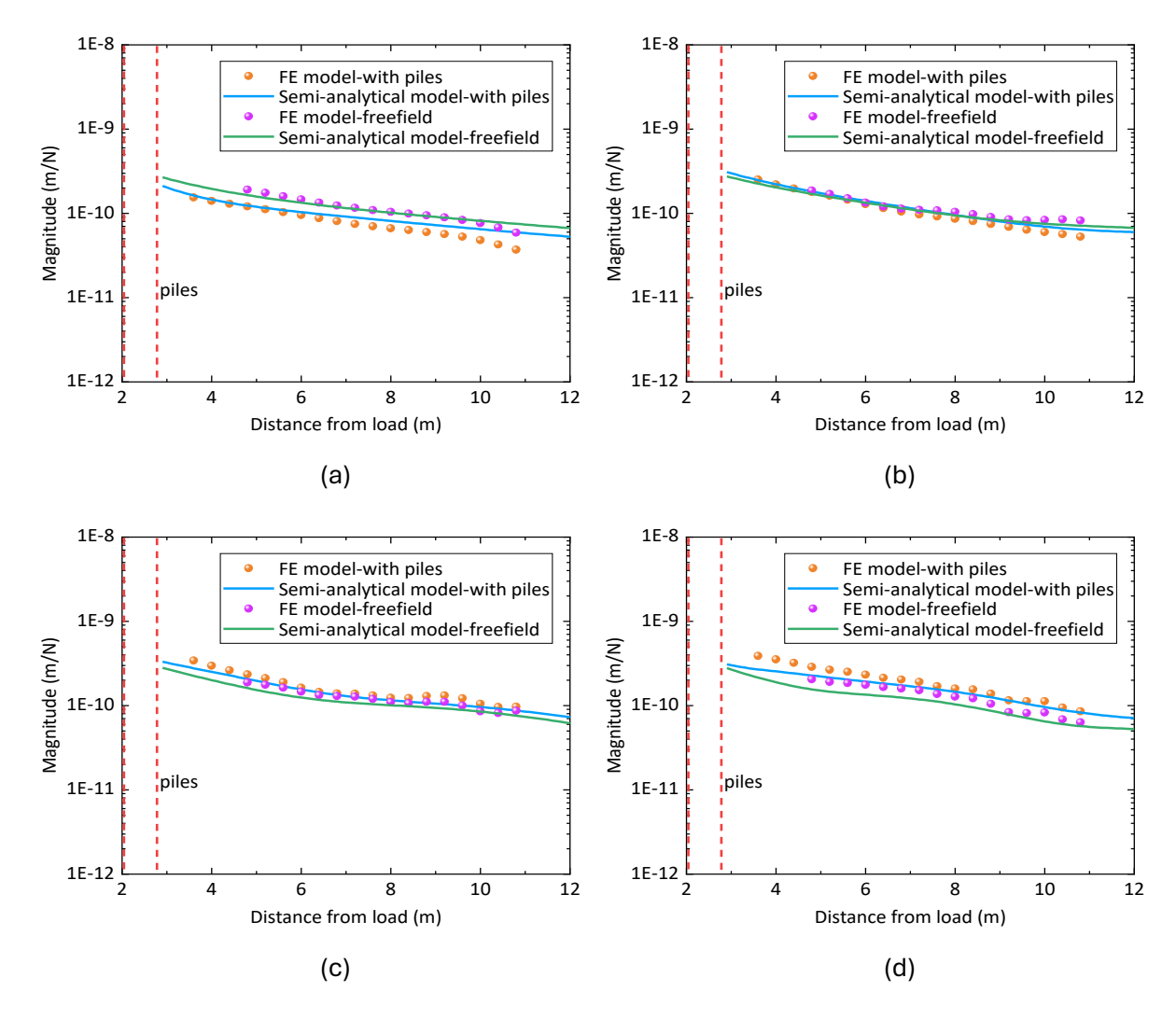


Figure 4-5 The magnitude of ground vibration influenced by two piles arranged beside one another: comparison between FE model and semi-analytical model (a) at 20 Hz, (b) at 40 Hz, (c) at 60 Hz and (d) at 80 Hz.

The IL results at frequencies of 20 Hz, 40 Hz, 60 Hz, and 80 Hz from the model with two piles aligned in the transverse direction are presented in Figure 4-6. The results are calculated on the centreline behind the piles. Compared with the IL results shown in Figure 4-3, the value of IL here is smaller, in some cases, such as at 40 Hz, the IL is near to zero. At higher frequencies (60 Hz and 80 Hz), the IL value is negative, which means the ground vibration on the centreline behind the pile is amplified.

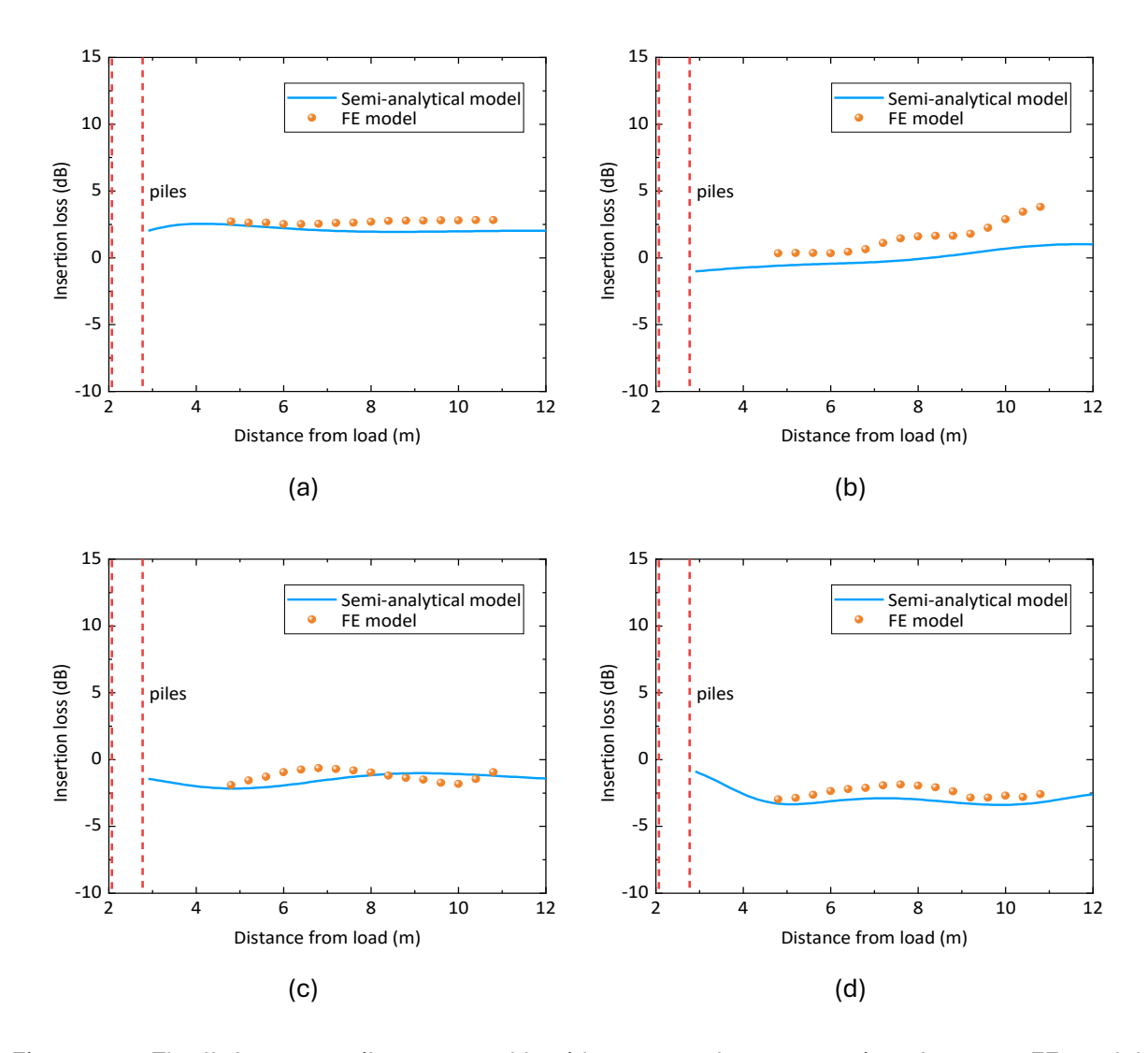


Figure 4-6 The IL from two piles arranged beside one another: comparison between FE model and semi-analytical model (a) at 20 Hz, (b) at 40 Hz, (c) at 60 Hz and (d) at 80 Hz.

4.2.3 Four piles in square arrangement

In this configuration, four piles are positioned in a square arrangement, or 2×2 pile group. The interval distance between each pile is 4 m. The schematic depiction of the FE model, featuring the arrangement of four piles, is illustrated in Figure 4-7.

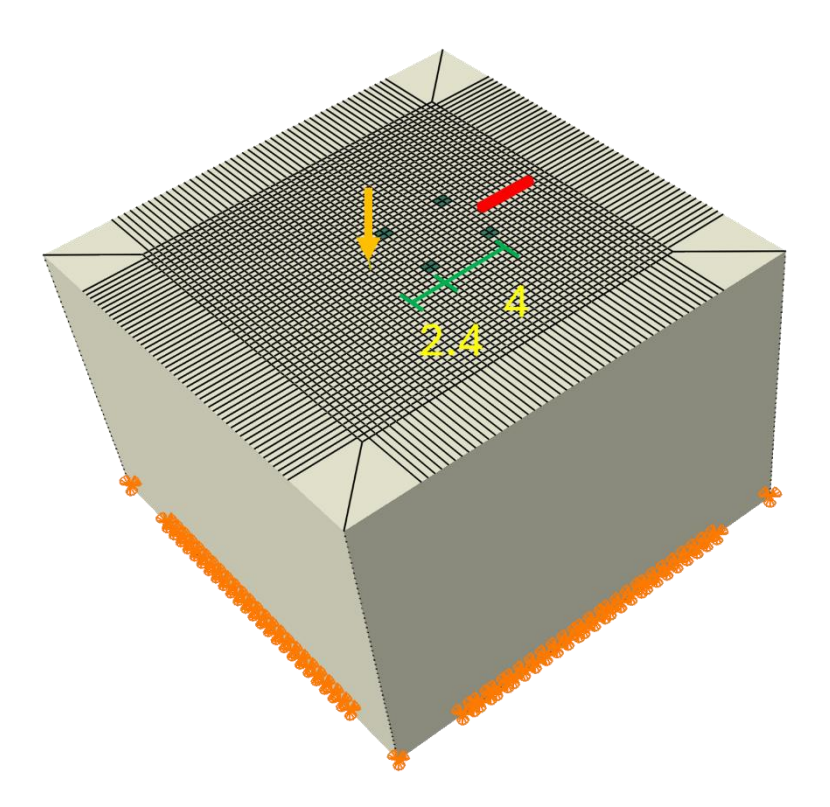


Figure 4-7 Four piles in two rows FE model.

Similar to the models introduced above, the comparison between the FE model and the semi-analytical model is shown in Figure 4-8. In this case, the results from the four pile semi-analytical model could also have good agreement with the results in the FE model, but compared with the cases of two piles, the level of agreement from the four piles model is not as good.

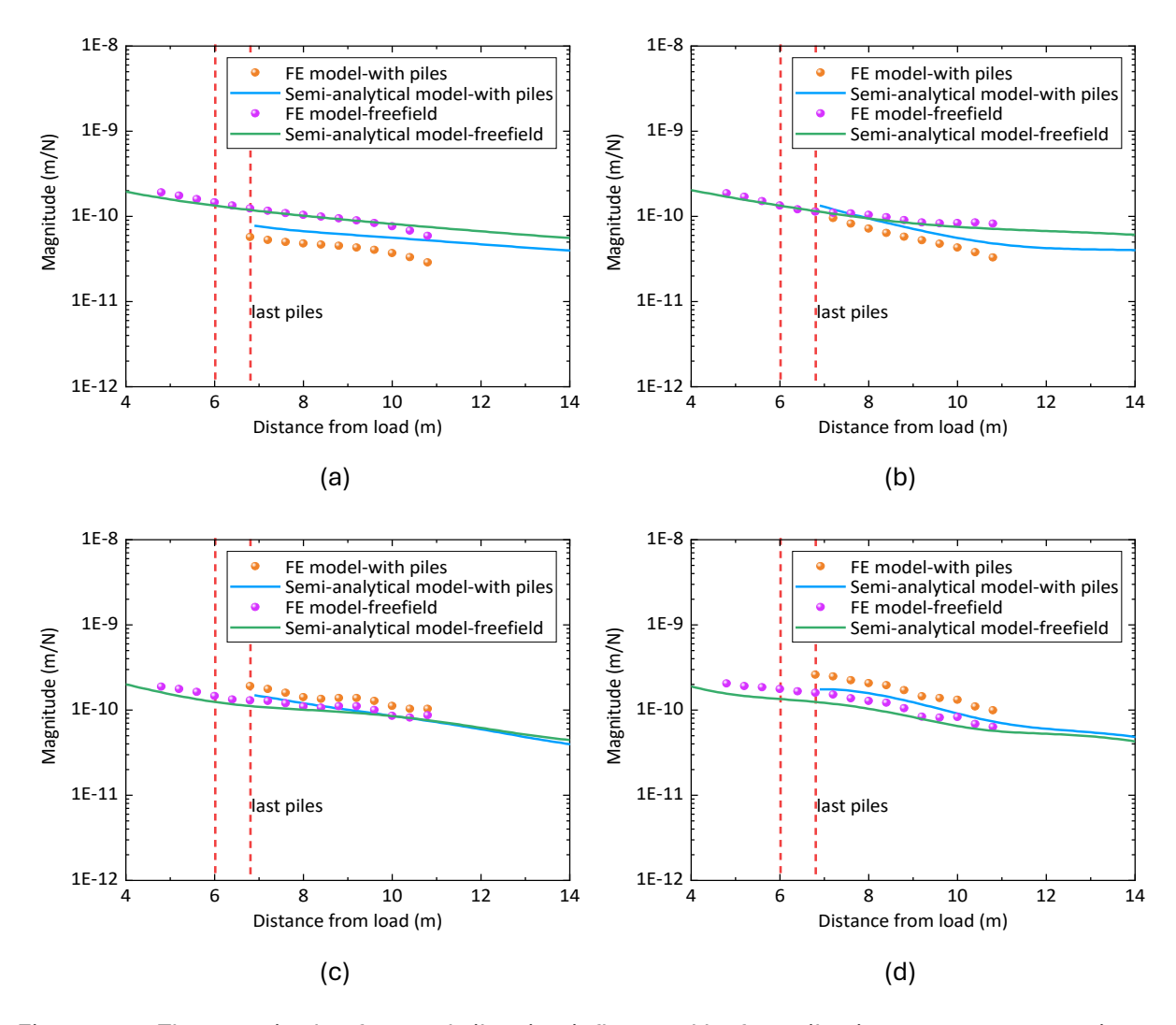


Figure 4-8 The magnitude of ground vibration influenced by four piles in two rows: comparison between FE model and semi-analytical model (a) at 20 Hz, (b) at 40 Hz, (c) at 60 Hz and (d) at 80 Hz.

The IL results are represented in Figure 4-9 at the frequencies of 20 Hz, 40 Hz, 60 Hz, and 80 Hz for the four piles in square arrangement. The IL value is positive at lower frequencies (20 Hz and 40 Hz) but negative at higher frequencies (60 Hz and 80 Hz). With the increase of the receiver distance from the load, the IL value also increased. This trend is significant especially at higher frequency.

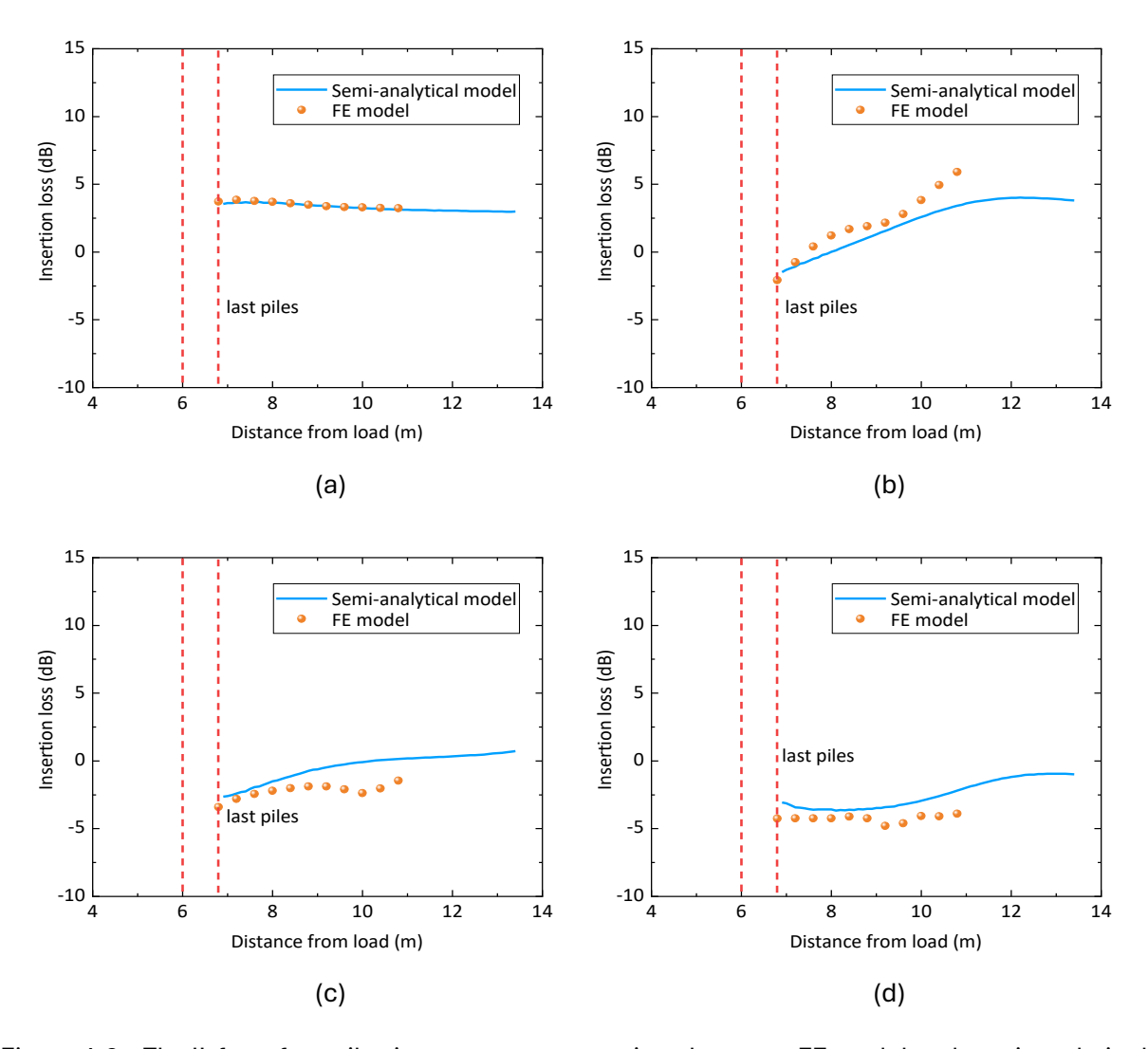


Figure 4-9 The IL from four piles in two rows: comparison between FE model and semi-analytical model (a) at 20 Hz, (b) at 40 Hz, (c) at 60 Hz and (d) at 80 Hz.

4.3 Model limitations

Based on the size limitation of the FE model, and the cumulative errors from the semi-analytical pile group model, the performance of the model may be compromised when there are a greater number of piles in the pile group. In this section, the relationship between the number of piles and the model accuracy is discussed.

A larger FE model is constructed for the purpose of this investigation, to avoid the additional piles being situated in close proximity to the boundary which would impact the outcomes. Different configurations of piles are considered as shown in Figure 4-10. The length and width of this FE model are both 40 m. On each side, there are infinite elements, which minimise the impact of wave reflection. The depth of the model is 20 m. There are fixed boundary conditions at the bottom of the model. As in the previous section, the shear wave velocity is 250 m/s, and the

compressional wave velocity is 500 m/s. The element dimension is 0.4 m, which ensures that there are a minimum of six elements per wavelength for frequencies up to 80 Hz. The interval between different piles is 2 m. The length of the piles is 10 m with the same dimensions and material properties as previously.

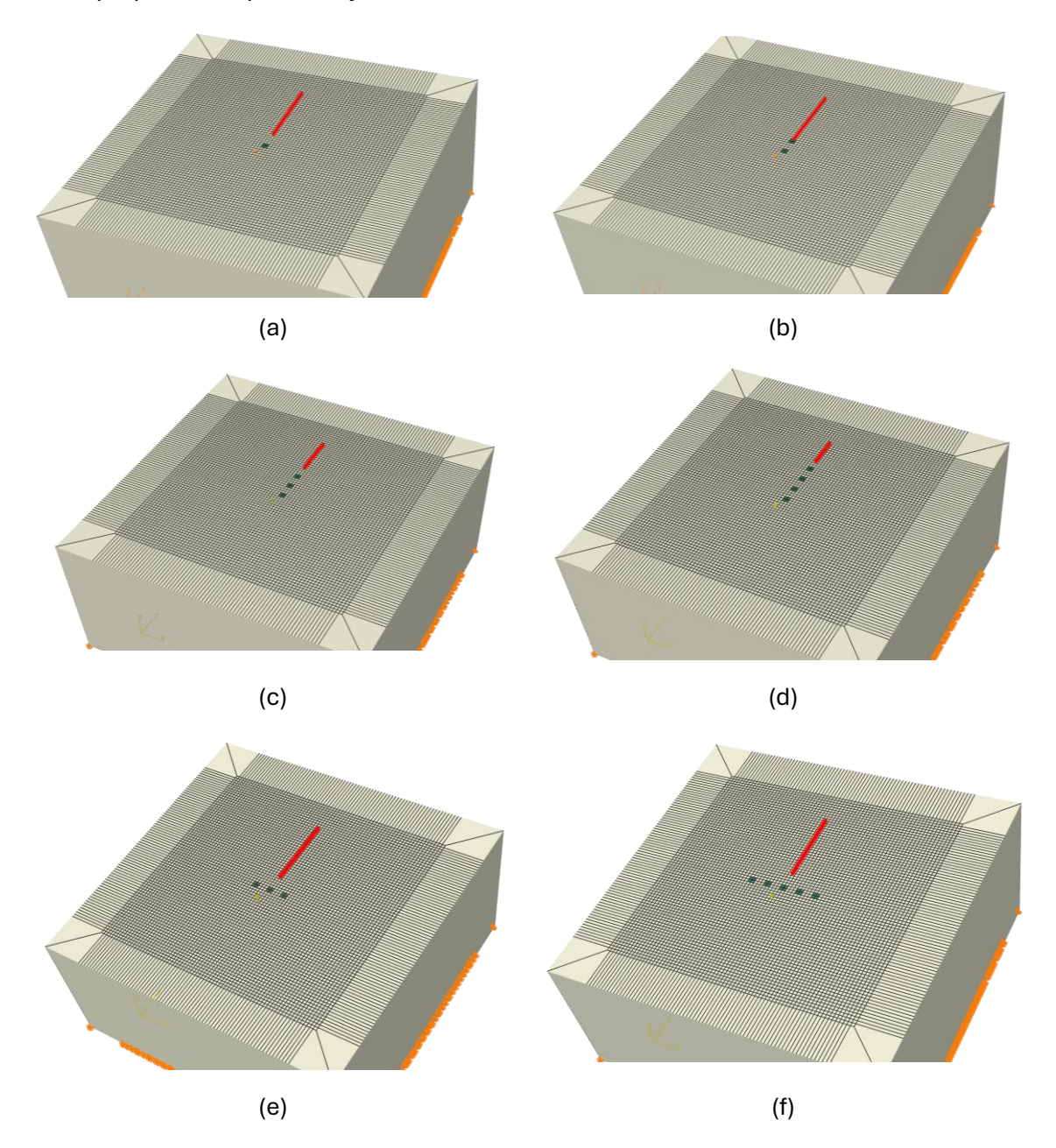


Figure 4-10 Different pile group arrangements for model limitation investigation with receivers on the centreline with (a) one pile (b) two piles arranged behind one another (c) three piles arranged behind one another (d) four piles arranged behind one another (e) three piles arranged beside one another and (f) five piles arranged beside one another.

The average level differences of the ground displacement response for different receiver points on the centreline, when the piles are arranged in the axial direction and in the transverse direction, are summarised in Figure 4-11. These differences are between the ground responses obtained from the semi-analytical model and the FE model. The average level difference is calculated

based on Eq. (3-15), with the results calculated from the 3D FE model used as the reference results. This allows the accuracy of the results from the semi-analytical pile group model to be evaluated.

In the low-frequency region, below 30 Hz, the average level differences are close to zero for all the cases, which means the semi-analytical model remains accurate regardless of the number of piles involved. But when the frequency is 30 Hz and above 50 Hz, when the piles are arranged behind one another, the model calculation error becomes large as the number of piles increases. The average level differences between FE model and semi-analytical model is less substantial when the piles are aligned in the axial direction. However, there is still a notable divergence, especially at higher frequencies.

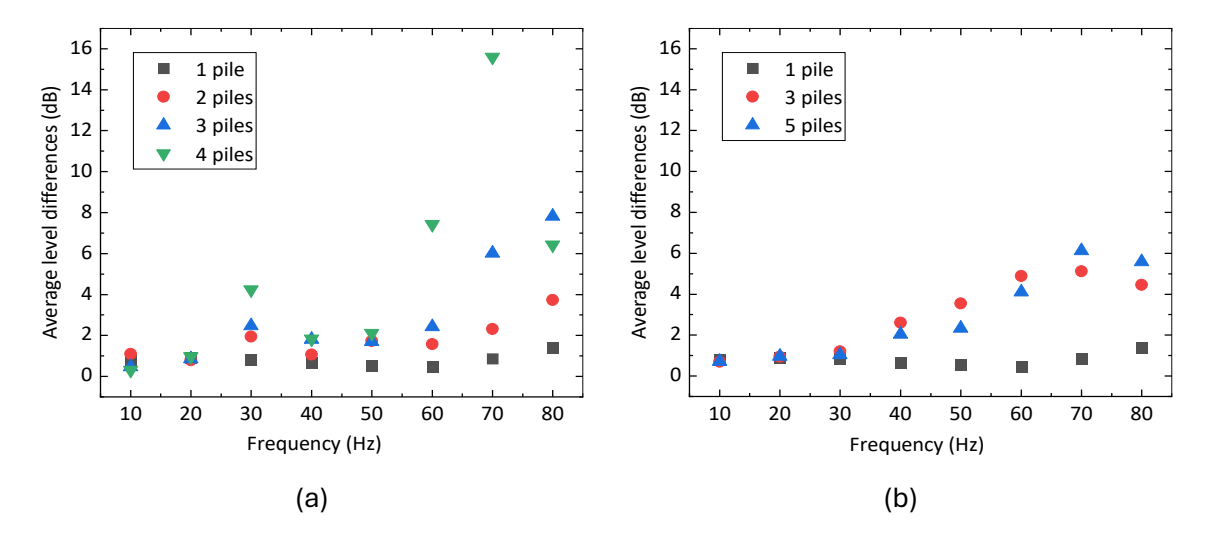


Figure 4-11 Summarised average ground displacement level differences on the centreline behind the pile group when the piles are arranged (a) behind one another, (b) beside one another.

The investigation also considers ground response receiver points located not only on the centreline but also in a region behind the pile group. A total of 28 receiver points, spaced 1.6 m apart, were selected to assess the accuracy of the model. The sketch of the pile group and receiver points are shown in Figure 4-12.

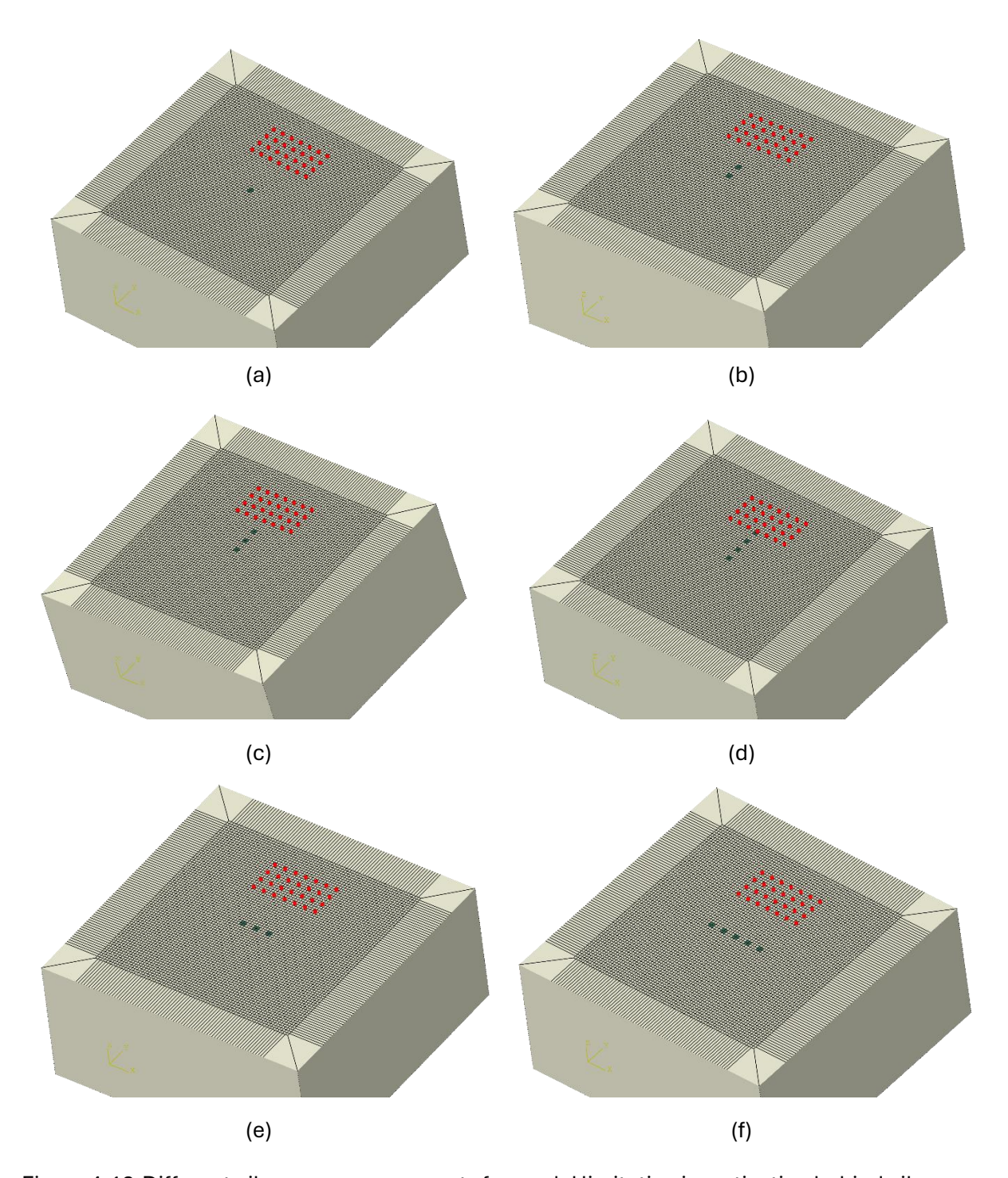


Figure 4-12 Different pile group arrangements for model limitation investigation behind pile group with (a) one pile (b) two piles arranged behind one another (c) three piles arranged behind one another (d) four piles arranged behind one another (e) three piles arranged beside one another and (f) five piles arranged beside one another.

The average level differences for the receivers behind the pile group are summarised in Figure 4-13. The results from all receiver points located behind the pile group exhibit a similar trend to the average level differences results observed on the centreline behind the pile group. The semi-analytical model yields accurate results when there are fewer than three piles arranged in the

direction of the load and receiver points, particularly at lower frequencies. When the number of piles exceeds three, the model's accuracy decreases due to the accumulation of errors.

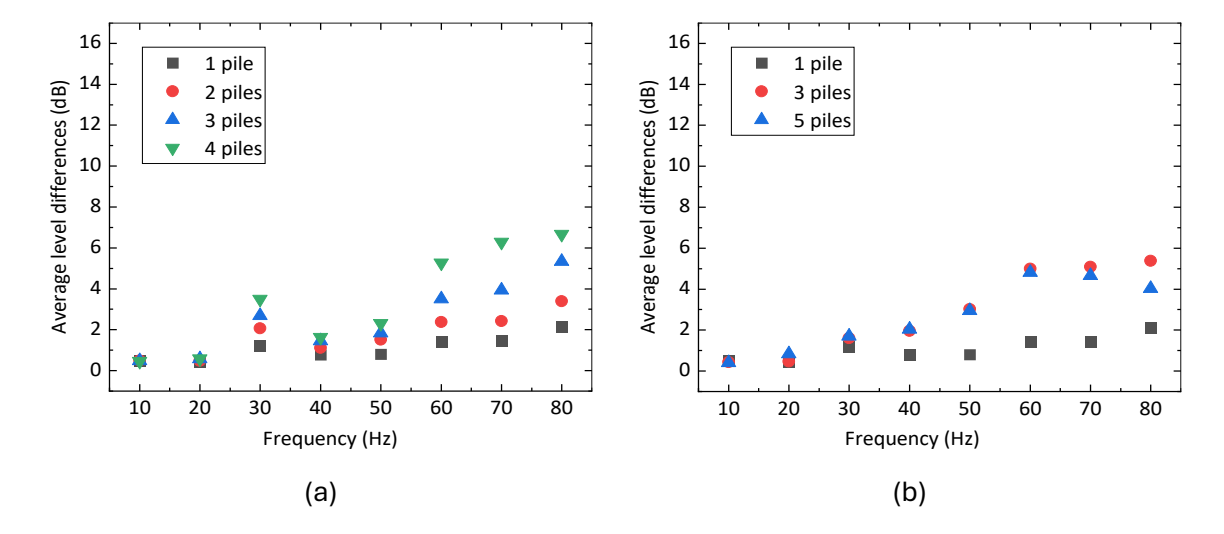


Figure 4-13 Summarised average ground displacement level differences for all the receiver points behind the pile group when the piles are arranged (a) behind one another, (b) beside one another.

4.4 Ground response

In this section, the IL of the ground influenced by the pile group is investigated using the semi-analytical model within the reliable range discussed in Section 4.3. Detailed results are presented in this section for the mitigation effect of pile groups, concentrating on 2×1, 1×2 and 2×2 configurations. Pile spacing of 2 m and 4 m are considered. The results are obtained using the semi-analytical model.

4.4.1 Ground centreline response under different source load positions

In this section, the influence of the distance between the load and the pile group is investigated. Various load-pile distances are considered: 1 m, 2.5 m, 5 m, 10 m, 20 m, and 40 m. The analysis includes three different pile group configurations, with two different pile spacings of 2 m and 4 m. The IL results are averaged over a width of ± 10 m over receivers which have same distance away from the pile in the y direction. Three receiver distances are investigated, which are 5 m, 10 m and 15 m away from the first pile location. The IL is calculated from the difference in overall ground velocity level with/without pile evaluated over the range 10-80 Hz. For each one-third octave band, there are at least three frequency samples. The results are shown in Figure 4-14.

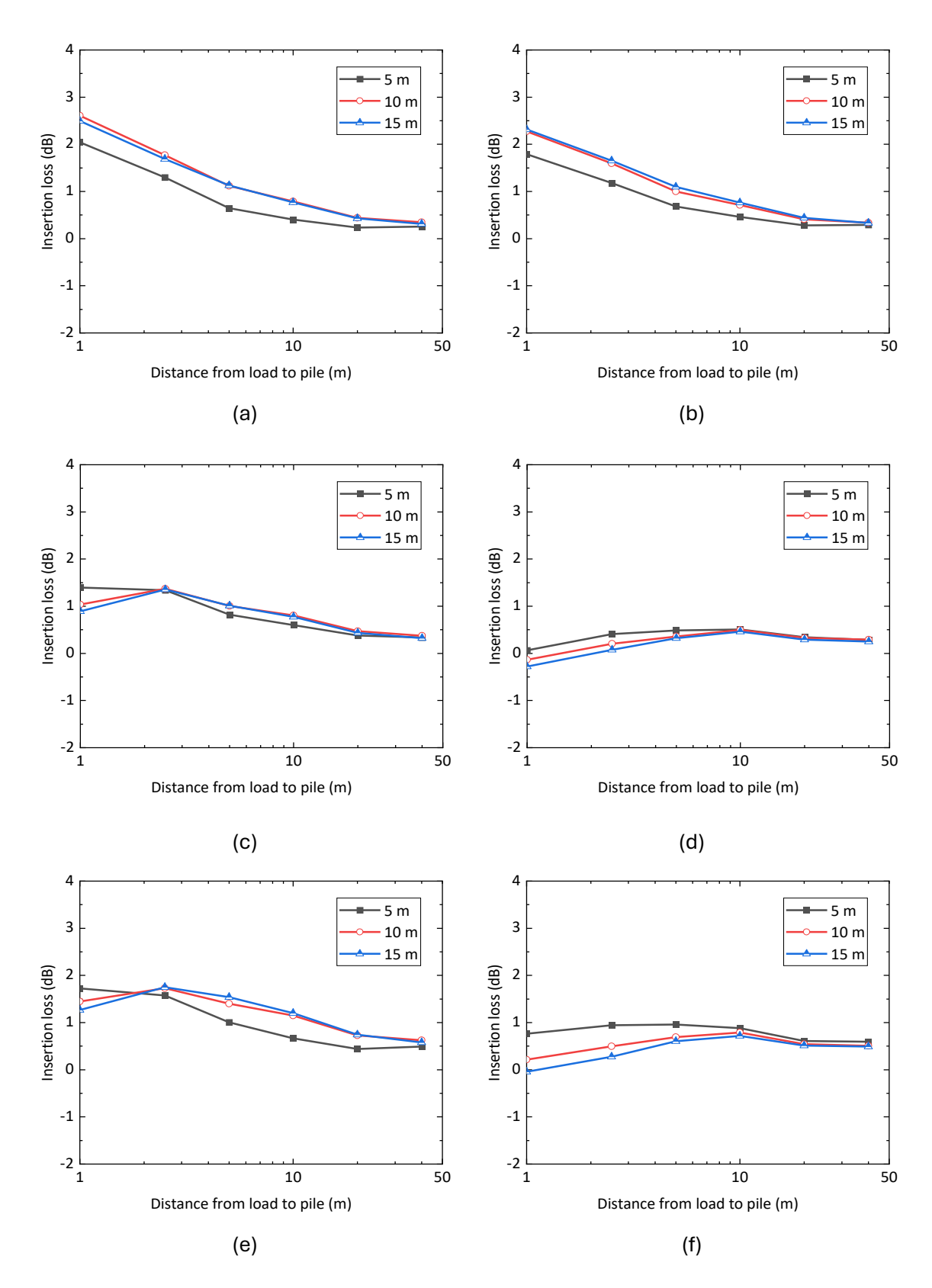


Figure 4-14 The IL averaged over ±10 m width on the ground which is 5 m, 10 m and 15 m behind the first pile and calculated from the difference in overall ground velocity level with/without piles evaluated over the range 10-80 Hz. under different load locations for two piles aligned in the axial direction with spacing (a) 2 m (b) 4 m, two piles aligned in the transverse direction with spacing (c) 2 m (d) 4 m, four piles in square arrangement with spacing (e) 2 m and (f) 4 m.

Chapter 4

If two piles are aligned in the axial direction, as the distance between the excitation load and the pile increases, the IL value decreases, indicating that the mitigation effects of ground vibration weakens if the distance between the load and the pile is large. Additionally, the value of IL at a receiver 5 m behind the first pile is lower than at 10 m and 15 m distance. The trend of declining IL is similar when the spacing is 2 m or 4 m, especially when the receivers are 10 m and 15 m away from the first pile.

If two piles are aligned in the transverse direction, or four piles are in a square arrangement, the value of IL is different under pile spacings of 2 m and 4 m. For receivers located 10 m and 15 m away from the pile, the IL typically first increases and then decreases as the distance between the load and the pile group increases. Because the load is applied on a line between the two piles of the configuration in the x-direction, this setup differs from that of two piles aligned in the axial direction. If the load is positioned too close to the pile group, such as a distance closer than the spacing between the piles, the IL may be smaller compared to when the load distance is similar to the pile spacing.

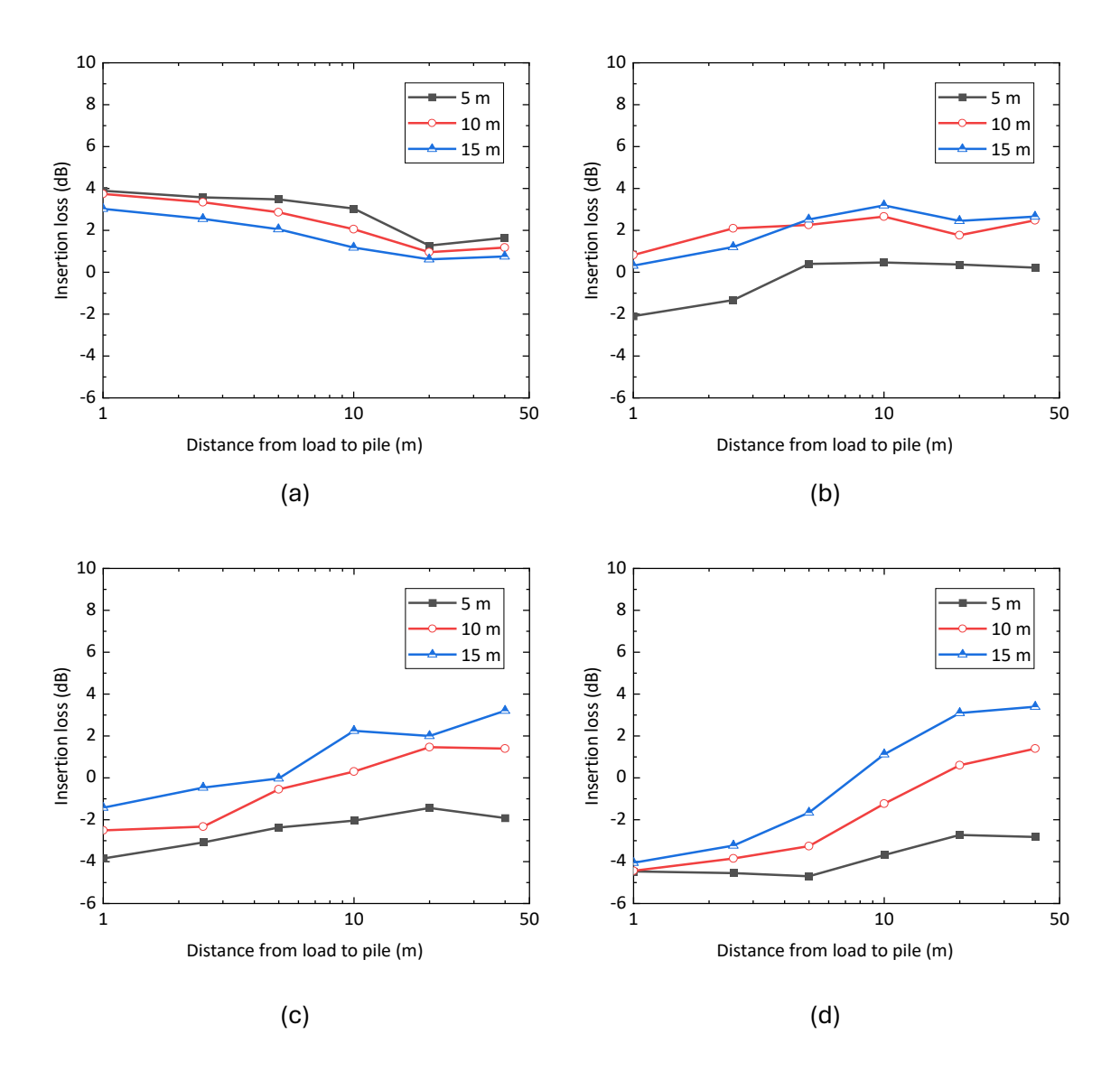


Figure 4-15 The different load location IL for four piles in square arrangement when spacing is 4 m at (a) 20 Hz, (b) 40 Hz, (c) 60 Hz and (d) 80 Hz.

Results at specific frequencies and receiver points were also investigated. For example, Figure 4-15 shows results for piles arranged in a 2×2 configuration with a pile spacing of 4 m. These results are at frequencies of 20 Hz, 40 Hz, 60 Hz, and 80 Hz, with receiver points on the centreline 5 m, 10 m, and 15 m behind the first pile. At lower frequencies, the IL value decreases as the pile-load distance increases. Additionally, the values for the three receiver points are similar. However, at 80 Hz, the IL value shows an increasing trend with the rise in the pile-load distance. Furthermore, notable discrepancies exist among the values observed for the three different receiver points.

In summary, the ground vibration mitigation effects influenced by the pile group foundation perform differently at different frequencies and different receiver points. In general, if the load is applied between two piles in the x direction, the pile group may amplify the ground vibration on

the centreline at some frequencies, particularly when the excitation load is in close proximity to the piles.

4.4.2 Average insertion loss values

In this section the IL is determined over an area behind the pile group. Contour plots are presented in Figure 4-16 for the three different pile group configurations mentioned above, located between the point load and receiver points. After investigating the effect of the distance between the load and the first pile, a distance of 10 m has been selected for further investigation by using the semi-analytical model. In these cases, the distance between the load and the first pile in the axial direction is 10 m to represent far field excitation. The IL value is presented as the average value across one-third octave bands 10 Hz to 80 Hz.

When two piles are aligned in the axial direction, the contour results reveal a significant zone of high IL directly behind the piles, indicating substantial ground vibration mitigation effects in that area. For two piles aligned in the transverse direction and four piles in a square arrangement, the contour results show that there is a region of high IL behind the piles. When the spacing between two piles is only 2 m, these regions may overlap. When the spacing is 4 m, the zones of high IL do not overlap and, between them, there are some zones of low IL, which indicate that when the spacing is 4 m, the ground vibration in the centreline may not be mitigated. In general, the overall IL behind the pile group is positive, which means the ground response behind the pile group is mitigated. There is a significant vibration mitigation effect directly behind the piles. So, when two piles are aligned in the transverse direction, or there are four piles in a square arrangement, the centreline on the ground behind the pile group may not have significant vibration mitigation, especially when the spacing of the piles is 4 m.

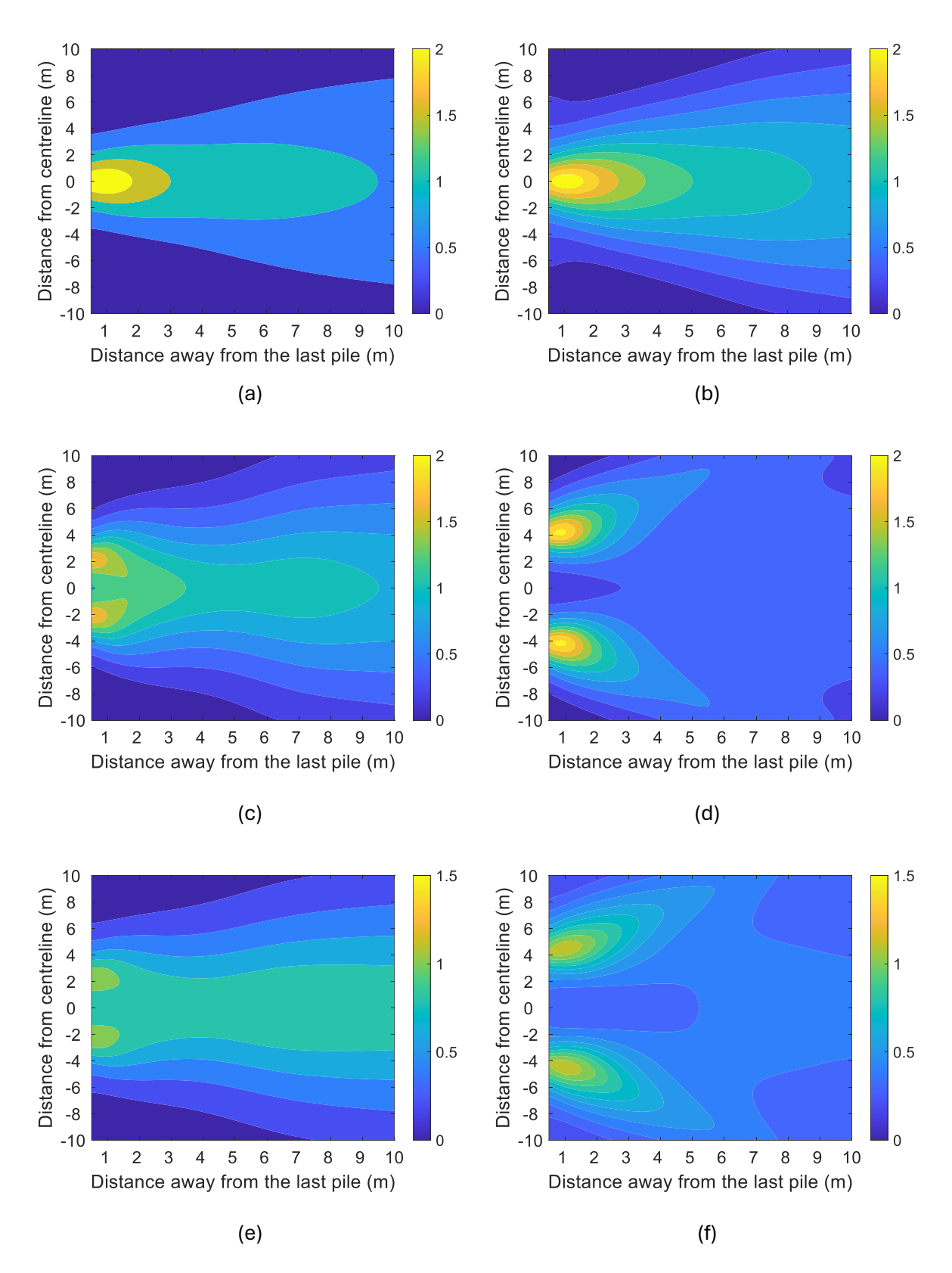


Figure 4-16 Contour plot of IL (in dB) on ground surface (sum over one-third octave bands ranging from 10-80 Hz) when (a) two piles aligned in the axial direction with 2 m spacing (b) two piles aligned in the axial direction with 4 m spacing (c) two piles aligned in the transverse direction with 2 m spacing (d) two piles aligned in the transverse direction with 4 m spacing (e) four piles in square arrangement with 2 m spacing and (f) four piles in square arrangement with 4 m spacing.

The vibration mitigation effects are assessed by calculating the average IL values at different distances behind the pile group. This average IL value is derived from the average free field and total ground response obtained at receiver points at the same distance behind the last pile, spanning a range of 10 m in the transverse direction. The calculation steps are based on Eq. (3-39) to Eq. (3-41). This gives a single representative value for each distance behind the piles and this average IL is plotted in Figure 4-17. It can be seen that the four piles in square arrangement can provide the greatest vibration mitigation effects. When the pile spacing is 4 m, the IL value is higher in the near field but lower in the far field. For the two piles aligned in the transverse direction, the trend is similar, but the IL values are lower. For the two piles aligned in the axial direction, the average IL value remains at about 0.75 dB, no matter how far from the pile foundation.

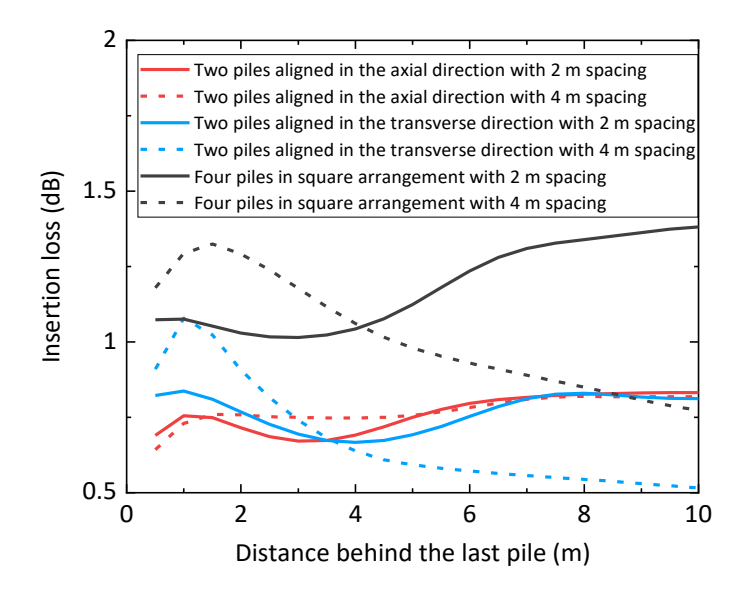


Figure 4-17 The overall IL results from one-third octave bands 10-80 Hz and average over ±10 m width on the ground with different distance away from the pile group.

The IL in one-third octave bands is shown in Figure 4-18 in the form of the mean values obtained from receiver points located at an equal distance behind the piles. Two receiver distances are selected at 4 m and 8 m from the last piles. The results indicate that various configurations of pile group can yield different peak IL values at distinct frequencies. At frequencies below 10 Hz, none of the configurations investigated are able to affect the ground vibration significantly as the IL value is close to zero. The configuration with four piles arranged in a square pattern with a 2 m spacing gives the highest IL values below 80 Hz. The spectral IL results at the peak vary depending on the spacing of the pile group and the location of the receiver points behind the pile group. Conversely, the IL reaches its lowest value at a frequency of 80 Hz and 100 Hz for the four piles arranged in square arrangement cases. In all cases, the IL value for the 4 m spacing configuration is generally lower than that of the 2 m spacing configuration at low frequencies. However, as the frequency increases, the situation reverses, with the IL value for the 2 m spacing configuration becoming larger than that for the 4 m spacing configuration.

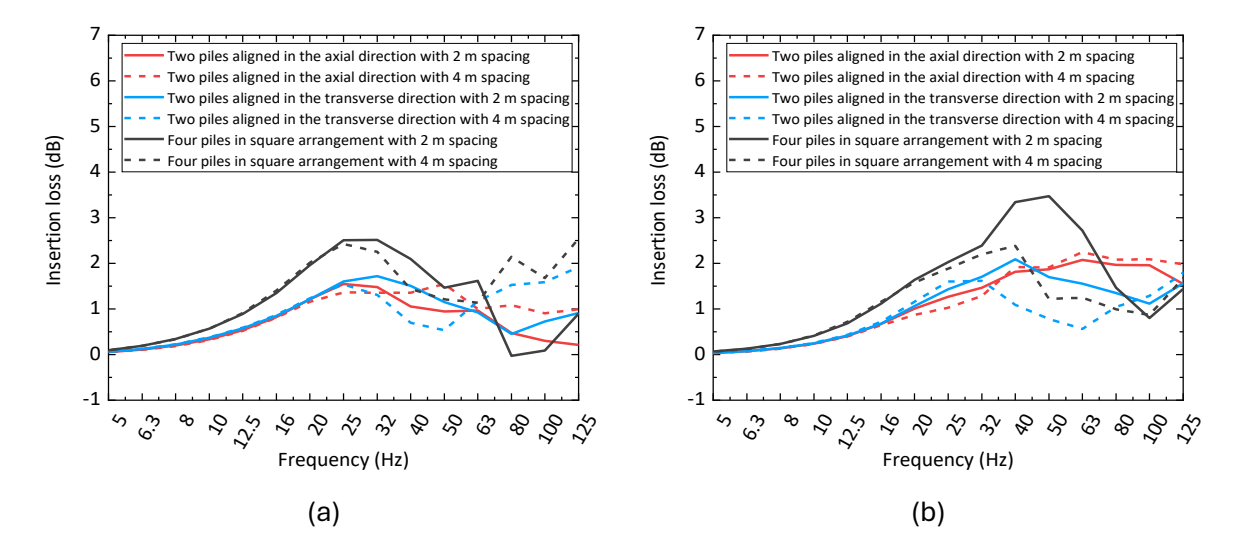


Figure 4-18 The average IL for the receiver points with same distance behind the pile group in onethird octave bands at (a) 4 m and (b) 8 m away from the pile group.

4.4.3 Insertion loss results on centreline behind the pile group

In this section, the IL on the centreline behind pile groups with different spacings is investigated. The IL of the ground along the centreline, beyond the last pile at specific frequencies, and the spectral IL results at certain receiver points on the centreline are presented. Additionally, the IL is calculated from the difference in overall velocity response level with/without pile evaluated over the range 10-80 Hz. As above, a distance of 10 m has been selected for investigation using the semi-analytical model. All the cases are within the reliable range identified in Section 4.3.

The IL values for these cases are summarised in Figure 4-19 when the spacing of the piles is 2 m. This shows the IL based on the ground response on the centreline behind the pile group at four frequencies. The IL value of the four piles in square arrangement at 80 Hz is high only in the far field. The IL value for two piles is a little bit lower than IL value from four piles in square arrangement at lower frequencies, while at high frequency (80 Hz) this is only the case in the far field. At 80 Hz, for the two piles aligned in the transverse direction and the four piles in square arrangement, the value of IL is negative within 5 m of the last pile but positive further away.

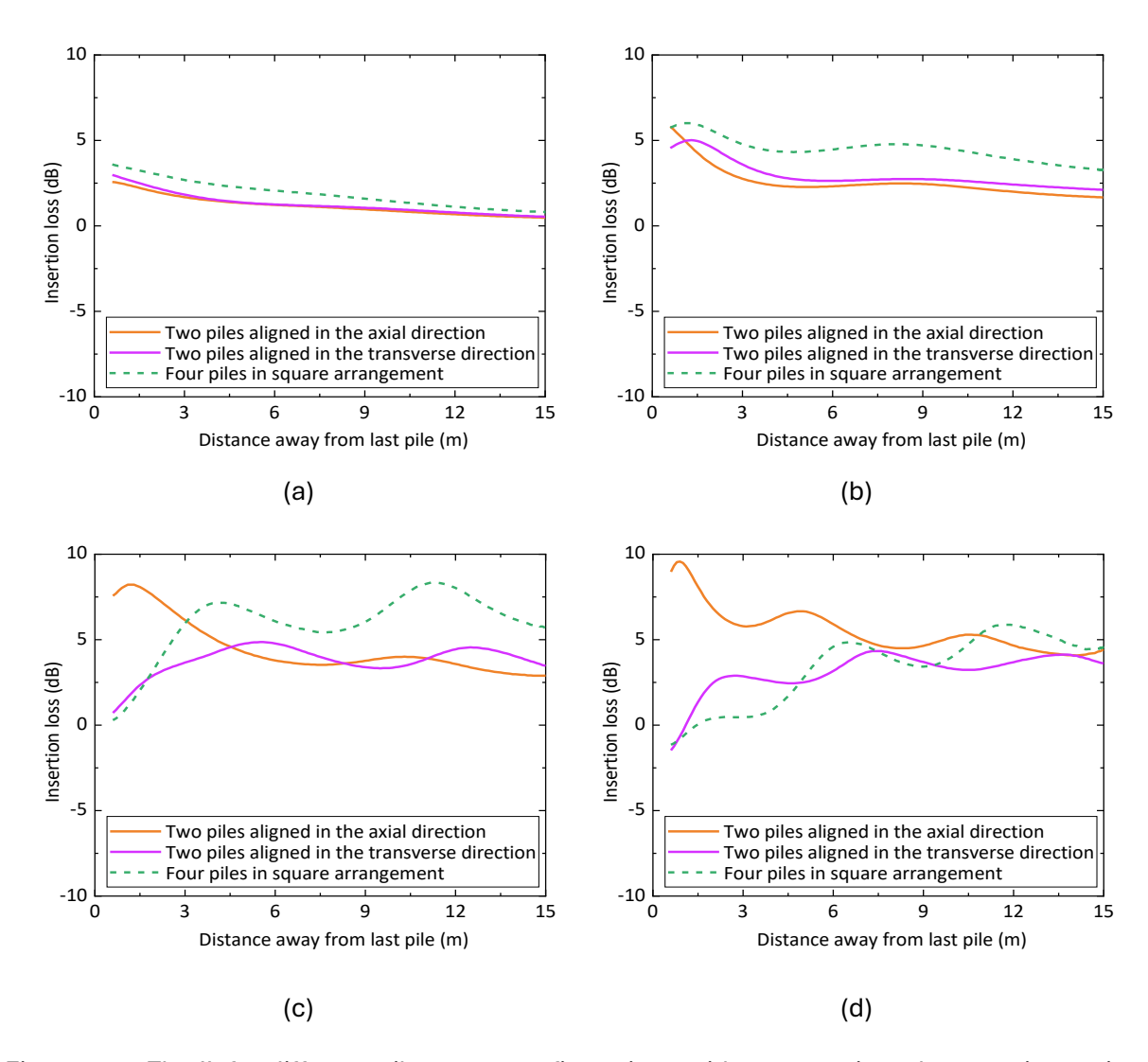


Figure 4-19 The IL for different pile group configurations with 2 m spacing when receiver points are located on the centreline behind the pile groups at (a) 20 Hz, (b) 40 Hz, (c) 60 Hz and (d) 80 Hz.

When the spacing between the different piles is 4 m, the IL value for the ground vibration is summarised in Figure 4-20. For the two piles aligned in the axial direction case, the IL value is high, especially at higher frequencies 40 Hz, 60 Hz and 80 Hz. As the distance from the last pile decreases, the IL value increases, indicating there is more significant ground vibration mitigation in the near field. For two piles aligned in the transverse direction and four piles in square arrangement, there are some negative IL values close to the piles. For these three pile group cases, ground vibration amplification effects only occur in the near field of the pile group when there are two piles aligned in the transverse direction or four piles arranged in a square arrangement. When the spacing is 4 m, the IL value and its trend with increasing distance from the pile are similar between the case of two piles aligned in the transverse direction and the case of four piles in square arrangement.

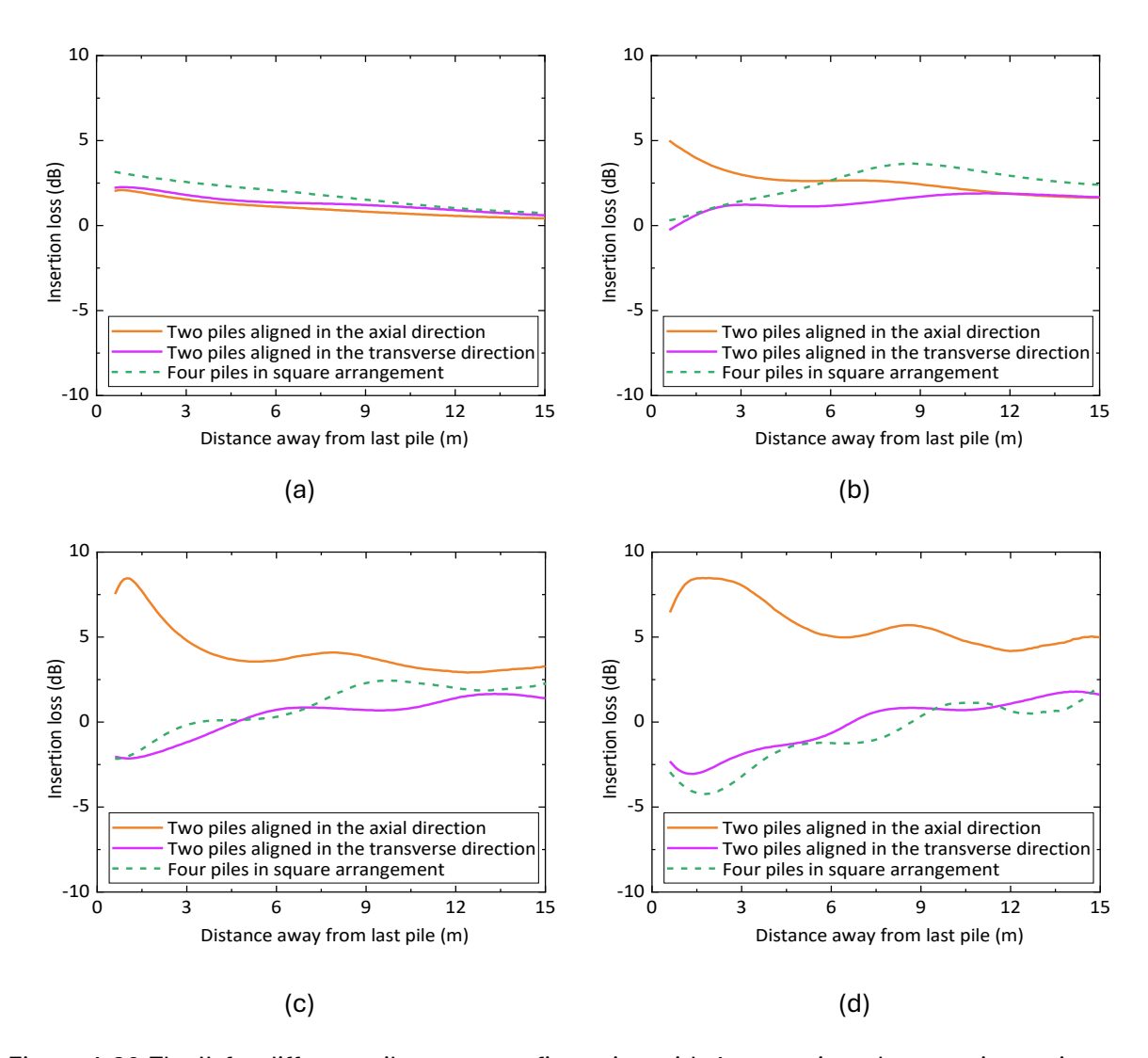


Figure 4-20 The IL for different pile group configuration with 4 m spacing when receiver points are located in the centreline behind pile groups at (a) 20 Hz, (b) 40 Hz, (c) 60 Hz and (d) 80 Hz.

To summarise the IL values at different frequencies, the narrow band spectrum of IL at different specific receiver points is investigated. Results are obtained at 100 frequency points on a logarithmic scale ranging from 5 Hz to 100 Hz. The pile group is still arranged under three different conditions: two piles aligned in the axial direction, two piles aligned in the transverse direction and four piles in square arrangement.

Six receiver points are investigated, located along the centreline behind the pile group. All the investigated model pile sizes, spacings, and soil shear wavelengths fall within the reliable range discussed in Section 4.2. Their locations are summarised in Table 4-2. The narrow band spectra of IL are shown in Figure 4-23. In each figure, two different pile spacing cases are compared: 2 m (solid line) and 4 m (dash line).

Table 4-2 Receiver points location.

Receiver points name	Description	Distance from load	
R1	5 m away from the first pile	15 m	
R2	10 m away from the first pile	20 m	
R3	15 m away from the first pile	25 m	
R4	5 m away from the last pile	10 m (2 piles in transverse arrangement), 12 m (2 m spacing) or 14 m (4 m spacing)	
R5	10 m away from the last pile	15 m (2 piles in transverse arrangement), 17 m (2 m spacing) or 19 m (4 m spacing)	
R6	15 m away from the last pile	20 m (2 piles in transverse arrangement), 22 m (2 m spacing) or 24 m (4 m spacing)	

The receiver points location is shown in Figure 4-21.

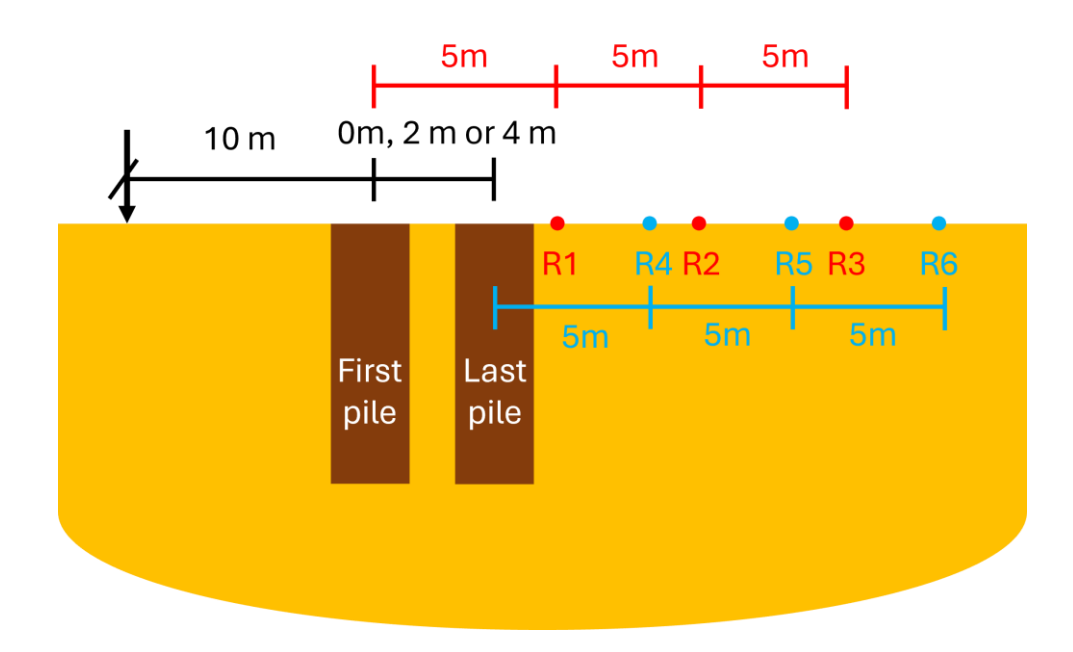


Figure 4-21 Sketch of the receiver points behind the piles.

The results from Figure 4-22 show that:

There are two cases where vibration amplification occurs, i.e. the IL value is negative at high frequency. One is when the two piles aligned in the transverse direction and the other is for four piles arranged in 2×2 square, in both cases with the spacing of 4 m.

For the two piles aligned in the axial direction, when the receiver point is close to the pile, such as R1 which is 5 m away from the first pile or R4 which is 5 m away from the last pile, the IL value is

Chapter 4

higher than other cases at frequencies above 50 Hz. However, when the receiver point is further away, the IL value is comparable to that of other cases. Especially when the pile spacing is 4 m, the IL value is higher when focusing on the receiver point R1. Thus, when the piles are aligned in the axial direction, the ground response is significantly mitigated, especially in closer zones.

However, for receivers further from the piles, these mitigation effects are less pronounced. For the two piles aligned in the transverse direction with 2 m spacing, the IL value is moderate compared with the other cases. When the receiver point is 15 m away from the pile, the IL results from two piles are similar with each other no matter whether the pile is aligned in the axial direction or in the transverse direction. When the receiver point is close to the pile group, such as only 5 m away, the IL value is positive at low frequency and then becomes negative as the frequency increases. However, when the receiver point is at a greater distance, such as 15 m away, the IL value is always positive.

In general, all the pile configurations affect the ground vibration above 10 Hz. Four piles arranged in a square configuration provide the most significant vibration mitigation, particularly at frequencies 50-60 Hz, no matter where the receiver point is. The ground vibration mitigation effects are more significant in the closer zone when there are two piles aligned in the axial direction. But the ground vibration maybe amplified above 40 Hz when two piles are aligned in the transverse direction or four piles are in a square arrangement.

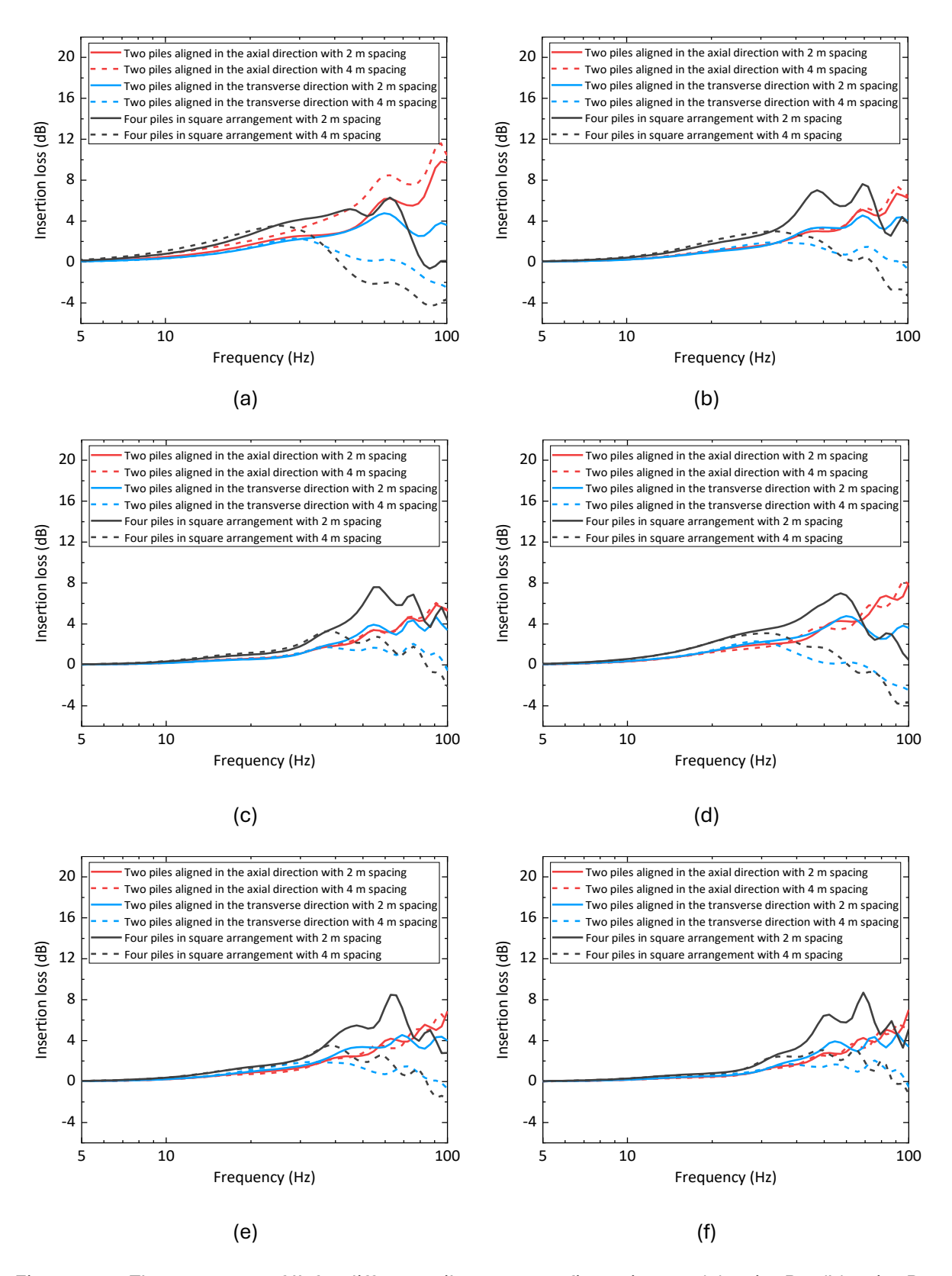


Figure 4-22 The spectrum of IL for different pile group configurations at (a) point R1, (b) point R2, (c) point R3, (d) point R4, (e) point R5 and (f) point R6 on the centreline behind the pile group.

Figure 4-23 shows the IL calculated from the difference in overall ground velocity level with/without pile evaluated over the range 10-80 Hz. for positions on the centreline at different distances. In general, the IL value is positive, which means the ground vibration behind the pile

group is mitigated no matter what the pile configuration is. When two piles are aligned in the axial direction, their position is on the centreline. As a result, the IL value behind the piles is larger, particularly near the pile site. But when two piles are aligned in the transverse direction or when four piles are arranged in a 2×2 configuration, the centreline is located in the middle, not just behind the piles, so the values of IL from these cases are small. The IL value remains stable regardless of the distance away from the last pile. Usually, the value of IL from the cases with spacing of 4 m is smaller than that from the cases with spacing of 2 m. The ground vibration mitigation from the cases with four piles is more effective than that from two piles aligned in the transverse direction.

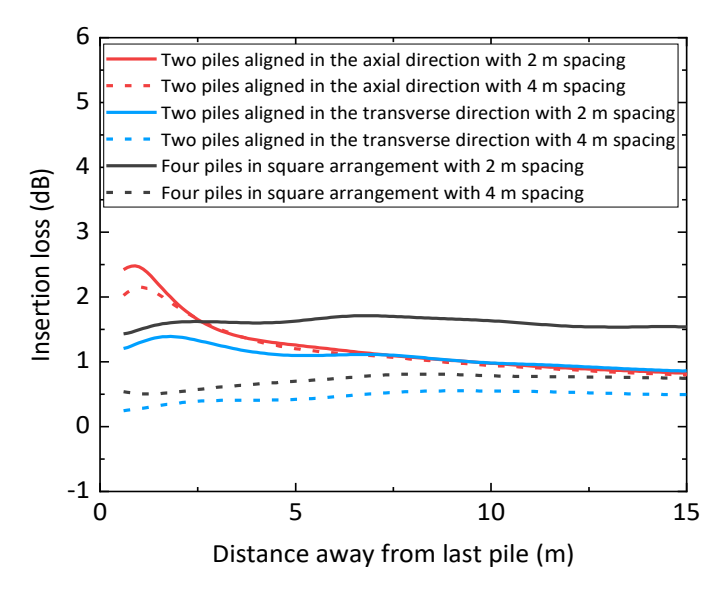


Figure 4-23 The IL results on the centreline calculated from the difference in overall velocity response level with/without pile evaluated over the range 10-80 Hz.

4.5 Summary

A pile group-soil semi-analytical model has been developed considering the soil transfer matrix between different piles, based on a single pile-soil semi-analytical model. From the comparison of results based on the semi-analytical model and the FE model, the agreement is favourable when the number of piles is small. Particularly at lower frequencies, the semi-analytical pile group model yields accurate results. However, this model for pile groups exhibits certain limitations. When focusing on the results on the ground behind the pile group, it tends to get accurate results at low frequencies or when the number of piles is limited. When the number of piles exceeds three, the model's accuracy diminishes. Additionally, when the piles are arranged beside one another, the model achieves higher accuracy compared to when the piles are arranged in the axial direction for the same number of piles.

Chapter 4

The IL was compared in more detail across three arrangements: two piles aligned in the axial direction, two piles aligned in the transverse direction, and four piles in a 2×2 configuration. The IL was also investigated when the load position changes; a distance of 10 m away from the pile group is used to represent far-field excitation. As the distance between the load and the pile group increases, the IL may initially increase and then decrease. Then, the contour map of overall IL from all the one-third octave band frequency samples is investigated on the ground surface under different pile group cases. The ground response behind each pile in the pile group is mitigated significantly. So, when there are two piles aligned in the axial direction on the centreline, the ground response is significantly mitigated. However, when the two piles are aligned in the transverse direction or four piles are located in a square arrangement, the ground response on the centreline is hardly mitigated. When the spacing between the piles is only 2 m, the ground response is mitigated on the centreline even in the far field due to the overlap of the attenuated zone from the two piles. Moreover, based on the average IL results obtained from the receiver points at the same distance away from the pile group in the axial direction, the IL value from the 4 m spacing is higher in the near field but lower in the far field compared with the IL from the 2 m spacing. It can be summarised that at some specific receiver points and frequencies, the vibration maybe amplified, but the ground response behind the pile group is always mitigated on average.

Chapter 5 Ground vibration in the vicinity of a building due to a fixed unit load

The aim of this chapter is to investigate the influence of a building with a piled foundation on the ground vibration, and to analyse the effect of the properties of the building. The excitation is taken as a fixed harmonic unit load. The ground is assumed to be a half space and is modelled using the semi-analytical DSM approach in the frequency-wavenumber domain. The details for the DSM method are shown in Appendix B. The building is represented by a column-plate system, which can be simulated by an FE model. For simplicity, it is still referred to as a semi-analytical model. The two models are coupled using a sub-modelling coupling technique in the frequency domain, which has already been introduced in the previous chapters. The building foundation is assumed to consist of several piles.

5.1 Methodology

A sketch of the modelling approach is shown in Figure 5-1. The ground is excited by a unit vertical harmonic force applied to the ground surface. The building and the ground are assumed to be coupled at a series of nodes, located on the piled foundation of the building. The response at a receiver point on the ground surface in the vicinity of the building can be separated into two parts: the response in the free field induced by the load, and the response induced by the reaction forces at the coupled nodes between the building and the ground.

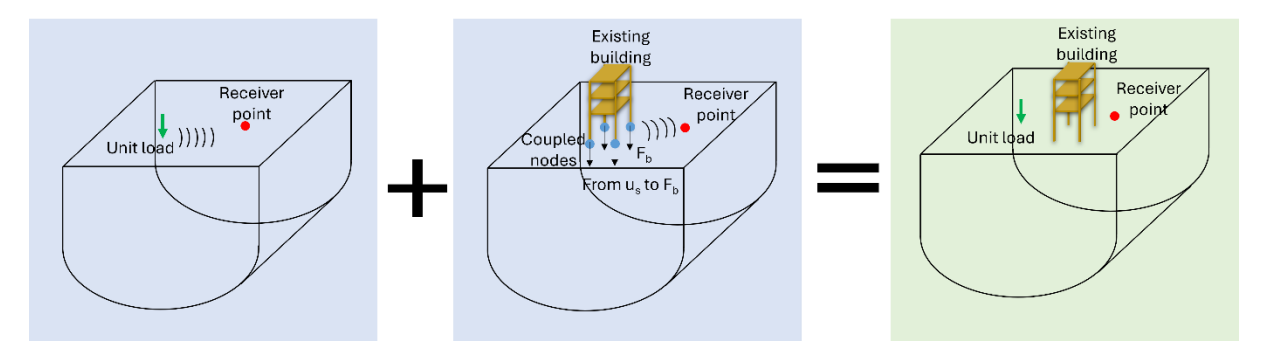


Figure 5-1 Overview of the modelling approach for the building, ground and interaction.

Based on Figure 5-1, the total displacement at a receiver point induced by a unit fixed harmonic load at circular frequency ω is, similar to Eq. (3-1),

$$\widehat{\mathbf{U}}(\omega) = \widehat{\mathbf{U}}_0(\omega) + \widehat{\mathbf{H}}_s(\omega)\widehat{\mathbf{f}}_s(\omega) \tag{5-1}$$

where $\hat{\mathbf{U}}_0(\omega)$ means the ground vibration at the receiver point induced by the unit load transmitted through the free field. $\hat{\mathbf{H}}_s(\omega)$ signifies the matrix of transfer receptances or Green's

functions of the soil, which are from the coupled nodes to the receiver point. $\hat{\mathbf{F}}_s(\omega)$ signifies the vector of reaction forces at frequency ω at the coupled nodes on the pile foundation. It can be calculated based on coupling the ground with an FE model of the building.

The relationship between dynamic forces and displacements at the coupled nodes in the building is given by

$$\widehat{\mathbf{f}}_{h}(\omega) = \widehat{\mathbf{K}}_{h}(\omega)\widehat{\mathbf{U}}_{h}(\omega) \tag{5-2}$$

where $\widehat{\mathbf{K}}_{\mathrm{b}}(\omega)$ is the dynamic stiffness matrix of the building structure. Similar to Eq. (3-5) and Eq. (3-6), when calculating the dynamic stiffness, the equivalent parameters of the structure are applied to the parts submerged below the ground level:

$$\rho = \rho_{\rm b} - \rho_{\rm s} \tag{5-3}$$

$$E = E_{\rm b} - E_{\rm s} \tag{5-4}$$

where ρ_s and E_s are the density and Young's modulus of the soil, while ρ_b and E_b are those of the building.

To determine $\hat{\mathbf{K}}_b(\omega)$, the global dynamic stiffness matrix of the building obtained from the FE model is partitioned into DOFs that will be linked to the soil (coupled nodes at the foundation, subscript f) and DOFs that will be internal to the building (subscript i). Interaction forces at the DOFs linked to the foundation (f) excite the system whereas there are no forces on the interior DOFs (i). The equation of motion for the building can be partitioned as follows:

$$\widehat{\mathbf{f}}_{b}(\omega) = \begin{bmatrix} \mathbf{0} \\ \widehat{\mathbf{f}}_{f}(\omega) \end{bmatrix} = \begin{bmatrix} \widehat{\mathbf{K}}_{ii}(\omega) & \widehat{\mathbf{K}}_{if}(\omega) \\ \widehat{\mathbf{K}}_{fi}(\omega) & \widehat{\mathbf{K}}_{ff}(\omega) \end{bmatrix} \begin{bmatrix} \widehat{\mathbf{U}}_{i}(\omega) \\ \widehat{\mathbf{U}}_{f}(\omega) \end{bmatrix}$$
(5-5)

where $\widehat{\mathbf{U}}_f(\omega)$ is the displacement at the coupled nodes belonging to the foundation, $\widehat{\mathbf{U}}_i(\omega)$ is the vector of the displacement at the internal nodes, $\widehat{\mathbf{F}}_f(\omega)$ represents the vector of external forces at the coupled nodes. More details of the FE dynamic stiffness matrix have already introduced in Section 3.5.

Referring to dynamic reduction method [224], Eq. (5-5) can be written in reduced form in terms of the DOFs at the coupled nodes. The reaction forces at the coupled nodes $\hat{\mathbf{F}}_f(\omega)$ can be calculated by

$$\widehat{\mathbf{f}}_{f}(\omega) = \left[\widehat{\mathbf{K}}_{ff}(\omega) - \widehat{\mathbf{K}}_{fi}(\omega)\widehat{\mathbf{K}}_{ii}(\omega)^{-1}\widehat{\mathbf{K}}_{if}(\omega)\right]\widehat{\mathbf{U}}_{f}(\omega) = \widehat{\mathbf{K}}_{f}(\omega)\widehat{\mathbf{U}}_{f}(\omega)$$
(5-6)

As the system does not have other external loads, according to the theory of soil-structure interaction, the interaction forces between the building foundation and the soil are equal but act in opposing directions:

$$\hat{\mathbf{F}}_{\mathbf{f}}(\omega) = -\hat{\mathbf{F}}_{\mathbf{c}}(\omega) \tag{5-7}$$

where subscript f denotes the nodes from the foundation of FE building that are in contact with the ground, i.e. the coupled nodes belonging to the building structure foundation. The subscript s indicates the nodes belonging to the soil and sharing the same position as the coupled nodes.

It is assumed that the displacement at coupled node k on the pile foundation is equal to the displacement of the soil at the same position, which means

$$\widehat{\mathbf{U}}_{s}(\omega) = \widehat{\mathbf{U}}_{f}(\omega) \tag{5-8}$$

The displacement of the soil $\widehat{\mathbf{U}}_{\mathrm{S}}(\omega)$ at the coupled nodes in the presence of the building is written as

$$\widehat{\mathbf{U}}_{s}(\omega) = \begin{bmatrix} \widehat{\mathbf{u}}_{s,1}(x_{c,1}, y_{c,1}, z_{c,1}, \omega) \\ \widehat{\mathbf{u}}_{s,2}(x_{c,2}, y_{c,2}, z_{c,2}, \omega) \\ \vdots \\ \widehat{\mathbf{u}}_{s,k}(x_{c,k}, y_{c,k}, z_{c,k}, \omega) \end{bmatrix}$$
(5-9)

It can be calculated by

$$\widehat{\mathbf{U}}_{s}(\omega) = \widehat{\mathbf{U}}_{s0}(\omega) + \widehat{\mathbf{H}}_{G}^{piles}(\omega)\widehat{\mathbf{F}}_{s}(\omega)$$
(5-10)

where $\widehat{\mathbf{U}}_{s0}(\omega)$ means the displacement at the coupled nodes induced by a unit load when the transmission path is in free field. It is denoted as

$$\widehat{\mathbf{U}}_{s0}(\omega) = \begin{bmatrix} \widehat{\mathbf{u}}_{s0,1}(x_{c,1}, y_{c,1}, z_{c,1}, \omega) \\ \widehat{\mathbf{u}}_{s0,2}(x_{c,2}, y_{c,2}, z_{c,2}, \omega) \\ \vdots \\ \widehat{\mathbf{u}}_{s0,k}(x_{c,k}, y_{c,k}, z_{c,k}, \omega) \end{bmatrix}$$
(5-11)

The forces at the coupled nodes $\hat{\mathbf{F}}_{s}(\omega)$ can be denoted as

$$\hat{\mathbf{f}}_{s}(\omega) = \begin{bmatrix} \mathbf{f}_{s1}(x_{c,1}, y_{c,1}, z_{c,1}, \omega) \\ \hat{\mathbf{f}}_{s2}(x_{c,2}, y_{c,2}, z_{c,2}, \omega) \\ \vdots \\ \hat{\mathbf{f}}_{sk}(x_{c,k}, y_{c,k}, z_{c,k}, \omega) \end{bmatrix}$$
(5-12)

The soil transfer receptance matrix $\widehat{\mathbf{H}}_{Piles}^G(\omega)$ at the pile group coupled nodes is based on the soil transfer receptances between the coupled nodes, and can be denoted as

$$\widehat{\mathbf{H}}_{\text{Piles}}^{G}(\omega) = \begin{bmatrix} \widehat{\mathbf{H}}_{11}^{G}(\omega) & \widehat{\mathbf{H}}_{12}^{G}(\omega) & \cdots & \widehat{\mathbf{H}}_{1n}^{G}(\omega) \\ \widehat{\mathbf{H}}_{21}^{G}(\omega) & \widehat{\mathbf{H}}_{22}^{G}(\omega) & \cdots & \widehat{\mathbf{H}}_{2n}^{G}(\omega) \\ \vdots & \vdots & \ddots & \vdots \\ \widehat{\mathbf{H}}_{m1}^{G}(\omega) & \widehat{\mathbf{H}}_{m2}^{G}(\omega) & \cdots & \widehat{\mathbf{H}}_{mn}^{G}(\omega) \end{bmatrix}$$
(5-13)

where

$$\widehat{\mathbf{H}}_{mn}(\omega) = \widehat{\mathbf{H}}(x_{c,m} - x_{c,n}, y_{c,m} - y_{c,n}, z_{c,m} - z_{c,n}, \omega)$$
(5-14)

means the 3×3 Green's function matrix of the soil from forces at coupled node m to the displacements at coupled node n.

Following the same approach as in Chapter 3, Eq. (5-9) can be written in terms of Eq. (5-8) which can then be combined with Eq. (5-2) to give

$$\widehat{\mathbf{U}}_{f}(\omega) = \left(\mathbf{I} + \widehat{\mathbf{H}}_{Piles}^{G}(\omega)\widehat{\mathbf{K}}_{f}(\omega)\right)^{-1}\widehat{\mathbf{U}}_{s0}(\omega)$$
 (5-15)

$$\widehat{\mathbf{U}}_{f}(\omega) = \left(\mathbf{I} + \widehat{\mathbf{H}}_{Piles}^{G}(\omega) \left[\widehat{\mathbf{K}}_{ff}(\omega) - \widehat{\mathbf{K}}_{fi}(\omega) \widehat{\mathbf{K}}_{ii}(\omega)^{-1} \widehat{\mathbf{K}}_{if}(\omega) \right] \right)^{-1} \widehat{\mathbf{U}}_{s0}(\omega)$$
 (5-16)

Based on Eqs. (5-8) and (5-6), the equivalent reaction forces at frequency ω at the coupled nodes $\hat{\mathbf{F}}_s(\omega)$ can be calculated.

Once the forces at the coupled nodes have been calculated, the SSI may be described by this set of equivalent forces, see Eq. (5-1). The ground-borne vibration induced by the external loads and by the reaction forces at the building may be estimated separately and then combined to give the response at receiver points behind the structure.

5.2 Building finite element model

The building is represented as a combined column and plate system using FEM, as shown in Figure 5-2 by using the Stabil FE MATLAB toolbox [225]. In view of the limitations identified in Chapter 4, a simple building with a single span in both x and y directions and a total of four columns is modelled. The building has three storeys.

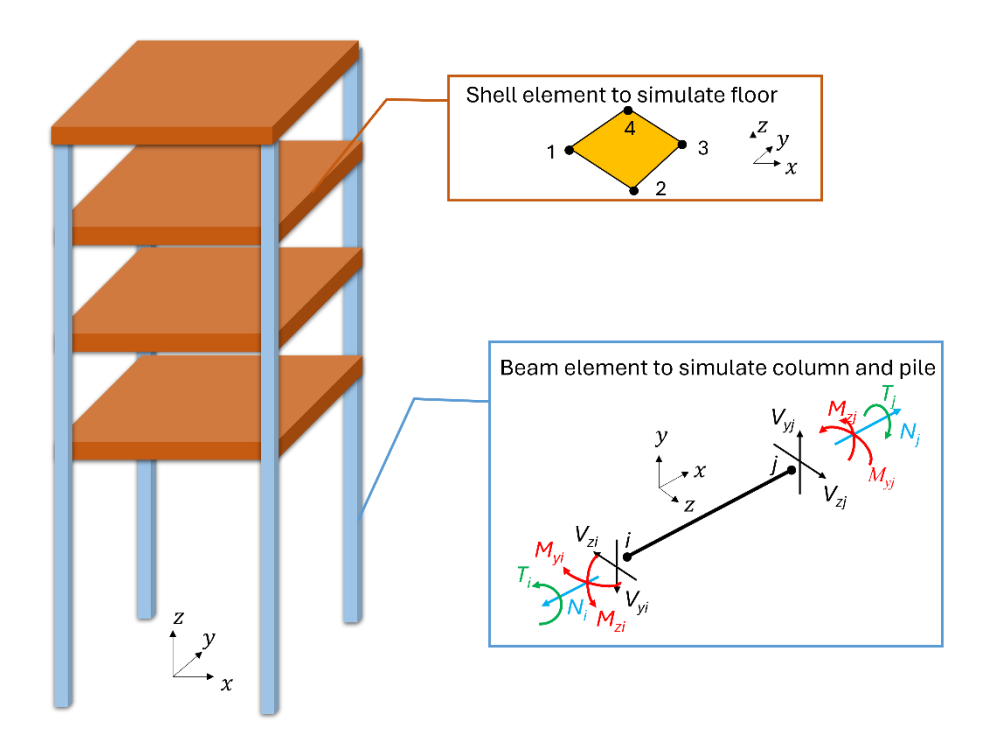


Figure 5-2 Building model sketch.

The columns are modelled using Timoshenko beam elements with a cubic interpolation of the beam deflection and linear shape function for axial and torsion deflection. The axial deflection, bending and torsion of the column are all included in this model. At each node there are six DOFs, three translations and three rotations.

Shell elements are used to represent the floor of the building. They allow for bending and in-plane motion. Each floor slab in the FE building model is comprised of a large number of shell elements. A four-noded quadrilateral shell element is used. More details of this type of element are introduced in [226] including the shape functions, stiffness and mass matrix. There are 6 DOFs at each node.

The dynamic stiffness matrix $\hat{\mathbf{K}}(\omega)$ is obtained from the FEM mass and stiffness matrices:

$$\widehat{\mathbf{K}}(\omega) = \mathbf{K}_0 (1 + \mathrm{i}\eta) - \omega^2 \mathbf{M}_0 \tag{5-17}$$

where \mathbf{K}_0 is the global stiffness matrix assembled from element stiffness matrices using the FE method, and \mathbf{M}_0 is the global mass matrix assembled from the element consistent mass matrices. Damping is introduced by making the stiffness matrix complex using a constant loss factor η . Following Eq. (5-17), the dynamic stiffness matrix $\hat{\mathbf{K}}(\omega)$ is partitioned into internal nodes and foundation-ground coupled nodes:

$$\widehat{\mathbf{K}}(\omega) = \begin{bmatrix} \widehat{\mathbf{K}}_{ii}(\omega) & \widehat{\mathbf{K}}_{if}(\omega) \\ \widehat{\mathbf{K}}_{fi}(\omega) & \widehat{\mathbf{K}}_{ff}(\omega) \end{bmatrix} = (1 + i\eta) \begin{bmatrix} \mathbf{K}_{ii} & \mathbf{K}_{if} \\ \mathbf{K}_{fi} & \mathbf{K}_{ff} \end{bmatrix} - \omega^2 \begin{bmatrix} \mathbf{M}_{ii} & \mathbf{M}_{if} \\ \mathbf{M}_{fi} & \mathbf{M}_{ff} \end{bmatrix}$$
(5-18)

Based on the relationship between the number of storeys and spans and the number of elements, this FE building model can be created parametrically. The MATLAB code for the parametrically constructed model is shown in Appendix D. The code can create the stiffness and mass matrices with a variety of storeys and spans in a matter of seconds.

Some dimensions of the FE building model are listed in Table 5-1. Timoshenko beam elements are used to simulate the columns and piles. Each beam element is 0.5 m long for the piles and 0.3 m long for the columns. The size of the shell elements in the FE model is 0.3 m×0.3 m, which equates to 784 shell elements for one floor. Because the column height in one storey is 3 m and one beam element length is 0.3 m, there are 10 beam elements for one column between each storey. Similarly, there are 20 beam elements (length: 0.5 m) for each pile foundation. There are therefore a total of 84 coupled nodes on the 4 piles in the foundation in this model. Based on the relationship shown in Figure 3-11 between the dimensionless value and model accuracy, thinner piles result in more accurate predictions than thicker piles. Since the width of the columns in the building model is smaller than the pile width in both the single pile and pile group models considered in Chapter 3 and Chapter 4, the results from the building model are considered reliable below 80 Hz.

Table 5-1 Dimensions of the building.

Parameter's name	Value
Length of pile (m)	10.0
Number of columns (piles)	4
Half width of the column (m)	0.3
Timoshenko beam shear correction factor for column	0.833
Second moment of area of the column for bending around local y -axis and z -axis (m ⁴)	0.0108
Thickness of the floor (m)	0.5
Span length (m)	4.2
Floor-floor height (m)	3.0

5.3 Model verification

A full 3D FE model is built to verify and evaluate the results calculated from the semi-analytical model. This 3D FE model was constructed using ABAQUS. The elements are 3 dimensional 8 nodes solid elements (C3D8). Infinite elements are applied at the boundaries to avoid wave reflections. There are 125000 elements in this three-storey building model with span length 4.2 m.

The embedded depth of the piles is 10 m. In this model the distance between the load and the building is 3 m. The model is shown in Figure 5-3. The receiver points are on the ground surface behind the building, shown as the red dots. The model dimensions are 40 m×40 m×40 m, with 5 m long infinite elements located along the surrounding sides of the soil model. The bottom of the soil model has a fixed boundary. The element size of the FE soil model is 0.3 m, ensuring that there are at least six elements per shear wavelength. In total, there are 448,656 elements in the whole model. When the plate at the bottom is not in contact with the ground, the ground response results do not significantly differ from the case where the plate is in contact with the ground. Therefore, for the convenience of model establishment, the bottom of the first-floor plate is assumed to be in contact with the ground in this model.

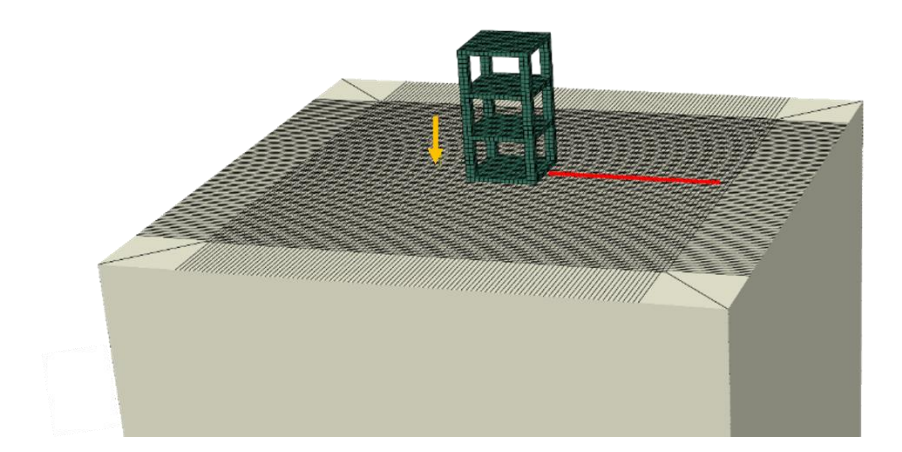


Figure 5-3 The 3D finite element model used for verification.

The building column and shell materials are considered to be concrete, and the parameters of the soil are assumed as clay. The material properties of the concrete and soil materials are listed in Table 5-2. In total, the mass of the building is 156,600 kg.

Table 5-2 The materials parameters of the model in this case study.

Parameters	Building (Concrete)	Soil
Density (kg/m³)	2500	2100
Poisson's ratio	0.3	0.33
Young's modulus (N/m²)	3×10 ¹⁰	3.5×10 ⁸
Loss factor	0.1	0.1
Shear wave velocity (m/s)	-	250
Compressional wave velocity (m/s)	-	500

The semi-analytical model and FE model results are compared in Figure 5-4 at two frequencies. Up to 80 Hz under this specific shear wave velocity (c_s =250 m/s), the results calculated by the two models have a good agreement.

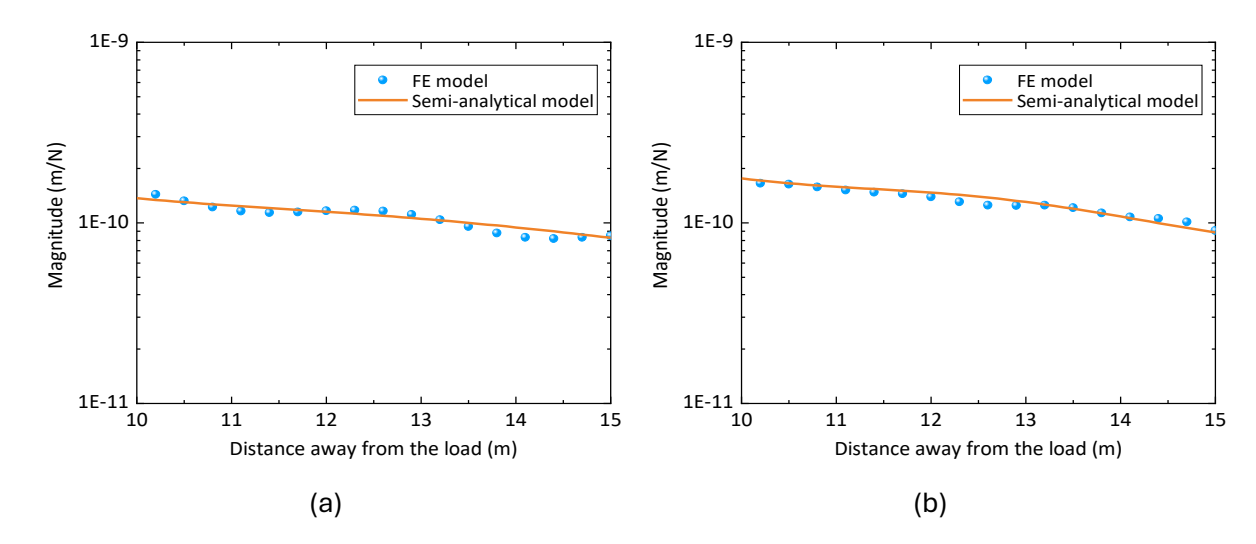


Figure 5-4 Ground response comparison between semi-analytical model and finite element model at (a) 40 Hz and (b) 80 Hz.

5.4 Ground response investigation

To explore the influence of the building on the ground response, results are calculated using the semi-analytical model for a simple example introduced above. The building model in this section consists of a three-storey structure with a single span in each direction.

5.4.1 Ground response in the vicinity of building

The model is shown schematically in Figure 5-5. The excitation point is located 20 m in front of the building.

Chapter 5

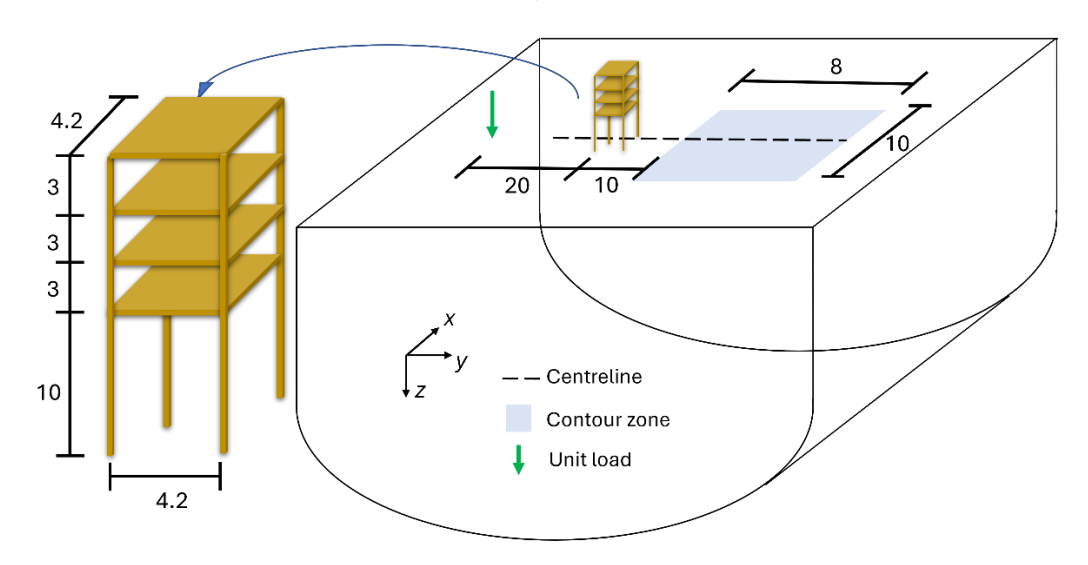


Figure 5-5 The semi-analytical model information including the model dimension, position and receiver point position.

The ground response with or without building is determined at 99 receiver points on the ground surface at 1 m intervals covering an area 8×10 m, as indicated in Figure 5-5. The surface area behind the building has different values of IL at different frequencies and different locations. The contour plot of IL in this region is shown in Figure 5-6 at two example frequencies. The coordinates in these figures have their origin at the force location, see Figure 5-5. Two lines in the x direction (marked as green and orange lines) and the y direction (marked as blue and pink lines) are chosen to plot the IL profile. The contours are symmetrical in the x direction; in the y direction there are areas of oscillatory amplification or reduction, but the overall trend is that the IL value is decreasing with increasing distance. At 40 Hz, the IL decreases along the y direction, i.e., away from the building. In the y direction, the IL on the blue and pink lines is similar. In the x direction, the IL on the orange line (y=36 m) is lower than on the green line (y=31 m), because the green line position is closer to the building. At 80 Hz, there are two notable zones, the bright zone near the building and the dark zone further away from the building. Similar to the response at 40 Hz, the IL on the blue line (x=1 m) and pink line (x=-2 m) in the y direction are similar to each other, but on the green line (y=31 m) and orange line (y=36 m) in the x direction, the results are quite different. On the green line (y=31 m), the IL increases and then decreases along the direction of increasing x. For the orange line, the IL value is oscillatory along the x direction.

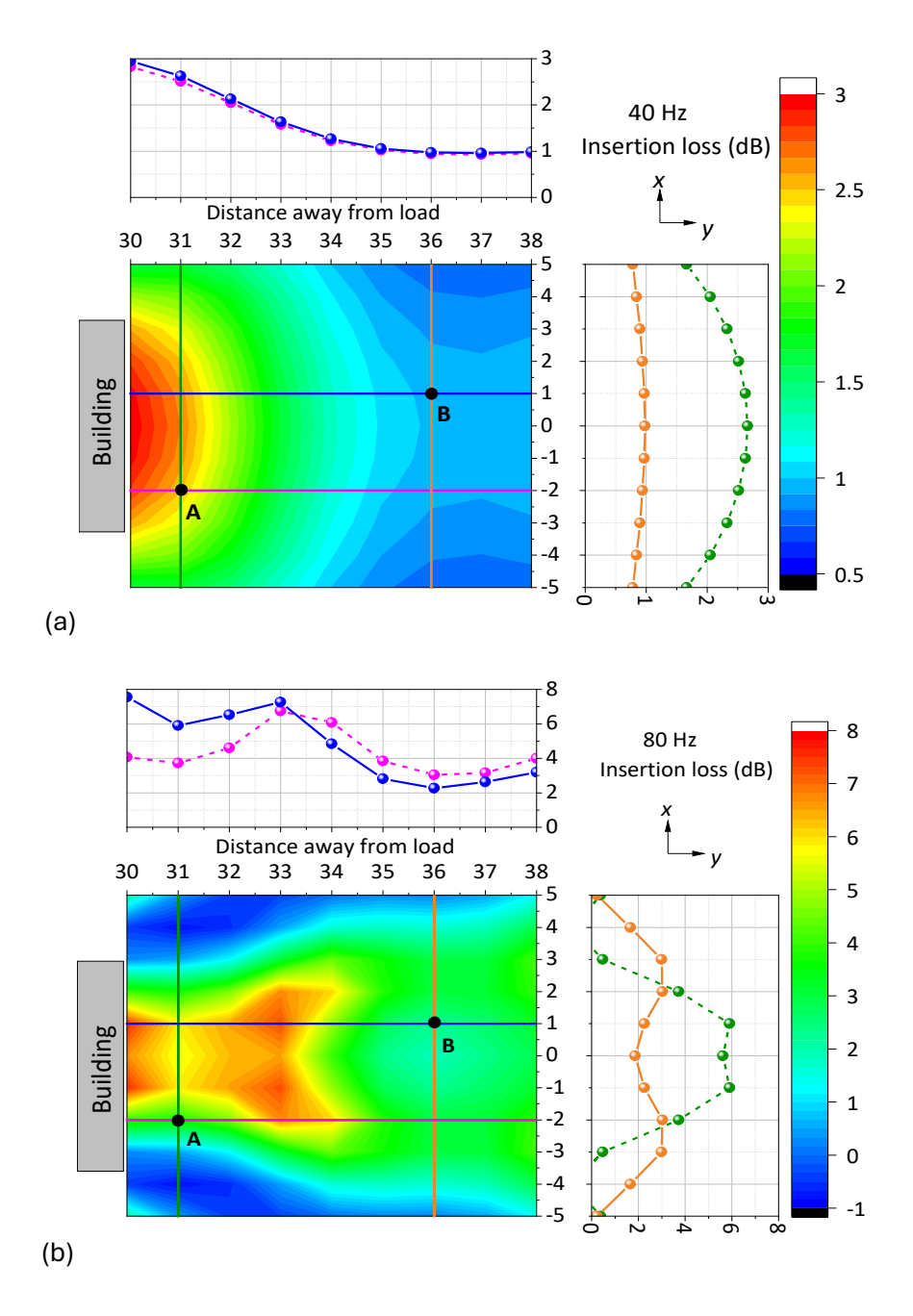


Figure 5-6 Insertion loss contour plot and profile along the lines indicated for a unit fixed load (a) at 40 Hz and (b) at 80 Hz.

Two receiver points A and B, which are marked in Figure 5-6, are chosen to represent two typical zones based on the contour plot results. The IL in one-third octave bands of these two receiver points is shown in Figure 5-7. For each one-third octave band, there are three frequency samples. The value of IL at point A is larger than that at point B, which means there are more significant effects close to the building. Also, with the increase of frequency, the IL value becomes larger.

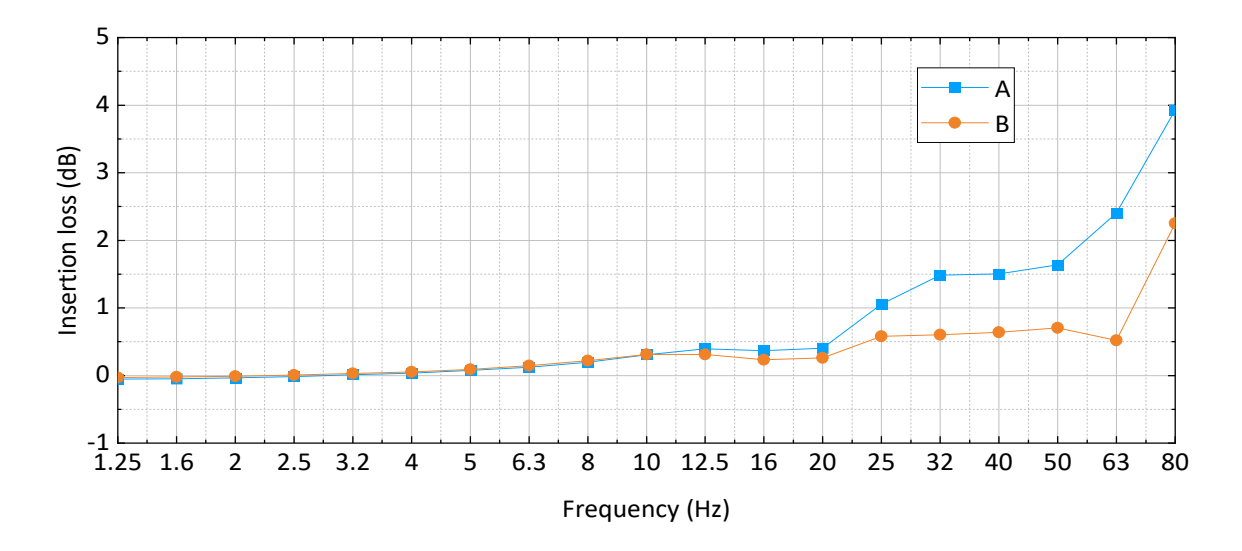


Figure 5-7 The insertion loss in one-third octave bands at positions A and B indicated in Figure 5-6.

5.4.2 The relationship between building modes and ground response

Modal analysis is used to study the modes of the building and their natural frequencies. These are calculated using the beam-shell FE model in Stabil with all nodes on the piles fully constrained. The soil provides an approximately fixed boundary condition for the foundation. Thus, the soil parameters do not significantly influence the building's modes. The natural frequencies of the first 20 modes and the corresponding mode shapes are shown in Figure 5-8. Due to the x and y symmetry of the structure, certain modes occur in pairs, of which only one is illustrated. These modes cover the frequency range up to 90 Hz and are important for the dynamic response of the building in this frequency range.

Chapter 5

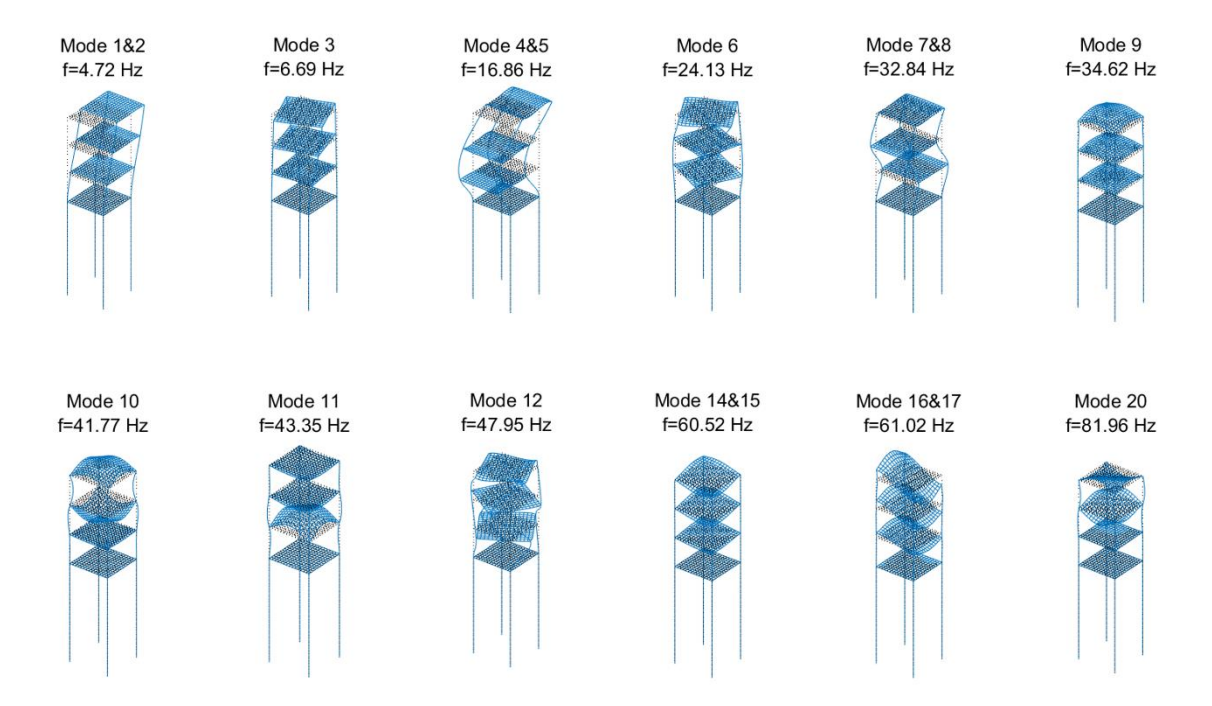


Figure 5-8 Mode shapes of the building with constrained foundation when shell Young's Modulus is 3×10^{10} N/m².

Figure 5-9 shows the displacement level spectrum at points A and B with the building present, as well as the contributions to this from the free field result and from the equivalent forces due to the building. There are 100 frequency points on a logarithmic scale ranging from 1 Hz to 100 Hz. The vibration level (in dB re 10⁻¹² m/N) in the free field is approximately constant for frequencies up to about 30 Hz, before dropping at higher frequencies due to the soil damping, whereas the vibration induced by the reaction forces is substantially lower in the low frequency region. There is a peak at about 40-80 Hz in the response due to the equivalent forces, which reduces the vibration relative to the free field level. Although there is also a peak at approximately 30 Hz, its low amplitude does not significantly impact the final total response on the ground. The peak at around 40 Hz, corresponds to the 10th mode and 11th mode that are related to the floor moving vertically. The peak value at around 60 Hz is related to 14th and 15th mode. The trends at points A and B are similar.

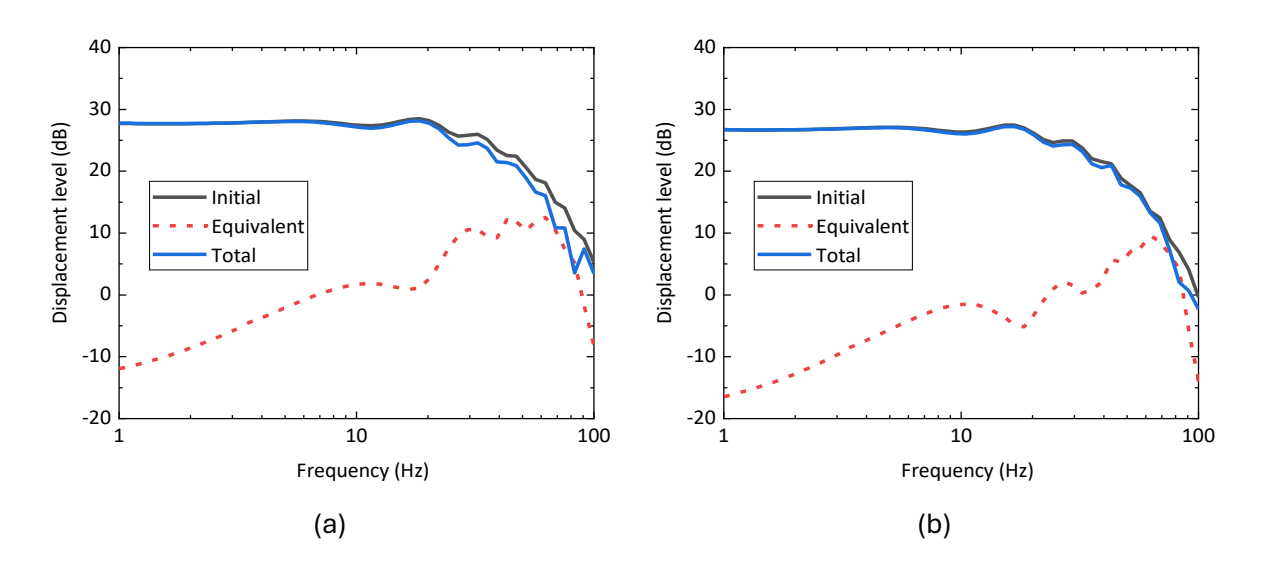


Figure 5-9 Displacement level of ground in vertical direction (dB ref= 10^{-12} m/N) at (a) point A and (b) point B.

Figure 5-10 shows the vertical displacement level (in dB re 10⁻¹² m/N) at the receiver points behind the building in comparison with the corresponding result for the free field case at specific frequencies corresponding to the building natural frequencies. The ground response is plotted with and without the building present. The difference between these two cases (i.e., the IL due to the building) is also shown. When the frequency is low, the building's fundamental modes that do not include vertical floor movement have minimal impact on ground vibration, resulting in the IL being close to zero at lower frequencies. The IL at the 10th and 11th modal frequencies is larger than others, corresponding to the modes with vertical floor vibration.

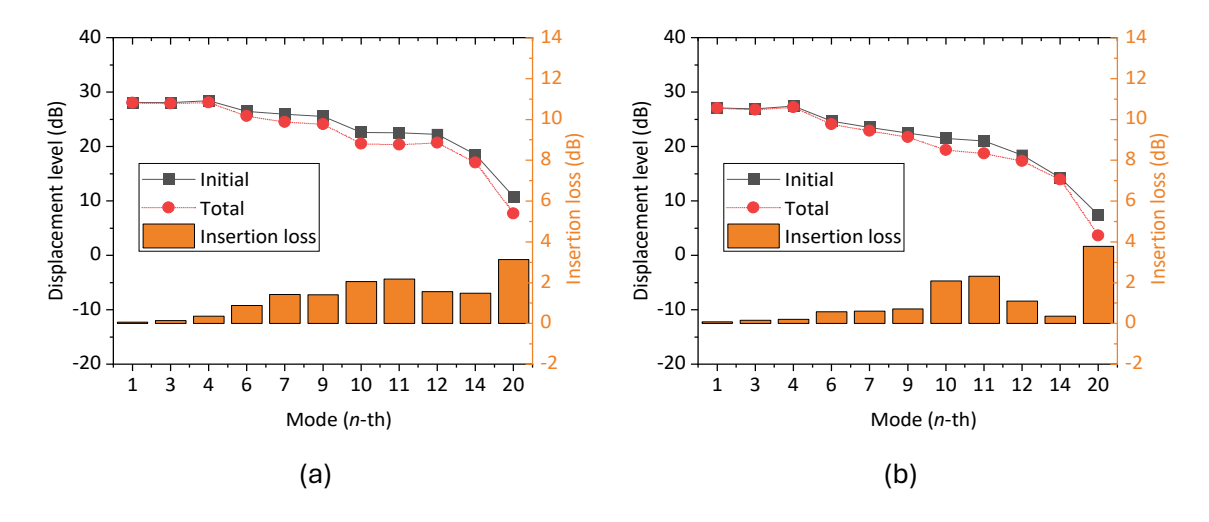


Figure 5-10 Displacement level and insertion loss at mode frequencies (dB ref= 10^{-12} m/N) at (a) point A and (b) point B.

To verify the relation with the building modes, the Young's modulus of the shell elements is increased from 3×10^{10} N/m² to 5×10^{10} N/m². The modes for the new building structure are shown in Figure 5-11. The corresponding frequencies for all modes are increased by up to 16%.

Chapter 5

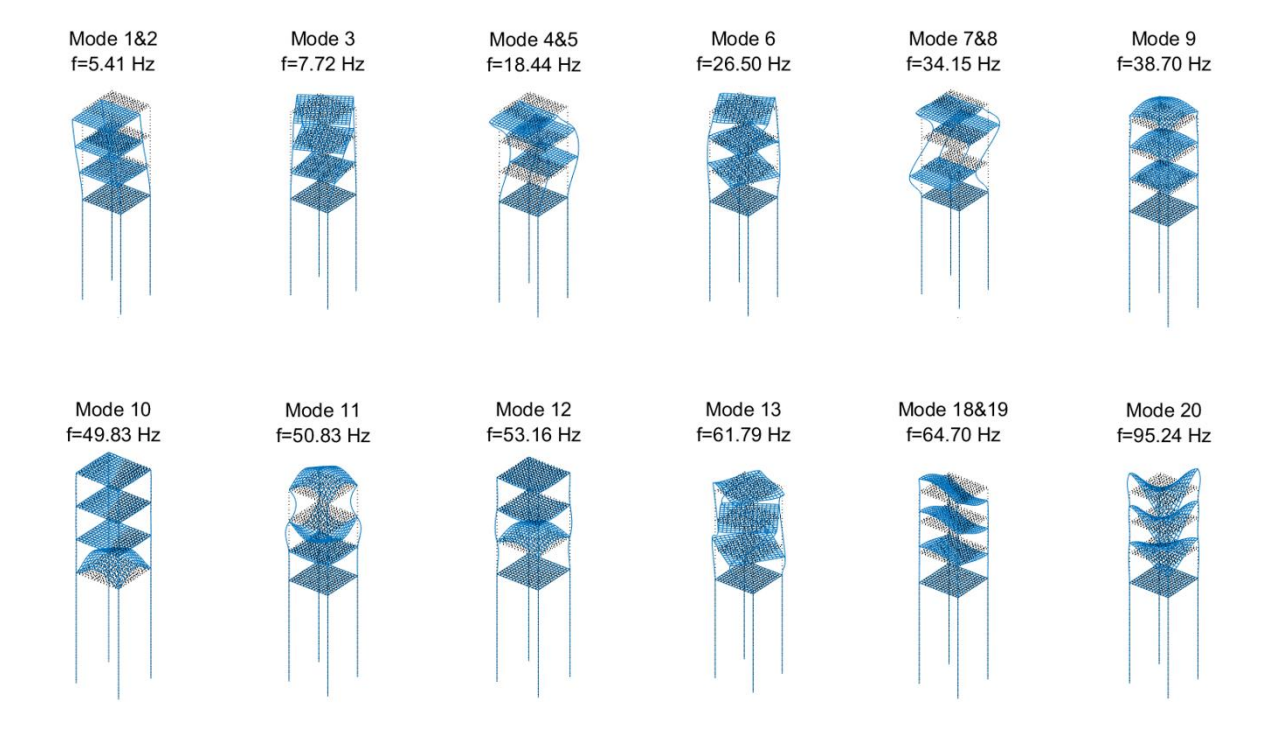


Figure 5-11 Mode shapes of the building with constrained foundation when shell Young's Modulus is increased to 5×10^{10} N/m².

When the Young's Modulus of the shell is increased to 5×10^{10} N/m², the vertical displacement level (in dB re 10^{-12} m/N) at the receiver points behind the building in comparison with the corresponding result for the free field case is shown in Figure 5-12. The larger IL values still correspond to the vertical floor movement modes, including the 10th, 11th, and 20th modes, indicating that these modes significantly influence ground vibration mitigation. Similar results were observed at points A and B.

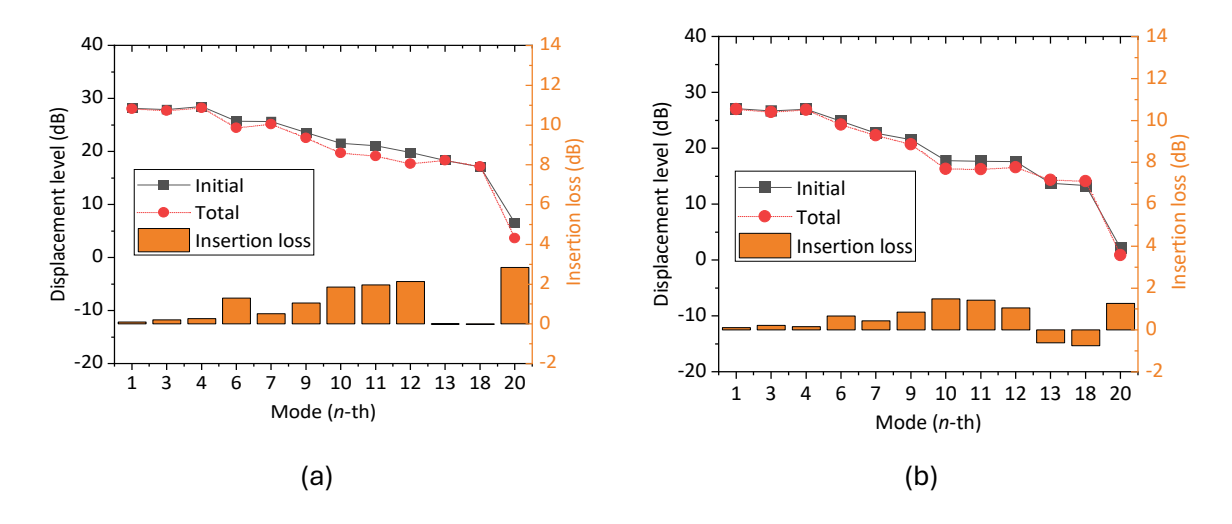


Figure 5-12 Displacement level and insertion loss at mode frequencies (dB ref= 10^{-12} m/N) at (a) point A and (b) point B when shell Young's Modulus is increased to 5×10^{10} N/m².

5.4.3 Parametric study

Focusing on points A and B identified in Figure 5-5, a parametric study is conducted in which the number of storeys and the span length are varied. The results are shown as a bubble plot of IL in Figure 5-13. The bubble size represents the peak IL value. The colour of each bubble identifies the frequency corresponding to the peak value. The x-axis represents the number of storeys, which ranges from 1 to 6. The y axis means the span length, which increases in steps of 0.5 m from 3 m to 6 m. 100 frequency samples are investigated, ranging from 1 Hz to 100 Hz. From Figure 5-13, the bubble size generally increases from the bottom left to top right (excluding some cases, such as 2-storey building with 4 m span length), while the colour changes from red to blue. If the number of building storeys is larger than five, while the span length is over 5 m, the IL value becomes smaller again. It can be concluded that as the number of storeys and span length rise, the IL value also increased, but the corresponding frequencies decreased.

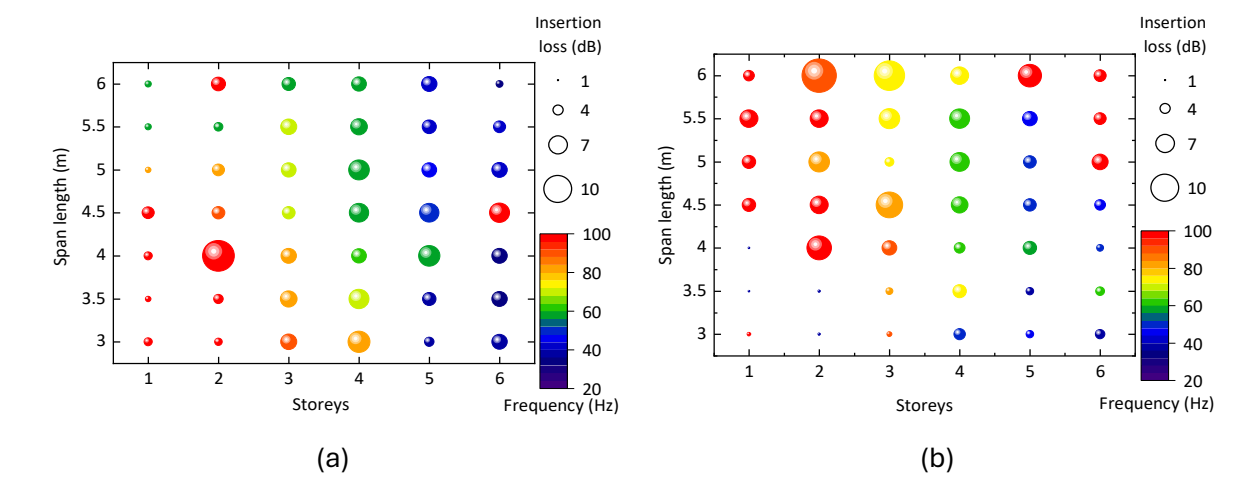


Figure 5-13 Result of parametric study for different span length and the number storeys (a) Insertion loss at point A (b) insertion loss at point B.

The spectral results for the ground response with different size of building are shown in Figure 5-14. Since the building primarily influences the frequency band above 10 Hz, the figures display frequencies ranging from 10 Hz to 100 Hz. There are two different single-span buildings, one with a single storey and the other with six storeys, both with the same span length of 4.2 m. There is a significant trend indicating that when a building has six storeys, the peak value of the building-induced equivalent response occurs at a lower frequency compared with the results for a one-storey building. The number of building storeys influences the frequency response of building-induced vibration, which in turn affects the frequency band for ground vibration mitigation. It can be observed that when the six-storey building with more mass is located along the transmission path, the frequency peak value is lower, which affects ground vibration at lower frequencies.

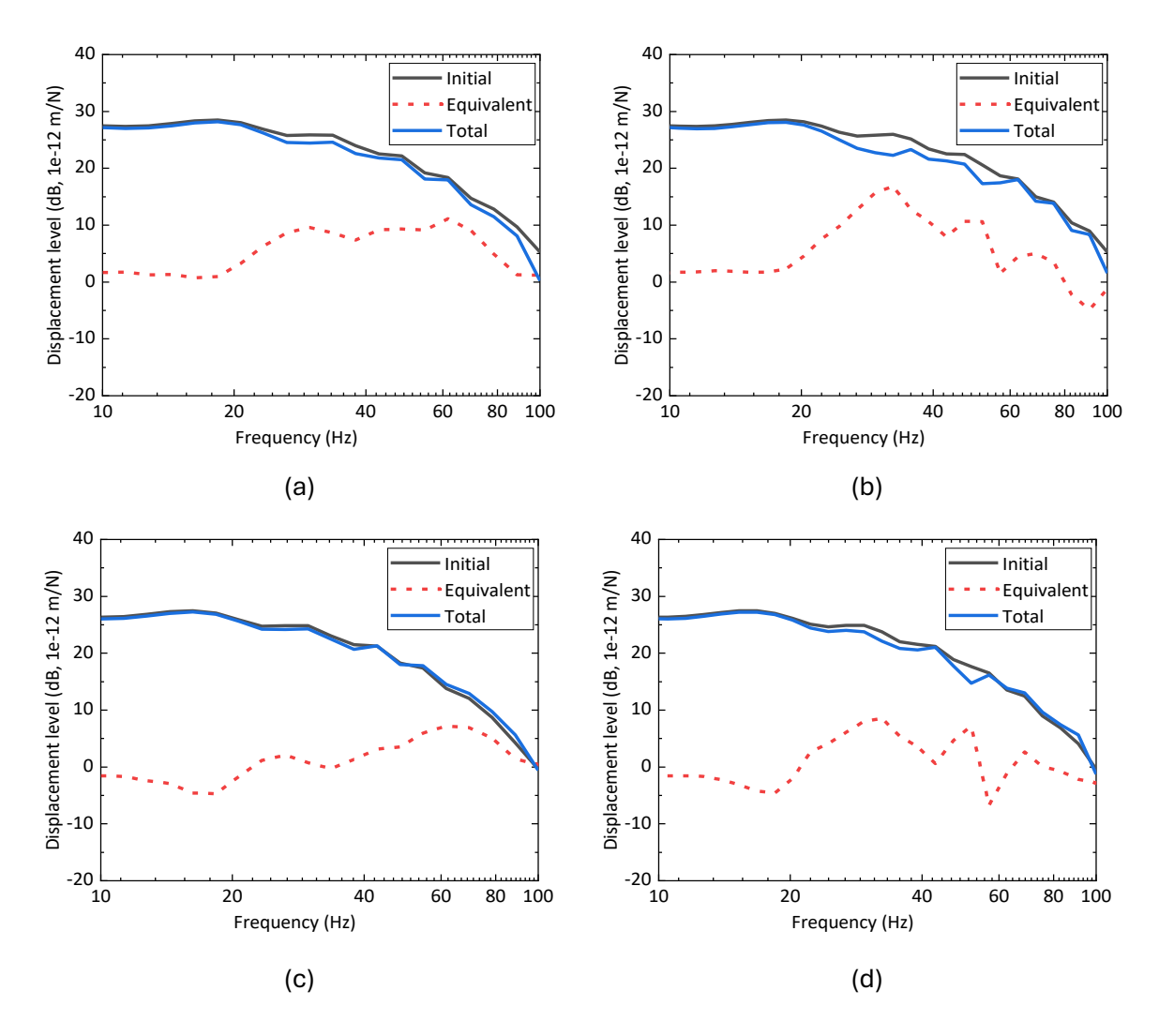


Figure 5-14 The spectral results for the ground response behind the (a) one-storey building and the (b) six-storey building at point A and (c) one-storey building and the (d) six-storey building at point B.

The spectral IL results are shown in Figure 5-14. These results are derived from narrowband frequency samples. Compared to a one-storey building, a six-storey building, which has a greater mass, tends to have a peak value at lower frequencies. These lower frequencies, corresponding to the building's modal frequency, significantly influence the ground. Therefore, a higher number of building storeys tends to affect the ground behind the building at lower frequencies.

Chapter 5

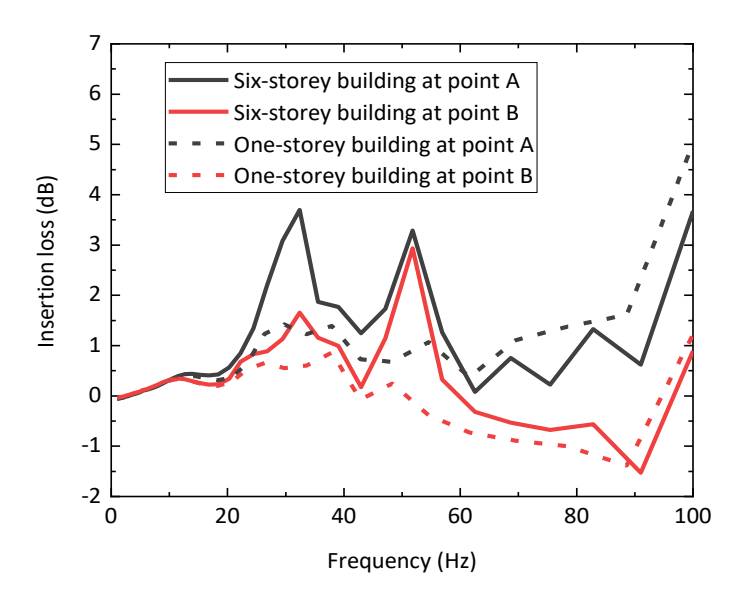


Figure 5-15 Spectral IL values for different number of storeys at point A and point B.

The contours of the IL from the ground behind the building with varying number of storeys are shown in Figure 5-16. The IL values are calculated from the difference in overall ground velocity level with/without the building evaluated over the range 1-80 Hz, so the IL values are generally lower than those at narrow band frequencies. The building's span length is 4.2 m, consistent with the dimensions in Figure 5-5. The results show that there is a significant vibration mitigation effects directly behind the pile locations. When the building has fewer storeys and therefore less mass, a notable vibration amplification zone with negative IL values appears just beneath the span on the ground. Conversely, as the number of building storeys increases and the building mass becomes greater, the IL values increase, leading to more effective ground vibration mitigation.

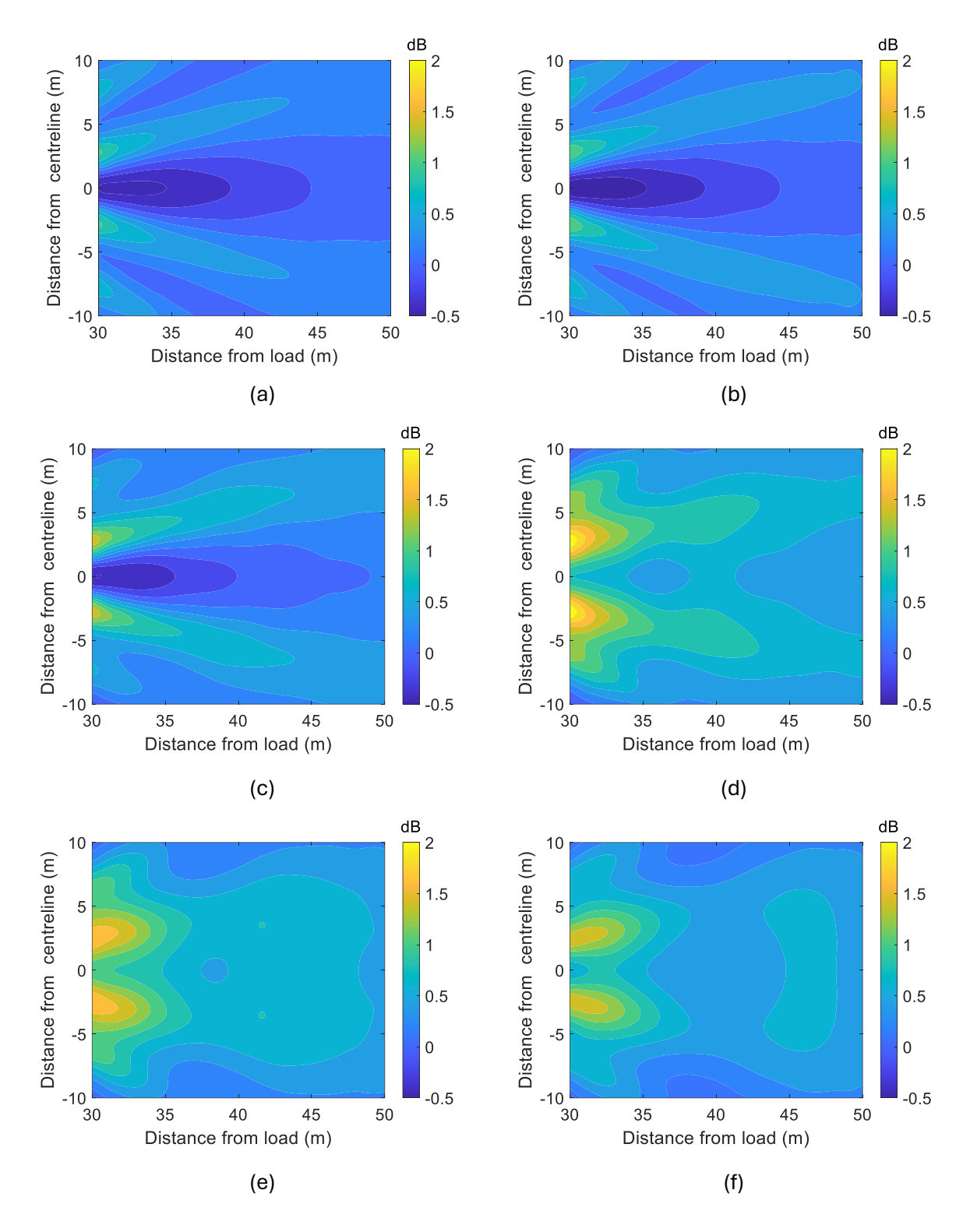


Figure 5-16 Contours of the ground IL calculated from the difference in overall ground velocity level with/without building evaluated over the range 1-80 Hz behind a building with varying storeys: (a) one storey, (b) two storeys, (c) three storeys, (d) four storeys, (e) five storeys, and (f) six storeys.

5.4.4 Overall ground response and comparison with pile group model

In this section, the ground response and IL results are compared for two cases: one involves the building supported by four piles located directly in the transmission path, and the other consists of the same four piles embedded in the ground without any superstructure. The dimensions of the building are the same as those introduced in Section 5.2.

5.4.4.1 Spectrum results for specific point

A specific receiver point on the centreline is selected to demonstrate the spectral results. This receiver point is 28 m away from the load location, which is means it is 3.8 m away from the building as the building span length is 4.2 m. The ground velocity response and IL value for the two cases are shown in Figure 5-17. The dimensions of the building and foundation are identical to those described in Section 5.4.1. The four-pile case includes four piles of the same dimensions as the piled foundation building, but without any upper structure.

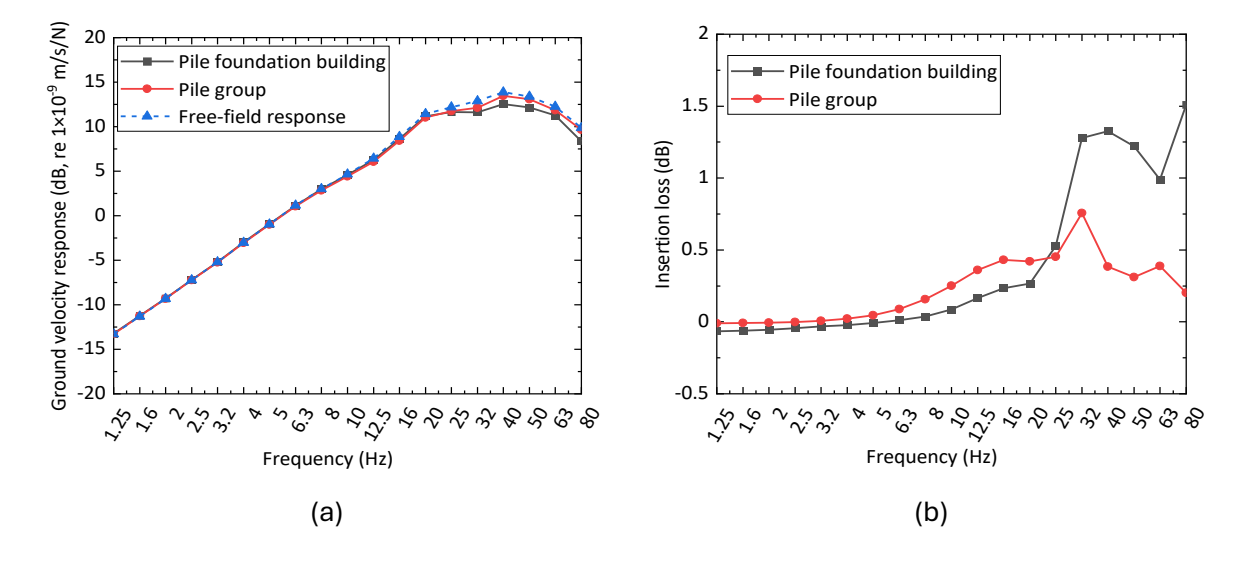


Figure 5-17 The spectrum results at specific point on the centreline which is 28 m away from the load (a) the ground velocity level and (b) IL results.

At this specific receiver point located on the centreline behind the structure and 28 m away from the load, the ground velocity response increases and then stabilizes as the frequency rises. This corresponds to the constant displacement at low frequencies, falling at higher frequencies, see Figure 5-9. The only minor differences in ground response between the pile foundation building and the pile group case, compared to the free-field response, occur in the frequency bands above 25 Hz. In the IL spectrum results, the largest IL values from both the building case and the pile group case occur above 25 Hz. The building provides more vibration mitigation, as evidenced by larger IL values compared with the pile group case.

5.4.4.2 Ground response on centreline behind the building

The ground response and the IL results on the centreline from the building case and pile group case are summarised in Figure 5-18 in terms of the overall velocity level for a unit load. All the receiver results are located on the centreline. Generally, as the distance between the load and the receiver point increases, the free-field response level and the ground response level for the two cases involving a structure in the transmission path decrease. Focusing on the IL results, when the piled foundation building is located in the transmission path, the IL values are significantly higher close to the building. In the case of the pile group, the IL values are negative in the near field along the centreline, indicating that the ground response influenced by the pile group may be amplified. In the far field, the IL values for the pile group case are larger. However, the amplitude of the ground response in the far field is not as large as in the near field.

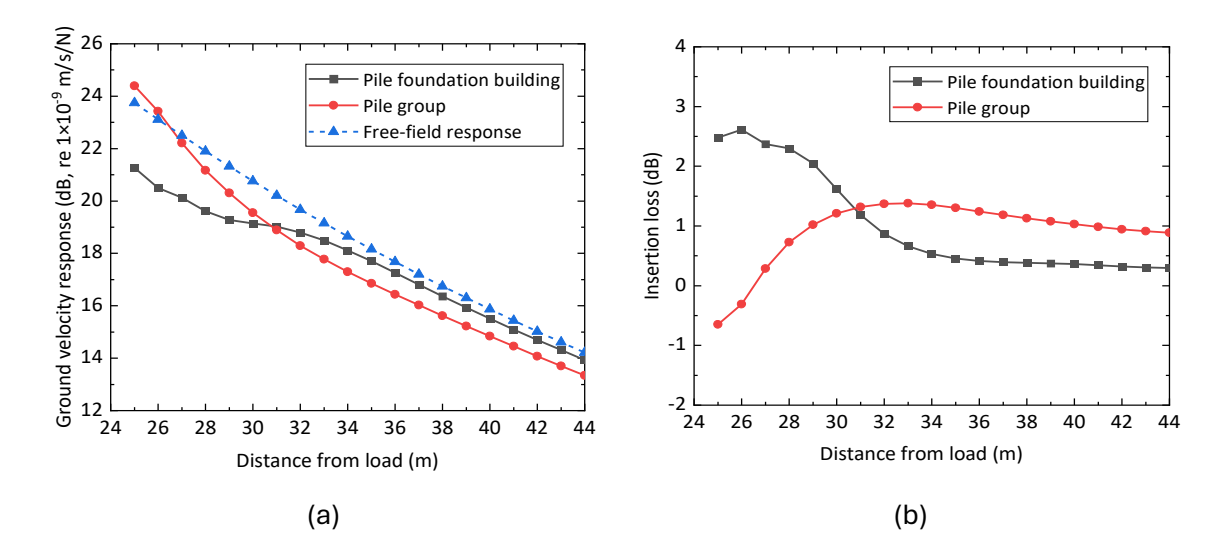


Figure 5-18 The overall results from all frequencies on the centreline receiver points (a) the ground velocity level (reference value is 1×10^{-9} m/s) and (b) IL results.

5.4.4.3 Overall insertion loss contour

A contour plot of the overall IL value is depicted in Figure 5-19. It is calculated by summing the velocity levels with and without the building in all one-third octave bands ranging from 1 Hz to 80 Hz and then taking the level difference. The calculation method is based on Eqs. (3-36) to (3-38). The region covered by these plots is larger than shown in Figure 5-6. The main difference between the two contours is in the near field. When the building is situated in the transmission path, the near field contour pattern is less regular compared with the pile group. In the middle of the building span, the ground vibration is still significantly mitigated, unlike in the pile group case where the ground vibration may be amplified. For the case involving only the pile group, the zone of greatest vibration mitigation is located directly behind each pile.

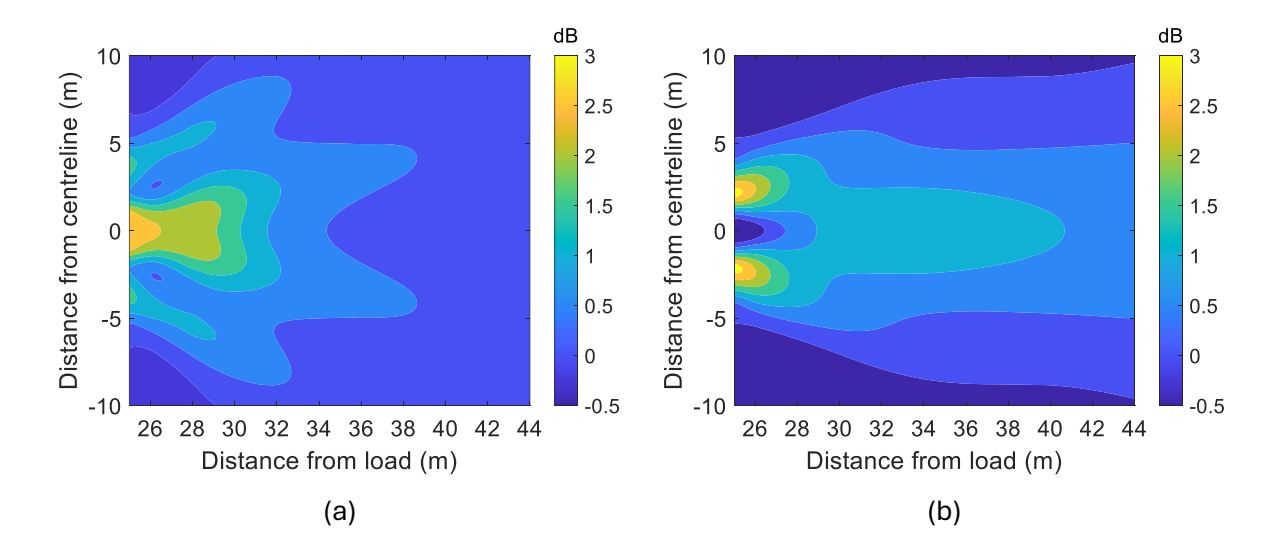


Figure 5-19 The overall IL contour for the (a) pile foundation building and (b) pile group with same dimensions located between the load and receiver points.

5.4.4.4 Average insertion loss results

The average ground velocity level and corresponding IL value from all receiver points positioned at identical distances from the load, are shown in Figure 5-20. The calculation method is based on Eqs. (3-39) to (3-41). For the average ground velocity response, an increase in distance from the load corresponds with a decrease in ground response, similar to Figure 5-18. If the piled foundation building or the pile group is situated in the transmission path between the load and receiver points, the ground response is further reduced. The IL results, particularly in the near field zone, indicate that the building generates greater average vibration mitigation effects than the pile group. However, when the distance between the load and the receiver points exceeds approximately 35 m, the IL due to the piled building and the pile group become similar. Thus, in terms of this average vibration across the width, the building upper structure mainly influences the ground vibration in the near field close to the building location. The upper part of the building enhances the ground vibration mitigation effects in the near field. However, in the far field over 34 m away from the load, the upper part of the building has negligible additional effect on the ground vibration response.

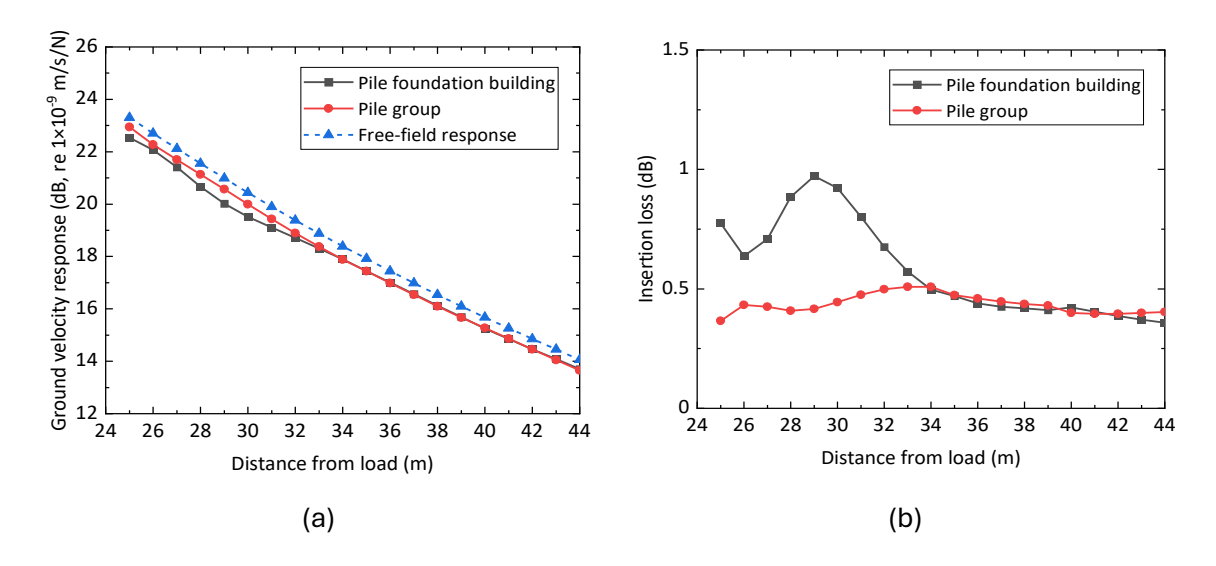


Figure 5-20 The average results from all the receiver points at the same distance away from the load (a) the ground velocity level and (b) IL results.

5.5 Summary

The ground vibration behind a building induced by a fixed unit load can be calculated using a semi-analytical model. This model is based on an FE model of the building and the dynamic stiffness matrix method to simulate the ground. Because this model does not require meshing of the soil, it offers advantages over the finite element method, particularly in calculating the high frequency surface responses over large distances. The equivalent forces are calculated at the coupled nodes between the foundation piles and the soil. This model is linear in the frequency-wavenumber domain and can calculate the free-field ground response, equivalent load induced ground response, as well as the total response. Based on the calculation results for the case study, some conclusions can be drawn.

From the IL spectrum from some specific receiver points, it is clear that the presence of a piled building leads to a mitigation in the ground vibration response under a fixed load. There are differences in the ground response behind the building at different frequencies. In particular, for the building considered, the ground response is more significantly suppressed in the frequency range 40-80 Hz, which is related to the building modes.

It is shown that the vibration of the ground may be significantly affected by the building's modes, especially those that include vertical movement of the floors. This may alter the vibration in the specific frequency region corresponding to these modes.

The number of building storeys influences both the frequency response of building-induced vibration and the frequency band for ground vibration mitigation. A greater number of storeys results in a reduction in the affected frequency region compared with buildings with fewer storeys.

Chapter 5

Comparative analysis of the piled foundation building and a similarly dimensioned pile group model allows for an investigation into the influence of the upper structure. Analysis of the ground response spectrum, IL values, and the ground contour behind the structure indicates that the upper building predominantly affects higher frequencies, specifically those above 30 Hz, and primarily influences the zone close to the structure's location. Although low-frequency modes contain more energy, their modal movement is predominantly horizontal. Therefore, they do not significantly influence the vertical response of the ground.

Chapter 6 Excitation by an underground railway

In this chapter, the investigation focuses on the ground response behind a building with a piled foundation when subjected to excitation from an underground railway. To calculate the ground response induced by underground railways, an established semi-analytical model based on MOTIV [7, 8] is used. The method for including the tunnel is developed based on the modelling strategy in [227] which couples the train, track, tunnel and soil. It is assumed that the near field displacement of the tunnel is not influenced by the existence of a building or the presence of the ground surface. The model is linear, i.e., all mechanical behaviour is assumed to be within the elastic range, allowing the calculations to be performed in the frequency-wavenumber domain. An inverse Fourier transform is used to obtain results in the frequency-spatial domain.

6.1 Methodology

As before, the displacement $\widehat{\mathbf{U}}$ at a receiver point can be divided into two parts, in this case the free field response induced by the underground railway, and the ground response caused by the equivalent forces at coupled nodes of the building pile foundation. The calculation procedure follows the same steps as outlined in Chapter 5.

The free-field response $\hat{\mathbf{U}}_0$ induced by the underground railway can be calculated by the MOTIV software. In the MOTIV software, there are four sub models: the train model, track model, tunnel model, and ground model. Additionally, the building model, as introduced in Chapter 5, serves as another sub-model.

6.1.1 Sub-model description

In this section, the train-track sub-model and tunnel-ground sub-model are introduced. These two sub-models are integral components of the MOTIV Matlab toolbox. The interaction between the train and the track is considered; however, it is assumed that the tunnel and building structures do not influence the train-track dynamic interaction. This model assumes a weak coupling between the railway tunnel and the building structure. This assumption has been validated by Coulier et al. [228] for situations where the distance between the building and the tunnel exceeds the compressional wavelength.

6.1.1.1 Train-track model

It is assumed that the train is stationary and excited by a "moving roughness". The dynamic equation of the train is given by

$$-\omega^{2}\mathbf{M}\widetilde{\mathbf{u}}_{T}(\omega) + \mathbf{K}\widetilde{\mathbf{u}}_{T}(\omega) = -\mathbf{B}\widetilde{\mathbf{P}}(\omega)$$
 (6-1)

where **M** is the mass matrix of the train, **K** is its stiffness matrix, **B** is a construction matrix consisting of zeros and ones to build different suspension system train matrices, and $\tilde{\boldsymbol{u}}_T$ is the displacement vector of the train. Construction matrix **B** is used to reduce the matrices down to the DOFs at the wheel/rail contacts. $\tilde{\mathbf{P}}(\omega)$ is the vector of vertical forces between the wheelsets and the rail in the frequency domain and it is denoted by $\tilde{\mathbf{P}}(\omega) = \{\tilde{P}_1(\omega), \tilde{P}_2(\omega), ..., \tilde{P}_l(\omega)\}^T$. The minus sign is due to the fact that the force acts in the opposite direction on the vehicle to that acting on the ground.

The receptance matrix of the train can be denoted by

$$\widehat{\mathbf{R}}_{\mathrm{T}}(\omega) = (\mathbf{K} - \omega^2 \mathbf{M})^{-1} \mathbf{B}$$
 (6-2)

Thus, the displacement of the train $\widetilde{\boldsymbol{u}}_T$ can be obtained by the receptance for the train DOFs:

$$\widetilde{\mathbf{u}}_{\mathrm{T}}(\omega) = -\widehat{\mathbf{R}}_{\mathrm{T}}(\omega)\widetilde{\mathbf{P}}(\omega) \tag{6-3}$$

As the wheelset displacement is part of the train, it can be written as

$$\widetilde{\mathbf{u}}_{\mathbf{W}}(\omega) = \mathbf{A}\widetilde{\mathbf{u}}_{\mathbf{T}}(\omega) \tag{6-4}$$

where \mathbf{A} is a matrix determined by the train type, $\mathbf{A} = \mathbf{B}^{\mathrm{T}}$. Eq. (6-4) gives

$$\widehat{\mathbf{R}}_{\mathbf{W}}(\omega) = \mathbf{A}\widehat{\mathbf{R}}_{\mathbf{T}}(\omega) = \mathbf{A}(\mathbf{K} - \omega^{2}\mathbf{M})^{-1}\mathbf{B}$$
(6-5)

Similarly, the rail receptance matrix $\widehat{\mathbf{R}}_R(\omega)$ can also be used to calculate the rail displacement induced by the contact forces:

$$\widetilde{\mathbf{u}}_{R}(\omega) = \widehat{\mathbf{R}}_{R}(\omega)\widetilde{\mathbf{P}}(\omega) \tag{6-6}$$

where

$$\widehat{\mathbf{R}}_{R} = \begin{pmatrix} \sigma_{11}^{R} & \dots & \sigma_{1N}^{R} \\ \vdots & \ddots & \vdots \\ \sigma_{N1}^{R} & \dots & \sigma_{NN}^{R} \end{pmatrix}$$
(6-7)

where N means the number of axles in the train. σ_{jk}^R means the rail receptance at the j-th wheel-rail contact point induced by a unit load at k-th wheel-rail point. The receptance of the rail $\widehat{\mathbf{R}}_R(\omega)$ is determined from the track and tunnel properties.

For a slab track, the dynamic equation of the rail represented as an Euler-Bernoulli beam is

$$E_{\rm R}I_{\rm R}\frac{\partial^4 u_{\rm R}}{\partial x^4} + m_{\rm R}\frac{\partial^2 u_{\rm R}}{\partial t^2} + k_{\rm P}(u_{\rm R} - u_{\rm S}) = P_0 e^{i\omega t}\delta(x)$$
 (6-8)

where $E_{\rm R}I_{\rm R}$ is the bending stiffness of the rail, $m_{\rm R}$ is the mass of the rails per unit length, $k_{\rm P}$ is the stiffness of the fasteners/pads, and $u_{\rm S}$ is the displacement of the slab. Both rails are assumed to vibrate together in phase so these parameters represent two rails. The slab is also represented by the Euler-Bernoulli beam model. The dynamic equation of the slab is

$$E_{S}I_{S}\frac{\partial^{4}u_{S}}{\partial x^{4}} + m_{S}\frac{\partial^{2}u_{S}}{\partial t^{2}} + k_{P}(u_{S} - u_{R}) + k_{C}(u_{S} - u_{G}) = 0$$
 (6-9)

where E_SI_S is the bending stiffness of the slab, m_S is the mass of the slab per unit length, k_C is the contact stiffness of the slab-ground interaction, and u_G is the displacement of the ground. The equations can be solved in the frequency-wavenumber domain, refer to [26].

The displacement vector of the rail at the wheel-rail contact points is denoted by

$$\widetilde{\mathbf{u}}_{R}(\omega) = \{\widetilde{u}_{R1}(\omega), \widetilde{u}_{R2}(\omega), \dots, \widetilde{u}_{RN}(\omega)\}^{T}$$
(6-10)

The wheels and rails are coupled through a contact spring and excited by the unevenness. Based on Ref. [229], the contact forces can be found from

$$[\widehat{\mathbf{R}}_{\mathbf{W}}(\omega) + \widehat{\mathbf{R}}_{\mathbf{R}}(\omega) + \mathbf{R}_{\mathbf{H}}]\widetilde{\mathbf{P}}(\omega) = -\widetilde{\mathbf{z}}(\omega)$$
(6-11)

where ${\bf R}_{\rm H}$ represents the receptance of the linearised wheel-rail contact spring, given by ${\bf R}_{\rm H}={\rm diag}\left(\frac{1}{k_H}\right)$ where k_H is the wheel-rail contact stiffness. $\tilde{\bf z}(\omega)$ is a vector containing the unevenness of the rail at each contact point. The dynamic axle load for different positions can be calculated:

$$\widetilde{\mathbf{P}}(\omega) = \begin{bmatrix} \widetilde{P}_1(\omega)e^{i\beta x_1} & \cdots & \widetilde{P}_l(\omega)e^{i\beta x_l} \end{bmatrix}$$
 (6-12)

where $\tilde{P}_l(\omega)$ means the dynamic axle load at the l-th wheelset of the train, and x_l is the position of the l-th wheelset of the train.

6.1.1.2 Tunnel-ground model

In this section a tunnel is introduced within the half-space soil. It is assumed that the underground railway only induces the dynamic component of vibration and that the quasi-static component from the moving axle loads can be neglected, as it only influences the response in the lower frequency bands and does not propagate away from the tunnel [85].

The tunnel is simulated by using the Pipe-in-Pipe model (PiP model) [35]. In this model, a thick-wall cylindrical shell is embedded in a full space ground. This model is part of MOTIV. For clarity, the equations are reformulated here using a notation consistent with the rest of thesis.

The wave equation governing motion in a three-dimensional, homogeneous, isotropic, elastic solid medium is derived from [230]:

$$(\lambda + \mu)\nabla\nabla \cdot \mathbf{u} + \mu\nabla^2 \mathbf{u} + \rho \mathbf{f} = \rho \frac{\partial^2 \mathbf{u}}{\partial t^2}$$
 (6-13)

where \mathbf{u} is the displacement vector, \mathbf{f} is the force vector, ρ is the density of the material, λ and μ are Lamé constants, and ∇ is gradient operator, $\nabla = \frac{\partial}{\partial x} \vec{i} + \frac{\partial}{\partial y} \vec{j} + \frac{\partial}{\partial z} \vec{k}$.

Based on the Helmholtz decomposition theorem, the wave can be solved by using the scalar and vector potentials:

$$\mathbf{u} = \nabla \phi + \nabla \times \mathbf{H} \tag{6-14}$$

where $\mathbf{H} = [H_r, H_\theta, H_z]^T$. In cylindrical coordinate, the Laplacians are

$$\nabla^2 \phi = \frac{1}{c_n^2} \frac{\partial^2 \phi}{\partial t^2} = \frac{1}{r} \frac{\partial \phi}{\partial r} + \frac{\partial^2 \phi}{\partial r^2} + \frac{1}{r^2} \frac{\partial^2 \phi}{\partial \theta^2} + \frac{\partial^2 \phi}{\partial z^2}$$
 (6-15)

$$\nabla^{2}\mathbf{H} = \frac{1}{c_{s}^{2}} \frac{\partial^{2}\mathbf{H}}{\partial t^{2}} = \left(\nabla^{2}H_{r} - \frac{H_{r}}{r^{2}} - \frac{2}{r^{2}} \frac{\partial H_{\theta}}{\partial \theta}\right) \vec{\mathbf{r}} + \left(\nabla^{2}H_{\theta} - \frac{H_{\theta}}{r^{2}} \frac{\partial H_{r}}{\partial \theta}\right) \vec{\mathbf{\theta}} + (\nabla^{2}H_{z})\vec{\mathbf{z}}$$
(6-16)

where $c_p=\sqrt{\frac{\lambda+2\mu}{\rho}}$ is the compression wave velocity, $c_s=\sqrt{\frac{\mu}{\rho}}$ is the shear wave velocity.

From Eq. (6-14), the displacement components can be written as

$$u_r = \frac{\partial \phi}{\partial r} + \frac{1}{r} \frac{\partial H_z}{\partial \theta} - \frac{\partial H_{\theta}}{\partial z} \tag{6-17}$$

$$u_{\theta} = \frac{1}{r} \frac{\partial \phi}{\partial \theta} + \frac{\partial H_r}{\partial z} - \frac{\partial H_z}{\partial r}$$
 (6-18)

$$u_z = \frac{\partial \phi}{\partial z} + \frac{1}{r} \frac{\partial (rH_{\theta})}{\partial r} - \frac{1}{r} \frac{\partial H_r}{\partial \theta}$$
 (6-19)

To solve Eqs (6-17) to (6-19), the harmonic solutions are considered

$$\phi = \check{f}(r)\cos(n\theta)e^{i\omega t}e^{i\beta x} \tag{6-20}$$

$$H_r = \breve{g}_r(r)\sin(n\theta)e^{i\omega t}e^{i\beta x} \tag{6-21}$$

$$H_{\theta} = \breve{g}_{\theta}(r)\cos(n\theta)e^{i\omega t}e^{i\beta x} \tag{6-22}$$

$$H_z = \breve{g}_z(r)\sin(n\theta)e^{i\omega t}e^{i\beta x}$$
 (6-23)

where n is the circumferential mode number, r is the radius.

Considering Eqs. (6-15) and (6-16), Eqs. (6-20) to (6-23), the components of **H** and ϕ are followed from the following differential equations:

$$r^2 \frac{\partial^2 \check{f}}{\partial r^2} + r \frac{\partial \check{f}}{\partial r} - \left[\left(\beta^2 - \frac{\omega^2}{c_1^2} \right) r^2 + n^2 \right] \check{f} = 0$$
 (6-24)

$$r^{2} \frac{\partial^{2} \breve{g}_{r}}{\partial r^{2}} + r \frac{\partial \breve{g}_{r}}{\partial r} - \left[\left(\beta^{2} - \frac{\omega^{2}}{c_{2}^{2}} \right) r^{2} + (n+1)^{2} \right] \breve{g}_{r} = 0$$
 (6-25)

$$r^{2} \frac{\partial^{2} \breve{g}_{z}}{\partial r^{2}} + r \frac{\partial \breve{g}_{z}}{\partial r} - \left[\left(\beta^{2} - \frac{\omega^{2}}{c_{2}^{2}} \right) r^{2} + n^{2} \right] \breve{g}_{z} = 0$$
 (6-26)

where n is the circumferential mode number, and it is corresponding to the order of modified Bessel functions.

The solutions of these equations based on modified Bessel functions are

$$\check{f} = AI_n(ar) + BK_n(ar) \tag{6-27}$$

$$\ddot{g}_r = -\ddot{g}_\theta = A_r I_{n+1}(br) + B_r K_{n+1}(br)$$
(6-28)

$$\ddot{g}_z = A_z I_n(br) + B_z K_n(br) \tag{6-29}$$

where $a^2 = \beta^2 - \omega^2/c_1^2$ and $b^2 = \beta^2 - \omega^2/c_2^2$. I_n is the modified Bessel function of the first kind. K_n is the modified Bessel function of the second kind.

Thus, based on Eqs. (6-20) to (6-23), the displacement in Eqs. (6-17) to (6-19) can be written as

$$u_r = \left[\frac{\partial \tilde{f}}{\partial r} + \frac{n}{r} \tilde{g}_z + i\beta \tilde{g}_r \right] \cos(n\theta) e^{i\omega t} e^{i\beta x}$$
 (6-30)

$$u_{\theta} = \left[-\frac{n}{r} \breve{f} + i\beta \breve{g}_r - \frac{\partial \breve{g}_z}{\partial r} \right] \sin(n\theta) e^{i\omega t} e^{i\beta x}$$
 (6-31)

$$u_{z} = \left[i\beta \breve{f} - \frac{(n+1)}{r} \breve{g}_{r} - \frac{\partial \breve{g}_{r}}{\partial r} \right] \cos(n\theta) e^{i\omega t} e^{i\beta x}$$
 (6-32)

Based on the properties of the derivative of the Bessel functions:

$$I'_{n}(z) = \frac{n}{z}I_{n}(z) + I_{n+1}(z)$$
(6-33)

$$K'_{n}(z) = \frac{n}{z}K_{n}(z) - K_{n+1}(z)$$
 (6-34)

Chapter 6

$$I'_{n}(z) = I_{n-1}(z) - \frac{n}{z}I_{n}(z)$$
 (6-35)

$$K'_{n}(z) = -K_{n-1}(z) - \frac{n}{z}K_{n}(z)$$
 (6-36)

The Eqs. (6-30) to (6-32) can be written as

$$\mathbf{u} = \mathbf{S} \mathbf{\breve{U}} \mathbf{\breve{C}} e^{\mathrm{i}\omega t} e^{\mathrm{i}\beta x} \tag{6-37}$$

where \mathbf{u} is the vector of the displacement, $\mathbf{u} = [u_r \quad u_\theta \quad u_z]^T$. $\mathbf{\breve{C}}$ is the vector of coefficients which can be determined by the boundary conditions, $\mathbf{\breve{C}} = [A \quad B \quad A_r \quad B_r \quad A_z \quad B_z]^T$. $\mathbf{\breve{U}}$ is the displacement coefficient matrix, the details of which are summarised in Appendix B. \mathbf{S} is the trigonometric functions matrix:

$$\mathbf{S} = \begin{bmatrix} \cos(n\theta) \\ \sin(n\theta) \\ \cos(n\theta) \end{bmatrix} \tag{6-38}$$

Based on the general stress-strain relation of Hooke's law, the stress can be calculated in a similar way. More details of calculation steps about the stress can be found in Ref. [35] and [227].

$$\mathbf{\tau} = \begin{bmatrix} \mathbf{S} & \mathbf{S} \end{bmatrix} \mathbf{T} \mathbf{\tilde{C}} e^{i\omega t} e^{i\beta x}$$
 (6-39)

where $\mathbf{\tau} = [\tau_{rr} \quad , \tau_{r\theta} \quad \tau_{rz} \quad \tau_{\theta\theta} \quad \tau_{\theta z} \quad \tau_{zz}]^T$. $\mathbf{\breve{T}}$ is the stress coefficient matrix, the details of which can be found in Appendix B.

Therefore, based on the PiP model, the displacement and traction in the frequency-wavenumber domain and decomposed in the circumferential direction can be represented as

$$\mathbf{\breve{u}} = \mathbf{\breve{U}}\mathbf{\breve{C}} \tag{6-40}$$

and

$$\breve{\mathbf{\tau}} = \breve{\mathbf{T}}\breve{\mathbf{C}} \tag{6-41}$$

For a unit load applied on the tunnel invert, it can be construed as the uniform normal stress acing on a unit area, as shown in Figure 6-1.

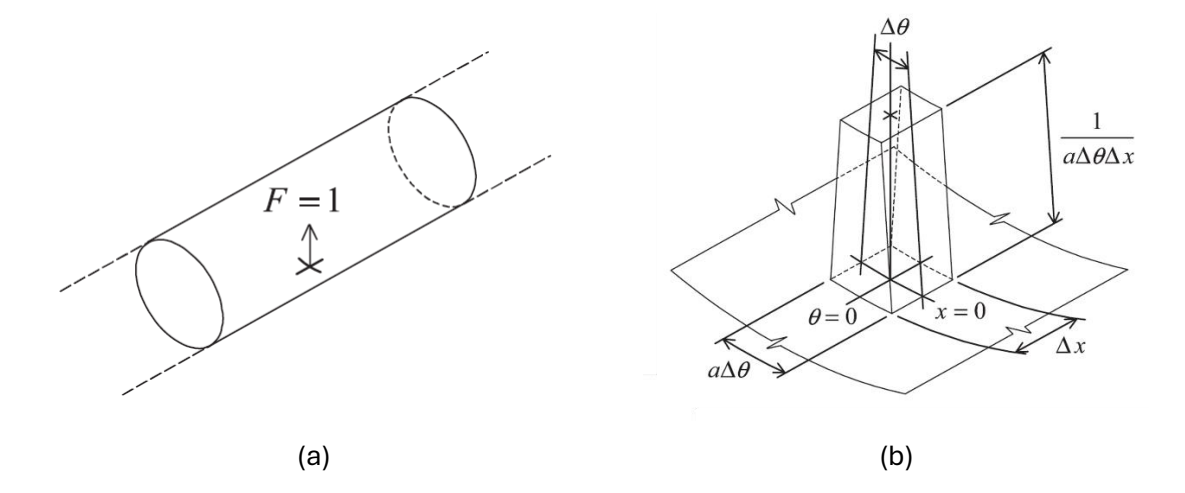


Figure 6-1 (a) A unit load acting on the infinitely long tunnel invert can be construed as (b) the uniform normal stress acting on the unit rectangular area [35].

The load applied on the tunnel can be represented as:

$$\mathbf{P} = \frac{1}{a}\delta(x)\delta(\theta)\delta(r-a)\mathbf{E}e^{\mathrm{i}\omega t}e^{\mathrm{i}\beta x}$$
(6-42)

where $\mathbf{P} = [p_r \quad p_\theta \quad p_x]^T$ is the load vector. a is the inner radius of the tunnel. $\mathbf{E} = [1 \quad 0 \quad 0]^T$ represents the load direction.

Around the circumference, the space-harmonic variation can be represented by the discrete ring modes, so,

$$\frac{\delta(\theta)}{a} = \frac{1}{2\pi a} + \sum_{n=1}^{\infty} \frac{1}{\pi a} \cos(n\theta)$$
 (6-43)

Thus, the load in the frequency-wavenumber domain in one particular circumferential mode can be represented as

$$\tilde{p}_r = \begin{cases} 1/2\pi a, n = 0 \\ 1/\pi a, n \neq 0 \end{cases}, \tilde{p}_{\theta} = 0, \tilde{p}_{\chi} = 0$$
(6-44)

6.1.2 Calculation process

To calculate the train-induced ground responses influenced by a building located in the transmission path, the following steps are undertaken.

In the first step, the displacement of a tunnel embedded in a full-space due to a vertical load at the tunnel invert is computed. The assumption that the tunnel is embedded in a full space allows a fast evaluation of the displacement at the tunnel-soil interface using the PiP model [36]. The boundary conditions of the PiP model are shown in Figure 6-2 (a). At the tunnel-soil interface, the displacement compatibility requires

$$\mathbf{\breve{u}}_{\mathrm{T2}} = \mathbf{\breve{u}}_{\mathrm{F}} \tag{6-45}$$

where $\mathbf{\breve{u}} = [\breve{u}_r \ \breve{u}_\theta \ \breve{u}_x]^T$, subscript T2 indicates the external radius of the tunnel, subscript F means the full space with a cylindrical cavity.

The traction equilibrium can be determined as

$$\mathbf{\breve{\tau}}_{\mathrm{T2}} + \mathbf{\breve{\tau}}_{\mathrm{F}} = \mathbf{0} \tag{6-46}$$

where $\mathbf{\breve{\tau}} = [\breve{\tau}_{rr} \quad \breve{\tau}_{r\theta} \quad \breve{\tau}_{rx}]^T$.

Based on Eq. (6-40) and Eq. (6-41), the displacement and traction equilibrium in Eq. (6-45) and Eq. (6-46) can be written as:

$$\mathbf{\breve{U}}_{T2}\mathbf{\breve{C}}_{T} = \mathbf{\breve{U}}_{F}\mathbf{\breve{C}}_{F} \tag{6-47}$$

$$\mathbf{\breve{T}}_{T2}\mathbf{\breve{C}}_{T} - \mathbf{\breve{T}}_{F}\mathbf{\breve{C}}_{F} = \mathbf{0} \tag{6-48}$$

where subscript T means the tunnel, subscript 2 means the external tunnel radius. For the case of tunnel internal and external radius, i.e. the subscript is T1 or T2, the traction $\mathbf{\tau} = [\tau_{rr} \quad \tau_{r\theta} \quad \tau_{rx}]^{\mathrm{T}}$, so the stress matrices \mathbf{T} is the top half of the stress matrix in Appendix B. Therefore, the displacement and stress matrix \mathbf{U} and \mathbf{T} are 3×6 matrices. For the full space case, i.e. the subscript is F, the matrix associated with the modified Bessel function $I_n(r)$ should be omitted due to the boundary condition, which states that the displacement at a large radius should approach zero [42]. Thus, the size of \mathbf{U}_F and \mathbf{T}_F are reduced to 3×3, the size of \mathbf{C}_F is reduced to 3×1.

Based on Eq. (6-47) and Eq. (6-48), the equation can be represented as

$$(\mathbf{\breve{T}}_{T2} - \mathbf{\breve{T}}_{F}\mathbf{\breve{U}}_{F}^{-1}\mathbf{\breve{U}}_{T2})\mathbf{\breve{C}}_{T} = \mathbf{0}$$
(6-49)

Based on Eq. (6-41), the traction at the internal tunnel radius can be written as:

$$\breve{\mathbf{\tau}}_{\mathrm{T}1} = -\breve{\mathbf{T}}_{\mathrm{T}1}\breve{\mathbf{C}}_{\mathrm{T}} \tag{6-50}$$

where subscript T means the tunnel structure, subscript 1 means the internal radius.

Combining Eq. (6-49) and Eq. (6-50), the following expression is obtained:

$$\begin{bmatrix} -\mathbf{\breve{T}}_{T1} \\ \mathbf{\breve{T}}_{T2} - \mathbf{\breve{T}}_{F} \mathbf{\breve{U}}_{F}^{-1} \mathbf{\breve{U}}_{T2} \end{bmatrix} \mathbf{\breve{C}}_{T} = \begin{bmatrix} \mathbf{\breve{t}}_{T1} \\ \mathbf{0} \end{bmatrix}$$
 (6-51)

The displacement at tunnel-soil interface can be calculated by:

$$\mathbf{\breve{u}}_{T2} = \mathbf{\breve{U}}_{T2} \begin{bmatrix} -\mathbf{\breve{T}}_{T1} \\ \mathbf{\breve{T}}_{T2} - \mathbf{\breve{T}}_{F} \mathbf{\breve{U}}_{F}^{-1} \mathbf{\breve{U}}_{T2} \end{bmatrix}^{-1} \begin{bmatrix} \mathbf{\breve{\tau}}_{T1} \\ \mathbf{0} \end{bmatrix}$$
(6-52)

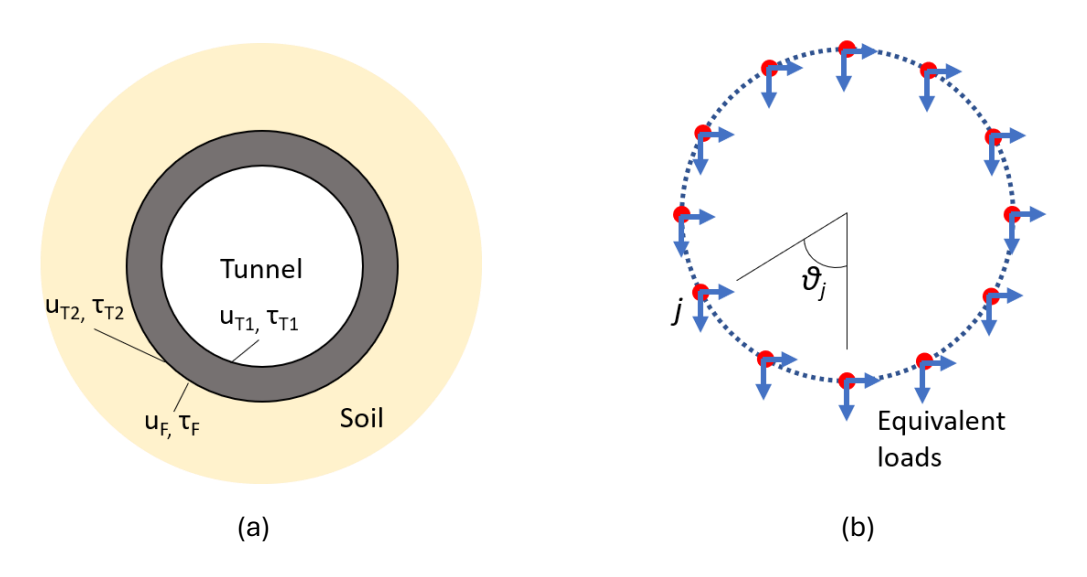


Figure 6-2 (a) Boundary conditions and (b) equivalent forces in PiP model.

In the second step, a model of a full space (without a tunnel) is considered. A finite number of equivalent loads in the full space, that produce the same displacement at the tunnel-soil interface as computed in the first step, are determined. The computation of these equivalent loads is fast and performed using analytical fundamental solutions for an elastic full space. The equivalent loads, depicted in Figure 6-2 (b), are used to replace the traction vector applied in the full space. The equivalent loads are seen as representing the tunnel-soil interaction effects. They are the forces acting on a full space that give the same response at the boundary position as the tunnel.

Based on the boundary condition that the displacement is equal for the cylinder and full space at the interface, it can be denoted as

$$\mathbf{\breve{u}}_{C} = \mathbf{\breve{u}}_{F} = \mathbf{\breve{u}}_{T2} \tag{6-53}$$

where the subscript C means the solid cylinder and subscript F means the full space.

The traction vector $\breve{\tau}$ applied in the full space can be calculated by:

$$\mathbf{\breve{\tau}} - \mathbf{\breve{\tau}}_{\mathrm{C}} - \mathbf{\breve{\tau}}_{\mathrm{F}} = 0 \tag{6-54}$$

Thus, the traction vector applied in full space can be calculated based on the displacement at tunnel-soil interface calculated from Eq. (6-52).

$$\mathbf{\breve{\tau}} = (\mathbf{\breve{T}}_C \mathbf{\breve{U}}_C^{-1} - \mathbf{\breve{T}}_F \mathbf{\breve{U}}_F^{-1}) \mathbf{\breve{u}}_{T2}$$
(6-55)

A set of equivalent loads is applied to represent the traction vector. The equivalent load for the tunnel in the half-space is

$$\widetilde{\widetilde{\mathbf{T}}}_{j} = \int_{0}^{2\pi} N_{j}(\theta) \, \check{\mathbf{\tau}} \mathrm{d}\theta \tag{6-56}$$

where $N_i(\theta)$ is the shape function of the tunnel. More details can be found in Ref. [227].

In the third step, the track is coupled to the tunnel using the equilibrium of displacements between the tunnel invert and the track. The equivalent loads between the slab track and tunnel are calculated for the train running on the rails with unit amplitude unevenness for all frequencies (wavelengths) [36]. The model is based on the sub-model described in Section 6.1.1.1. In this model, it is assumed that there is a continuous resilient layer between the slab beam and the tunnel invert. For a rigid slab the resilient layer is made very stiff. The contact force normal to the interface between the invert and the tunnel wall can be obtained. The details can be found in Ref. [36]. The sketch of the track model in the MOTIV is shown in Figure 6-3.

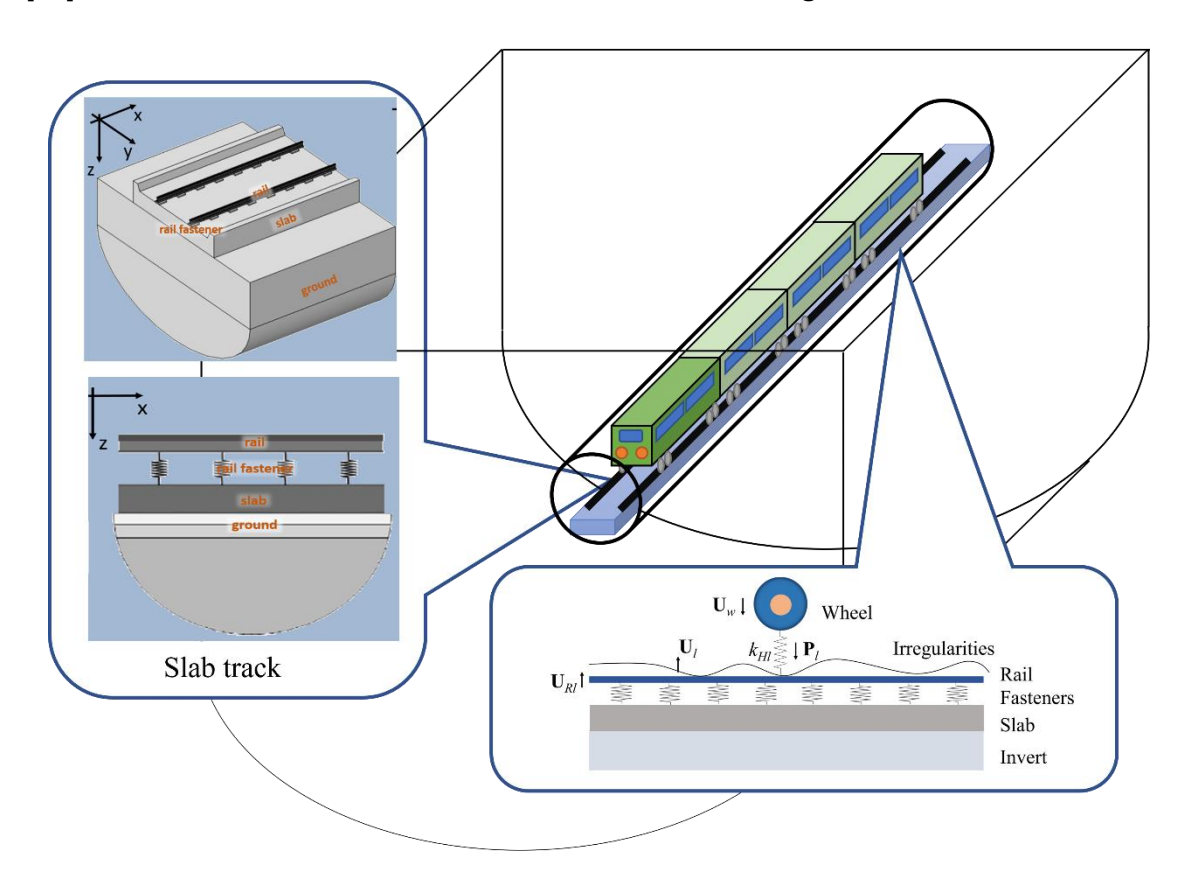


Figure 6-3 Sketch of the track model in MOTIV: coupling of wheel, track and invert.

Thus, the equivalent force representing the tunnel in a full-space in frequency-wavenumber domain is

$$\widetilde{\mathbf{F}}_{j} = \widetilde{\mathbf{T}}_{j}\widetilde{\mathbf{H}} \tag{6-57}$$

where $\widetilde{\mathbf{T}}_j$ represents the equivalent load induced by a unit load applied in the tunnel, which can be obtained from Eq. (6-56). $\widetilde{\widetilde{\mathbf{H}}}$ is the contact force normal to the interface between the invert and the tunnel wall.

In the fourth step, a model of a multi-layered half-space (without a tunnel) is considered. The half-space layered soil model introduced in Section 3.5 is used to replace the full space in the second step, which means the equivalent forces are applied in the layered soil. The equivalent loads from the third step are multiplied by Green's functions of the multi-layered half-space. These Green's functions are evaluated numerically by means of the dynamic stiffness method [44].

The ground response at the selected point induced by the equivalent loads at tunnel circumference position can be calculated as follows:

$$\widetilde{\widetilde{\mathbf{u}}}_1 = \sum_{j=1}^N \widetilde{\widetilde{\mathbf{f}}}_j \widetilde{\widetilde{\mathbf{H}}}^G \tag{6-58}$$

where $\widetilde{\widetilde{\mathbf{H}}}^G$ means the displacement for the layered soil model induced by the unit load at point j. $\widetilde{\widetilde{\mathbf{F}}}_j$ means the equivalent force calculated from the third step. N is the number of equivalent loads at tunnel-soil interface.

The wheel-rail interaction force is calculated by the train-track model as indicated in Figure 6-3. Based on [229], it is assumed that the wheelset is always in contact with the rail surface. The ground response induced by the train load can be calculated from the ground response induced by the unit load:

$$\widetilde{\widetilde{\mathbf{u}}} = \sum_{j=1}^{M} \widetilde{\widetilde{\mathbf{u}}}_{1} \widetilde{\widetilde{P}}_{j} \tag{6-59}$$

where M is the number of train axis. $\tilde{\tilde{P}}_j$ means the dynamic axle load at the j-th wheelset of the train in frequency-wavenumber domain. It can be calculated from Eq. (6-11) and Eq. (6-12).

The ground response can be calculated in the spatial domain by applying the inverse Fourier transform from the wavenumber domain:

$$\widehat{\mathbf{u}} = \frac{1}{4\pi} \int_{-\infty}^{+\infty} \int_{-\infty}^{+\infty} \widetilde{\widetilde{\mathbf{u}}} \, \mathrm{e}^{\mathrm{i}(k_x x + k_y y)} \mathrm{d}k_x \mathrm{d}k_y \tag{6-60}$$

In the fifth step, the building model is constructed using the FE method. The floors are represented by shell elements, and the columns and piled foundation are modelled with beam elements. A detailed description of the building model has already introduced in Chapter 5. This step is calculated in the spatial domain. In this Chapter, the building size can be determined in the same manner as described in Figure 5-5 in Chapter 5.

In the sixth step, after getting the ground response behind the building from the underground railway excitation by a unit roughness, the response under different track roughness can be determined. The response of the ground given by the superposition of the unit roughness induced ground response at the receiver points is then normalised to the actual rail unevenness.

6.2 Model parameters

The parameters used for the train, track, tunnel, and the ground are summarised in this section. The frequency range of interest for ground borne vibration is 1–80 Hz. The track structure is modelled as multiple infinite beams supported by vertical springs (rail fasteners) to represent a slab track. The train vehicles are modelled as 10 DOF multibody systems. The parameters of the train and the slab track are given in Table 6-1 and Table 6-2 respectively. In this model, there are four carriages present. All the parameters can be found in the SILVARSTAR project report [231]. As the focus of this thesis is to investigate the influence of the building on the ground, the same parameters are used for the underground and surface trains, which are from an InterCity train. The tunnel and the soil parameters are shown in Table 6-3 and Table 6-4 respectively.

Chapter 6

Table 6-1 The parameters of the train.

Property	Value	Unit
Vehicle length	23	m
Wheelset distance	2.5	m
Bogie distance	17	m
Vehicle body mass	32000	kg
Vehicle pitching moment of inertia	1.2×10 ⁶	kgm²
Bogie mass (without axles)	5000	kg
Bogie pitching moment of inertia	6000	kgm²
Wheelset mass	1200	kg
Static axle load	1.148×10 ⁵	N
Contact stiffness (per wheel)	1.13×10 ⁹	N/m
Primary suspension stiffness	2.0×10 ⁶	N/m
Primary suspension damping	4×10 ⁴	Ns/m
Lateral distance between springs	1.8	m
Secondary suspension stiffness	5×10 ⁵	N/m
Secondary suspension damping	3.16×10 ⁴	Ns/m

Table 6-2 The parameters of the track.

	Property	Value	Unit
Rail UIC 60 (per rail)	Bending stiffness	6.42×10 ⁶	Nm²
	Mass per unit length	60	kg/m
	Damping loss factor	0.01	-
Rail pad	Stiffness	2.5×10 ⁷	N/m
	Damping loss factor	0.2	-
	Fastener spacing	0.65	m
Slab	Width (at base)	3.4	m
	Height	0.54	m
	Mass per unit length	3720	kg/m
	Bending stiffness	2.33×10 ⁸	Nm²
	Damping loss factor	0.015	-
	Torsional stiffness	3.39×10 ⁸	Nm²
	Polar moment of inertia	3086	kgm

Table 6-3 The parameters of the tunnel structure.

Parameters	Value
External radius (m)	3.0
Thickness of tunnel wall (m)	0.3
Density (kg/m³)	2500
Young's modulus (GPa)	50
Poisson's ratio	0.3
Mass per unit length for invert (kg/m)	2500
Bending stiffness for invert (MNm²)	100
Loss factor for tunnel and invert	0.02

Table 6-4 The parameters of the soil.

Parameters	Value
Density (kg/m³)	2100
Young's modulus (Pa)	3.5×10 ⁸
Poisson's ratio	0.333
Loss factor	0.1
Shear wave velocity (m/s)	250
Compression wave velocity (m/s)	500

The track roughness is the "normal slab track roughness" obtained from the SILVARSTAR report [231]. The roughness levels at different wavelengths in one-third octave bands are plotted in Figure 6-4.

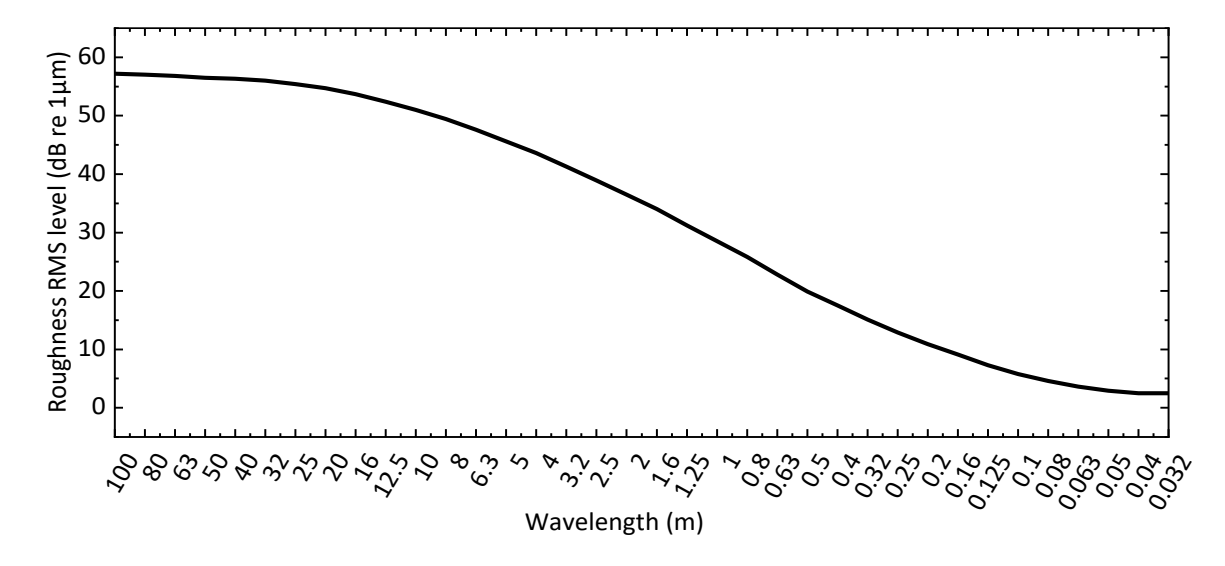


Figure 6-4 The track roughness spectrum.

6.3 Ground response results

In this section, two influencing factors are investigated: the train speed and the distance between the railway and the building. The location of the railway, building, and the receiver points are shown in Figure 6-5.

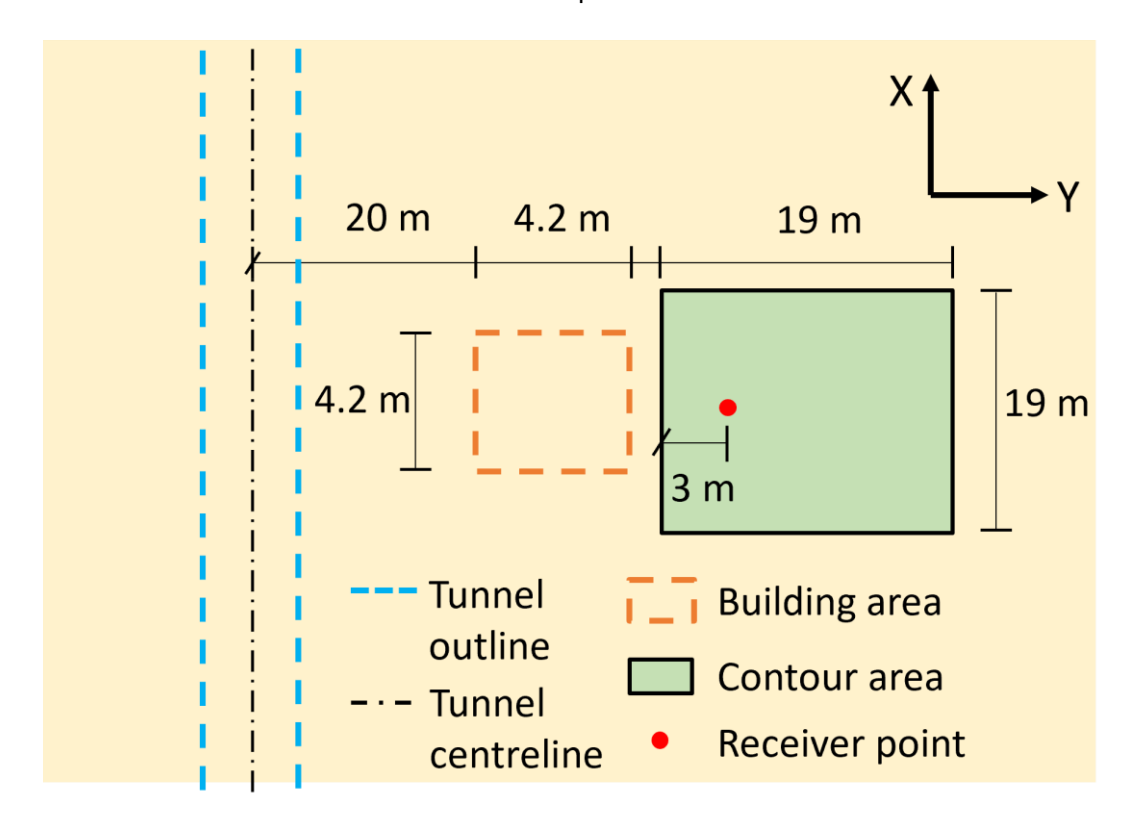


Figure 6-5 The location of the railway, building and receiver points.

6.3.1 Ground vibration and mitigation effects under different train speeds

The tunnel in the underground railway model is embedded with its centre at 10 m depth. The piled foundation building is located at a horizontal distance of 20 m away from the railway and has the same dimensions and properties as the one studied in Chapter 5. The ground response behind the building is investigated for different train speeds: 60 km/h, 80 km/h, 100 km/h, 120 km/h and 140 km/h.

6.3.1.1 Specific receiver points at specific frequencies

A receiver point is first selected which is on the centreline behind the building and 28 m away from the tunnel centreline (i.e. 3.8 m away from the rear of the building). The free-field velocity level and the corresponding ground velocity level response behind the building are shown in Figure 6-6. The results are presented in one-third octave bands, with each band consisting of three sample frequencies. The spectrum indicates that the ground velocity response increases with frequency, regardless of train speed, up to a peak at 50-63 Hz, which corresponds to the P2 resonance [1] of the train on the underground railway track. As the train speed increases, the ground response level at the peak increases, although the difference is not substantial, only around 3 dB.

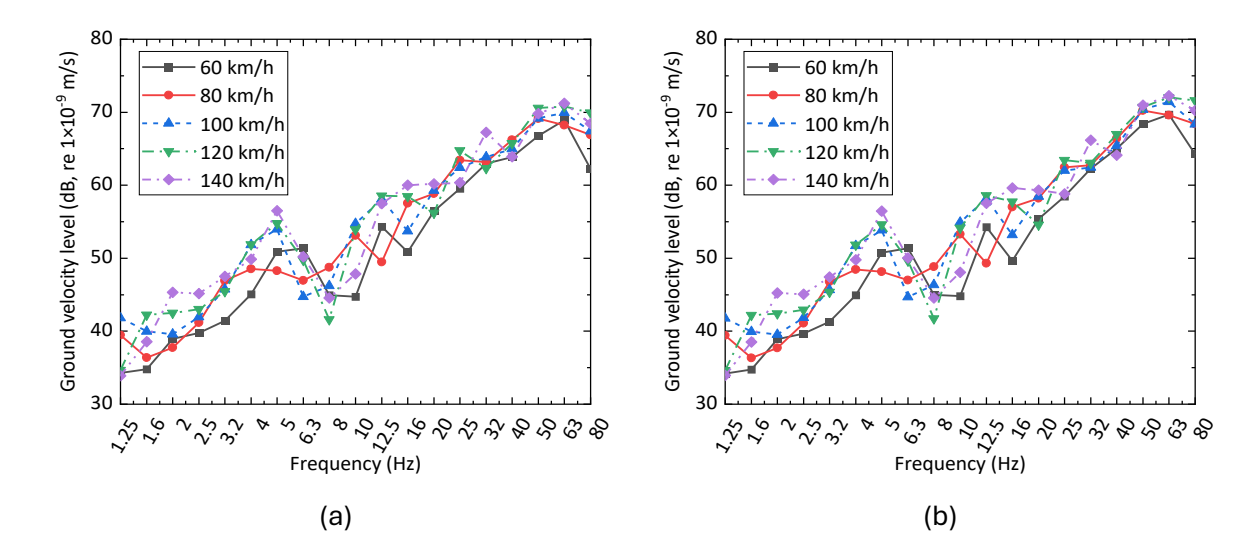


Figure 6-6 The ground response spectrum at 28 m away from the railway on the building centreline for an underground railway with different train speeds: (a) the free field ground response and (b) the ground response in the presence of the building.

Taking the level difference between the results with and without the building, the insertion loss results at this specific receiver point on the centreline behind the building are obtained as shown in Figure 6-7. The spectral results of IL at 10.8 m away from the building (35 m away from the railway track) are also shown for comparison. At lower frequency bands, below 10 Hz, the IL values from all different speed cases are close to zero. The value of IL rises to a peak between 16 Hz and 32 Hz and then becomes negative above about 40 Hz. Different train speeds do not generate significant differences in the IL.

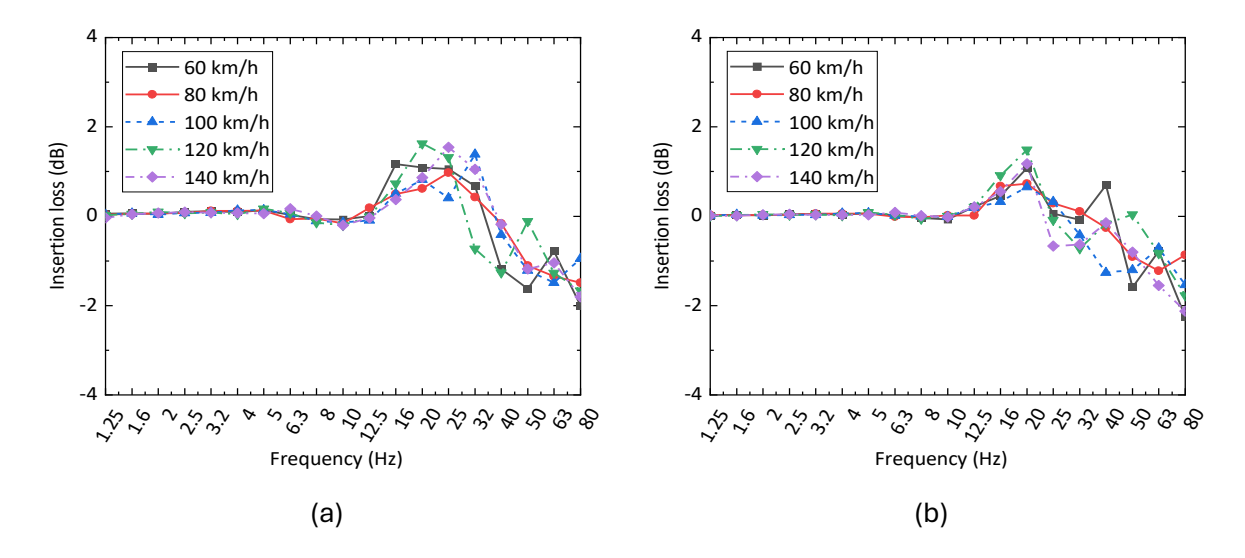


Figure 6-7 The IL result at (a) 28 m away from the railway (3.8 m from near of the building) and (b) 35 m away from the railway (10.8 m from near of the building) on the building centreline for an underground railway at different train speeds.

6.3.1.2 Ground response on the centreline behind the building

In this section the ground velocity level at all the receiver points on the centreline behind the building is investigated. The overall ground velocity response without and with the building at receiver points on the centreline is shown in Figure 6-8. These results are calculated from the sum over all the one-third octave bands from 1 Hz to 80 Hz. The results both with and without the building decrease as the distance between the receiver point and the railway increases. As the train speed increases, the ground response also increases.

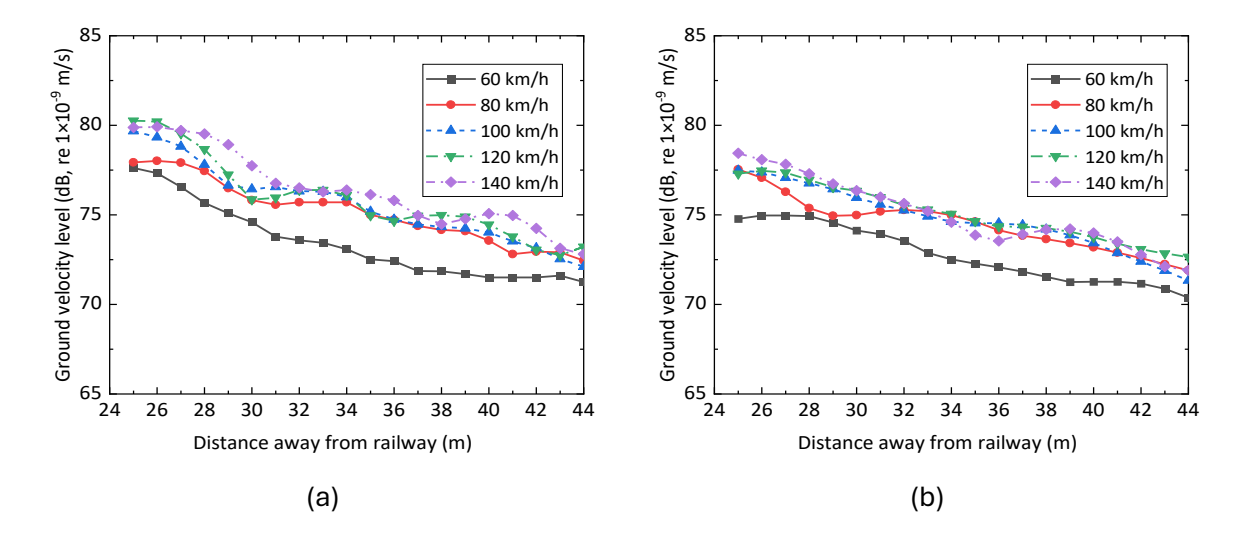


Figure 6-8 The results from overall velocity levels include (a) free field response and (b) total ground response on the centreline receiver points located behind the building.

The IL on the centreline obtained from these results is shown in Figure 6-9. In most cases the IL is larger than zero, which means the overall ground response is mitigated by the presence of the piled building. When the train speed is 140 km/h, the IL value is the largest compared with other train speed cases. In general, however there is no significant correlation between the speed of the train and the IL value.

Chapter 6

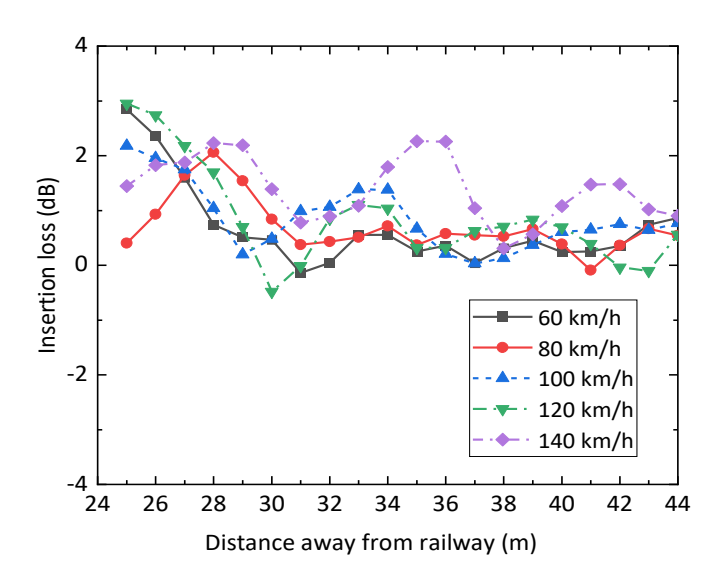


Figure 6-9 The IL results on the centreline behind the building derived from overall velocity levels.

6.3.1.3 Overall insertion loss contour for underground railway case

The IL determined from the overall vibration velocity level between 1 Hz and 80 Hz is investigated over a region on the ground surface behind the building. The overall response is calculated from these results using the equations outlined in Eq. (3-36), Eq. (3-37) and the IL from Eq. (3-38).

The edges of the region considered are 10 m away from the building's centreline in the direction of the train's movement. Perpendicular to the direction of train movement, the receivers are located at distances ranging from 25 m to 44 m from the railway. The rear of the building is 24.2 m from the railway. The spacing between each receiver point is 1 m. In total, 420 receiver points have been selected for plotting the contour.

Contour plots of the IL results at all the receiver points are shown in Figure 6-10 for five different train speed cases: 60 km/h, 80 km/h, 100 km/h, 120 km/h and 140 km/h. The insertion loss contour for all the cases is symmetric with respect to the centreline behind the building. Compared with the ground vibration induced by a unit load on the ground surface, shown in Figure 5-19, the pattern generated by the train loads appears more complex.

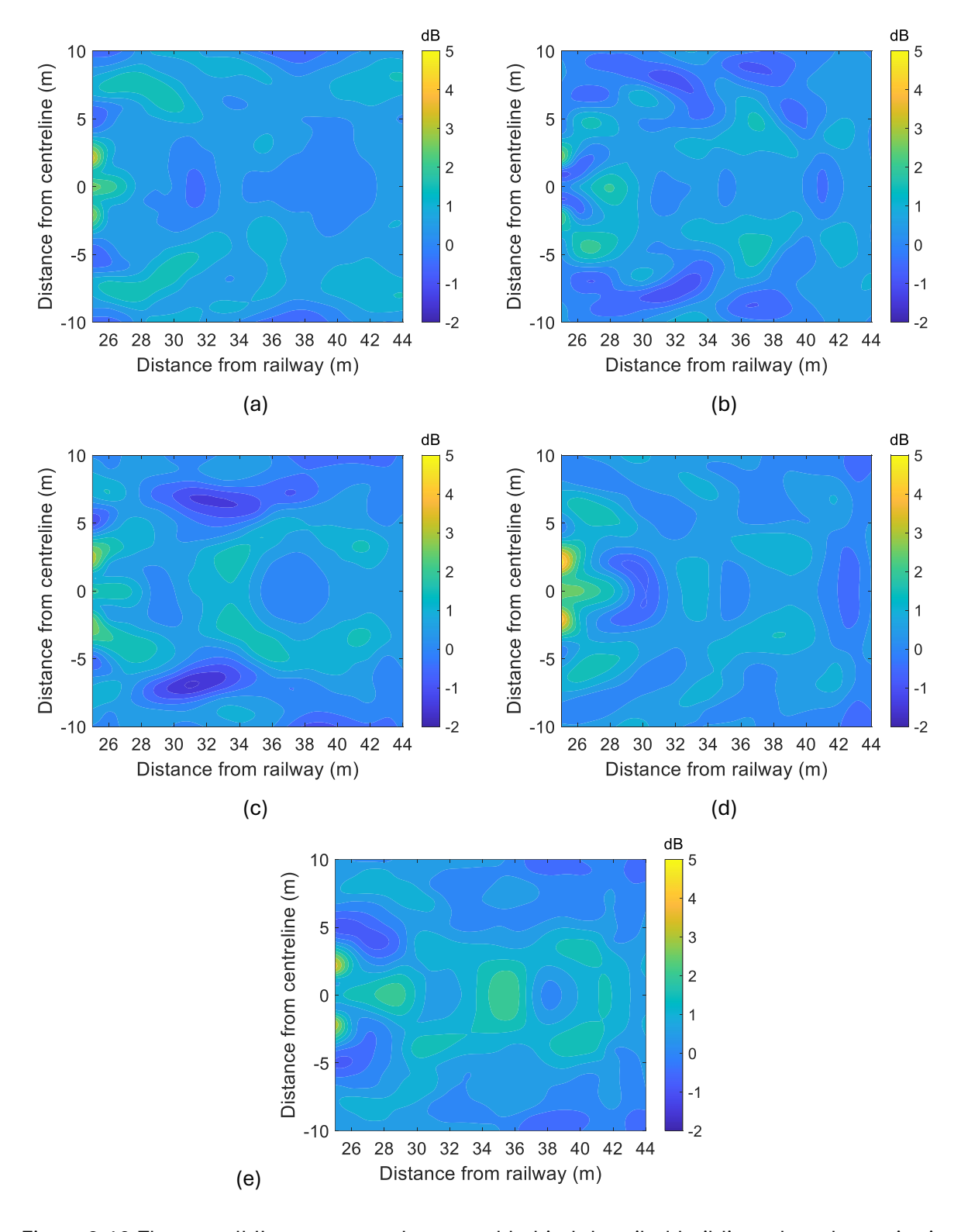


Figure 6-10 The overall IL contour on the ground behind the piled building when the excitation underground train speed is (a) 60 km/h (b) 80 km/h (c) 100 km/h (d) 120 km/h and (e) 140 km/h.

6.3.1.4 Average results for different underground railway train speed cases

The average results from all the receiver points at the same distance away from the railway are shown in Figure 6-11. These are evaluated using Eq. (3-39) to Eq. (3-41). For both the free-field ground velocity response and the response with the building, an increase in train speed results in

Chapter 6

a corresponding rise in the overall ground response. However, the increase in ground vibration is not significant when the train speed reaches 120 km/h and 140 km/h.

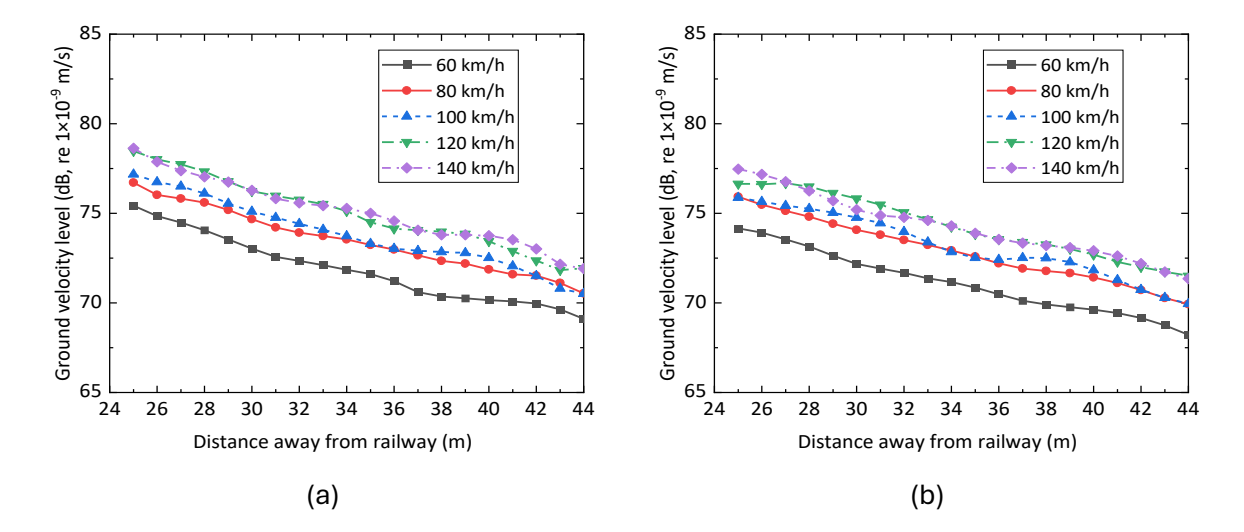


Figure 6-11 The average (a) free field ground response level and (b) ground response level with the building under different underground train speeds, average calculated over ±10 m width.

The average IL results calculated from these results are shown in Figure 6-12. For all the cases, the IL value is between 0 and 2 dB. The IL results do not vary significantly with train speed. As the distance from the railway increases, the regions of amplification may occur at different locations. It can be because the spectrum shape differs but the shape in Figure 6-6 does not change that much.



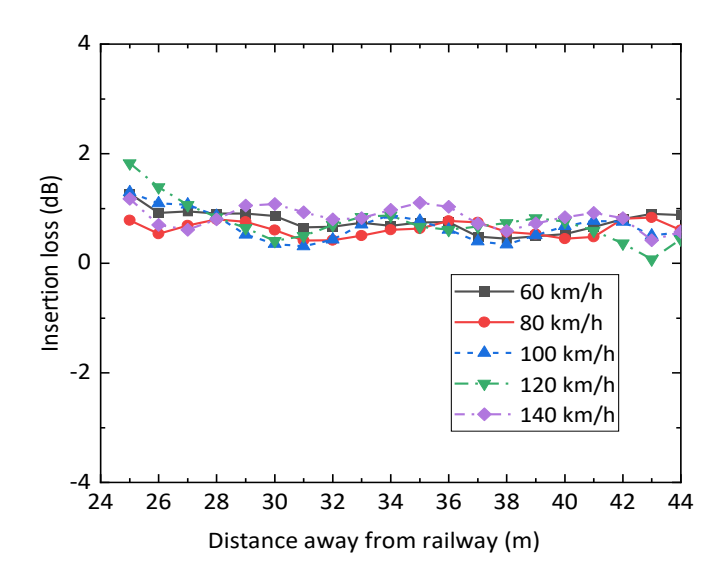


Figure 6-12 The average IL calculated from overall velocity levels averaged over ±10 m width under different underground train speeds.

6.3.2 Ground vibration and mitigation effects for different distances between railway and building

The distance between the underground railway and the building can influence the ground vibration when a piled foundation building is situated in the transmission path. In this section, five different distances between the railway and the building are investigated: 10 m, 15 m, 20 m, 25 m, and 30 m. The train speed is maintained at 100 km/h for all cases and the tunnel depth is 10 m.

6.3.2.1 The results at 3.8 m away from the building on the centreline

The spectrum of the ground velocity level and the IL results at one specific receiver point on the centreline is investigated first. The receiver point is 3.8 m away from the rear of the building in each case. The results are shown in Figure 6-13. The results for a 20 m distance between the railway and the building are consistent with those in Figure 6-7 when the train speed is 100 km/h. It can be observed that at this specific receiver point, varying distance between the railway and the building does not significantly affect the ground vibration at lower frequencies, such as below 16 Hz. Typically, when the distance between the railway and the building is reduced, the ground vibration intensifies at frequencies above 16 Hz. For the IL results, at frequencies below 10 Hz, the IL is close to zero. Different distances between the railway and the building result in ground vibration mitigation at different frequencies. For instance, at 32 Hz, an IL value of approximately 2 dB is observed when the railway-building distance is 15 m or 20 m. However, when this distance is 25 m, the IL value drops to approximately -3 dB. When the distance between the building and the underground railway is 10 m, the IL value is also negative at this frequency.

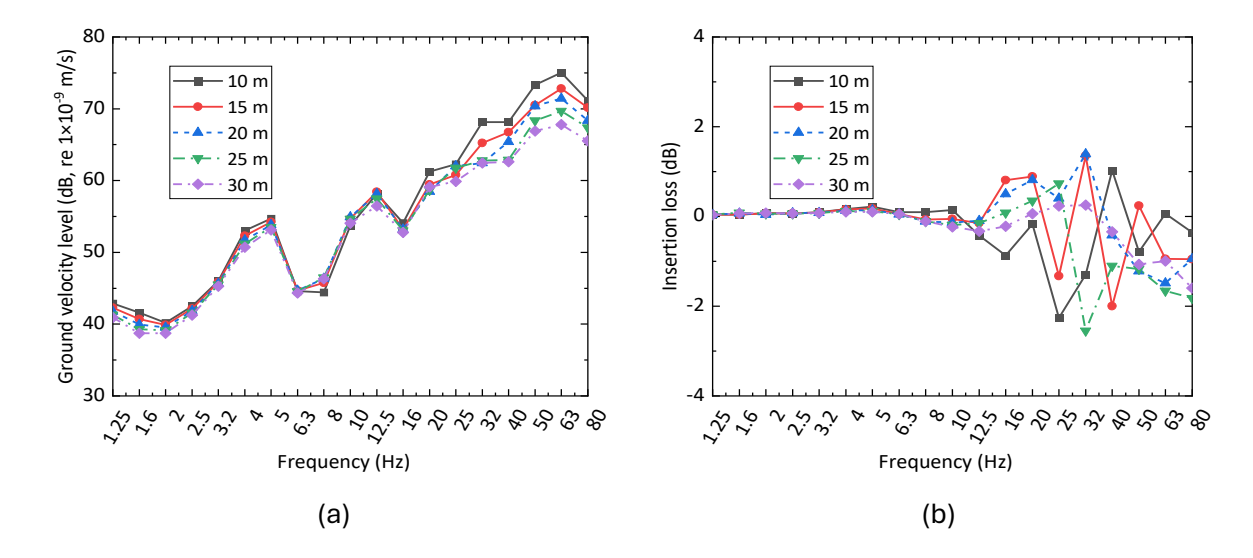


Figure 6-13 The spectrum results on the centreline which is 3.8 m away from the building for (a) the ground velocity level response in the presence of the building and (b) IL results.

6.3.2.2 Ground response on the centreline behind the building

The response at all the receiver points on the centreline behind the building is investigated in this section. The results are expressed as the overall vibration velocity level in the range 1 - 80 Hz. The ground velocity levels and IL results are shown in Figure 6-14. Generally, as the distance between the railway and the building increases, the velocity level decreases. For the IL results, cases with different distances between the tunnel and the building exhibit distinct peaks in various zones away from the building. For example, in the 10 m case, peak IL values occur at 6 m and 14 m from the building, while in the 15 m case, the peaks are observed at 13 m. Generally, the IL results across all cases are at a similar level.

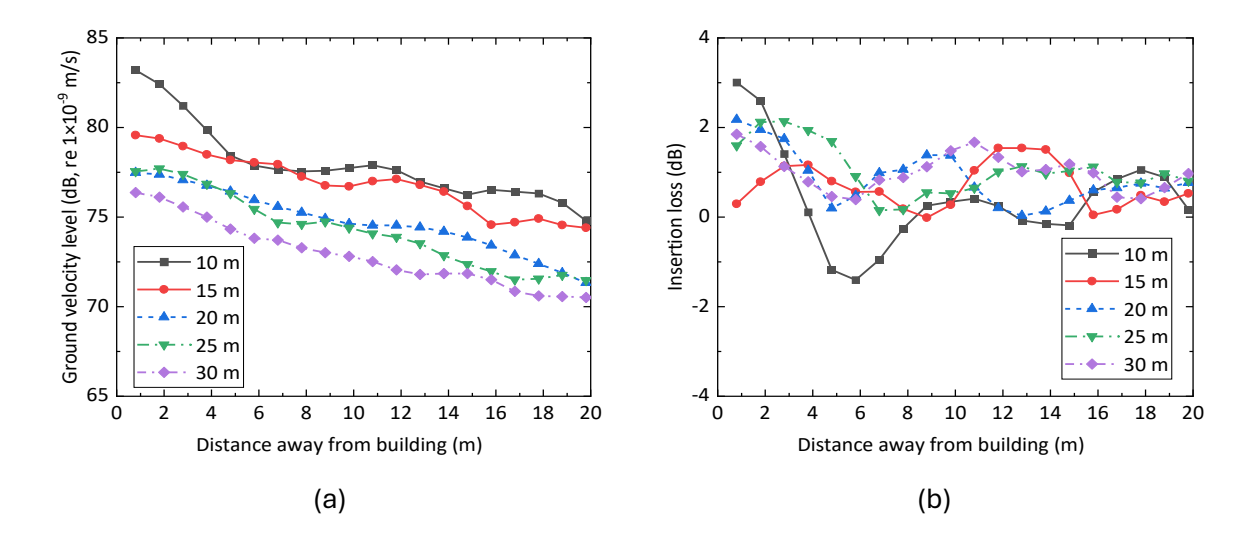


Figure 6-14 The overall (a) ground velocity level in the presence of the building and (b) IL results from all frequencies for receiver points on the centreline, for cases with different distances between the railway and the building, train speed 100 km/h.

6.3.2.3 Overall insertion loss contour for underground railway case

The overall IL for all the receiver points in the region behind the building is shown as a contour plot in Figure 6-15. Again, these results are derived from the level differences between the overall velocity level with and without the building. Analysis of the contour patterns reveals that when the distance between the railway and building is reduced, such as 10 m or 15 m, the area directly behind the building exhibits vibration mitigation effects. However, as the distance from the tunnel increases, zones of vibration mitigation emerge just behind the building. In all cases, there are zones closely behind the building that exhibit mitigated vibration.

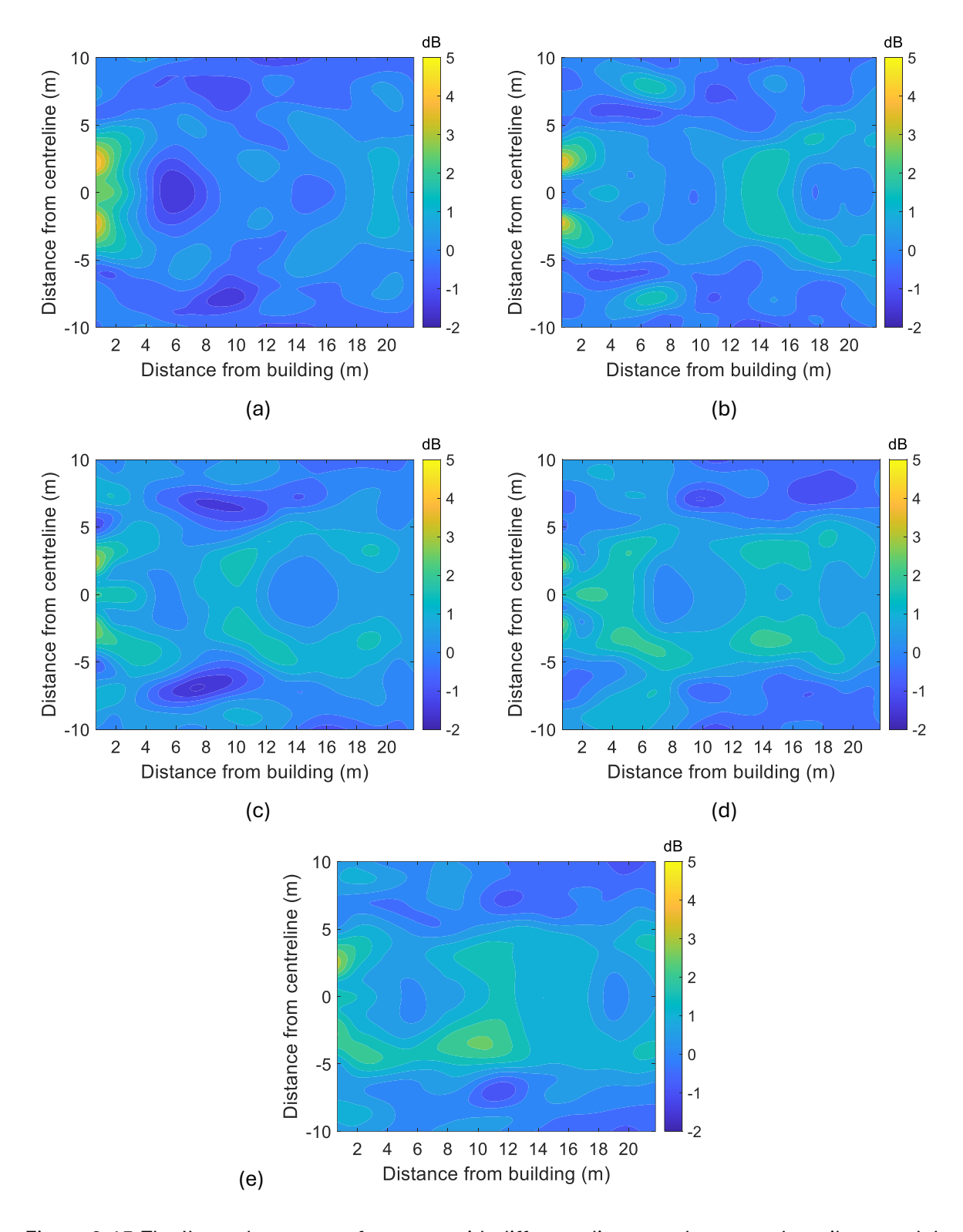


Figure 6-15 The IL results contour for cases with different distances between the railway and the building. (a) 10 m (b) 15 m (c) 20 m (d) 25 m and (e) 30 m.

6.3.2.4 Average insertion loss results at different distances

The ground velocity level and IL results, averaged from all receiver points at the same distance from the building, are shown in Figure 6-16. Generally, it can be observed that as the distance of the receiver points from the building increases, the ground response level decreases. In all five

cases, an increase in the distance between the railway and the building corresponds with a decrease in ground response. However, in terms of IL results, when the distance between the railway and building is just 10 m, vibration amplification effects are observed particularly at ground points 4 m away from the building. Conversely, as the railway-building distance increases to 25 m or 30 m, more significant ground vibration mitigation effects occur. In general, apart from the 10 m case, the ground velocity response behind the building is reduced by around 1 dB across all cases, regardless of the distance between the underground railway and the building.

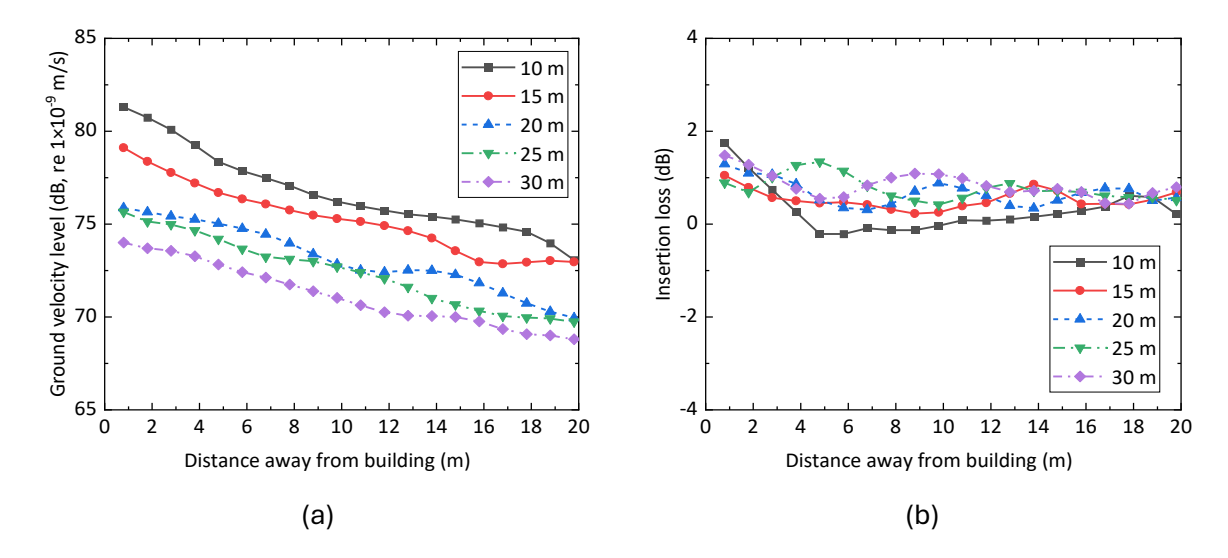


Figure 6-16 (a) Ground velocity level in the presence of the building and (b) IL results average from all receiver points at the same distance from the building, for cases with different distance between the railway and the building, train speed 100 km/h.

6.4 Summary

A comprehensive model is presented which can be used to investigate the ground vibration behind building in the transmission path when an underground railway acts as the excitation. This model is based on the MOTIV semi-analytical model and an FE piled foundation building model. The ground response behind the building is investigated under varying conditions, including different train speeds and distances between the railway and the building.

The new model encompasses the train, track, tunnel, ground, and building structures. It is designed to investigate the ground response to underground railway excitation and consider the impact of a piled foundation building on the transmission path. It is assumed that the dynamic response of the building does not affect the dynamic behaviour of the railway.

The ground vibration response and IL results are examined using this model for different train speeds. Generally, higher train speeds result in greater ground vibration. However, when analysing the IL results to assess the building's impact on ground vibration, it appears that across

Chapter 6

varying train speeds, the IL results maintain a similar level. The results suggest that the building may slightly mitigate the ground response when the train operates in a tunnel at a depth of 10 m.

The ground vibration behind the building is also investigated for tunnels situated between 10 m and 30 m away from the building. Regarding the ground response influenced by the building, when the railway is as close as 10 m, the building contributes to vibration amplification effects at some receiver distances. However, when the railway is further from the building, the building may mitigate the ground vibration especially at some specific locations.

Chapter 7 Influence of various foundation types using a hybrid model

In this chapter, a hybrid model is implemented to explore the influence of various building foundation types on the ground vibration induced by railways. Applying semi-analytical models to various types of foundations can be problematic. The use of a hybrid model can allow complex building foundations to be considered more efficiently. This approach is simpler and less computationally intensive than fully numerical models. This hybrid method integrates two components: the line source transfer mobility (LSTM) level is obtained using an FE model, which incorporates different building foundations. Tunnel structures are also included for the underground railway case. The force density level (FDL), representing the excitation, is determined using a semi-analytical model of the train, track and ground.

7.1 Line-source transfer mobility level: numerical model

Two situations have been investigated: an underground railway and a ground surface railway. For both cases, the 3D FE models were constructed in ABAQUS. For the case of the underground railway, the model encompasses the tunnel structure, the surrounding soil, and a building structure complete with foundations. A sketch of the underground railway model is depicted in Figure 7-1.

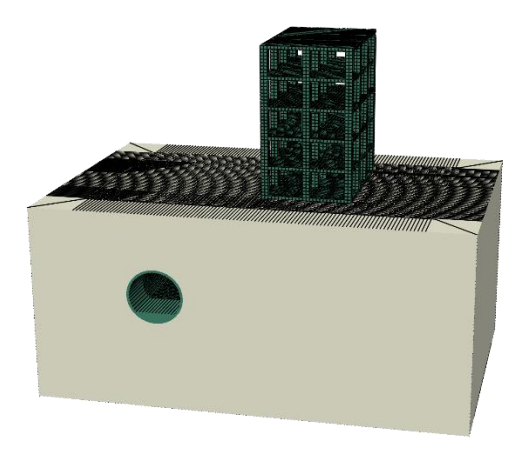


Figure 7-1 Sketch of underground railway FE model in ABAQUS.

In the surface railway model, the tunnel structure is omitted. However, the model dimensions, element sizes, and material properties remain consistent with those of the underground railway model. The sketch of surface railway model is shown in Figure 7-2.

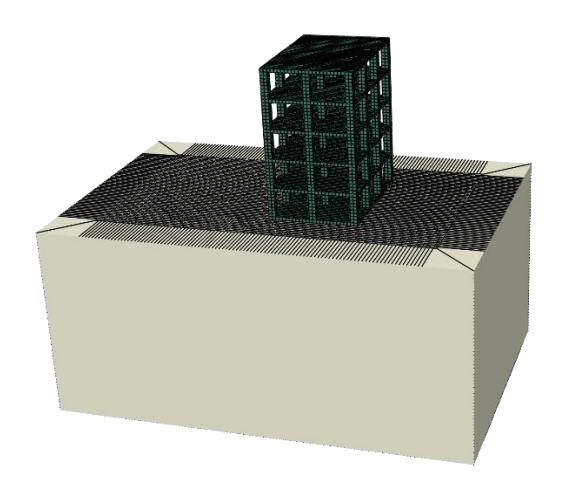


Figure 7-2 Sketch of surface railway FE model in ABAQUS.

7.1.1 Model parameters

The building structures and their foundation as well as the tunnel structure are indicated by the green elements in Figure 7-1 and Figure 7-2. They are constructed from concrete. The soil is shown in cream colour. The properties for these materials are listed in Table 7-1.

Table 7-1 Material parameters used in FE model.

Materials	Density (kg/m³)	Young's modulus (MPa)	Poisson's ratio	Loss	P-wave velocity (m/s)	S-wave velocity (m/s)
Soil	2100	350	0.333	0.1	500	250
Concrete	2500	30000	0.2	0.1	3652	2236

The dimension of the two models is $50 \text{ m} \times 34 \text{ m}$, with a depth of 24 m. For the underground railway case, the outer diameter of the tunnel is 6 m, and the thickness of the tunnel wall is 0.3 m.

Infinite elements are applied on the side boundaries of the soil, to minimise wave reflections. The bottom of the FE model is fixed. In this ABAQUS model, the element type is designated as C3D8, denoting a three-dimensional, eight-node brick element. Receiver points are designated for contour plotting within an area measuring 17.6 m by 8.4 m, located immediately behind the building structure. In both models, the building encompasses five storeys, configured in a layout of 3 by 2 bays. Each storey has a height of 3.2 m, and each bay has a span width of 4.8 m. The thickness of the floor and the side wall is 0.4 m and 0.8 m respectively, and the columns have a square cross-section defined by dimensions of 0.8 m by 0.8 m. The side walls are omitted. The

distance between the loads and the front of the building is 10 m in each case. The boundary condition situation and the position of a point load and the receiver points are shown in Figure 7-3.

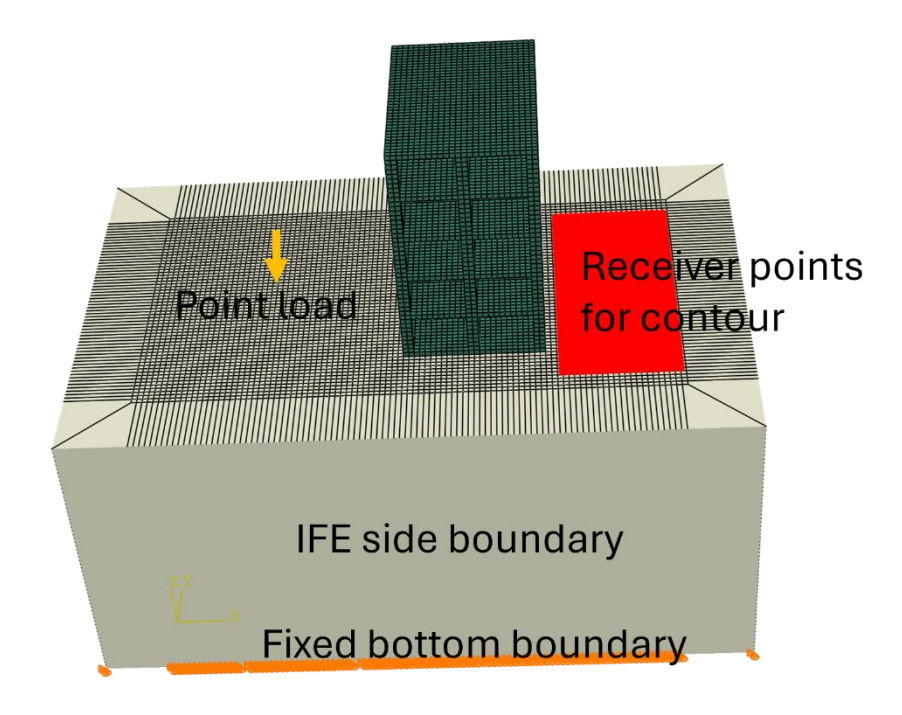


Figure 7-3 The boundary conditions, load and receiver points in the FE model for surface railway.

In the FE model, there are in total 360,000 elements for the underground railway model and 373,000 elements for the surface railway model. Usually, it is required that there are at least six elements within one wavelength, i.e.

$$\Delta l = \frac{C_s}{6f_{\text{max}}} \tag{7-1}$$

To ensure that the model can accurately calculate the propagation of vibration waves, given that the maximum frequency considered is 80 Hz and shear wave velocity is 250 m/s, the model requires that the element size be smaller than 0.5 m. The current soil model adheres to this requirement with an element size set at 0.4 m. The verification of the free-field FE model, in comparison with the DSM semi-analytical model, has been previously addressed in Section 3.3.1.

The excitation due to the train can be represented by a set of incoherent loads. As the model is symmetric, 10 incoherent loads are applied in the model on one side of the centreline, as shown in Figure 7-4. For the underground railway case, the incoherent loads are applied on the invert of the tunnel, whereas for the surface railway case, they are applied on the ground surface. The interval between these loads is 1.2 m in each case.

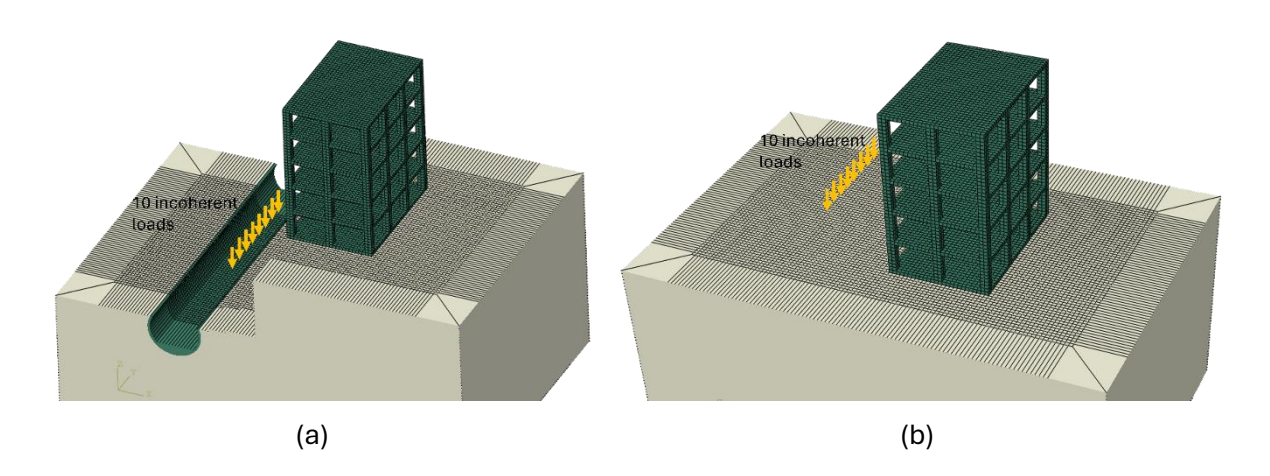


Figure 7-4 The sketch of incoherent load for (a) underground railway case and (b) surface railway case.

The LSTM can be determined by combining a set of transfer mobilities obtained for these point loads. The LSTM [115, 116] for the line load excitation at position \mathbf{X} can be calculated by

$$Y_{\mathrm{L}}(\mathbf{X}, \mathbf{x}_{\mathrm{r}}) = \sqrt{\frac{L}{n} \sum_{i=1}^{n} |Y_{i}(x_{i}, \mathbf{x}_{\mathrm{r}})|^{2}}$$
 (7-2)

where L is the length of the line load, n is the number of incoherent point loads, $Y_i(x_i, \mathbf{x_r})$ is the transfer mobility from the point load applied at position x_i to the receiver position $\mathbf{x_r}$.

Then the LSTM level in decibels (with reference value 1 m^{3/2}N⁻¹s⁻¹) is written as

$$L_{\text{LSTM}}(\mathbf{X}, \mathbf{x}_{r}) = 20 \log_{10}(Y_{L}(\mathbf{X}, \mathbf{x}_{r}))$$
(7-3)

7.1.2 Foundation types

The influence of different foundation types is investigated using the FE models. Four common foundation types are summarised in reference [232]. Two are shallow foundations, the pad/strip foundation and the raft foundation, and the others are deep foundations, the piled foundation and embedded basement foundation. They are shown schematically in Figure 7-5 [232].

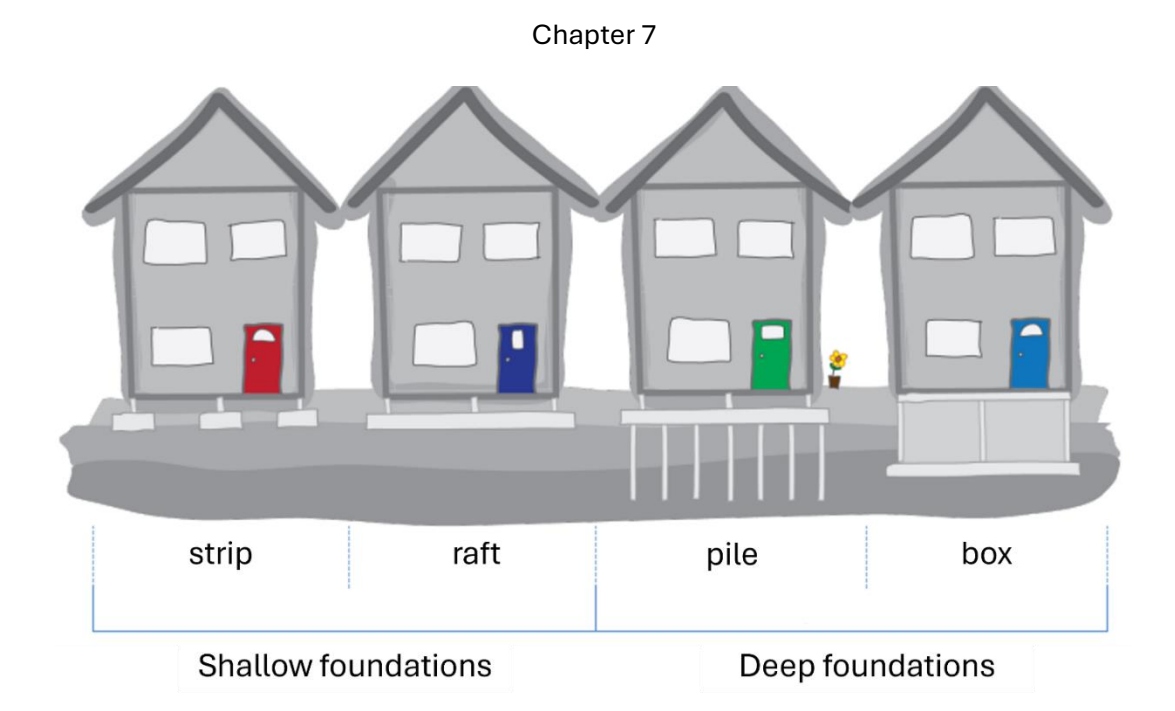


Figure 7-5 Common foundation types of buildings [232].

FE models representing these four different foundation types have been created in ABAQUS and are shown in Figure 7-6.

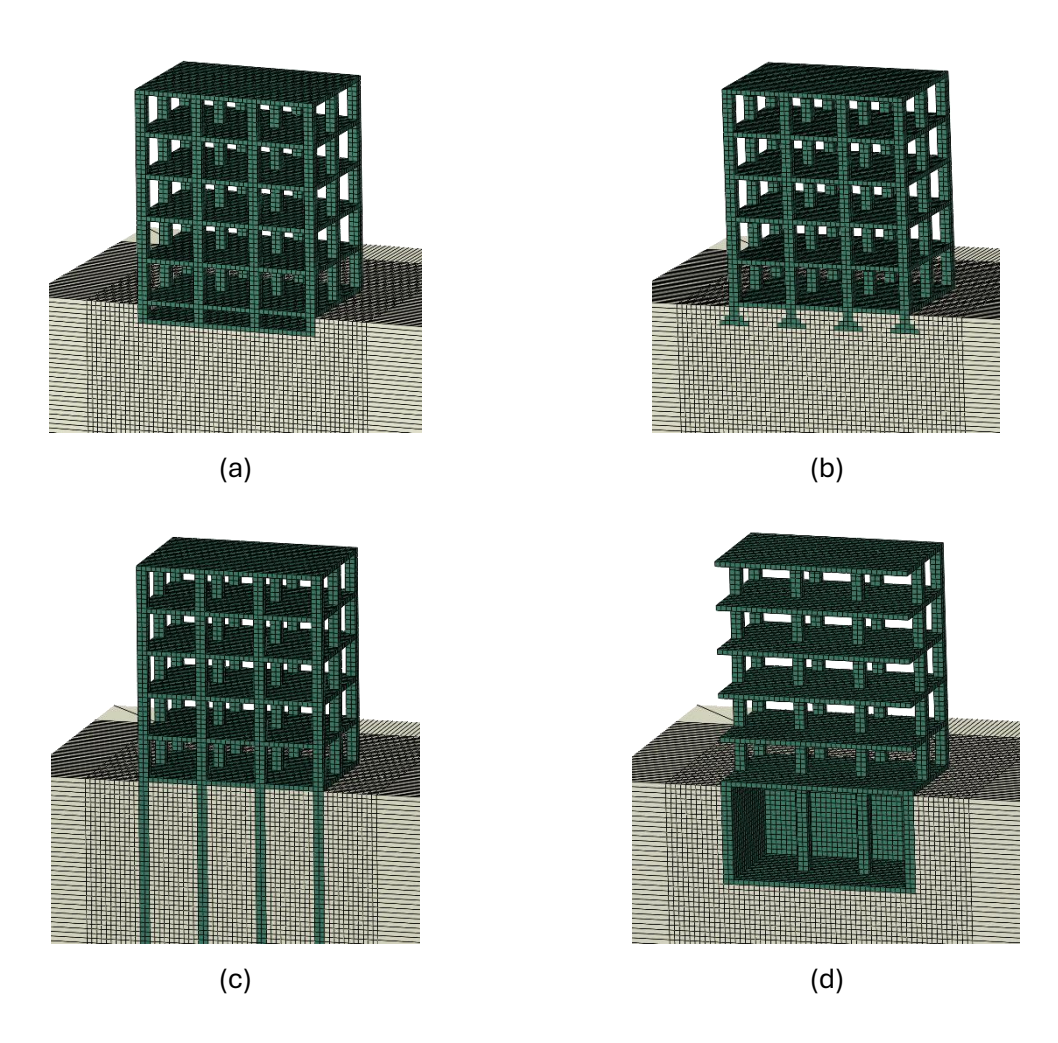


Figure 7-6 The profile of structure with different foundation types including (a) raft foundation (b) strip foundation (c) pile foundation and (d) box foundation.

Figure 7-6 (a) shows the raft foundation. There are 12 small columns with height 1.2 m. The area of the raft is 10.4×15.2=158.08 m². The thickness of the walls around the perimeter is 0.4 m. Figure 7-6 (b) shows the strip foundation. The height of each strip is 1.6 m. The strip foundation is designed with two orientations: one perpendicular to the direction of the railway's passage (in the normal direction of train's passing, denoted 'StripN' shown in Figure 7-6 (b)), and the other parallel to it (in the tangential direction to the train's passing, denoted 'StripT'). The length of the strip is commensurate with the building's dimensions. Figure 7-6 (c) shows the pile foundation. There are 12 piles in this model. The depth of each pile is 10 m. Finally, Figure 7-6 (d) shows the box foundation. The height of box is 8 m, and the thickness of the wall is 0.8 m. It contains two internal columns.

7.1.3 Results

The results from the numerical models are analysed in this section including the LSTM level and IL spectral results, the overall results across all frequency bands, and the contour plot of the overall IL. These results pertain to both the surface railway and underground railway cases, including the five foundation types.

The average LSTM results from all the receiver points over ± 9 m width at distance of 5.6 m away from the rear of the building (26 m away from the railway track) are shown in Figure 7-7. It includes the LSTM level results for both the surface case and the underground case. The calculation is based on Eq. (3-36) and Eq. (3-37). In the surface railway case, the free-field response is larger than in the presence of the building when the frequency ranges from 20 Hz to 80 Hz. The box foundation case shows the lowest LSTM level results. For the underground railway model, the trend across all foundation cases is similar to that of the surface railway case. However, the values in the underground railway cases are generally lower than those in the surface railway cases due to the influence of the tunnel structure. The differences between the free-field response and the foundation cases are much smaller in the underground railway cases.

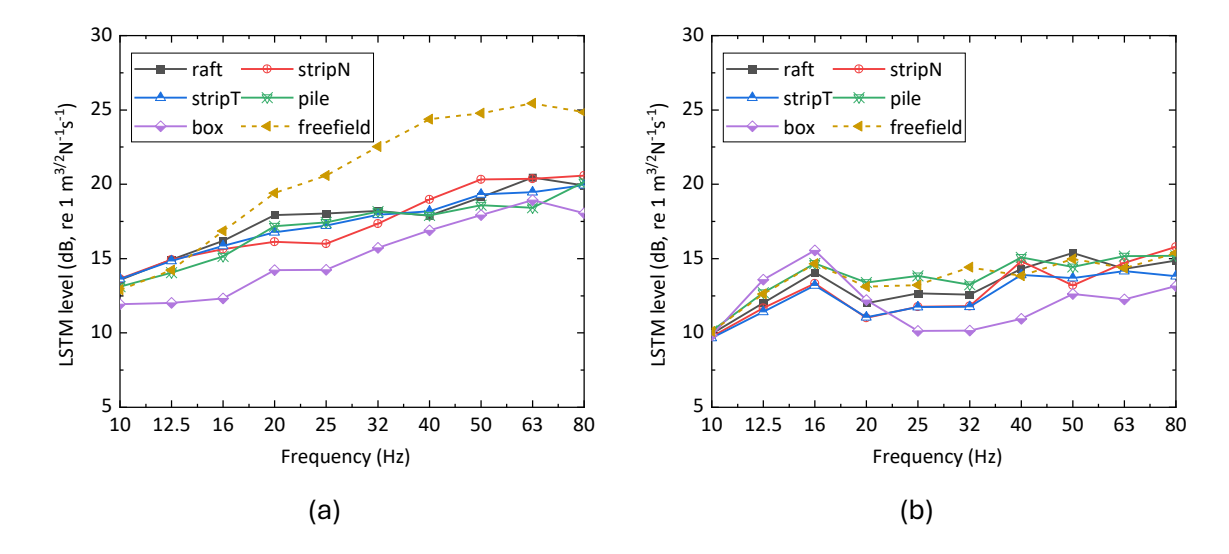


Figure 7-7 The average LSTM level from all the receivers 5.6 m away from the rear of the building excited by the (a) surface railway and (b) underground railway.

An overall value of the LSTM level is calculated from the LSTM in one-third octave bands between 10 Hz and 80 Hz. Each one-third octave band includes three frequency samples. The LSTM can be expressed as

$$L_{\text{LSTM,overall}}(\mathbf{X}, \mathbf{x}_{r}) = 10 \log_{10} \sum_{i=1}^{n} 10^{\frac{1}{10} (L_{\text{LSTM},i}(\mathbf{X}, \mathbf{x}_{r}))}$$
 (7-4)

where $L_{\mathrm{LSTM},i}(\mathbf{X},\mathbf{x_r})$ is the LSTM level in one-third octave bands between 10 Hz and 80 Hz.

The overall LSTM levels of the different foundation types are shown in Figure 7-8 for receiver points positioned in a line behind the centre of the building. When the excitation is at the ground surface, the LSTM value is larger than in the case where the excitation is at the underground railway as seen in Figure 7-7. The box foundation produces the lowest LSTM level values. The strip foundation building, especially when the strip orientation is normal to the train's moving direction, yields the highest LSTM values of the building foundation.

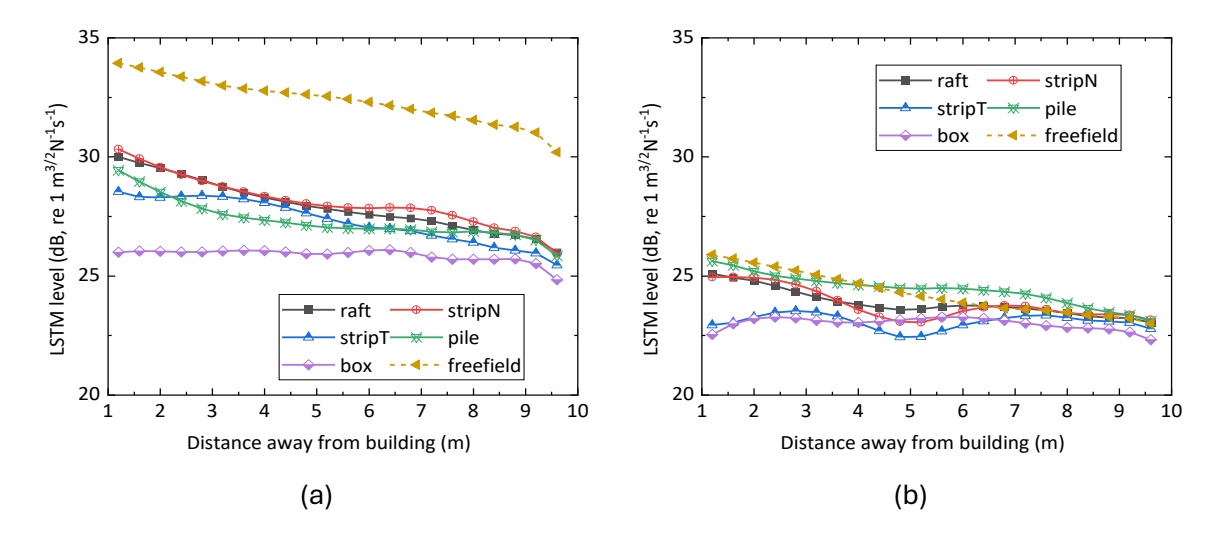


Figure 7-8 The overall LSTM level on the centreline on the ground for different foundation types when the excitation is (a) surface railway and (b) underground railway.

The overall IL results on the centreline derived from these results are shown in Figure 7-9. For all surface railway cases, the IL values are positive at all distances considered. The box foundation case yields the highest IL value, while the strip foundation oriented perpendicular to the train's direction shows the lowest IL value. The IL value from the pile foundation is larger than that from the strip foundation oriented parallel to the train's direction at distances between 3 m and 7 m away from the building. For all underground railway cases, the IL values are smaller than those from the surface railway cases. The pile foundation case yields the lowest IL value in this case. Additionally, the IL value for the box foundation is lower than that of the strip foundation oriented perpendicular to the train's direction at distances between 5 m and 7 m away from the building. For the strip foundation case oriented parallel to the train's direction, the IL value increases with distance up to 5 m away from the building, after which it begins to decrease.

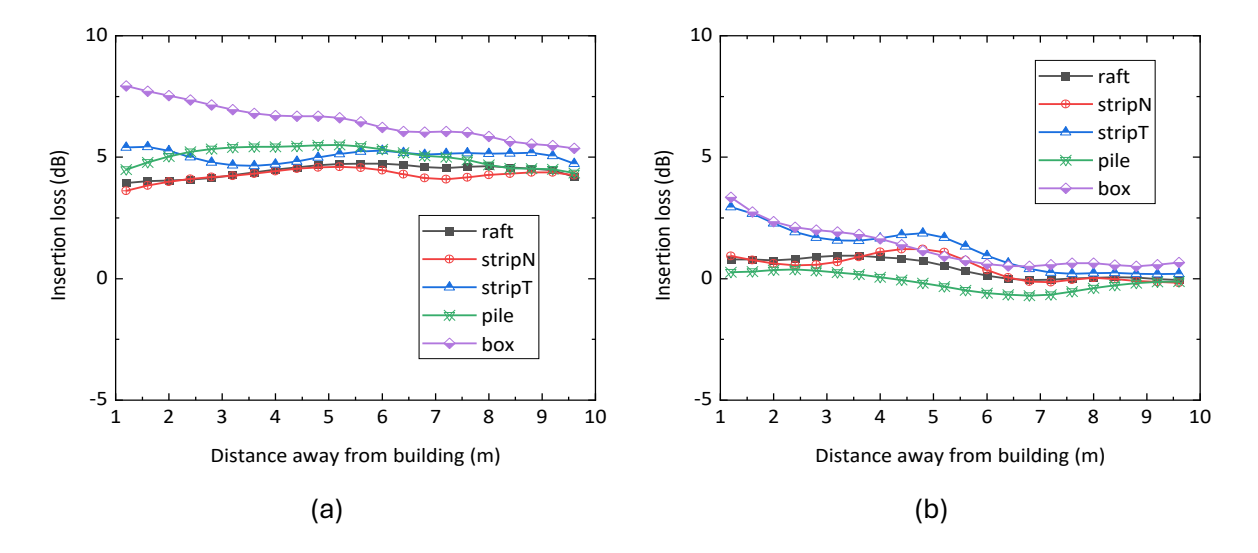


Figure 7-9 The overall IL on the centreline on the ground for different foundation types when the excitation is (a) surface railway and (b) underground railway.

The contour plots of the overall IL values on the ground surface for the five different foundation types are shown in Figure 7-10 for the cases in which the incoherent train loads are applied on the surface. The location of the building is also indicated on these contour plots. It can be observed that, the IL value is positive in all cases. The IL value for the box foundation is significantly larger than in the other cases. Generally, the IL value on the ground closer to the building is higher than that further from the building.

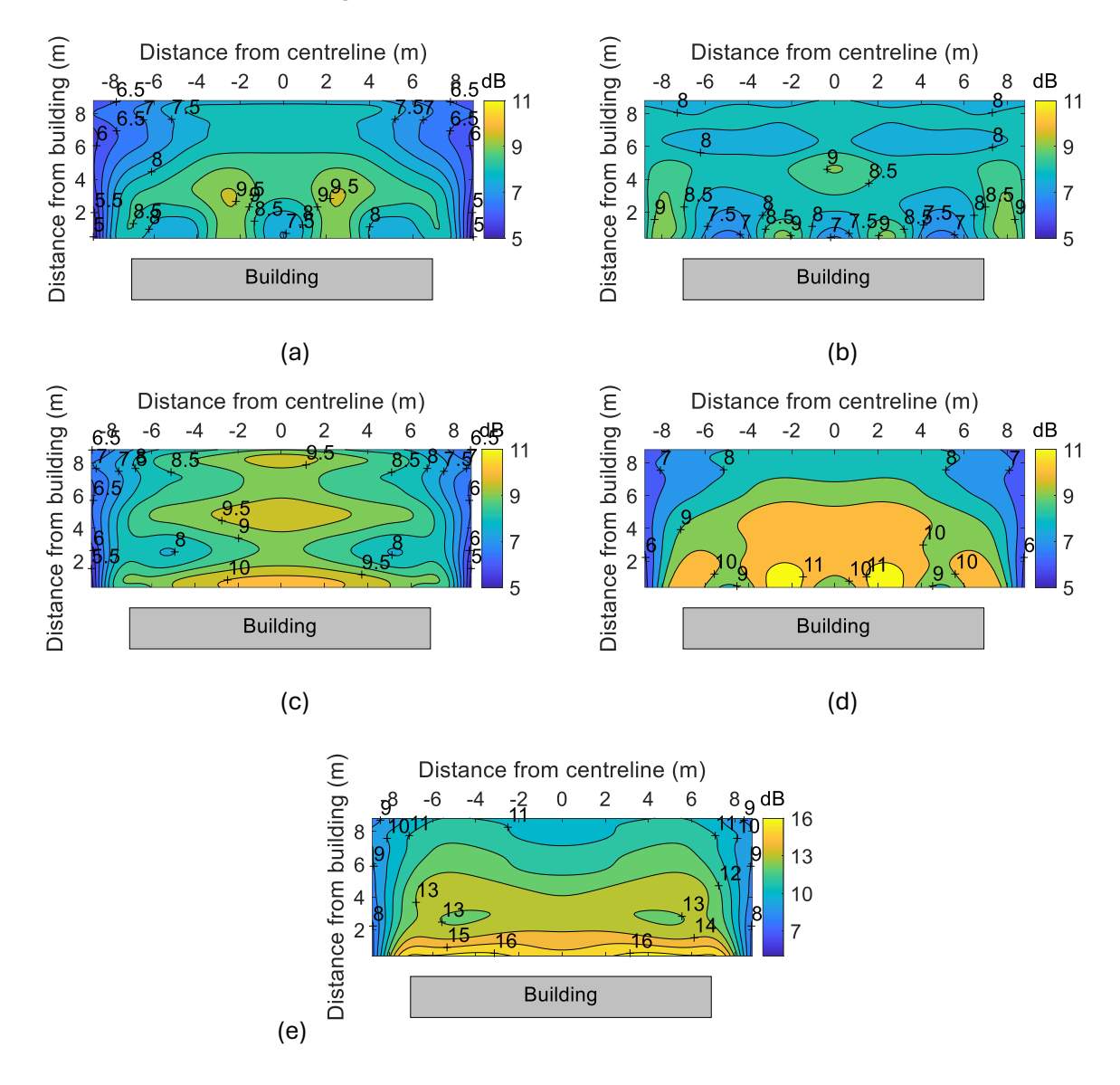


Figure 7-10 The contour plots of IL on the ground behind different types of building in the surface railway case (a) raft foundation (b) strip foundation in normal direction (c) strip foundation in tangential direction (d) pile foundation and (e) box foundation.

The corresponding contour plots of the overall IL for the incoherent train load applied in the embedded tunnel structure are shown in Figure 7-11. It can be observed that the IL values for the underground railway cases are significantly lower than those for the surface railway cases. In all underground railway cases, there are zones where the IL values are negative.

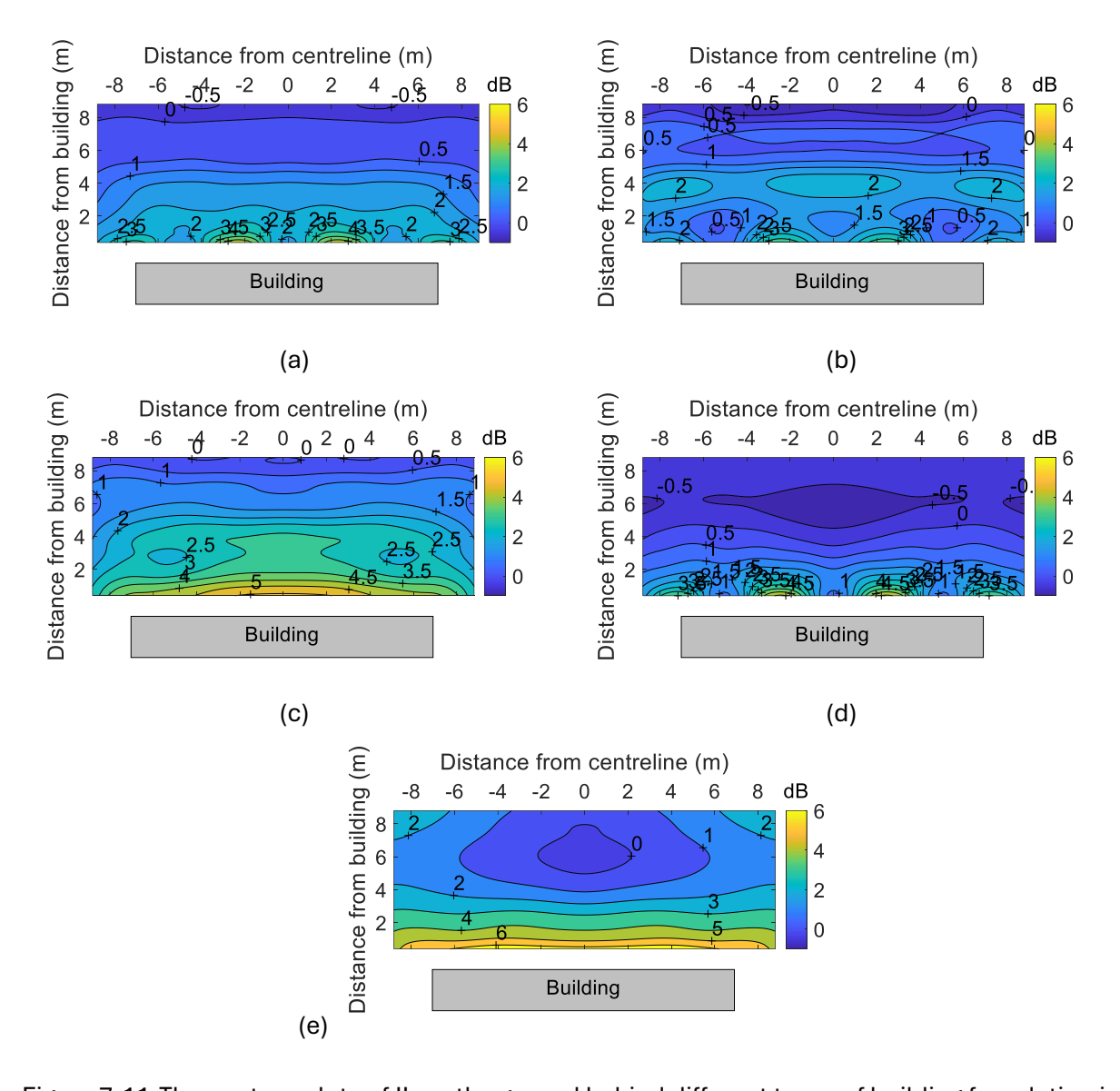


Figure 7-11 The contour plots of IL on the ground behind different types of building foundation in the underground railway case (a) raft foundation (b) strip foundation in normal direction (c) strip foundation in tangential direction (d) pile foundation and (e) box foundation.

The overall LSTM level averaged over ±9 m width is plotted against distance in Figure 7-12 for excitation from surface railway and underground railway. The calculation method is based on Eqs. (3-39) to (3-41). In both cases, as the distance from the building increases, the LSTM level decreases. For the surface railway, similar to the results on the centreline behind the building, the free-field LSTM is higher than in the presence of the building, with the box foundation yielding the lowest LSTM results. The LSTM levels for the other cases are similar to each other. For the underground railway cases, the LSTM levels are generally lower than those from the surface railway cases. Similar to the results on the centreline, the free-field LSTM is the highest when the distance from the building is less than 5 m. Moreover, the box foundation case produces the lowest LSTM levels for all distance, which is a little bit different with the results on the centreline.

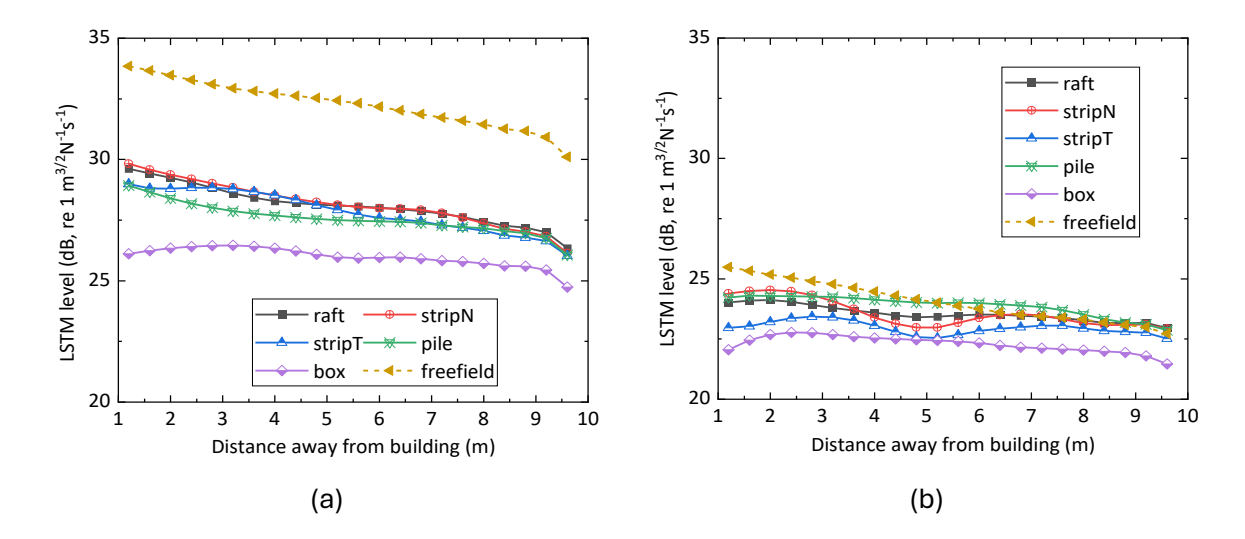


Figure 7-12 The overall LSTM level averaged over ±9 m width plotted against distance when the excitation is from (a) surface railway and (b) underground railway.

The overall IL averaged over ±9 m width is plotted in Figure 7-13 against distance from the surface railway and underground railway. The calculations are based on Eqs. (3-39) to (3-41). In summary, as noted in Figure 7-9, the IL results from the surface railway case are generally larger than those from the underground railway case. The box foundation consistently produces the highest IL value, regardless of whether the excitation is from the incoherent load representing surface or underground railway. These trends are similar to the results on the centreline behind the building. For the underground railway case, the IL for the pile foundation is the lowest between 3.2 m and 8 m behind the rear of the building (23.6 m and 28.4 m from the railway track, respectively), while in the surface railway case, it is the second highest. This trend also slightly differs from the IL on the centreline in underground railway, as shown in Figure 7-9, where the pile foundation displays the lowest IL at distances ranging from 1 m to 9 m.

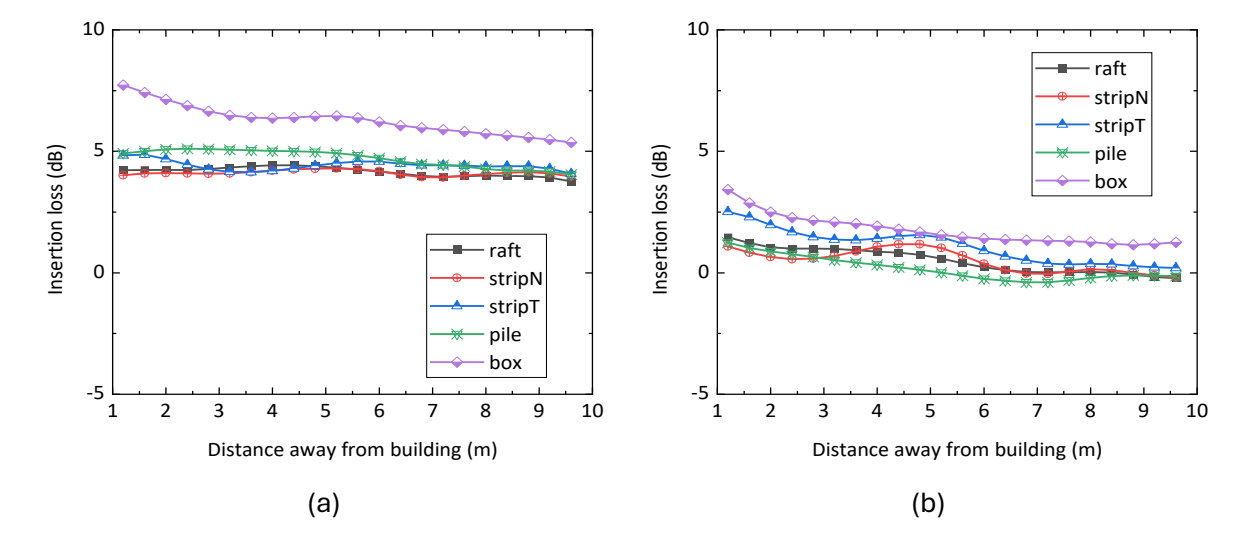


Figure 7-13 The overall IL averaged over ±9 m width plotted against distance when the excitation is from (a) surface railway and (b) underground railway.

7.2 Force density level: semi-analytical model

The excitation in the form of the force density level is calculated using the train-track-tunnel-soil semi-analytical model MOTIV [7, 233].

For both the underground railway case and the surface railway case, the FDL is derived from the ground response during a train pass-by and the LSTM calculated from the semi-analytical model. For the underground railway case, the FDL should be evaluated for excitation on the slab as the FE model does not contain the track apart from the slab. For the surface railway case, the excitation should be represented by the FDL on the ground surface. This affects the position of the force in the corresponding LSTM calculation.

The FDLs from both models are calculated by

$$L_{\rm FD}(\mathbf{X}) = L_{\rm G}(x_{\rm gr}) - L_{\rm LSTM}(\mathbf{X}, x_{\rm gr})$$
(7-5)

where $L_{\rm G}(x_{
m gr})$ is the ground response velocity level at the specific receiver position $x_{
m gr}$ (selected from receiver position vector ${\bf x}_{
m r}$) during a train pass-by calculated from the semi-analytical model when the excitation is the underground railway or surface railway. $L_{\rm LSTM}({\bf X},x_{
m gr})$ is the LSTM level when the excitation position is ${\bf X}$. For the surface railway case, the incoherent line load is applied on the ground surface, while for the underground railway case, the incoherent load is applied on the slab. In these models, the ground response receiver point $x_{
m gr}$ is a horizontal distance of 8 m away from the railway location.

The underground railway model in MOTIV includes several sub-models, including those for the train, track, tunnel, and soil. The model used for the surface ground railway case consists of sub-models representing the train, track, and soil components. The surface railway includes a moving load [229] whereas the underground case uses a fixed train load position. Consistent parameters and properties for the train, track, and soil are used for both the underground and surface railway cases. The parameters of the train (a typical InterCity train) is the same as introduced in Chapter 6 are already summarised in Table 6-1 [234]. The train speed is 60 km/h. The parameters of the track are summarised in Table 7-2 [234]. The track type is a slab track. For the underground railway case, there is a tunnel located in the surrounding soil. The tunnel structure parameters are summarised in Table 6-3. The surrounding soil parameters in both cases are summarised in Table 6-4.

Table 7-2 Track model parameters.

	Property	Value	Unit
Rail UIC 60	Bending stiffness	6.42×10 ⁶	Nm²
	Mass per unit length	60	kg/m
	Damping loss factor	0.01	-
Rail pad	Stiffness	1.20×10 ⁸	N/m
	Damping loss factor	0.15	-
	Fastener spacing	0.65	m
Slab	Width (at base)	3.4	m
	Height	0.54	m
	Mass per unit length	3720	kg/m
	Bending stiffness	2.33×10 ⁸	Nm²
	Damping loss factor	0.015	-
	Torsional stiffness	3.39×10 ⁸	Nm²
	Polar moment of inertia	3086	kgm

The FDLs for the underground railway case and the surface railway case are shown in Figure 7-14. There is a significant peak at 50 Hz for both cases which corresponds to the P2 resonance [1]. The FDL of the underground railway case is larger than that from ground surface case.

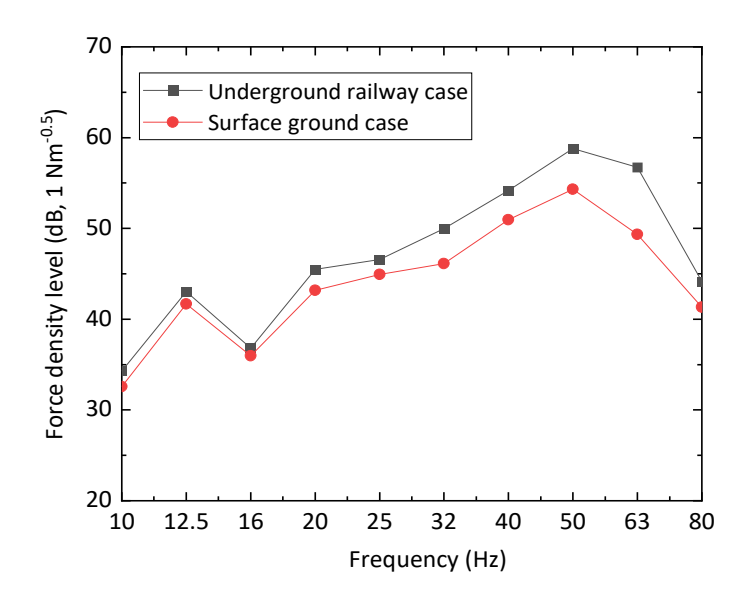


Figure 7-14 Force density levels.

7.3 Ground response under different foundation types

Combining the FE model of the LSTM with the FDL, the ground response level $L_{\rm G}$ at a receiver point ${\bf x}_r$ behind the building is calculated by

$$L_{G}(\mathbf{x}_{r}) = L_{FD}(\mathbf{X}) + L_{LSTM}(\mathbf{X}, \mathbf{x}_{r})$$
(7-6)

where $L_{\rm FD}({\bf X})$ is the FDL calculated using the semi-analytical model, $L_{\rm LSTM}({\bf X},{\bf x}_{\rm r})$ is the LSTM level calculated using FEM with different foundation types. Both of them are calculated in one-third octave bands. Thus, the ground velocity response level $L_{\rm G}$ is also in one-third octave bands. Each one-third octave band includes three frequency samples. The overall ground velocity response levels can be calculated by

$$L_{\text{G,overall}}(\mathbf{x}_{\text{r}}) = 10 \log_{10} \left(\sum_{i=1}^{n} 10^{\frac{L_{\text{G,}i}(\mathbf{x}_{\text{r}})}{10}} \right)$$
 (7-7)

where $L_{G,i}(\mathbf{x_r})$ means the ground response level in the *i*-th one-third octave band. The frequency range considered is from 10 Hz to 80 Hz.

An overall value of IL at receiver point \mathbf{x}_r can be calculated by

$$IL(\mathbf{x}_r) = L_{G \text{ overall}}^{\text{free}}(\mathbf{x}_r) - L_{G \text{ overall}}^{\text{foundation}}(\mathbf{x}_r)$$
 (7-8)

where $L_{\rm G, overall}^{\rm free}({\bf x_r})$ means the overall ground response level from the free-field model, and $L_{\rm G, overall}^{\rm foundation}({\bf x_r})$ means the overall ground response level for the building with different foundation types.

7.3.1 Surface railway case

The results for the surface railway case were obtained using the FDL and LSTM models specific to surface railways. The ground velocity levels from the five types of foundation, introduced in Section 7.1.2, are investigated.

7.3.1.1 The spectral results at a specific receiver point

The ground velocity level and IL spectra for different types of foundation are shown in Figure 7-15 for a receiver point located 5.6 m away from the rear of the building (26 m away from the railway track), on the centreline of the building model. It is observed that the free-field case exhibits the largest ground response. The different types of building foundations exhibit similar ground responses. Focusing on the IL spectra, a trend emerges in which the IL generally increases with frequency. At frequencies less than 40 Hz, the box foundation consistently gives the highest IL values. However, the building with pile foundation can achieve the highest IL values, approximately 10 dB, at 63 Hz. In contrast, buildings with raft foundations exhibit the lowest IL values in the frequency bands below 32 Hz, but they have a peak at 40 Hz.

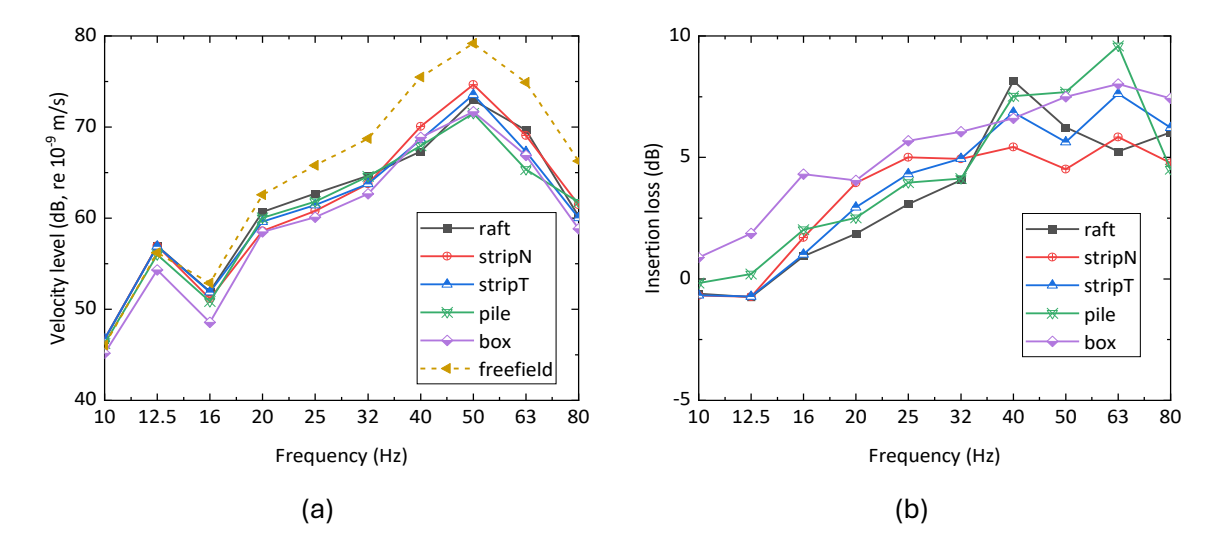


Figure 7-15 The results on the centreline at 5.6 m away from the building (a) the ground velocity response level and (b) IL value.

The IL results from all the receiver points averaged over ± 9 m width at the same distance away from the track calculated according to Eq. (3-36) to Eq. (3-38) are shown in Figure 7-16. The IL is positive for all cases above 16 Hz, indicating that regardless of the foundation type, the building can mitigate ground vibration behind it. It can be observed that the box foundation model typically achieves the largest IL values, especially at frequencies below 50 Hz. The raft foundation case exhibits the lowest IL values at frequencies below 32 Hz. The stripN case shows moderate IL values at frequencies below 32 Hz, but it gives the lowest values when the frequency at 40 Hz and above. The pile and stripT cases display similar trends at lower frequencies. Notably, there is a

peak for the pile foundation case at 63 Hz. These results are generally consistent with the results in Figure 7-15.

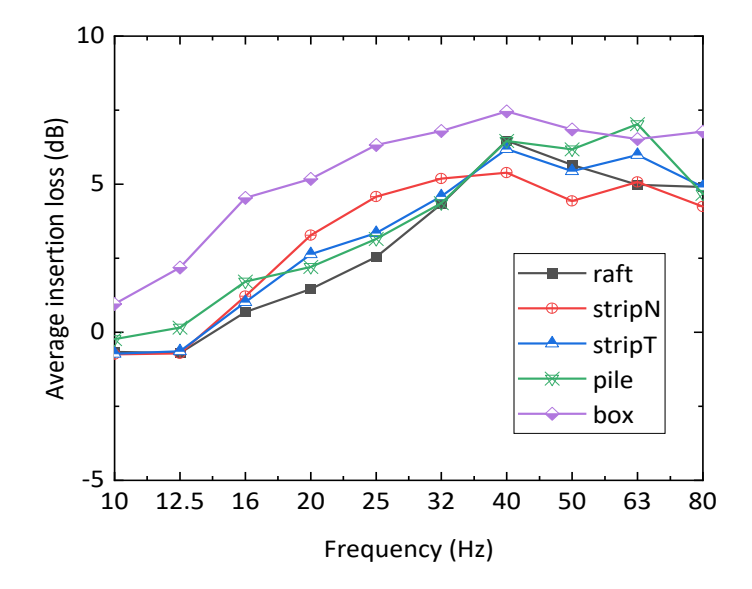


Figure 7-16 The average insertion loss results from all receivers 5.6 m away from the building excited by the surface railway.

In conclusion, when a building is situated in the transmission path between the railway and ground receiver points, the ground vibration is typically mitigated. The box foundation generally provides the largest ground vibration mitigation across all frequency bands. The raft foundation offers only slight vibration mitigation compared with other foundation types, particularly at frequencies below 32 Hz. For buildings with strip foundations, the effectiveness in mitigating the ground vibration depends on their orientation. When the strip is oriented normal to the train's passing direction, it more effectively mitigates ground vibration behind the building than when the strip foundation is oriented tangential to the train's passing direction, particularly at frequencies below 32 Hz.

7.3.1.2 The results at a specific frequency (50 Hz)

The results at 50 Hz for all receiver points positioned on the centreline behind the building are presented as a specific case. The reason for choosing 50 Hz as the example is that the results indicate a peak in the vibration level at this frequency (the P2 resonance). Figure 7-17 presents the results at 50 Hz at various distances from the railway. The ground response is depicted for different foundation types, as well as the free field. All receivers are positioned on the centreline, at distances ranging from 1 m to 10 m away from the rear of the building.

It can be observed that, the ground response on the centreline behind the building at 50 Hz is always lower than the free-field ground response. The stripN case exhibits the second highest ground response, while the box foundation case demonstrates the lowest, particularly near the

building. The IL values indicate the ground vibration mitigation effects at 50 Hz. The stripN foundation perpendicular to the train's direction of travel exhibits the least ground vibration mitigation. In contrast, the two deep foundations, the box foundation and the pile foundation, show the largest mitigation effects when the distance from the building is less than 6 m. Beyond 7 m, the raft and stripT foundation types display higher IL values.

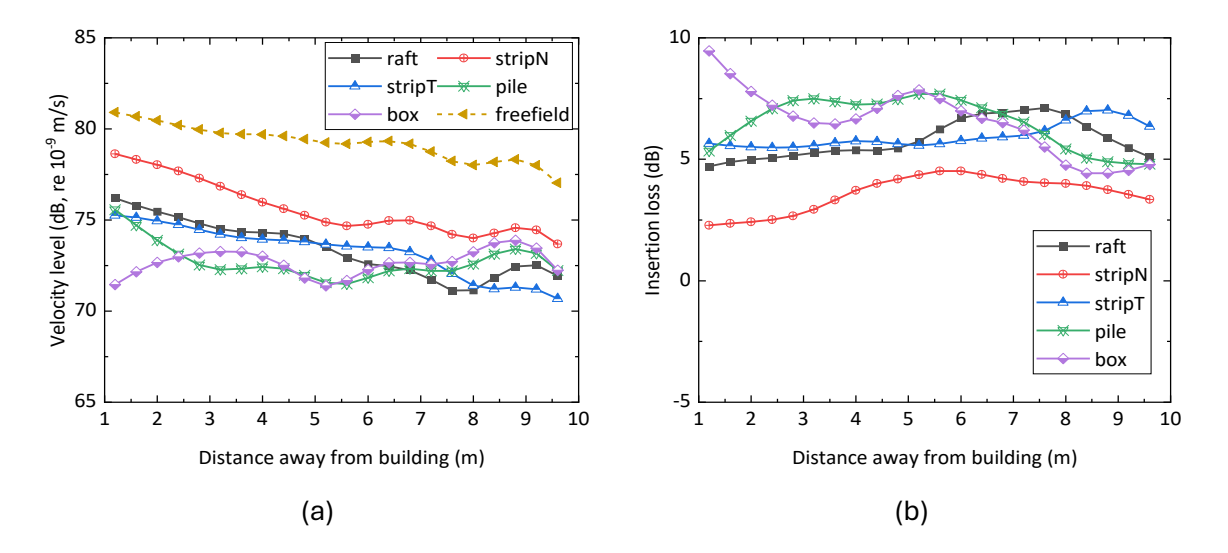


Figure 7-17 The results on the centreline behind the building at 50 Hz: (a) the ground velocity response level and (b) IL value.

The average insertion loss from all the receiver points located at the same distance away from the railway is shown in Figure 7-18. The results, which focus again on 50 Hz, reveal that closer to the building (as well as between 25 m and 28 m from the track), the box foundation exhibits the highest IL values. The pile foundation also gives higher IL levels than strip and raft foundation when the distance behind the building is less than 7 m. Conversely, the stripN foundation consistently shows the lowest average IL values across all distances. The raft foundation exhibits IL values similar to those of the stripT foundation case.

Chapter 7

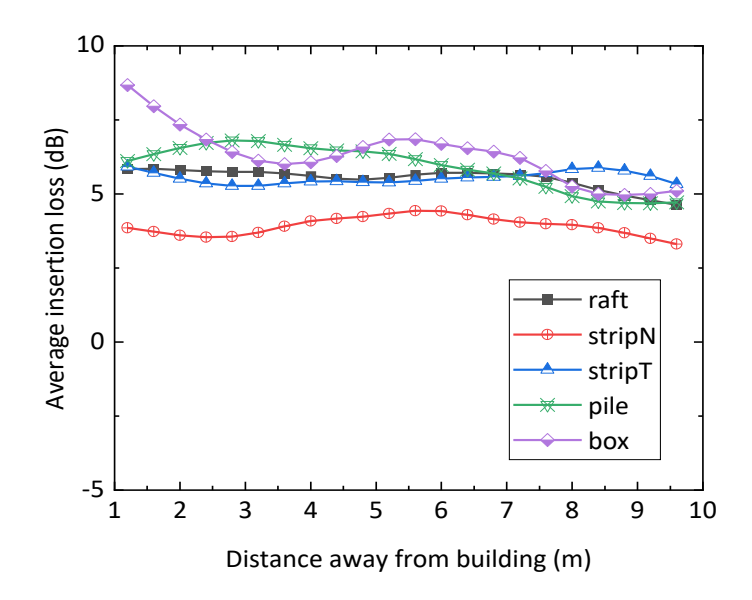


Figure 7-18 The average insertion loss from all receivers at same distance away from the surface railway at 50 Hz.

Overall, at 50 Hz, different foundation types may provide different ground vibration mitigation effects in different zones. The deep foundations, i.e. box foundation and pile foundation, provide the largest ground vibration mitigation particularly close to the building. For strip foundations, the orientation of the strip significantly influences the ground vibration mitigation effectiveness: when the orientation is normal to the train's moving direction, the mitigation effects are lower than when the orientation is parallel to the train's passing direction.

7.3.1.3 Results based on overall levels

Based on the overall velocity level across all frequencies, the ground response and IL for all the building foundation cases are plotted in Figure 7-19 for receiver points on the centreline behind the building. It can be observed that all foundation types effectively mitigate ground vibration, as evidenced by positive IL values at all distances. The box foundation, in particular, provides the largest ground vibration mitigation effects. Especially close to the building, the IL value from the box foundation is significantly higher than those from other foundation types. The stripT foundation ranks second in terms of IL values in the near field; however, as the distance increases, the pile foundation emerges as the second highest. The stripN and raft foundations, both shallow types, exhibit the lowest ground vibration mitigation effects, with the stripN case showing the smallest effects.

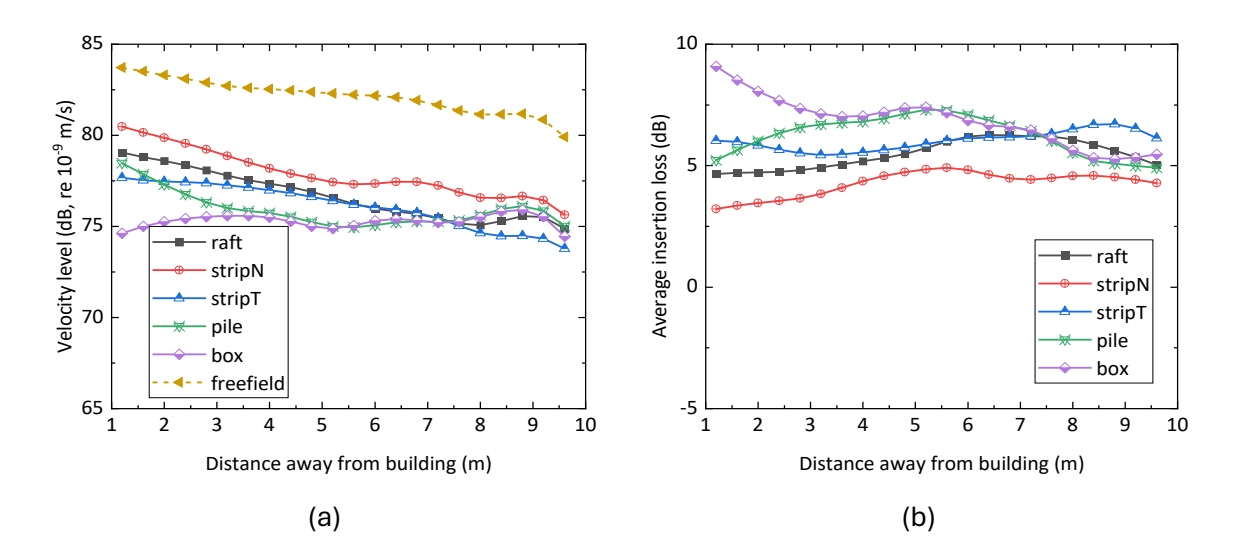


Figure 7-19 The overall results at different distances away from surface railway on the centreline.

(a) The overall ground velocity response level and (b) corresponding IL value.

The overall IL results at each receiver point over a region behind the building are plotted as a contour plot on the ground surface in Figure 7-20 corresponding to various types of foundation.

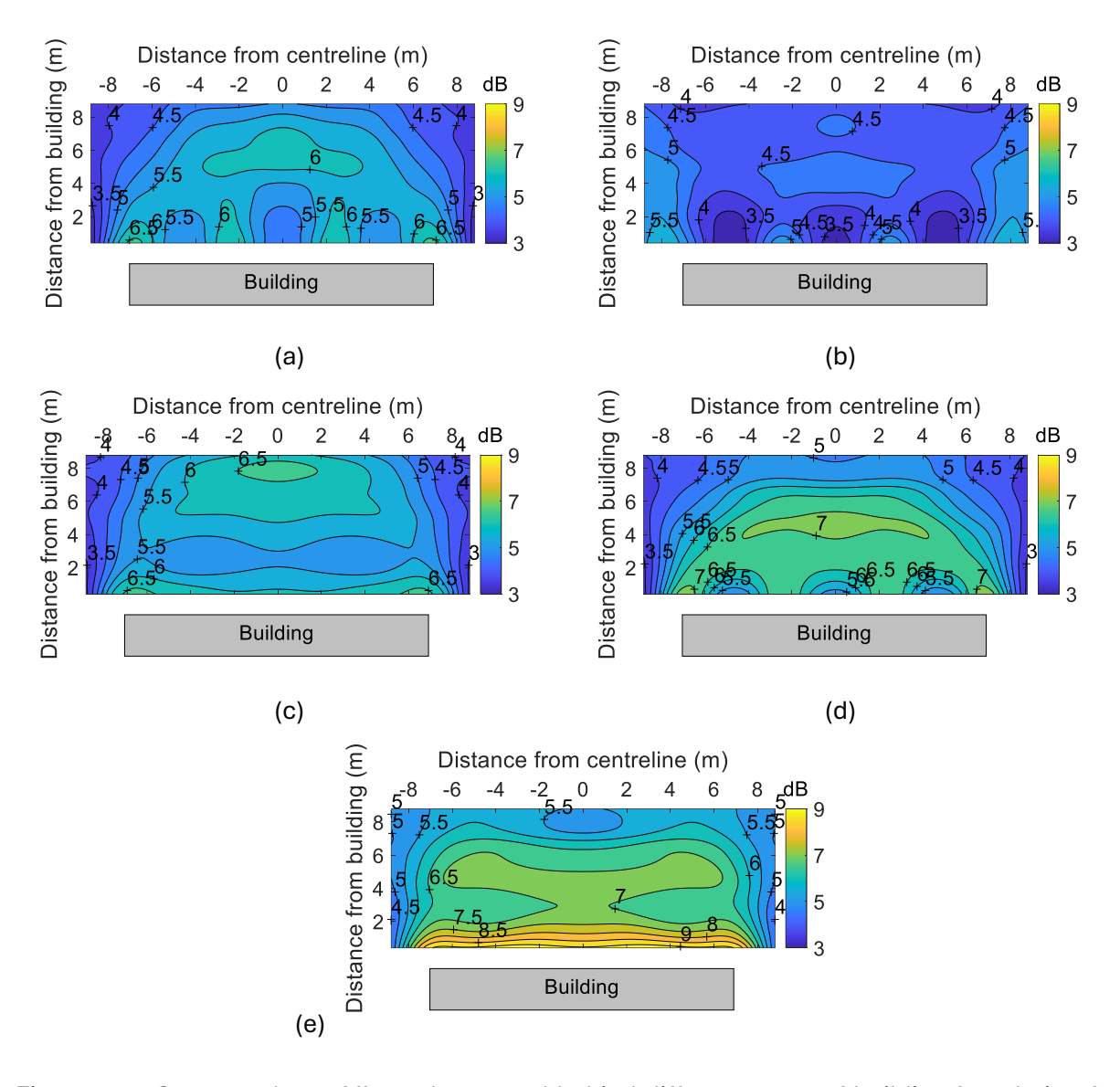


Figure 7-20 Contour plots of IL on the ground behind different types of building foundation for surface railway excitation: (a) raft foundation (b) strip foundation in normal direction (c) strip foundation in tangential direction (d) pile foundation and (e) box foundation.

For the shallow foundations raft and strip (normal direction), as well as the pile foundation case, higher values of IL are observed in proximity to the building. This is particularly evident near the columns of the building, where the IL values surpass those of the surrounding regions. As the distance between the receiver point and the building increases, there is a gradual decrease in the IL values. Nonetheless, certain specific areas exhibit local maxima. However, in the case involving the building with box foundation, a larger area of increased IL is discernible in the vicinity of the building, along with a pronounced trend of reducing IL at greater distances from the building. When the strip foundation is oriented tangentially to the train's movement, an isolated zone of increased IL is observed. This zone is located between 4 m to 8 m away from the building.

7.3.1.4 Overall results averaged over receiver points

The overall ground velocity response results are averaged over ±9 m width for each specific distance from the rear of the building, covering a range from 1 m to 10 m. The ground velocity levels for the five different foundation cases, along with the free-field response, are shown in Figure 7-21 (a). It can be observed that for all the cases, the ground response is lower than the free-field response level. As the distance from the building increases, the ground response in the free field decreases. A similar trend is observed for all foundation types. Of the different foundation types, the box foundation typically exhibits the lowest response, while the stripN case generally gives the highest.

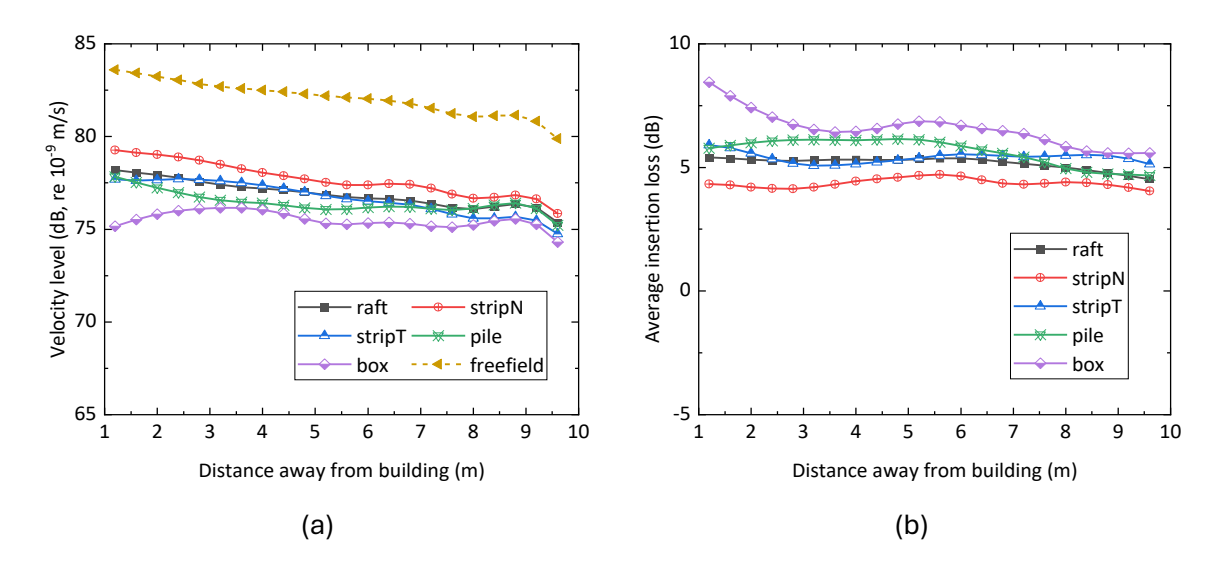


Figure 7-21 The (a) ground velocity level and (b) average over ±9 m width plotted against distance (surface railway case).

Figure 7-21 (b) shows the IL values calculated from the average velocity levels at positions equidistant from the building structure, which indicate how the average IL varies with changes in distance from the building. It can be observed that the box foundation consistently gives the largest values compared with other foundation type cases, irrespective of the distance from the building. Notably, the IL values from the box foundation are higher close to the building. When the strip foundation is oriented perpendicular to the train's direction of passing, it exhibits the lowest IL value among all the cases. Overall, the results indicate that for shallow foundations, i.e. raft and strip foundations, the average IL values are lower than those observed for deep foundations, i.e., pile and box foundations. In the case of strip foundations, when the orientation of the strip is normal to the train's passage (stripN), the IL is lower than when it is aligned tangentially to the direction of the train's movement (stripT). At 3-5 m away from the building, the IL values for the stripT case are as low as those from the raft case. However, in the far field, specifically at distances greater than 5.6 m, the IL value for the stripT case is comparable to those for the pile case. Typically, a declining trend in IL value is observed as the distance from the building

increases. However, some isolated areas exhibit a peak in the IL, which means there are significant localised ground vibration mitigation effects. Overall, for the surface railway case, the deep foundations could provide more vibration mitigation effects, especially in the proximity of the building.

7.3.2 Underground railway case

The results for the underground railway case are obtained by applying the underground railway FDL and the LSTM determined using an FE model that contains a tunnel structure. Similar to the surface railway case, five foundation types are investigated for the underground railway cases. The dimensions of the building and foundations are identical to those in the surface railway cases.

7.3.2.1 The spectral results at specific receiver point (5.6 m)

The ground velocity level and IL value for different types of foundation are shown in Figure 7-22, for a specific receiver point: at 5.6 m away from the building and located on the centreline behind the building. For all building foundation cases, as well as the free field velocity, the response increases with frequency up to a peak at 50 Hz. The box foundation gives the lowest value of IL at frequencies below 20 Hz, while the pile foundation shows the lowest IL value above 20 Hz. The strip foundation can deliver consistent ground vibration mitigation regardless of the orientation, as indicated by similar IL values across lower frequency bands. Overall, however, there is no clear trend in the magnitude relationships among the various foundation types. Compared with the surface railway case the IL is much smaller for the tunnel case and may be negative, with values between -2 dB and 3 dB

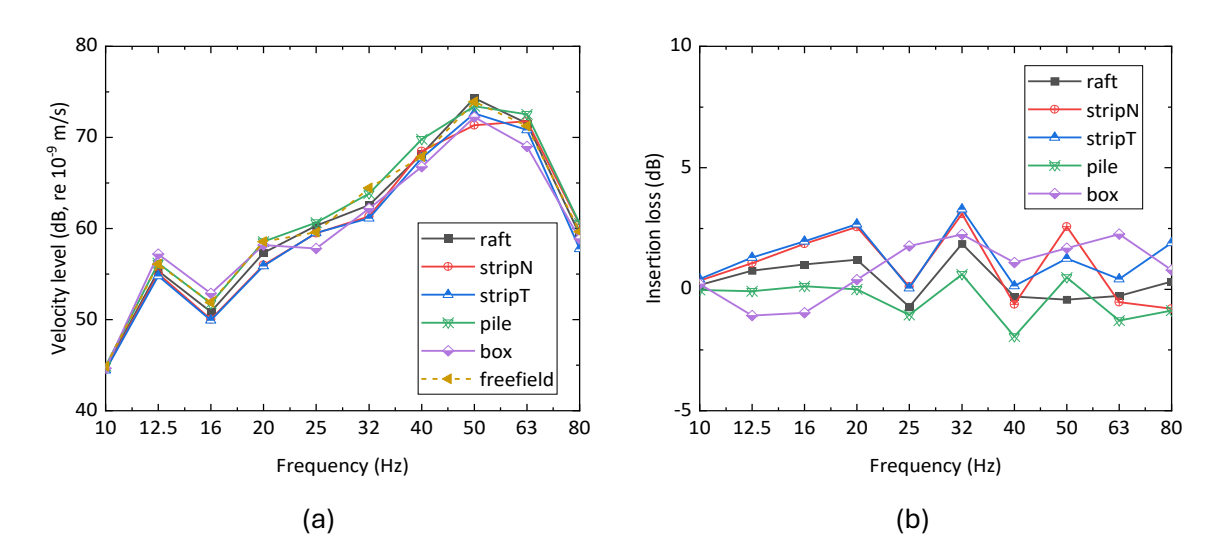


Figure 7-22 The results on the centreline at 5.6 m away from the building excited by the underground railway (a) the ground velocity response level and (b) IL value.

Figure 7-23 shows the IL results obtained from the average responses of all the receiver points located 5.6 m away from the building. It can be observed that the box foundation exhibits the lowest IL values at lower frequencies, but at frequencies over 25 Hz it displays the highest values compared to other different types of foundation This trend is clearer than at the single point shown in Figure 7-22. This suggests that the box foundation primarily influences ground vibration in the higher frequency band, notably above 25 Hz. The pile foundation exhibits the lowest IL value, differing from the surface railway case. At certain frequencies such as 40 Hz, the IL value is negative, indicating that the response may be amplified due to the presence of the pile foundation building. At 10–32 Hz, the strip foundation can deliver similar ground vibration mitigation effects regardless of the orientation of the strip. The raft foundation exhibits moderate effectiveness in ground vibration mitigation.

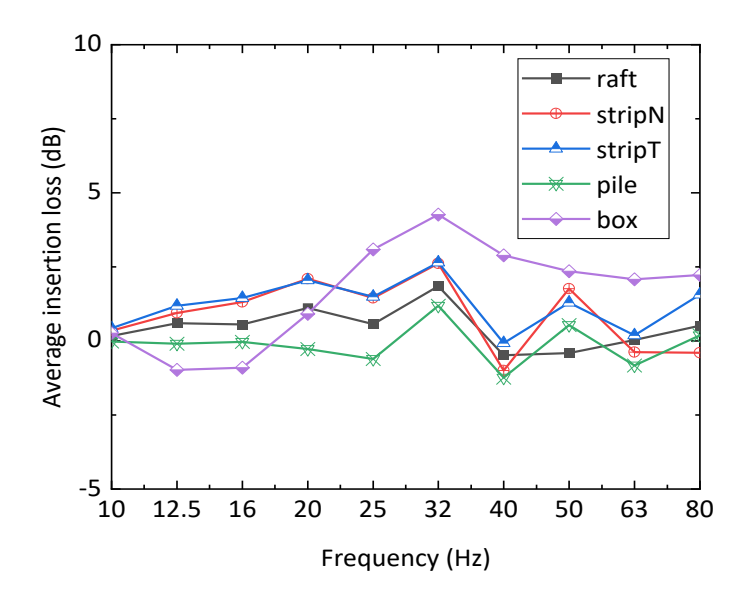


Figure 7-23 The average insertion loss results from all the receivers 5.6 m away from the rear of the building excited by underground railway.

7.3.2.2 The results at specific frequency (50 Hz)

The ground response results at 50 Hz are shown in Figure 7-24. This frequency is chosen because the response at 50 Hz is the largest in Figure 7-22(a). Figure 7-24 gives the ground velocity response level and IL on the centreline on the ground behind the building. Under the same railway excitation conditions, the stripN foundation gives the highest ground response in the near field, whereas the box foundation gives the lowest. At distances greater than 5.6 m from the rear of the building (26 m from the railway track), the raft foundation exhibits the highest ground response, exceeding that of the free-field case. Conversely, the box foundation continues to show the lowest response in this region. Regarding the IL results, in the near field, the box foundation gives the largest mitigation of ground response, followed by the stripT foundation. Further away, the box foundation continues to exhibit the highest mitigation effects, with the pile foundation ranking

second. As the distance from the building increases, a peak in the IL is observed. For the raft foundation, this peak occurs at approximately 4.4 m from the building, while for the stripT and stripN foundations, the peaks are around 4.8 m and 5.2 m, respectively. The peak for the box foundation is the farthest, occurring at approximately 6.4 m.

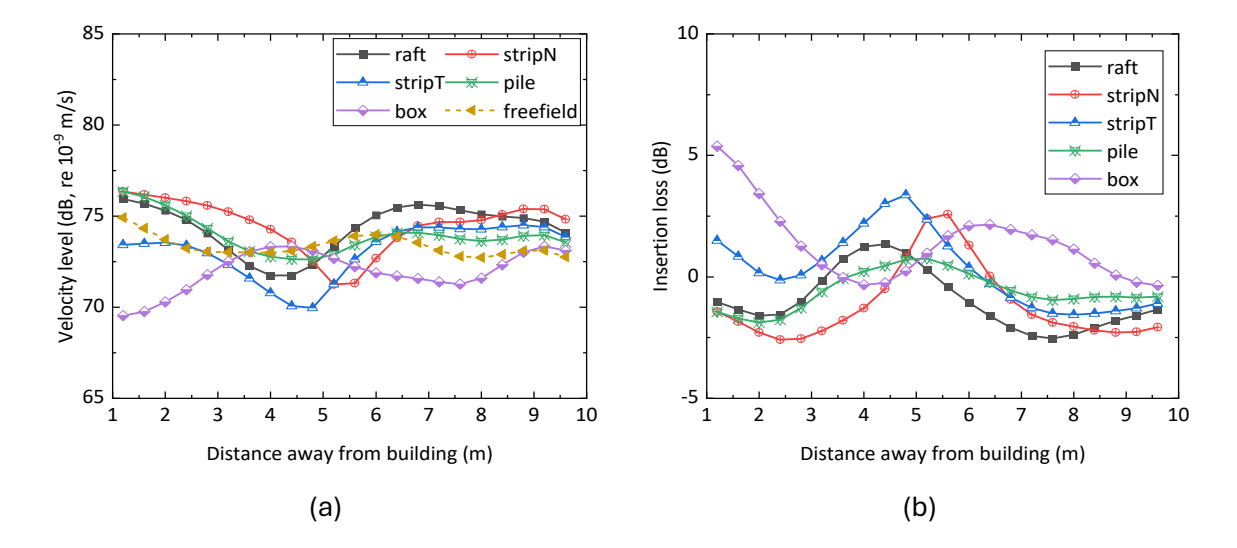


Figure 7-24 The results on the centreline behind the building at 50 Hz including (a) the ground velocity response level and (b) IL value.

Figure 7-25 presents the IL results at 50 Hz calculated from average response over all receiver points located at identical distances from the railway. These show similar trends to the results on the centreline in Figure 7-24(b). Typically, as the distance from the building increases, the average IL value initially rises and then decreases. At most distances, the box foundation exhibits the highest values. But the maximum IL value is observed in the strip foundation case between 3.5 m and 5 m from the building, for the orientation tangential to the train's movement. The strip foundation oriented perpendicular to the train's direction and the raft foundation consistently exhibit the lowest IL values, which can even be negative.



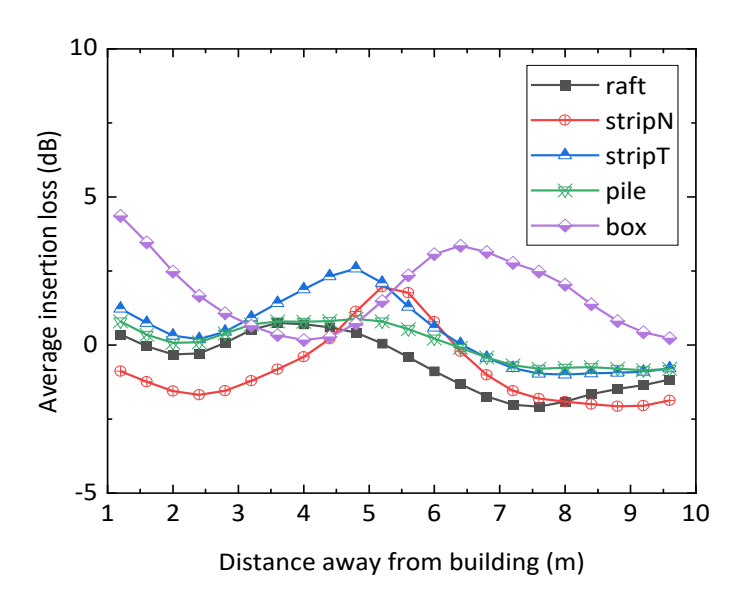


Figure 7-25 The average insertion loss from all receivers at the same distance away from the underground railway at 50 Hz.

7.3.2.3 Results based on overall levels

Based on the overall velocity levels across the range from 10 Hz to 80 Hz, Figure 7-26 shows the ground response and IL value on the centreline behind the building. Unlike the ground surface situation where the free-field response is the largest (Figure 7-19), for the underground railway the free-field response lies in the middle of the results for the various types of foundation buildings. For the box foundation, the ground response is the lowest in areas further than 5 m from the building and closer than 3 m. Correspondingly, the IL values for the box foundation case are the highest at these locations. When the strip orientation is normal to the train passing direction, the ground vibration is amplified near the building and in areas more than 7 m away from the building, as indicated by negative IL values. The pile foundation case would also amplify the ground vibration at some receiver points. The strip foundation oriented parallel to the train travel direction has a peak in the IL when the distance away from the railway is approximately 5 m.

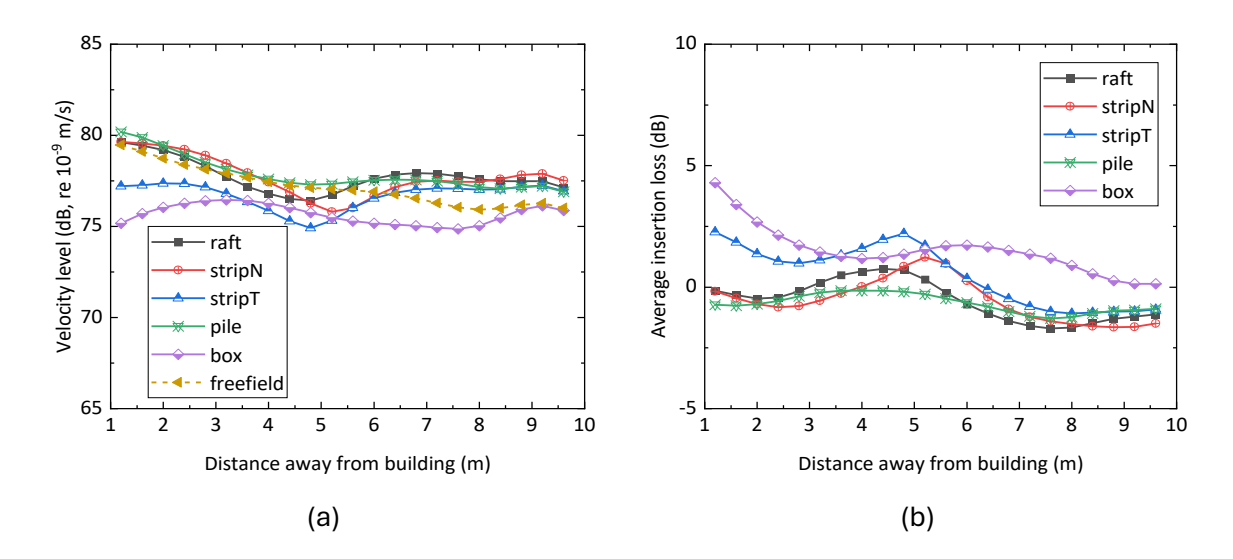


Figure 7-26 The overall results at different distances away from underground railway on the centreline. (a) The overall ground velocity response level and (b) corresponding IL value.

The contour plot of the overall IL value, i.e. based on the level difference in overall velocity levels, is shown in Figure 7-27. The building position is also marked in these figures.

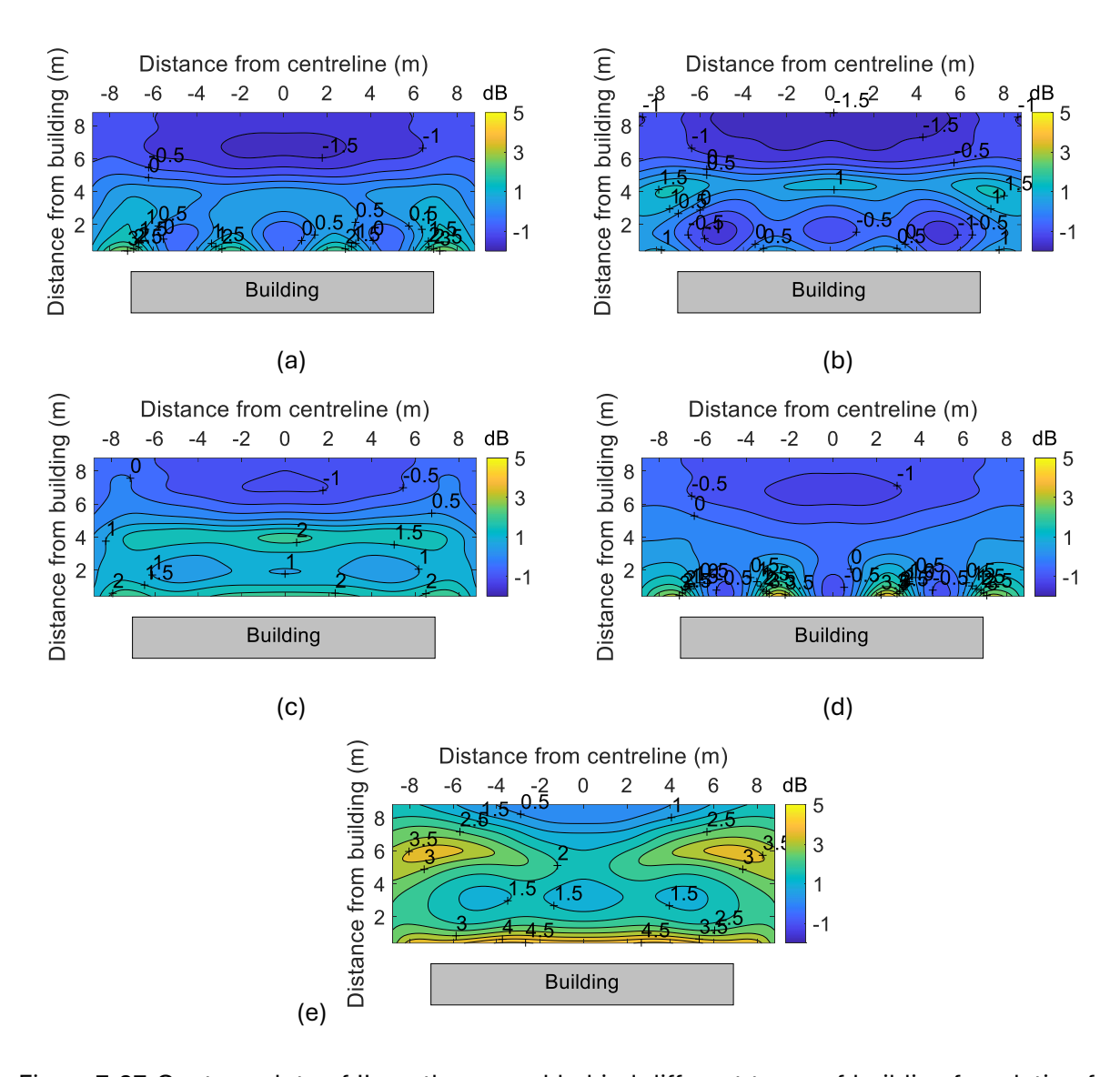


Figure 7-27 Contour plots of IL on the ground behind different types of building foundation for underground railway excitation: (a) raft foundation (b) strip foundation in normal direction (stripN) (c) strip foundation in tangential direction (stripT) (d) pile foundation and (e) box foundation.

In the case of the underground railway, the IL contours display more erratic patterns than for the surface railway. In the proximity of the building, the stripT foundation tends to result in higher IL values. However, for the building with the box foundation, the values of IL in areas close to the building are relatively high compared with other locations. For other types of building foundations, the pillars influence the ground vibration in their vicinity. Typically, for all the building foundation there are regions where both ground vibration mitigation and amplification are observed.

7.3.2.4 Overall results averaged over receiver points

Figure 7-28 shows the overall ground velocity response and IL results averaged over ±9 m width for each specific distance from the rear of the building, covering a range from 1 m to 10 m. Results are shown for the five different foundation cases, along with the free-field response. The overall ground velocity levels are evaluated over the frequency range 10 Hz to 80 Hz.

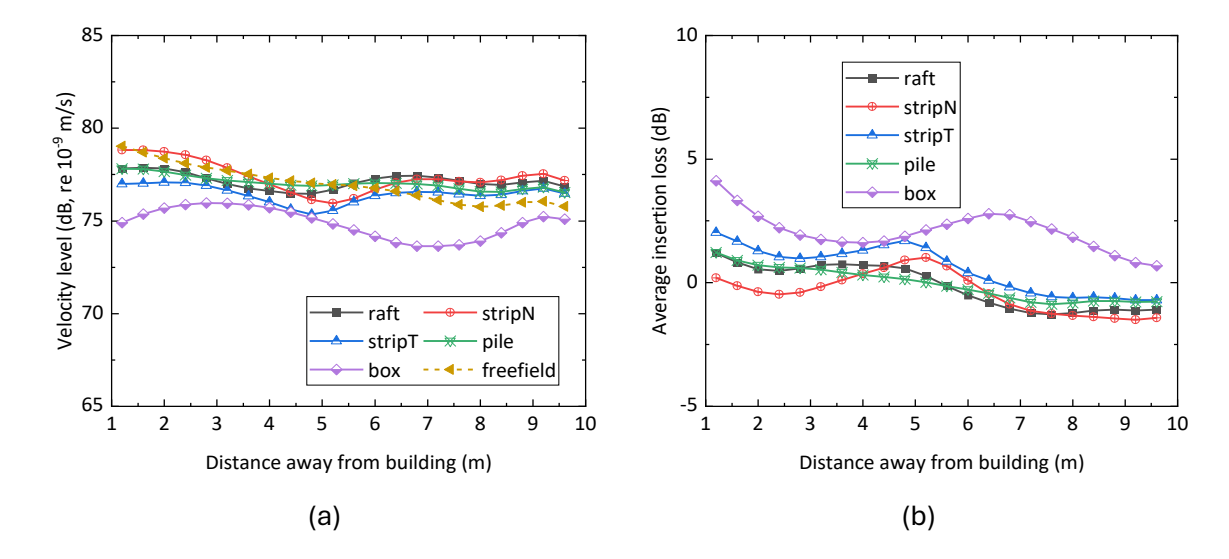


Figure 7-28 The average (a) ground velocity level and (b) IL at different distances average over ±9 m width plotted against distance from the building (underground railway case).

In Figure 7-28 (a), it is evident that the box foundation consistently gives the lowest ground response across all distances. Conversely, the strip foundation oriented perpendicular to the train's direction of travel gives the largest ground response in the near field. The ground response for the raft foundation case and pile foundation case are similar to the free-field response.

These results are shown in the form of IL in Figure 7-28 (b). The box foundation gives the largest vibration mitigation, as also found in the surface railway case in Figure 7-21. However, in the underground railway case, all the other foundation types have similar vibration mitigation effects, and the IL is much smaller than for the surface railway. The strip foundations give some vibration attenuation at the surface behind the building, particularly at certain distances where the IL has a peak. The positions of these IL peaks are influenced by the orientation of the strip foundation. Pile foundations do not have a more significant vibration mitigation effect compared to shallow foundations, unlike in the surface railway case.

7.3.3 Embedded load case

When comparing the average IL results from the surface railway case and the underground railway case, the biggest difference in vibration mitigation behaviour occurs for the pile foundation. Consequently, this type of structure has been selected for further investigation in this section.

The study firstly examines the relationship between the depth of the embedded incoherent line load and the length of the piles. The overall IL values obtained from the vibration levels in the one-third octave bands between 10 Hz and 80 Hz at the ground surface behind the building, with varying pile lengths but a constant embedded load depth of 10 m, are shown in Figure 7-29. The

calculation steps are outlined in Eqs. (3-36) to (3-38). For this model, the primary focus is on the depth of the load. To simplify the model, no tunnel structure is included in the FE model, which results in slightly different outcomes compared with the previous cases results in Figure 7-27(d).

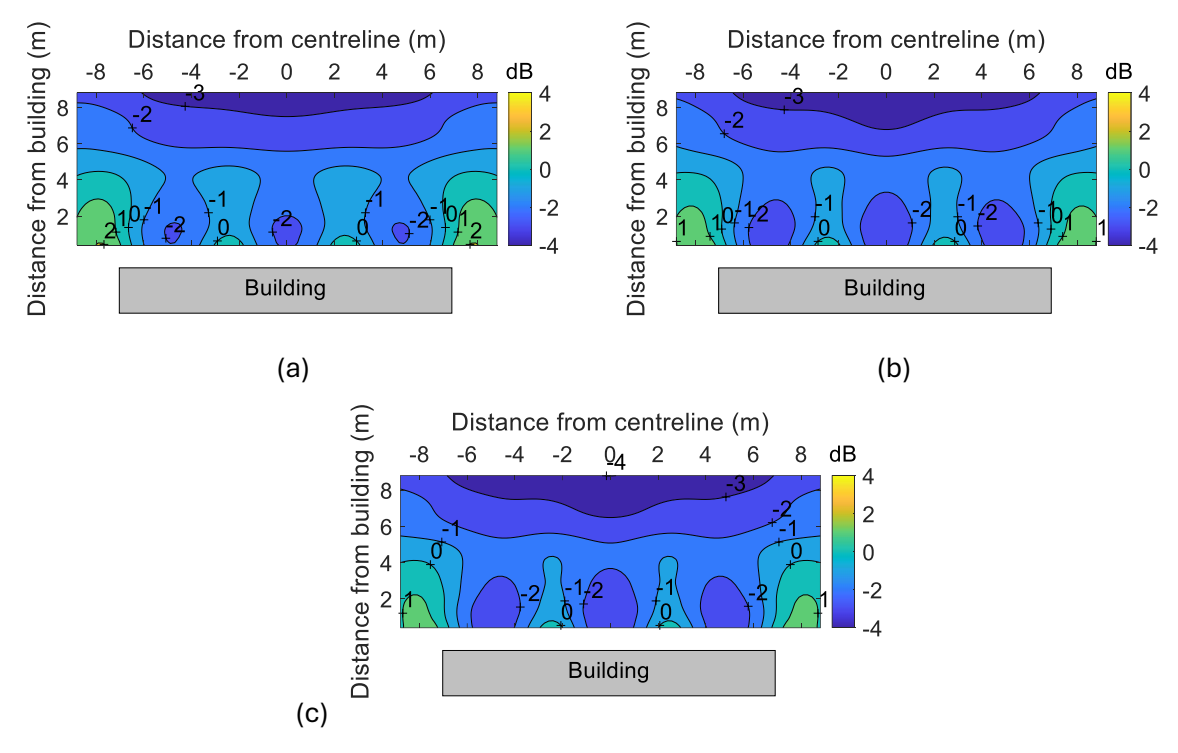


Figure 7-29 Contour plot of IL for embedded load at depth of 10 m and pile foundation with (a) pile length 5 m, (b) pile length 10 m, and (c) pile length 15 m.

It can be concluded that the IL contour undergoes minimal change with variations in the length of the pile. It is observed that certain zones exhibit amplification of the vibration, as indicated by negative IL values. The overall IL value at different distances away from the line load position averaged over the width is shown in Figure 7-30. The IL is influenced to a small extent by the depth of the pile. As the length of the pile increases, the IL decreases. However, the overall trends remain similar in each case. Generally, with the increase of the distance away from the line load, the IL value reduces. In all cases the average IL is negative, indicating a slight amplification of vibration.

Chapter 7

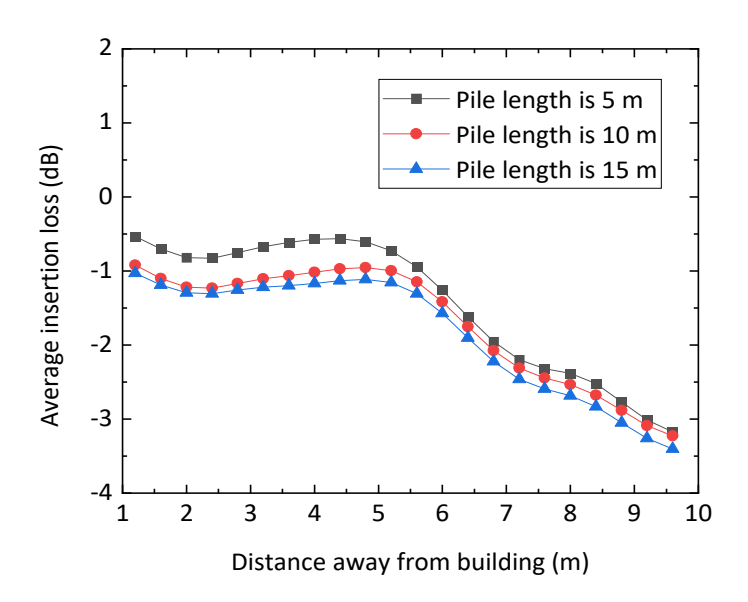


Figure 7-30 The average IL for the influence of various length of pile foundation.

Additionally, the effect of the depth at which the line load is embedded is explored. For this analysis, the pile length is held constant at 10 m, while the load is embedded at depths of 0 m (i.e. the load is applied on the surface), 5 m, 10 m, and 15 m. The IL contours are shown in Figure 7-31. Since there is no tunnel structure in this case, the results in Figure 7-31(b) are different compared with the results in Figure 7-27(d).

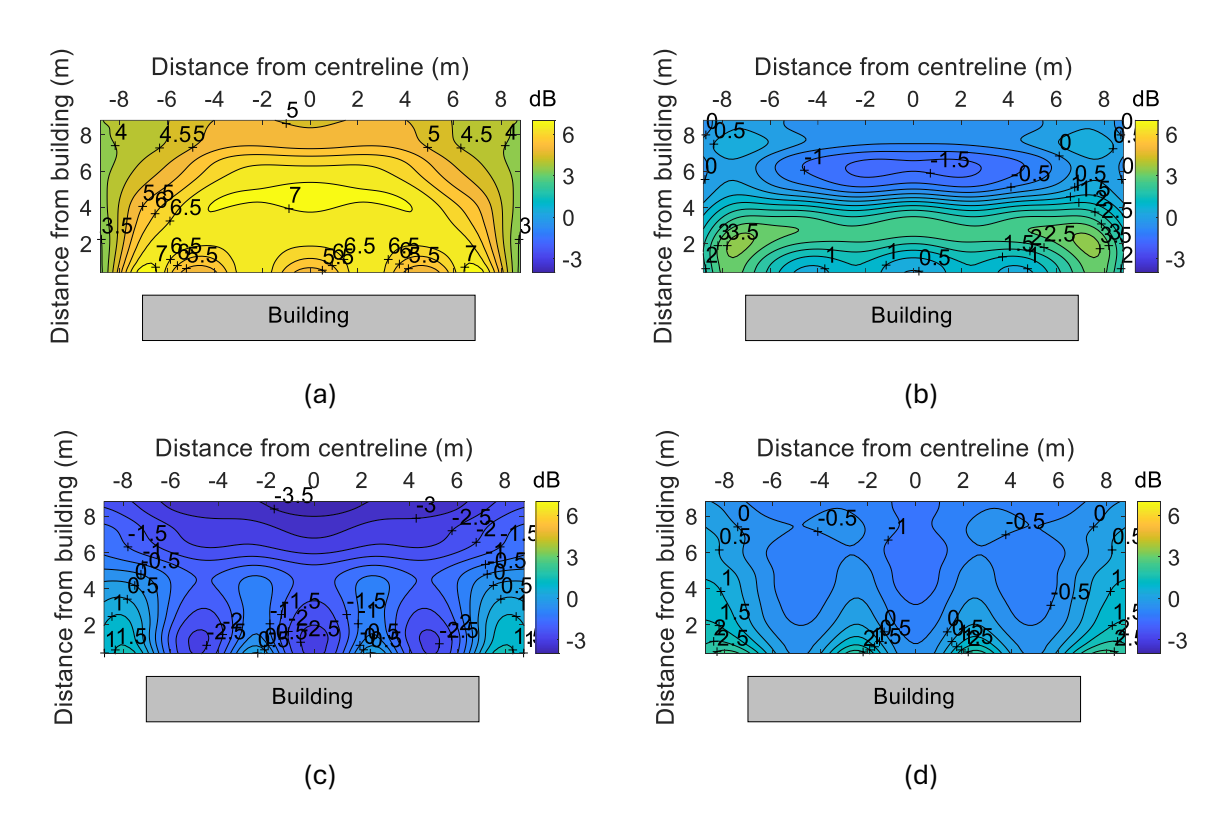


Figure 7-31 Contour plot of IL for building with pile foundation with pile depth 10 m when (a) load depth is 0 m (b) load depth is 5 m, (c) load depth is 10 m, and (d) load depth is 15 m.

There are significant differences in the IL contours among the three cases where the incoherent load is applied embedded and the one case where the load is applied on the surface. The vibration amplification zone is quite different for each case. The overall IL results averaged over the width are shown in Figure 7-32.

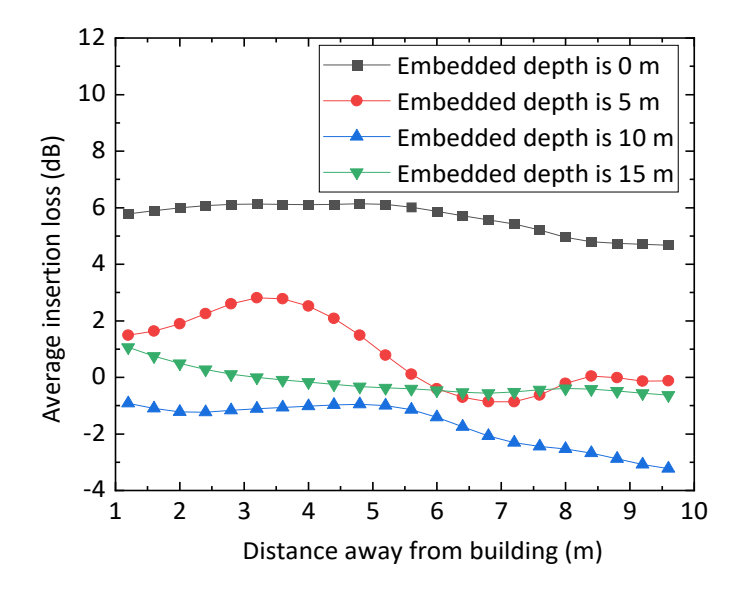


Figure 7-32 The average IL for pile foundation building under different load depth.

It can be summarised that varying the load depth results in markedly different IL outcomes. The depth of the load has a much more substantial influence on the IL than changes in the pile length. When the load is applied on the surface, the pile foundation could mitigate the ground vibration significantly. When the embedded depth is 5 m, the average IL value is the higher than other cases where the load is embedded.

7.4 Summary

In this chapter, a hybrid ground vibration prediction model is developed to assess the impact of various types of building foundations on ground vibration. This allows assessment of the raft and strip foundations, categorised as shallow foundations, as well as the pile and box foundations, classified as deep foundations and overcomes some of the limitation of the semi-analytical model for pile foundation.

The force density is calculated from the semi-analytical model MOTIV. It is determined from the ground response due to a running train minus the incoherent line source transfer mobility. In the underground railway case, the semi-analytical model contains the train, track, tunnel, and soil components. For the surface railway case, the model includes the train, track, and soil. All parameters are kept consistent across both models to investigate the different influences from

the building foundations. The LSTM is evaluated at different excitation positions for the two different cases, underground railway and surface railway. For the underground railway case, it is calculated from excitation on the track slab, while for the surface railway case, it is calculated from excitation on the ground.

Subsequently, the LSTM level for the ground, influenced by the various building foundations, is calculated using a 3D FE model equipped with an infinite element boundary. Following this, the FDL and the LSTM level are combined to determine the total ground response. The IL value at the ground surface in proximity to the building is then investigated to determine the ground vibration mitigation.

When examining the LSTM level results for different foundation types under excitation from the incoherent load representing the railway, the IL values for the surface railway case are generally larger than these for the underground railway case. The box foundation consistently produces the highest IL value for both surface and underground railways. For the underground railway case, the IL for the pile foundation is the lowest between 3.6 m and 7.6 m from the rear of the building (24 m and 28 m from the railway), whereas in the surface railway case, it is the second highest.

From this hybrid model, it can be summarised that the presence of the building foundation in the transmission path can reduce ground vibration especially for excitation at the ground surface. The IL shows that the deep foundations have greater vibration mitigation effects than the shallow foundations, especially for the surface railway case. This trend is consistent with the results obtained from the LSTM level analysis without FDL. Additionally, it is observed that ground vibration mitigation is more pronounced in the near field compared with the results obtained further away from the building. Regarding the impact of pile foundations, the depth at which the load is applied significantly affects the ground vibration attenuation, much more so than variations in the length of the pile.

Chapter 8 Conclusions and recommendations

The work presented in this thesis aims to reveal the influence of structures located in the transmission path on railway-induced ground vibration. The main conclusions and some recommendations for the next steps are summarised in this chapter.

8.1 Conclusions

When predicting train-induced ground vibration, it is important to consider the influence of structures embedded in the transmission path especially for excitation by surface railways. Analysis begins with the simplest case, a single pile, and progressively addresses more complex models, culminating in a building on a piled foundation. The excitation considers both fixed unit loads and dynamic train loads. The investigation focuses on the effects on the ground response behind these structures. From this analysis, several conclusions can be drawn.

For the embedded single pile structure, a simple semi-analytical model has been developed to simulate the dynamic interaction between the pile and the soil, as well as the ground response behind the pile. The accuracy range of the model is thoroughly investigated, showing that the semi-analytical model provides reliable results, at lower frequencies (less than 80 Hz) and higher shear wave velocities (over 160 m/s). When the load is applied at the top of the pile, the range of accurate and reliable results is more extensive. However, when the load is applied at a distance from the pile, the model yields a narrower range of reliable results. The accuracy of the external load model is significantly improved when the rotational DOFs of the pile-soil coupled nodes are considered.

The presence of the pile results in a reduction in the ground response behind it. The mitigation effects are more significant with increasing frequency or decreasing shear wave velocity. If the load point is moved further from the pile, the mitigation effect diminishes, stabilising at a roughly constant value for distances exceeding 10 m. When the surrounding soil is layered, and the upper soil typically has a lower shear wave velocity than the subsoil, greater mitigation of ground vibration is observed when the subsoil shear wave velocity is higher, and the upper soil layer is shallow.

For a pile group structure embedded in the transmission path, a similar semi-analytical model is developed which can consider more piles, including the transfer functions between the different piles. The accuracy of the model is determined by comparison with an FE model. However, this model for pile groups exhibits certain limitations. It tends to yield accurate results primarily at low frequencies or when the number of piles is limited. Different pile group configurations would

cause different ground response mitigation effects. Typically, when multiple piles are aligned along the line from the load to the receiver points, the mitigation effects on ground vibration directly behind the piles are more significant compared with configurations in which the orientation of the line of piles is perpendicular to this line.

For a building with a piled foundation subject to excitation by a fixed unit load, a finite element model has been created using beam and shell elements. The ground response behind the building can be calculated using the semi-analytical method. Peaks of the IL in the ground response are found corresponding to the building floor modes. The presence of a piled building results in a mitigation of the ground vibration response which is more significant in the frequency range 40 - 80 Hz for the parameters considered.

By integrating the MOTIV model, which calculates ground responses induced by underground railways, with the addition of an FE building model, a comprehensive model is obtained containing five sub-models for the train, track, tunnel, ground and building. The ground response and IL results suggest that higher train speeds lead to greater ground responses, but the IL value is similar regardless of the train speed. For train loads located in the embedded tunnel, the presence of the building may amplify the ground response depending on the distance between the railway and the building.

To study different types of building foundation, a hybrid model has been produced in which the FD and LSTM are computed separately using the semi-analytical MOTIV model and the 3D FE method. Four different types of foundations are considered: raft and strip foundations, which are categorised as shallow foundations, and pile and box foundations, classified as deep foundations. The strip foundation has two different orientations, normal to the train moving direction and parallel to the train moving direction. Deep foundations exhibit more significant vibration mitigation effects compared to shallow foundations, particularly in cases when the excitation is the surface railway. Ground vibration mitigation is notably more effective near the building compared to farther away. Additionally, the depth at which the load is applied significantly influences vibration attenuation of pile foundations, more than changes in pile length.

Overall, the presence of a structure in the transmission path between the excitation source and the receiver point impacts the ground response between -3 dB and +10 dB. Different pile group configurations and building foundation types lead to differences in ground vibration. The building's modes also influence the ground response. Therefore, for more accurate ground vibration predictions, it is advisable to consider any structures located along the transmission path. A model that incorporates the influence of structures in the transmission path can predict train-induced ground vibrations more accurately.

8.2 Recommendations for future work

The following recommendations for further work are suggested.

In the single pile model, the pile is simulated using beam elements. However, at higher dimensionless values, corresponding to higher frequencies and lower shear wave velocities of the surrounding ground soil, the model's accuracy diminishes. To achieve more precise results in this situation, the next step is to develop a new model to simulate the single pile-soil dynamic interaction. This model could discretise the cross-section of the beam element or consider displacements in the radial direction within the pile's cross-section. Boundary elements can be used to simulate the soil and investigate the dynamics of a single pile in high-frequency and soft soil conditions.

In the pile group model, each pile within the group is simulated using beam elements. A limitation of this model arises when there are more than two piles aligned parallel to the line connecting the load location and the receiver points at the centreline. The next step is to enhance the accuracy of the pile group model across a broader dimensionless frequency range based on the pile-soil-pile interaction (PSPI) model. The technique for the pile group can be based on the discretised single pile-soil interaction model mentioned above. The wave scattering effects at higher frequencies should be simulated and investigated based on the PSPI model.

The impact of a building with a piled foundation on the ground response, analysed using the substructure method, has a similar accuracy to that of the pile group model. The next step is to enhance the model's reliability across a broader range based on the PSPI model. In addition to pile foundation structures, a wide range of foundation types need to be simulated using the FE method and coupled with the surrounding soil based on the sub-structure method. Further investigation is required to understand the ground response under the influence of different foundation types.

The hybrid approach detailed in Chapter 7 has been applied to only one building design and one ground stiffness level. To draw more general conclusions, it would be beneficial to consider additional cases. These should include the influence of groups of buildings on ground vibration and the impact of layered soil on vibration behind buildings.

A scaled model experiment could be established for validating the semi-analytical single pile-soil models. By measuring the ground response behind the pile in a scaled experiment, it would be possible to investigate the influence of a single pile inclusion on the ground response in that area. It would be beneficial to identify an engineering case that allows for field measurements, which would aid in model validation and evaluation of structural influence.

Appendix A The beam element matrices

The stiffness matrix of the Timoshenko beam finite element [235] used in Chapter 3 is

$$\mathbf{K}^e = \begin{bmatrix} \mathbf{K}_{ii}^e & \mathbf{K}_{ij}^e \\ \mathbf{K}_{ji}^e & \mathbf{K}_{jj}^e \end{bmatrix}$$
(A-1)

Where

$$\mathbf{K}_{ii}^{e} = \begin{bmatrix} \frac{EA}{L} & 0 & 0 & 0 & 0 & 0 \\ 0 & \frac{12EI_{zz}}{L^{3}(1+\phi_{y})} & 0 & 0 & 0 & \frac{6EI_{zz}}{L^{2}(1+\phi_{y})} \\ 0 & 0 & \frac{12EI_{yy}}{L^{3}(1+\phi_{z})} & 0 & -\frac{6EI_{yy}}{L^{2}(1+\phi_{z})} & 0 \\ 0 & 0 & 0 & \frac{GI_{xx}}{L} & 0 & 0 \\ 0 & 0 & -\frac{6EI_{yy}}{L^{2}(1+\phi_{z})} & 0 & \frac{(4+\phi_{z})EI_{yy}}{L(1+\phi_{z})} & 0 \\ 0 & \frac{6EI_{zz}}{L^{2}(1+\phi_{y})} & 0 & 0 & 0 & \frac{(4+\phi_{y})EI_{zz}}{L(1+\phi_{y})} \end{bmatrix}$$
(A-2)

$$\mathbf{K}_{jj}^{e} = \begin{bmatrix} \frac{EA}{L} & 0 & 0 & 0 & 0 & 0 \\ 0 & \frac{12EI_{zz}}{L^{3}(1+\phi_{y})} & 0 & 0 & 0 & -\frac{6EI_{zz}}{L^{2}(1+\phi_{y})} \\ 0 & 0 & \frac{12EI_{yy}}{L^{3}(1+\phi_{z})} & 0 & \frac{6EI_{yy}}{L^{2}(1+\phi_{z})} & 0 \\ 0 & 0 & 0 & \frac{GI_{xx}}{L} & 0 & 0 \\ 0 & 0 & \frac{6EI_{yy}}{L^{2}(1+\phi_{z})} & 0 & \frac{(4+\phi_{z})EI_{yy}}{L(1+\phi_{z})} & 0 \\ 0 & -\frac{6EI_{zz}}{L^{2}(1+\phi_{y})} & 0 & 0 & 0 & \frac{(4+\phi_{y})EI_{zz}}{L(1+\phi_{y})} \end{bmatrix}$$
(A-3)

$$\mathbf{K}_{ij}^{e} = \begin{bmatrix} -\frac{EA}{L} & 0 & 0 & 0 & 0 & 0 & 0 \\ 0 & -\frac{12EI_{zz}}{L^{3}(1+\phi_{y})} & 0 & 0 & 0 & -\frac{6EI_{zz}}{L^{2}(1+\phi_{y})} \\ 0 & 0 & -\frac{12EI_{yy}}{L^{3}(1+\phi_{z})} & 0 & \frac{6EI_{yy}}{L^{2}(1+\phi_{z})} & 0 \\ 0 & 0 & 0 & -\frac{GI_{xx}}{L} & 0 & 0 \\ 0 & 0 & -\frac{6EI_{yy}}{L^{2}(1+\phi_{z})} & 0 & \frac{(2-\phi_{z})EI_{yy}}{L(1+\phi_{z})} & 0 \\ 0 & \frac{6EI_{zz}}{L^{2}(1+\phi_{y})} & 0 & 0 & 0 & \frac{(2-\phi_{y})EI_{zz}}{L(1+\phi_{y})} \end{bmatrix}$$
(A-4)

$$K_{ii}^e = \left(K_{ij}^e\right)^T \tag{A-5}$$

In these equations E is the elastic modulus, I is the second moment of area, G is the shear modulus, and A is the cross-section area. κ is the shear correction factor; for a rectangular section, the value is

$$\kappa = \frac{10(1+\mu)}{12+11\mu} \tag{A-6}$$

where μ is the Poisson's ratio.

The shear deformation parameter is

$$\phi_{y} = \frac{12EI_{zz}}{GA\kappa_{y}L^{2}} \tag{A-7}$$

$$\phi_z = \frac{12EI_{yy}}{GA\kappa_z L^2} \tag{A-8}$$

The consistent mass matrix of beam element can be found as

$$\mathbf{M}^{e} = \begin{bmatrix} \mathbf{M}_{ii}^{e} & \mathbf{M}_{ij}^{e} \\ \mathbf{M}_{ji}^{e} & \mathbf{M}_{jj}^{e} \end{bmatrix}$$
(A-9)

In which

$$\mathbf{M}_{ii}^{e} = \begin{bmatrix} \frac{\rho AL}{3} & 0 & 0 & 0 & 0 & 0 & 0 \\ & \frac{\rho AL}{\left(1+\phi_{y}\right)^{2}}f_{1z} & 0 & 0 & 0 & \frac{\rho AL^{2}}{\left(1+\phi_{y}\right)^{2}}f_{3z} \\ & \frac{\rho AL}{\left(1+\phi_{z}\right)^{2}}f_{1y} & 0 & -\frac{\rho AL^{2}}{\left(1+\phi_{z}\right)^{2}}f_{3y} & 0 \\ & \frac{\rho L}{3}\left(I_{yy}+I_{zz}\right) & 0 & 0 \\ & \frac{\rho AL^{3}}{\left(1+\phi_{z}\right)^{2}}f_{2y} & 0 \\ & \frac{\rho AL^{3}}{\left(1+\phi_{y}\right)^{2}}f_{2z} \end{bmatrix}$$
 (A-10)

$$\mathbf{M}_{jj}^{e} = \begin{bmatrix} \frac{\rho AL}{3} & 0 & 0 & 0 & 0 & 0 & 0 \\ & \frac{\rho AL}{\left(1+\phi_{y}\right)^{2}}f_{1z} & 0 & 0 & 0 & -\frac{\rho AL^{2}}{\left(1+\phi_{y}\right)^{2}}f_{3z} \\ & \frac{\rho AL}{\left(1+\phi_{z}\right)^{2}}f_{1y} & 0 & \frac{\rho AL^{2}}{\left(1+\phi_{z}\right)^{2}}f_{3y} & 0 \\ & & \frac{\rho L}{3}\left(l_{yy}+l_{zz}\right) & 0 & 0 \\ & \frac{\rho AL^{3}}{\left(1+\phi_{z}\right)^{2}}f_{2y} & 0 \\ & \frac{\rho AL^{3}}{\left(1+\phi_{y}\right)^{2}}f_{2z} \end{bmatrix}$$
 (A-11)

$$\mathbf{M}_{ij}^{e} = \begin{bmatrix} \frac{\rho AL}{6} & 0 & 0 & 0 & 0 & 0 & 0 \\ 0 & \frac{\rho AL}{\left(1 + \phi_{y}\right)^{2}} f_{4z} & 0 & 0 & 0 & -\frac{\rho AL^{2}}{\left(1 + \phi_{y}\right)^{2}} f_{6z} \\ 0 & 0 & \frac{\rho AL}{\left(1 + \phi_{z}\right)^{2}} f_{4y} & 0 & \frac{\rho AL^{2}}{\left(1 + \phi_{z}\right)^{2}} f_{6y} & 0 \\ 0 & 0 & 0 & \frac{\rho L}{6} \left(I_{yy} + I_{zz}\right) & 0 & 0 \\ 0 & 0 & -\frac{\rho AL^{2}}{\left(1 + \phi_{z}\right)^{2}} f_{6y} & 0 & -\frac{\rho AL^{3}}{\left(1 + \phi_{z}\right)^{2}} f_{3y} & 0 \\ 0 & \frac{\rho AL^{2}}{\left(1 + \phi_{y}\right)^{2}} f_{6z} & 0 & 0 & 0 & -\frac{\rho AL^{3}}{\left(1 + \phi_{y}\right)^{2}} f_{3z} \end{bmatrix}$$
 (A-12)

$$M_{ii}^e = \left(M_{ij}^e\right)^T \tag{A-13}$$

where

$$f_{1i} = \frac{13}{35} + \frac{7}{10}\phi_n + \frac{1}{3}\phi_n^2 + \frac{6}{5}\left(\frac{r_i}{L}\right)^2 \tag{A-14}$$

$$f_{2i} = \frac{1}{105} + \frac{1}{60}\phi_n + \frac{1}{120}\phi_n^2 + \left(\frac{2}{15} + \frac{1}{6}\phi_n + \frac{1}{3}\phi_n^2\right)\left(\frac{r_i}{L}\right)^2 \tag{A-15}$$

$$f_{3i} = \frac{11}{210} + \frac{11}{120}\phi_n + \frac{1}{24}\phi_n^2 + \left(\frac{1}{10} - \frac{1}{2}\phi_n\right)\left(\frac{r_i}{L}\right)^2 \tag{A-16}$$

$$f_{4i} = \frac{9}{70} + \frac{3}{10}\phi_n + \frac{1}{6}\phi_n^2 - \frac{6}{5}\left(\frac{r_i}{L}\right)^2 \tag{A-17}$$

$$f_{5i} = \frac{1}{140} + \frac{1}{60}\phi_n + \frac{1}{120}\phi_n^2 + \left(\frac{1}{30} + \frac{1}{6}\phi_n + \frac{1}{6}\phi_n^2\right)\left(\frac{r_i}{L}\right)^2 \tag{A-18}$$

$$f_{6i} = \frac{13}{420} + \frac{3}{40}\phi_n + \frac{1}{24}\phi_n^2 - \left(\frac{1}{10} - \frac{1}{2}\phi_n\right)\left(\frac{r_i}{L}\right)^2 \tag{A-19}$$

where

$$r_i = \sqrt{\frac{I_{ii}}{A}} \quad (i = y, z) \tag{A-20}$$

$$n = \begin{cases} y & i = z \\ z & i = y \end{cases} \tag{A-21}$$

Appendix B Dynamic stiffness matrix for the ground

The ground is modelled using the approach introduced by Kausel and Roesset [44]. It is assumed to be horizontally layered and each layer is represented by a dynamic stiffness matrix at frequency ω and wavenumbers k_x and k_y in the x and y directions. The soil around the single pile should be divided into layers at the coupled nodes. For a homogeneous soil, each layer possesses identical properties. Beyond this, the soil can also be divided into layers at varying depths with different properties to approximate the real situation. The global stiffness matrix of the soil is assembled after calculating the dynamic stiffness matrices of each layer. A sketch of the soil model is shown in Figure B-1.

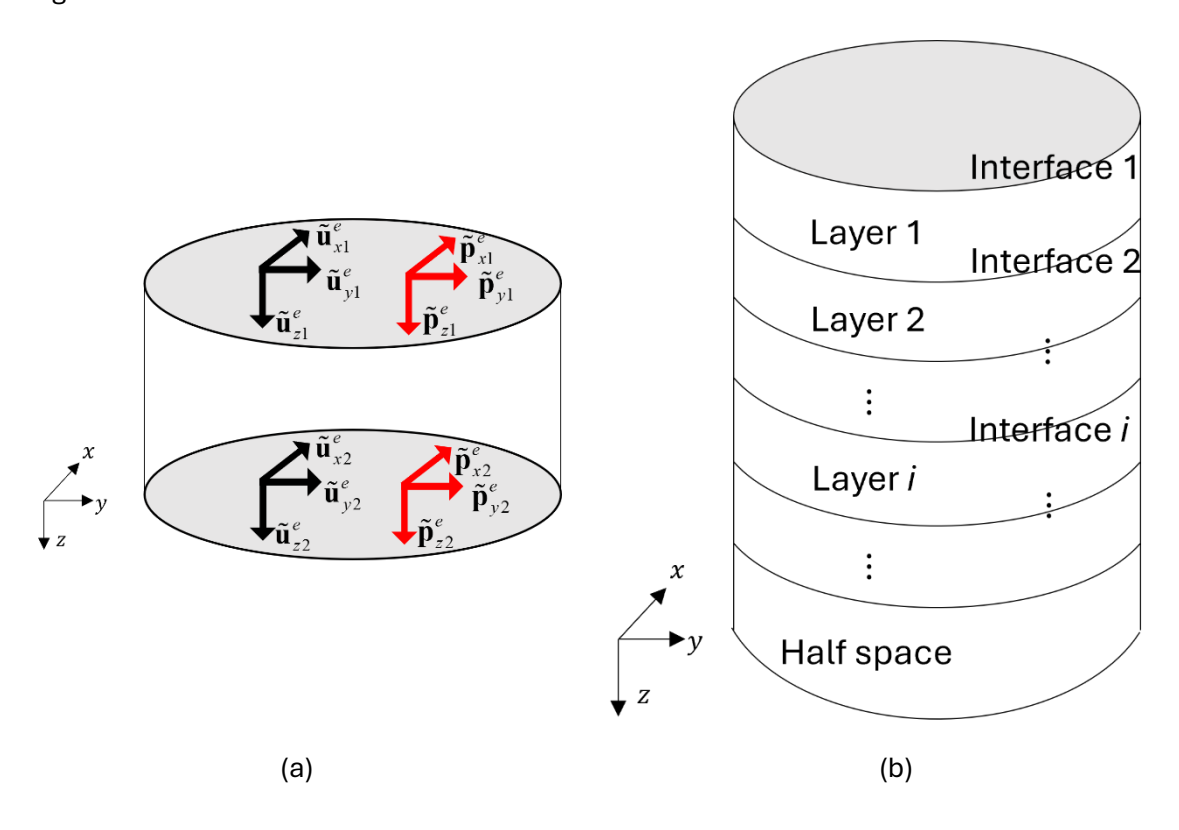


Figure B-1 The sketch of the layered soil. (a) Layer element and (b) Global model of layered soil.

The relationship between the displacements $\tilde{\mathbf{U}}^e$ and tractions $\tilde{\mathbf{P}}^e$ at the top and bottom of a layer in the frequency-wavenumber domain is

$$\widetilde{\mathbf{K}}^e \widetilde{\mathbf{U}}^e = \widetilde{\mathbf{P}}^e \tag{B-1}$$

where $\widetilde{\mathbf{K}}^e$ is the element dynamic stiffness matrix of the e-th layer. More details can be found in [44].

The matrices for the layered medium can be combined to give the overall dynamic equation as

$$\begin{bmatrix} \widetilde{\mathbf{K}}_{11}^{1} & \widetilde{\mathbf{K}}_{12}^{1} \\ \widetilde{\mathbf{K}}_{21}^{1} & \widetilde{\mathbf{K}}_{12}^{2} + \widetilde{\mathbf{K}}_{11}^{2} & \widetilde{\mathbf{K}}_{12}^{2} \\ & \widetilde{\mathbf{K}}_{21}^{2} & \widetilde{\mathbf{K}}_{22}^{2} + \widetilde{\mathbf{K}}_{11}^{3} & \widetilde{\mathbf{K}}_{12}^{3} \\ & & \widetilde{\mathbf{K}}_{21}^{3} & \widetilde{\mathbf{K}}_{22}^{3} + \widetilde{\mathbf{K}}_{11}^{4} & \cdots \\ \vdots & & \ddots \end{bmatrix} \begin{bmatrix} \widetilde{\mathbf{u}}^{1} \\ \widetilde{\mathbf{u}}^{2} \\ \widetilde{\mathbf{u}}^{3} \\ \widetilde{\mathbf{u}}^{4} \\ \widetilde{\mathbf{u}}^{5} \end{bmatrix} = \begin{bmatrix} \widetilde{\mathbf{p}}^{1} \\ \widetilde{\mathbf{p}}^{2} \\ \widetilde{\mathbf{p}}^{3} \\ \widetilde{\mathbf{p}}^{4} \\ \widetilde{\mathbf{p}}^{5} \end{bmatrix}$$
(B-2)

where \mathbf{K}^e_{ij} refers to the dynamic stiffness matrix of the e-th layered element that relates the displacements at interface i due to the loads at interface i. $\widetilde{\mathbf{u}}^i$ and $\widetilde{\mathbf{p}}^i$ denote the displacement and load vectors at interface i between layer i-1 and i. After obtaining the displacements and tractions at the interface, it is possible to determine the displacement at any depth inside the soil layer, using the Green's function \widetilde{H}^G in the frequency-wavenumber domain.

The transfer functions in the spatial-frequency domain can be calculated from the response in the frequency-wavenumber domain by using a two-dimensional inverse Fourier transform over wavenumber. It can be written as

$$\widehat{H}^{G}(x, y, z, \omega) = \frac{1}{4\pi} \iint \widetilde{\widetilde{H}}^{G}(k_{x}, k_{y}, z, \omega) e^{i(k_{x}x + k_{y}y)} dk_{x} dk_{y}$$
(B-3)

where k_x and k_y are the wavenumbers in x and y direction.

Appendix C Coefficients for the elastic continuum

The displacement matrices $\breve{\mathbf{U}}$ in Chapter 3 and Chapter 6 are used to determine the displacement components of the continuum. The elements of these matrices are:

$$u_{11} = -\frac{n}{r}I_n(ar) + aI_{n+1}(ar)$$
 (C-1)

$$u_{12} = -\frac{n}{r}K_n(ar) - aK_{n+1}(ar)$$
 (C-2)

$$u_{13} = \mathrm{i}\beta I_{n+1}(br) \tag{C-3}$$

$$u_{14} = i\beta K_{n+1}(br)$$
 (C-4)

$$u_{15} = -\frac{n}{r}I_n(br) \tag{C-5}$$

$$u_{16} = \frac{n}{r} K_n(br) \tag{C-6}$$

$$u_{21} = -\frac{n}{r}I_n(ar) \tag{C-7}$$

$$u_{21} = -\frac{n}{r}I_n(ar) \tag{C-8}$$

$$u_{23} = \mathrm{i}\beta I_{n+1}(br) \tag{C-9}$$

$$u_{24} = i\beta K_{n+1}(br) \tag{C-10}$$

$$u_{25} = -\frac{n}{r}I_n(br) - bI_{n+1}(br)$$
 (C-11)

$$u_{26} = -\frac{n}{r}K_n(br) + bK_{n+1}(br)$$
 (C-12)

$$u_{31} = \mathrm{i}\beta I_n(ar) \tag{C-13}$$

$$u_{32} = i\beta K_n(ar) \tag{C-14}$$

$$u_{33} = -bI_n(br) \tag{C-15}$$

$$u_{34} = bK_n(br) \tag{C-16}$$

$$u_{35} = 0$$
 (C-17)

$$u_{36} = 0$$
 (C-18)

The stress matrices \mathbf{T} in Chapter 3 and Chapter 6 are used to determine the stress components of the continuum. The elements of these matrices are:

$$t_{11} = \left(2\mu \frac{(n^2 - n)}{r^2} - \lambda \beta^2 + (\lambda + 2\mu)a^2\right) I_n(ar) - 2\mu \frac{a}{r} I_{n+1}(ar)$$
 (C-19)

$$t_{12} = \left(2\mu \frac{(n^2 - n)}{r^2} - \lambda \beta^2 + (\lambda + 2\mu)a^2\right) K_n(ar) + 2\mu \frac{a}{r} K_{n+1}(ar)$$
 (C-20)

$$t_{13} = 2\mu i\beta b I_n(br) - 2\mu i\beta \frac{(n+1)}{r} I_{n+1}(br)$$
 (C-21)

$$t_{14} = -2\mu i\beta b K_n(br) - 2\mu i\beta \frac{(n+1)}{r} K_{n+1}(br)$$
 (C-22)

$$t_{15} = 2\mu \frac{(n^2 - n)}{r^2} I_n(br) + 2\mu \frac{n}{r} b I_{n+1}(br)$$
 (C-23)

$$t_{16} = 2\mu \frac{(n^2 - n)}{r^2} K_n(br) - 2\mu \frac{n}{r} b K_{n+1}(br)$$
 (C-24)

$$t_{21} = -2\mu \frac{(n^2 - n)}{r^2} I_n(ar) - 2\mu \frac{n}{r} \alpha I_{n+1}(ar)$$
 (C-25)

$$t_{22} = -2\mu \frac{(n^2 - n)}{r^2} K_n(ar) + 2\mu \frac{n}{r} a K_{n+1}(ar)$$
 (C-26)

$$t_{23} = \mu i \beta b I_n(br) - 2\mu i \beta \frac{(n+1)}{r} I_{n+1}(br)$$
 (C-27)

$$t_{24} = -\mu i\beta b K_n(br) - 2\mu i\beta \frac{(n+1)}{r} K_{n+1}(br)$$
 (C-28)

$$t_{25} = \left(-2\mu \frac{(n^2 - n)}{r^2} - \mu b^2\right) I_n(br) + 2\mu \frac{b}{r} I_{n+1}(br)$$
 (C-29)

$$t_{26} = \left(-2\mu \frac{(n^2 - n)}{r^2} - \mu b^2\right) K_n(\beta r) - 2\mu \frac{b}{r} K_{n+1}(br)$$
 (C-30)

$$t_{31} = 2\mu i \beta \frac{n}{r} I_n(ar) + 2\mu i \beta a I_{n+1}(ar)$$
 (C-31)

$$t_{32} = 2\mu i \beta \frac{n}{r} K_n(ar) - 2\mu i \beta a K_{n+1}(ar)$$
 (C-32)

$$t_{33} = -\mu \frac{n}{r} b I_n(br) - \mu (\beta^2 + b^2) I_{n+1}(br)$$
 (C-33)

$$t_{34} = \mu \frac{n}{r} b K_n(br) - \mu(\beta^2 + b^2) K_{n+1}(br)$$
 (C-34)

$$t_{35} = \mu i\beta \frac{n}{r} I_n(br) \tag{C-35}$$

$$t_{36} = \mu i \beta \frac{n}{r} K_n(br) \tag{C-36}$$

$$t_{41} = \left(-2\mu \frac{(n^2 - n)}{r^2} + \lambda(a^2 - \beta^2)\right) I_n(ar) + 2\mu \frac{a}{r} I_{n+1}(ar)$$
 (C-37)

$$t_{42} = \left(-2\mu \frac{(n^2 - n)}{r^2} + \lambda(a^2 - \beta^2)\right) K_n(ar) - 2\mu \frac{a}{r} K_{n+1}(ar)$$
 (C-38)

$$t_{43} = 2\mu i\beta \frac{(n+1)}{r} I_{n+1}(br)$$
 (C-39)

$$t_{44} = 2\mu i\beta \frac{(n+1)}{r} K_{n+1}(br)$$
 (C-40)

$$t_{45} = -2\mu \frac{(n^2 - n)}{r^2} I_n(br) - 2\mu \frac{n}{r} b I_{n+1}(br)$$
 (C-41)

$$t_{46} = -2\mu \frac{(n^2 - n)}{r^2} K_n(br) + 2\mu \frac{n}{r} b K_{n+1}(br)$$
 (C-42)

$$t_{51} = -2\mu i\beta \frac{n}{r} I_n(ar) \tag{C-43}$$

$$t_{52} = -2\mu i\beta \frac{n}{r} K_n(ar) \tag{C-44}$$

$$t_{53} = \mu \frac{n}{r} b I_n(br) - \mu \beta^2 I_{n+1}(br)$$
 (C-45)

$$t_{54} = -\mu \frac{n}{r} b K_n(br) - \mu \beta^2 K_{n+1}(br)$$
 (C-46)

$$t_{55} = -\mu i\beta \frac{n}{r} I_n(br) - \mu i\beta b I_{n+1}(br)$$
 (C-47)

$$t_{56} = -\mu i \beta \frac{n}{r} K_n(br) + \mu i \beta b K_{n+1}(br)$$
 (C-48)

$$t_{61} = (\lambda a^2 - (\lambda + 2\mu)\beta^2)I_n(ar)$$
 (C-49)

$$t_{62} = (\lambda a^2 - (\lambda + 2\mu)\beta^2)K_n(ar)$$
 (C-50)

$$t_{63} = -2\mu i\beta b I_n(br) \tag{C-51}$$

$$t_{64} = 2\mu i\beta b K_n(br) \tag{C-52}$$

$$t_{65} = 0$$
 (C-53)

$$t_{66} = 0$$
 (C-54)

Appendix D MATLAB code for building model

% the number of span at X direction

Based on the Stabil FE MATLAB toolbox [225], the stiffness matrix and mass matrix can be constructed parametrically. This is achieved by establishing a relationship between the number of spans and storeys in a piled-foundation building and the corresponding node and element numbers.

The MATLAB code is:

Xn=1:

```
Yn=1;
                                    % the number of span at Y direction
Zn=3;
                                    % the number of storeys at Z direction, story
Gn=12;
                                        % the number of foundation element at one pile
                                       % the number of element at X direction span
Xe=14;
Ye=14;
                                      % the number of element at Y direction span
Ze=10;
                                      % the number of elements at one story
XL=4.2:
                                         % the length of each span at X direction (m)
YL=4.2;
                                         % the length of each span at Y direction (m)
ZL=3;
                                    % the height of each span at Z direction (m)
GL=0.5;
                                          % the length of each foundation element (m)
% column
A=[]; % The summarised information about nodes number and coordinates.
for k=1:Yn+1
     for j=1:Xn+1
           for i=1:Gn+1
                A((Ze*Zn+Gn+1)*(Xn+1)*(K-1)+(Ze*Zn+Gn+1)*(j-1)+j,:)=[(Ze*Zn+Gn+1)*(Xn+1)*(K-1)+j,:)=[(Ze*Zn+Gn+1)*(Xn+1)*(Xn+1)*(Xn+1)*(Xn+1)*(Xn+1)*(Xn+1)*(Xn+1)*(Xn+1)*(Xn+1)*(Xn+1)*(Xn+1)*(Xn+1)*(Xn+1)*(Xn+1)*(Xn+1)*(Xn+1)*(Xn+1)*(Xn+1)*(Xn+1)*(Xn+1)*(Xn+1)*(Xn+1)*(Xn+1)*(Xn+1)*(Xn+1)*(Xn+1)*(Xn+1)*(Xn+1)*(Xn+1)*(Xn+1)*(Xn+1)*(Xn+1)*(Xn+1)*(Xn+1)*(Xn+1)*(Xn+1)*(Xn+1)*(Xn+1)*(Xn+1)*(Xn+1)*(Xn+1)*(Xn+1)*(Xn+1)*(Xn+1)*(Xn+1)*(Xn+1)*(Xn+1)*(Xn+1)*(Xn+1)*(Xn+1)*(Xn+1)*(Xn+1)*(Xn+1)*(Xn+1)*(Xn+1)*(Xn+1)*(Xn+1)*(Xn+1)*(Xn+1)*(Xn+1)*(Xn+1)*(Xn+1)*(Xn+1)*(Xn+1)*(Xn+1)*(Xn+1)*(Xn+1)*(Xn+1)*(Xn+1)*(Xn+1)*(Xn+1)*(Xn+1)*(Xn+1)*(Xn+1)*(Xn+1)*(Xn+1)*(Xn+1)*(Xn+1)*(Xn+1)*(Xn+1)*(Xn+1)*(Xn+1)*(Xn+1)*(Xn+1)*(Xn+1)*(Xn+1)*(Xn+1)*(Xn+1)*(Xn+1)*(Xn+1)*(Xn+1)*(Xn+1)*(Xn+1)*(Xn+1)*(Xn+1)*(Xn+1)*(Xn+1)*(Xn+1)*(Xn+1)*(Xn+1)*(Xn+1)*(Xn+1)*(Xn+1)*(Xn+1)*(Xn+1)*(Xn+1)*(Xn+1)*(Xn+1)*(Xn+1)*(Xn+1)*(Xn+1)*(Xn+1)*(Xn+1)*(Xn+1)*(Xn+1)*(Xn+1)*(Xn+1)*(Xn+1)*(Xn+1)*(Xn+1)*(Xn+1)*(Xn+1)*(Xn+1)*(Xn+1)*(Xn+1)*(Xn+1)*(Xn+1)*(Xn+1)*(Xn+1)*(Xn+1)*(Xn+1)*(Xn+1)*(Xn+1)*(Xn+1)*(Xn+1)*(Xn+1)*(Xn+1)*(Xn+1)*(Xn+1)*(Xn+1)*(Xn+1)*(Xn+1)*(Xn+1)*(Xn+1)*(Xn+1)*(Xn+1)*(Xn+1)*(Xn+1)*(Xn+1)*(Xn+1)*(Xn+1)*(Xn+1)*(Xn+1)*(Xn+1)*(Xn+1)*(Xn+1)*(Xn+1)*(Xn+1)*(Xn+1)*(Xn+1)*(Xn+1)*(Xn+1)*(Xn+1)*(Xn+1)*(Xn+1)*(Xn+1)*(Xn+1)*(Xn+1)*(Xn+1)*(Xn+1)*(Xn+1)*(Xn+1)*(Xn+1)*(Xn+1)*(Xn+1)*(Xn+1)*(Xn+1)*(Xn+1)*(Xn+1)*(Xn+1)*(Xn+1)*(Xn+1)*(Xn+1)*(Xn+1)*(Xn+1)*(Xn+1)*(Xn+1)*(Xn+1)*(Xn+1)*(Xn+1)*(Xn+1)*(Xn+1)*(Xn+1)*(Xn+1)*(Xn+1)*(Xn+1)*(Xn+1)*(Xn+1)*(Xn+1)*(Xn+1)*(Xn+1)*(Xn+1)*(Xn+1)*(Xn+1)*(Xn+1)*(Xn+1)*(Xn+1)*(Xn+1)*(Xn+1)*(Xn+1)*(Xn+1)*(Xn+1)*(Xn+1)*(Xn+1)*(Xn+1)*(Xn+1)*(Xn+1)*(Xn+1)*(Xn+1)*(Xn+1)*(Xn+1)*(Xn+1)*(Xn+1)*(Xn+1)*(Xn+1)*(Xn+1)*(Xn+1)*(Xn+1)*(Xn+1)*(Xn+1)*(Xn+1)*(Xn+1)*(Xn+1)*(Xn+1)*(Xn+1)*(Xn+1)*(Xn+1)*(Xn+1)*(Xn+1)*(Xn+1)*(Xn+1)*(Xn+1)*(Xn+1)*(Xn+1)*(Xn+1)*(Xn+1)*(Xn+1)*(Xn+1)*(Xn+1)*(Xn+1)*(Xn+1)*(Xn+1)*(Xn+1)*(Xn+1)*(Xn+1)*(Xn+1)*(Xn+1)*(Xn+1)*(Xn+1)*(Xn+1)*(Xn+1)*(Xn+1)*(Xn+1)*(Xn+1)*(Xn+1)*(Xn+1)*(Xn+1)*(Xn+1)*(Xn+1)*(Xn+1)*(Xn+1)*(Xn+1)*(Xn+1)*(Xn+1)*(Xn+1)*(Xn+1)*(Xn+1)*(Xn+1)*
 1)+(Ze*Zn+Gn+1)*(j-1)+i ...
                      (j-1)*XL (k-1)*YL (i-1)*GL];
           end
      end
end
fdnnodename=A(:,1);
% the internal node coordinate
for k=1:Yn+1
     for j=1:Xn+1
           for i=1:Zn
                for m=1:Ze
                 A((Ze*Zn+Gn+1)*(Xn+1)*(k-1)+(Ze*Zn+Gn+1)*(j-1)+Ze*(i-1)
 1)+Gn+1+m,:)=[(Ze*Zn+Gn+1)*(Xn+1)*(k-1)+(Ze*Zn+Gn+1)*(j-1)+Ze*(i-1)+Gn+1+m ...
```

(j-1)*XL (k-1)*YL Gn*GL+(i-1)*ZL+m*(ZL/Ze)];

end end

```
end
end
 Nodes=A;
 % column elements
 for k=0:Yn
 for j=0:Xn
   for i=1:Ze*Zn+Gn
   B((Ze*Zn+Gn)*(Xn+1)*k+(Ze*Zn+Gn)*j+i,:)=[(Ze*Zn+Gn)*(Xn+1)*k+(Ze*Zn+Gn)*j+i...
   (Ze*Zn+Gn+1)*(Xn+1)*k+(Ze*Zn+Gn+1)*j+i (Ze*Zn+Gn+1)*(Xn+1)*k+(Ze*Zn+Gn+1)*j+i+1];\\
  end
 end
Elements=[B(:,1) 2*ones(size(B,1),3) B(:,2) B(:,3) ones(size(B,1),1) zeros(size(B,1),1)*NaN];
% plate
 for i=1:Zn+1
   H=GL*Gn+(i-1)*ZL; % the height of plate
   Line1=[0 0 H; Lx 0 H];
   Line2=[Lx 0 H;Lx Ly H];
   Line3=[Lx Ly H;0 Ly H];
   Line4=[0 Ly H;0 0 H];
   [Nodes_p,Elements_p,Edge1,Edge2,Edge3,Edge4] =
makemesh(Line1,Line2,Line3,Line4,num_y,num_x,Types(1,:),1,1);
   Nodes_p(:,1)=size(A,1)+(i-1)*size(Nodes_p,1)+Nodes_p(:,1);
   Elements_p(:,1)=size(B,1)+(i-1)*size(Elements_p,1)+Elements_p(:,1);
   Elements_p(:,[5:8])=size(A,1)+(i-1)*size(Nodes_p,1)+ Elements_p(:,[5:8]);
   Nodes=[Nodes;Nodes_p];
   Elements=[Elements; Elements_p];
  end
 Nodes=roundn(Nodes,-3);
  % replace connect nodes between column and plate
  [c,ia,ic]=unique(Nodes(:,2:4),'rows');
  ndatpl=setdiff(Nodes(:,1),ia); % Point with repeated coordinates at plate
  part_ele=Elements(size(B,1)+1:end,[5 6 7 8]);
  for ii=1:numel(ndatpl)
  ndatpl2 = find(Nodes(:,2)==Nodes(ndatpl(ii),2) & Nodes(:,3)==Nodes(ndatpl(ii),3) &
Nodes(:,4)==Nodes(ndatpl(ii),4));
  part_ele(part_ele==ndatpl2(2))=ndatpl2(1);
  end
  Elements(size(B,1)+1:end,[5 6 7 8])=part_ele;
  % added reference nodes
  Nodes(end+1,:)=[size(Nodes,1)+1 1 5 0];
  Elements(1:size(B,1),7)=Nodes(end,1)*ones(size(B,1),1);
```

- 1. Thompson, D.J., Kouroussis, G. & Ntotsios, E., Modelling, simulation and evaluation of ground vibration caused by rail vehicles. *Vehicle System Dynamics*, **57(7)**,936-983 (2019).
- 2. Yang, J., Zhu, S., Zhai, W., Kouroussis, G., Wang, Y., Wang, K., Lan, K. & Xu, F., Prediction and mitigation of train-induced vibrations of large-scale building constructed on subway tunnel. *Science of The Total Environment*, **668**,485-499 (2019).
- 3. Sadeghi, J. & Esmaeili, M.H., Safe distance of cultural and historical buildings from subway lines. *Soil Dynamics and Earthquake Engineering*, **96**,89-103 (2017).
- 4. Ma, M., Liu, W., Qian, C., Deng, G. & Li, Y., Study of the train-induced vibration impact on a historic Bell Tower above two spatially overlapping metro lines. *Soil Dynamics and Earthquake Engineering*, **81**,58-74 (2016).
- 5. Gupta, S., Liu, W.F., Degrande, G., Lombaert, G. & Liu, W.N., Prediction of vibrations induced by underground railway traffic in Beijing. *Journal of Sound and Vibration*, **310(3)**,608-630 (2008).
- 6. Kuo, K., Papadopoulos, M., Lombaert, G. & Degrande, G., The coupling loss of a building subject to railway induced vibrations: Numerical modelling and experimental measurements. *Journal of Sound and Vibration*, **442**,459-481 (2019).
- 7. Ntotsios, E., Thompson, D. & Hussein, M., The effect of track load correlation on ground-borne vibration from railways. *Journal of Sound and Vibration*, **402**,142-163 (2017).
- 8. Ntotsios, E., Thompson, D.J. & Hussein, M.F., A comparison of ground vibration due to ballasted and slab tracks. *Transportation Geotechnics*, **21**,100256 (2019).
- 9. Gutowski, T.G. & Dym, C.L., Propagation of ground vibration: a review. *Journal of Sound and Vibration*, **49(2)**,179-193 (1976).
- 10. Yang, Y. & Hsu, L., A review of researches on ground-borne vibrations due to moving trains via underground tunnels. *Advances in Structural Engineering*, **9(3)**,377-392 (2006).
- 11. Sheng, X., A review on modelling ground vibrations generated by underground trains. *International Journal of Rail Transportation*, **7(4)**,241-261 (2019).
- 12. Kouroussis, G., Connolly, D.P. & Verlinden, O., Railway-induced ground vibrations—a review of vehicle effects. *International Journal of Rail Transportation*, **2(2)**,69-110 (2014).
- 13. ISO 14837-1: Mechanical vibration—ground-borne noise and vibration arising from rail systems. *International Organization for Standardization, Geneva, Switzerland* (2005).
- 14. Kuo, K., Verbraken, H., Degrande, G. & Lombaert, G., Hybrid predictions of railway induced ground vibration using a combination of experimental measurements and numerical modelling. *Journal of Sound and Vibration*, **373**,263-284 (2016).
- 15. Connolly, D., Kouroussis, G., Giannopoulos, A., Verlinden, O., Woodward, P. & Forde, M., Assessment of railway vibrations using an efficient scoping model. *Soil Dynamics and Earthquake Engineering*, **58**,37-47 (2014).
- 16. Connolly, D., Kouroussis, G., Woodward, P.K., Giannopoulos, A., Verlinden, O. & Forde, M.C., Scoping prediction of re-radiated ground-borne noise and vibration near high speed rail lines with variable soils. *Soil Dynamics and Earthquake Engineering*, **66**,78-88 (2014).

- 17. Paneiro, G., Durão, F., e Silva, M.C. & Neves, P.F., Prediction of ground vibration amplitudes due to urban railway traffic using quantitative and qualitative field data. *Transportation Research Part D: Transport and Environment*, **40**,1-13 (2015).
- 18. Liang, R., Liu, W., Ma, M. & Liu, W., An efficient model for predicting the train-induced ground-borne vibration and uncertainty quantification based on Bayesian neural network. *Journal of Sound and Vibration*, **495**,115908 (2021).
- 19. Pak, R.Y. & Guzina, B.B., Three-dimensional Green's functions for a multilayered half-space in displacement potentials. *Journal of Engineering Mechanics*, **128(4)**,449-461 (2002).
- 20. Liu, Z., Liang, J. & Wu, C., Dynamic Green's function for a three-dimensional concentrated load in the interior of a poroelastic layered half-space using a modified stiffness matrix method. *Engineering Analysis with Boundary Elements*, **60**,51-66 (2015).
- 21. He, C., Zhou, S., Guo, P., Di, H. & Xiao, J., Dynamic 2.5-D Green's function for a point load or a point fluid source in a layered poroelastic half-space. *Engineering Analysis with Boundary Elements*, **77**,123-137 (2017).
- 22. Eason, G., The stresses produced in a semi-infinite solid by a moving surface force. *International Journal of Engineering Science*, **2(6)**,581-609 (1965).
- 23. Sheng, X., Jones, C. & Thompson, D., Moving Green's functions for a layered circular cylinder of infinite length. ISVR Technical Memorandum. **885** (2002).
- 24. Jones, D., Le Houedec, D., Peplow, A. & Petyt, M., Ground vibration in the vicinity of a moving harmonic rectangular load on a half-space. *European Journal of Mechanics-A/Solids*, **17(1)**,153-166 (1998).
- 25. Hu, A., Li, Y., Deng, Y. & Xie, K., Vibration of layered saturated ground with a tunnel subjected to an underground moving load. *Computers and Geotechnics*, **119**,103342 (2020).
- 26. Sheng, X., Jones, C. & Petyt, M., Ground vibration generated by a harmonic load acting on a railway track. *Journal of sound and vibration*, **225(1)**,3-28 (1999).
- 27. Sheng, X., Jones, C. & Petyt, M., Ground vibration generated by a load moving along a railway track. *Journal of sound and vibration*, **228(1)**,129-156 (1999).
- 28. Karlström, A. & Boström, A., An analytical model for train-induced ground vibrations from railways. *Journal of Sound and Vibration*, **292(1-2)**,221-241 (2006).
- 29. Xia, H., Cao, Y.M. & De Roeck, G., Theoretical modeling and characteristic analysis of moving-train induced ground vibrations. *Journal of Sound and Vibration*, **329(7)**,819-832 (2010).
- 30. Jones, S. & Hunt, H., Effect of Inclined Soil Layers on Surface Vibration from Underground Railways Using the Thin-Layer Method. *Journal of Engineering Mechanics*, **137(12)**,887-900 (2011).
- 31. Bian, X.C., Jiang, H.G., Chang, C., Hu, J. & Chen, Y.M., Track and ground vibrations generated by high-speed train running on ballastless railway with excitation of vertical track irregularities. *Soil Dynamics and Earthquake Engineering*, **76**,29-43 (2015).
- 32. Metrikine, A.V. & Vrouwenvelder, A.C.W.M., Surface Ground Vibration Due to a Moving Train in a Tunnel: Two-Dimensional Model. *Journal of Sound and Vibration*, **234(1)**,43-66 (2000).

- 33. Koziol, P., Mares, C. & Esat, I., Wavelet approach to vibratory analysis of surface due to a load moving in the layer. *International Journal of Solids and Structures*, **45(7-8)**,2140-2159 (2008).
- 34. Yuan, Z., Xu, C., Cai, Y. & Cao, Z., Dynamic response of a tunnel buried in a saturated poroelastic soil layer to a moving point load. *Soil Dynamics and Earthquake Engineering*, **77**,348-359 (2015).
- 35. Forrest, J.A. & Hunt, H.E.M., A three-dimensional tunnel model for calculation of traininduced ground vibration. *Journal of Sound and Vibration*, **294(4-5)**,678-705 (2006).
- 36. Forrest, J.A. & Hunt, H.E.M., Ground vibration generated by trains in underground tunnels. *Journal of Sound and Vibration*, **294(4-5)**,706-736 (2006).
- 37. Hussein, M.F.M. & Hunt, H.E.M., A numerical model for calculating vibration from a railway tunnel embedded in a full-space. *Journal of Sound and Vibration*, **305(3)**,401-431 (2007).
- 38. Gupta, S., Hussein, M., Degrande, G., Hunt, H. & Clouteau, D., A comparison of two numerical models for the prediction of vibrations from underground railway traffic. *Soil Dynamics and Earthquake Engineering*, **27(7)**,608-624 (2007).
- 39. Kuo, K., Hunt, H. & Hussein, M., The effect of a twin tunnel on the propagation of ground-borne vibration from an underground railway. *Journal of Sound and Vibration*, **330(25)**,6203-6222 (2011).
- 40. Clot, A., Arcos, R., Romeu, J. & Pàmies, T., Dynamic response of a double-deck circular tunnel embedded in a full-space. *Tunnelling and Underground Space Technology*, **59**,146-156 (2016).
- 41. He, C., Zhou, S., Guo, P., Di, H. & Yang, X., A three-dimensional semi-analytical method for calculating vibrations from a moving load on a periodic jointed tunnel. *Computers and Geotechnics*, **114**,103150 (2019).
- 42. Hussein, M., François, S., Schevenels, M., Hunt, H., Talbot, J. & Degrande, G., The fictitious force method for efficient calculation of vibration from a tunnel embedded in a multi-layered half-space. *Journal of sound and vibration*, **333(25)**,6996-7018 (2014).
- 43. Tadeu, A.J. & Kausel, E., Green's functions for two-and-a-half-dimensional elastodynamic problems. *ASCE-Journal of Engineering Mechanics*, **126(10)**,1093-1097 (2000).
- 44. Kausel, E. & Roësset, J.M., Stiffness matrices for layered soils. *Bulletin of the seismological Society of America*, **71(6)**,1743-1761 (1981).
- 45. Yuan, Z., Boström, A. & Cai, Y., Benchmark solution for vibrations from a moving point source in a tunnel embedded in a half-space. *Journal of Sound and Vibration*, **387**,177-193 (2017).
- 46. He, C., Zhou, S., Di, H., Guo, P. & Xiao, J., Analytical method for calculation of ground vibration from a tunnel embedded in a multi-layered half-space. *Computers and Geotechnics*, **99**,149-164 (2018).
- 47. Thomson, W.T., Transmission of elastic waves through a stratified solid medium. *Journal of Applied Physics*, **21(2)**,89-93 (1950).
- 48. Haskell, N.A., The dispersion of surface waves on multilayered media. *Bulletin of the Seismological Society of America*, **43**,17-34 (1953).

- 49. Yuan, Z., Cao, Z., Cai, Y., Geng, X. & Wang, X., An analytical solution to investigate the dynamic impact of a moving surface load on a shallowly-buried tunnel. *Soil Dynamics and Earthquake Engineering*, **126**,105816 (2019).
- 50. Yuan, Z., Cao, Z., Tang, H., Xu, Y. & Wu, T., Analytical layer element with a circular cavity and its application in predicting ground vibrations from surface and underground moving sources. *Computers and Geotechnics*, **137**,104262 (2021).
- 51. He, C., Zhou, S., Di, H. & Zhang, X., An efficient prediction model for vibrations induced by underground railway traffic and experimental validation. *Transportation Geotechnics*, **31**,100646 (2021).
- 52. He, C., Zhou, S. & Guo, P., An efficient three-dimensional method for the prediction of building vibrations from underground railway networks. *Soil Dynamics and Earthquake Engineering*, **139**,106269 (2020).
- 53. Dominguez, J., *Boundary Elements in Dynamics*. Computational Mechanics Publications (1993).
- 54. Schillemans, L., Impact of sound and vibration of the North–South high-speed railway connection through the city of Antwerp Belgium. *Journal of Sound and Vibration*, **267(3)**,637-649 (2003).
- 55. Connolly, D., Giannopoulos, A. & Forde, M., Numerical modelling of ground borne vibrations from high speed rail lines on embankments. *Soil Dynamics and Earthquake Engineering*, **46**,13-19 (2013).
- 56. Kouroussis, G., Verlinden, O. & Conti, C., Influence of some vehicle and track parameters on the environmental vibrations induced by railway traffic. *Vehicle System Dynamics*, **50(4)**,619-639 (2012).
- 57. Kouroussis, G., Verlinden, O. & Conti, C., A two-step time simulation of ground vibrations induced by the railway traffic. *Proceedings of the Institution of Mechanical Engineers, Part C: Journal of Mechanical Engineering Science*, **226(2)**,454-472 (2012).
- 58. Hung, H.H. & Yang, Y.B., Elastic waves in visco-elastic half-space generated by various vehicle loads. *Soil dynamics and earthquake engineering*, **21(1)**,1-17 (2001).
- 59. El Kacimi, A., Woodward, P.K., Laghrouche, O. & Medero, G., Time domain 3D finite element modelling of train-induced vibration at high speed. *Computers & Structures*, **118**,66-73 (2013).
- 60. Hall, L., Simulations and analyses of train-induced ground vibrations in finite element models. *Soil Dynamics and Earthquake Engineering*, **23(5)**,403-413 (2003).
- 61. Real, T., Zamorano, C., Ribes, F. & Real, J., Train-induced vibration prediction in tunnels using 2D and 3D FEM models in time domain. *Tunnelling and Underground Space Technology*, **49**,376-383 (2015).
- 62. Yaseri, A., Bazyar, M. & Hataf, N., 3D coupled scaled boundary finite-element/finite-element analysis of ground vibrations induced by underground train movement. *Computers and Geotechnics*, **60**,1-8 (2014).
- 63. Kouroussis, G., Van Parys, L., Conti, C. & Verlinden, O., Using three-dimensional finite element analysis in time domain to model railway-induced ground vibrations. *Advances in Engineering Software*, **70**,63-76 (2014).

- 64. Qu, X., Thompson, D., Ma, M., Li, M. & Ntotsios, E., Sources of variability in metro traininduced vibration. *Proceedings of the Institution of Mechanical Engineers, Part F: Journal of Rail and Rapid Transit*, **237(4)**,490-499 (2022).
- 65. Shih, J.-Y., Thompson, D. & Zervos, A., The effect of boundary conditions, model size and damping models in the finite element modelling of a moving load on a track/ground system. *Soil Dynamics and Earthquake Engineering*, **89**,12-27 (2016).
- 66. Gardien, W. & Stuit, H.G., Modelling of soil vibrations from railway tunnels. *Journal of Sound and Vibration*, **267(3)**,605-619 (2003).
- 67. Kouroussis, G., Verlinden, O. & Conti, C., Ground propagation of vibrations from railway vehicles using a finite/infinite-element model of the soil. *Proceedings of the Institution of Mechanical Engineers, Part F: Journal of Rail and Rapid Transit*, **223(4)**,405-413 (2009).
- 68. Thach, P.-N., Liu, H.-L. & Kong, G.-Q., Vibration analysis of pile-supported embankments under high-speed train passage. *Soil Dynamics and Earthquake Engineering*, **55**,92-99 (2013).
- 69. Basu, U., Explicit finite element perfectly matched layer for transient three dimensional elastic waves. *International journal for numerical methods in engineering*, **77(2)**,151-176 (2009).
- 70. Ju, S.H., Liao, J.R. & Ye, Y.L., Behavior of ground vibrations induced by trains moving on embankments with rail roughness. *Soil Dynamics and Earthquake Engineering*, **30(11)**,1237-1249 (2010).
- 71. Ju, S.H. & Wang, Y.M., Time dependent absorbing boundary conditions for elastic wave propagation. *International Journal for Numerical Methods in Engineering*, **50(9)**,2159-2174 (2001).
- 72. Rasmussen, K.M., Nielsen, S.R.K. & Kirkegaard, P.H., Boundary element method solution in the time domain for a moving time-dependent force. *Computers & Structures*, **79(7)**,691-701 (2001).
- 73. Galvín, P., Romero, A. & Domínguez, J., Fully three-dimensional analysis of high-speed train–track–soil-structure dynamic interaction. *Journal of Sound and Vibration*, **329(24)**,5147-5163 (2010).
- 74. Shih, J.Y., Thompson, D.J. & Zervos, A., The influence of soil nonlinear properties on the track/ground vibration induced by trains running on soft ground. *Transportation Geotechnics*, **11**,1-16 (2017).
- 75. Fernández-Ruiz, J., Castanheira-Pinto, A., Costa, P.A. & Connolly, D.P., Influence of non-linear soil properties on railway critical speed. *Construction and Building Materials*, **335**,127485 (2022).
- 76. Castanheira-Pinto, A., Fernández-Ruiz, J. & Costa, P.A., Predicting the non-linear critical speed for high-speed railways in singular geotechnical scenarios. *Soil Dynamics and Earthquake Engineering*, **165**,107722 (2023).
- 77. Xu, Q., Xiao, Z., Liu, T., Lou, P. & Song, X., Comparison of 2D and 3D prediction models for environmental vibration induced by underground railway with two types of tracks. *Computers and Geotechnics*, **68**,169-183 (2015).
- 78. Ma, L., Ouyang, H., Sun, C., Zhao, R. & Wang, L., A curved 2.5D model for simulating dynamic responses of coupled track-tunnel-soil system in curved section due to moving loads. *Journal of Sound and Vibration*, **451**,1-31 (2019).

- 79. Bian, X., Jin, W. & Jiang, H., Ground-borne vibrations due to dynamic loadings from moving trains in subway tunnels. *Journal of Zhejiang University SCIENCEA*, **13(11)**,870-876 (2012).
- 80. Hu, J. & Bian, X., Experimental and numerical studies on dynamic responses of tunnel and soils due to train traffic loads. *Tunnelling and Underground Space Technology*, **128**,104628 (2022).
- 81. Bian, X., Hu, J., Thompson, D. & Powrie, W., Pore pressure generation in a poro-elastic soil under moving train loads. *Soil Dynamics and Earthquake Engineering*, **125**,105711 (2019).
- 82. Yang, Y., Liang, X., Hung, H.-H. & Wu, Y., Comparative study of 2D and 2.5 D responses of long underground tunnels to moving train loads. *Soil Dynamics and Earthquake Engineering*, **97**,86-100 (2017).
- 83. Hung, H.H., Chen, G.H. & Yang, Y.B., Effect of railway roughness on soil vibrations due to moving trains by 2.5D finite/infinite element approach. *Engineering Structures*, **57**,254-266 (2013).
- 84. Costa, P.A., Calçada, R., Cardoso, A.S. & Bodare, A., Influence of soil non-linearity on the dynamic response of high-speed railway tracks. *Soil Dynamics and Earthquake Engineering*, **30(4)**,221-235 (2010).
- 85. Jin, Q., Thompson, D.J., Lurcock, D.E.J., Toward, M.G.R. & Ntotsios, E., A 2.5D finite element and boundary element model for the ground vibration from trains in tunnels and validation using measurement data. *Journal of Sound and Vibration*, **422**,373-389 (2018).
- 86. Sheng, X., Jones, C.J.C. & Thompson, D.J., Prediction of ground vibration from trains using the wavenumber finite and boundary element methods. *Journal of Sound and Vibration*, **293(3-5)**,575-586 (2006).
- 87. Zhou, S., He, C., Guo, P. & Yu, F., Dynamic response of a segmented tunnel in saturated soil using a 2.5-D FE-BE methodology. *Soil Dynamics and Earthquake Engineering*, **120**,386-397 (2019).
- 88. He, C., Zhou, S., Guo, P., Di, H. & Zhang, X., Modelling of ground vibration from tunnels in a poroelastic half-space using a 2.5-D FE-BE formulation. *Tunnelling and Underground Space Technology*, **82**,211-221 (2018).
- 89. He, C., Zhou, S., Di, H. & Shan, Y., A 2.5-D coupled FE–BE model for the dynamic interaction between saturated soil and longitudinally invariant structures. *Computers and Geotechnics*, **82**,211-222 (2017).
- 90. Galvín, P., François, S., Schevenels, M., Bongini, E., Degrande, G. & Lombaert, G., A 2.5 D coupled FE-BE model for the prediction of railway induced vibrations. *Soil Dynamics and Earthquake Engineering*, **30(12)**,1500-1512 (2010).
- 91. Lopes, P., Ruiz, J.F., Costa, P.A., Rodríguez, L.M. & Cardoso, A.S., Vibrations inside buildings due to subway railway traffic. Experimental validation of a comprehensive prediction model. *Science of the Total Environment*, **568**,1333-1343 (2016).
- 92. Lopes, P., Costa, P.A., Ferraz, M., Calçada, R. & Cardoso, A.S., Numerical modeling of vibrations induced by railway traffic in tunnels: From the source to the nearby buildings. *Soil Dynamics and Earthquake Engineering*, **61**,269-285 (2014).
- 93. Wang, L., Han, Y., Zhu, Z., Hu, P. & Cai, C., Efficient time–frequency approach for prediction of subway train-induced tunnel and ground vibrations. *Proceedings of the Institution of Mechanical Engineers, Part F: Journal of Rail and Rapid Transit*, **236(3)**,288-301 (2022).

- 94. Ma, L., Zhang, C., Ouyang, H., Yan, Q. & Yu, W., 2.5 D modelling of wave propagation in longitudinally curved viscoelastic structure using a coupled FEM-PML approach. *Engineering Structures*, **226**,111337 (2021).
- 95. Ruiz, J.F., Soares, P.J., Costa, P.A. & Connolly, D.P., The effect of tunnel construction on future underground railway vibrations. *Soil Dynamics and Earthquake Engineering*, **125**,105756 (2019).
- 96. Yang, Y., Li, J., Wang, Z., Nie, Q., Zhou, Z. & Liu, Q., Enhanced mixed boundary for modeling infinite domain in 2.5 D soil vibration analysis. *Soil Dynamics and Earthquake Engineering*, **172**,108021 (2023).
- 97. Yaseri, A., Bazyar, M. & Javady, S., 2.5 D coupled FEM-SBFEM analysis of ground vibrations induced by train movement. *Soil Dynamics and Earthquake Engineering*, **104**,307-318 (2018).
- 98. Peng, Y., Lu, J., Sheng, X. & Yang, J., Modelling ground vibration from a high-speed railway track resting on a periodic pile-plank structure-enhanced embankment. *Journal of Sound and Vibration*, **539**,117281 (2022).
- 99. Xu, L., Ma, M., Cao, R., Tan, X. & Liang, R., Effect of longitudinally varying characteristics of soil on metro train-induced ground vibrations based on wave propagation analysis. *Soil Dynamics and Earthquake Engineering*, **152**,107020 (2022).
- 100. Clouteau, D., Arnst, M., Al-Hussaini, T.M. & Degrande, G., Freefield vibrations due to dynamic loading on a tunnel embedded in a stratified medium. *Journal of sound and vibration*, **283(1-2)**,173-199 (2005).
- 101. Degrande, G., Clouteau, D., Othman, R., Arnst, M., Chebli, H., Klein, R., Chatterjee, P. & Janssens, B., A numerical model for ground-borne vibrations from underground railway traffic based on a periodic finite element–boundary element formulation. *Journal of Sound and Vibration*, **293(3-5)**,645-666 (2006).
- 102. Gupta, S., Stanus, Y., Lombaert, G. & Degrande, G., Influence of tunnel and soil parameters on vibrations from underground railways. *Journal of Sound and Vibration*, **327(1-2)**,70-91 (2009).
- 103. Gupta, S. & Degrande, G., Modelling of continuous and discontinuous floating slab tracks in a tunnel using a periodic approach. *Journal of Sound and Vibration*, **329(8)**,1101-1125 (2010).
- 104. Germonpré, M., Degrande, G. & Lombaert, G., Periodic track model for the prediction of railway induced vibration due to parametric excitation. *Transportation Geotechnics*, **17**,98-108 (2018).
- 105. Germonpré, M., Nielsen, J., Degrande, G. & Lombaert, G., Contributions of longitudinal track unevenness and track stiffness variation to railway induced vibration. *Journal of Sound and Vibration*, **437**,292-307 (2018).
- 106. Sheng, X., Jones, C. & Thompson, D., Modelling ground vibration from railways using wavenumber finite-and boundary-element methods. *Proceedings of the Royal Society A: Mathematical, Physical and Engineering Sciences*, **461(2059)**,2043-2070 (2005).
- 107. Jones, C., Thompson, D. & Petyt, M. A model for ground vibration from railway tunnels. in *Proceedings of the Institution of Civil Engineers-Transport*. Thomas Telford Ltd (2002).
- 108. François, S., Schevenels, M., Galvín, P., Lombaert, G. & Degrande, G., A 2.5 D coupled FE–BE methodology for the dynamic interaction between longitudinally invariant

- structures and a layered halfspace. Computer methods in applied mechanics and engineering, 199(23-24),1536-1548 (2010).
- 109. Auersch, L., Dynamics of the railway track and the underlying soil: the boundary-element solution, theoretical results and their experimental verification. *Vehicle System Dynamics*, **43(9)**,671-695 (2005).
- 110. Liravi, H., Clot, A., Arcos, R., Fakhraei, J., Godinho, L., Conto, K.F. & Romeu, J., A 2.5 D hybrid SBM-MFS methodology for elastic wave propagation problems. *Journal of Sound and Vibration*, **586**,118501 (2024).
- 111. Wei, X., Liu, D., Luo, W., Chen, S. & Sun, L., A half-space singular boundary method for predicting ground-borne vibrations. *Applied Mathematical Modelling*, **111**,630-643 (2022).
- 112. Liravi, H., Arcos, R., Clot, A., Godinho, L. & Conto, K.F. A 2.5 D hybrid SBM-MFS methodology for the evaluation of free-field vibrations induced by underground railway infrastructures. in *INTER-NOISE and NOISE-CON Congress and Conference Proceedings*. Institute of Noise Control Engineering (2023).
- 113. Triepaischajonsak, N. & Thompson, D.J., A hybrid modelling approach for predicting ground vibration from trains. *Journal of Sound and Vibration*, **335**,147-173 (2015).
- 114. Koroma, S.G., Thompson, D.J., Hussein, M.F.M. & Ntotsios, E., A mixed space-time and wavenumber-frequency domain procedure for modelling ground vibration from surface railway tracks. *Journal of Sound and Vibration*, **400**,508-532 (2017).
- 115. Hanson, C.E., Ross, J.C., Towers, D.A. & Harris, M., High-speed ground transportation noise and vibration impact assessment. United States Federal Railroad Administration. Office of Railroad Policy and Development (2012).
- 116. Hanson, C., Towers, D. & Meister, L., Transit noise and vibration impact assessment, Report FTA-VA-90-1003-06. US Department of Transportation, Federal Transit Administration (2006).
- 117. Thompson, D., Railway noise and vibration: mechanisms, modelling and means of control. Elsevier (2008).
- 118. Kurzweil, L.G., Ground-borne noise and vibration from underground rail systems. *Journal of Sound and Vibration*, **66(3)**,363-370 (1979).
- 119. Melke, J., Noise and vibration from underground railway lines: proposals for a prediction procedure. *Journal of Sound and Vibration*, **120(2)**,391-406 (1988).
- 120. Madshus, C., Bessason, B. & Hårvik, L., Prediction model for low frequency vibration from high speed railways on soft ground. *Journal of sound and vibration*, **193(1)**,195-203 (1996).
- 121. Hood, R., Greer, R., Breslin, M. & Williams, P., The calculation and assessment of ground-borne noise and perceptible vibration from trains in tunnels. *Journal of sound and vibration*, **193(1)**,215-225 (1996).
- 122. Kuppelwieser, H. & Ziegler, A., A tool for predicting vibration and structure-borne noise immissions caused by railways. *Journal of Sound and Vibration*, **193(1)**,261-267 (1996).
- 123. Rossi, F. & Nicolini, A., A simple model to predict train-induced vibration: theoretical formulation and experimental validation. *Environmental Impact Assessment Review*, **23(3)**,305-322 (2003).

- 124. With, C., Bahrekazemi, M. & Bodare, A., Validation of an empirical model for prediction of train-induced ground vibrations. *Soil Dynamics and Earthquake Engineering*, **26(11)**,983-990 (2006).
- 125. Gjelstrup, H., Alcover, I.F., Andersen, J.E. & Larsen, A., Probabilistic empirical model for train-induced vibrations. *Proceedings of the Institution of Civil Engineers Structures and Buildings*, **169(8)**,563-573 (2016).
- 126. Auersch, L., Simple and fast prediction of train-induced track forces, ground and building vibrations. *Railway Engineering Science*, **28(3)**,232-250 (2020).
- 127. Verbraken, H., Lombaert, G. & Degrande, G., Verification of an empirical prediction method for railway induced vibrations by means of numerical simulations. *Journal of Sound and Vibration*, **330(8)**,1692-1703 (2011).
- 128. Kouroussis, G., Vogiatzis, K.E. & Connolly, D.P., Assessment of railway ground vibration in urban area using in-situ transfer mobilities and simulated vehicle-track interaction. *International Journal of Rail Transportation*, **6(2)**,113-130 (2018).
- 129. Kouroussis, G., Vogiatzis, K.E. & Connolly, D.P., A combined numerical/experimental prediction method for urban railway vibration. *Soil Dynamics and Earthquake Engineering*, **97**,377-386 (2017).
- 130. Colaço, A., Castanheira-Pinto, A., Costa, P.A. & Ruiz, J.F., Combination of experimental measurements and numerical modelling for prediction of ground-borne vibrations induced by railway traffic. *Construction and Building Materials*, **343**,127928 (2022).
- 131. Bouvet, P., Nélain, B., Thompson, D., Ntotsios, E., Nuber, A., Fröhling, B., Reumers, P., Seyfaddini, F., Herremans, G. & Lombaert, G. A hybrid prediction tool for railway induced vibration. in *International Workshop on Railway Noise*. Springer (2022).
- 132. Lai, C.G., Callerio, A., Faccioli, E., Morelli, V. & Romani, P., Prediction of railway-induced ground vibrations in tunnels. *Journal of vibration and acoustics*, **127(5)**,503-514 (2005).
- 133. Liu, W., Wu, Z., Li, C. & Xu, L., Prediction of ground-borne vibration induced by a moving underground train based on excitation experiments. *Journal of Sound and Vibration*, **523**,116728 (2022).
- 134. Kuo, K.A. & Hunt, H.E.M., Dynamic Models of Piled Foundations. *Applied Mechanics Reviews*, **65(3)**,031003 (2013).
- 135. Novak, M., Dynamic stiffness and damping of piles. *Canadian Geotechnical Journal*, **11(4)**,574-598 (1974).
- 136. Novak, M. & Howell, J.F., Torsional vibration of pile foundations. *Journal of the Geotechnical Engineering Division*, **103(4)**,271-285 (1977).
- 137. Novak, M., Vertical vibration of floating piles. *Journal of the Engineering Mechanics Division*, **103(1)**,153-168 (1977).
- 138. Novak, M. & Grigg, R., Dynamic experiments with small pile foundations. *Canadian Geotechnical Journal*, **13(4)**,372-385 (1976).
- 139. Maheshwari, B.K. & Watanabe, H., Nonlinear dynamic behavior of pile foundations: Effects of separation at the soil-pile interface. *Soils and foundations*, **46(4)**,437-448 (2006).
- 140. Wang, K., Wu, W., Zhang, Z. & Leo, C.J., Vertical dynamic response of an inhomogeneous viscoelastic pile. *Computers and Geotechnics*, **37(4)**,536-544 (2010).

- 141. Li, Z.-y., Wang, K.-h., Wu, W.-b. & Leo, C.J., Vertical vibration of a large diameter pile embedded in inhomogeneous soil based on the Rayleigh-Love rod theory. *Journal of Zhejiang University-Science A*, **12(17)**,974-988 (2016).
- 142. Gao, L., Wang, K., Xiao, S., Li, Z. & Wu, J., An analytical solution for excited pile vibrations with variable section impedance in the time domain and its engineering application. *Computers and Geotechnics*, **73**,170-178 (2016).
- 143. Luan, L., Ding, X., Zheng, C., Kouretzis, G. & Wu, Q., Dynamic response of pile groups subjected to horizontal loads. *Canadian Geotechnical Journal*, **57(4)**,469-481 (2020).
- Luan, L., Gao, L., Kouretzis, G., Ding, X., Qin, H. & Zheng, C., Response of pile groups in layered soil to dynamic lateral loads. *Computers and Geotechnics*, **142**,104564 (2022).
- 145. Novak, M. & Nogami, T., Soil pile interaction in horizontal vibration. *Earthquake Engineering & Structural Dynamics*, **5(3)**,263-281 (1977).
- 146. Nogami, T. & Novák, M., Soil pile interaction in vertical vibration. *Earthquake Engineering & Structural Dynamics*, **4(3)**,277-293 (1976).
- 147. Kuo, K.A. & Hunt, H.E.M., An efficient model for the dynamic behaviour of a single pile in viscoelastic soil. *Journal of Sound and Vibration*, **332(10)**,2549-2561 (2013).
- 148. Peng, Y., Sheng, X. & Lu, J., Improvement to the fictitious pile method for pile-soil interaction problems. *Soil Dynamics and Earthquake Engineering*, **162**,107465 (2022).
- 149. Muki, R. & Sternberg, E., On the diffusion of an axial load from an infinite cylindrical bar embedded in an elastic medium. *International Journal of Solids and Structures*, **5(6)**,587-605 (1969).
- 150. Cui, C., Meng, K., Xu, C., Wang, B. & Xin, Y., Vertical vibration of a floating pile considering the incomplete bonding effect of the pile-soil interface. *Computers and Geotechnics*, **150**,104894 (2022).
- 151. Kaynia, A.M. & Kausel, E., Dynamics of piles and pile groups in layered soil media. *Soil Dynamics and Earthquake Engineering*, **10(8)**,386-401 (1991).
- 152. Kattis, S., Polyzos, D. & Beskos, D., Vibration isolation by a row of piles using a 3 D frequency domain BEM. *International Journal for Numerical Methods in Engineering*, **46(5)**,713-728 (1999).
- 153. Kaynia, A.M., Dynamic stiffness and seismic response of pile groups. Massachusetts Institute of technology (1982).
- 154. Poulos, H.G. & Mattes, N., The behaviour of axially loaded end-bearing piles. *Geotechnique*, **19(2)**,285-300 (1969).
- 155. Masoumi, H.R. & Degrande, G., Numerical modeling of free field vibrations due to pile driving using a dynamic soil-structure interaction formulation. *Journal of Computational and Applied Mathematics*, **215(2)**,503-511 (2008).
- 156. Auersch, L., Wave propagation in the elastic half-space due to an interior load and its application to ground vibration problems and buildings on pile foundations. *Soil Dynamics and Earthquake Engineering*, **30(10)**,925-936 (2010).
- 157. Sen, R., Davies, T. & Banerjee, P., Dynamic analysis of piles and pile groups embedded in homogeneous soils. *Earthquake engineering & structural dynamics*, **13(1)**,53-65 (1985).

- 158. Maeso, O., Aznárez, J.J. & García, F., Dynamic impedances of piles and groups of piles in saturated soils. *Computers & structures*, **83(10-11)**,769-782 (2005).
- 159. Talbot, J. & Hunt, H., A computationally efficient piled-foundation model for studying the effects of ground-borne vibration on buildings. *Proceedings of the Institution of Mechanical Engineers, Part C: Journal of Mechanical Engineering Science*, **217(9)**,975-989 (2003).
- 160. Edirisinghe, T.L. & Talbot, J.P., A parametric study of the train-induced vibration of a single pile near an underground railway tunnel. *Soil Dynamics and Earthquake Engineering*, **158**,107274 (2022).
- 161. Edirisinghe, T.L. & Talbot, J.P., Inertial interaction in pile-groups: A study of the influence of coupling via an iterative wave-scattering approach. *Computers and Geotechnics*, **128**,103804 (2020).
- 162. Edirisinghe, T.L. & Talbot, J.P., The significance of source-receiver interaction in the response of piled foundations to ground-borne vibration from underground railways. *Journal of Sound and Vibration*, **506**,116178 (2021).
- 163. Conto, K.F., Arcos, R., Clot, A., Ntotsios, E., Liravi, H., Colaço, A. & Thompson, D.J., A pile–soil interaction model for ground-borne vibration problems based on the singular boundary method. *Journal of Sound and Vibration*, **568**,118057 (2024).
- 164. Maheshwari, B.K., Truman, K.Z., Naggar, M.H.E. & Gould, P.L., Three-dimensional finite element nonlinear dynamic analysis of pile groups for lateral transient and seismic excitations. *Canadian geotechnical journal*, **41(1)**,118-133 (2004).
- 165. Kuhlemeyer, R.L., Static and dynamic laterally loaded floating piles. *Journal of the Geotechnical Engineering Division*, **105(2)**,289-304 (1979).
- 166. Kuhlemeyer, R.L., Vertical vibration of piles. *Journal of the Geotechnical Engineering Division*, **105(2)**,273-287 (1979).
- 167. Kuo, K.A., Jones, S., Hunt, H.E. & Hussein, M.F. Applications of PiP: Vibration of embedded foundations near a railway tunnel. in 7 th European Conference on Structural Dynamics (EURODYN). (2008).
- 168. Hussein, M., Hunt, H., Kuo, K., Costa, P.A. & Barbosa, J., The use of sub-modelling technique to calculate vibration in buildings from underground railways. *Proceedings of the Institution of Mechanical Engineers, Part F: Journal of Rail and Rapid Transit*, 229(3),303-314 (2013).
- 169. Sanayei, M., Moore, J.A. & Brett, C.R., Measurement and prediction of train-induced vibrations in a full-scale building. *Engineering Structures*, **77**,119-128 (2014).
- 170. Sanayei, M., Zhao, N., Maurya, P., Moore, J.A., Zapfe, J.A. & Hines, E.M., Prediction and mitigation of building floor vibrations using a blocking floor. *Journal of Structural Engineering*, **138(10)**,1181-1192 (2012).
- 171. Zou, C., Moore, J.A., Sanayei, M. & Wang, Y., Impedance model for estimating train-induced building vibrations. *Engineering Structures*, **172**,739-750 (2018).
- 172. Li, X., Chen, Y., Zou, C., Wu, J., Shen, Z. & Chen, Y., Building coupling loss measurement and prediction due to train-induced vertical vibrations. *Soil Dynamics and Earthquake Engineering*, **164**,107644 (2023).

- 173. Auersch, L., Dynamic stiffness of foundations on inhomogeneous soils for a realistic prediction of vertical building resonance. *Journal of geotechnical and geoenvironmental engineering*, **134(3)**,328-340 (2008).
- 174. Clot, A., Arcos, R. & Romeu, J., Efficient three-dimensional building-soil model for the prediction of ground-borne vibrations in buildings. *Journal of Structural Engineering*, **143(9)**,04017098 (2017).
- 175. Bucinskas, P., Ntotsios, E., Thompson, D.J. & Andersen, L.V., Modelling train-induced vibration of structures using a mixed-frame-of-reference approach. *Journal of Sound and Vibration*, **491**,115575 (2021).
- 176. Ropars, P., Vuylsteke, X. & Augis, E. Vibrations induced by metro in sensitive buildings; experimental and numerical comparisons. in *EURONOISE 2018 Conference*. *Heraklion, Greece*. (2018).
- 177. Villot, M., Ropars, P., Jean, P., Bongini, E. & Poisson, F., Modeling the influence of structural modifications on the response of a building to railway vibration. *Noise Control Engineering Journal*, **59(6)**,641-651 (2011).
- 178. Coulier, P., François, S., Lombaert, G. & Degrande, G., Application of hierarchical matrices to boundary element methods for elastodynamics based on Green's functions for a horizontally layered halfspace. *Engineering Analysis with Boundary Elements*, 37(12),1745-1758 (2013).
- 179. Fiala, P., Degrande, G. & Augusztinovicz, F., Numerical modelling of ground-borne noise and vibration in buildings due to surface rail traffic. *Journal of Sound and Vibration*, **301(3-5)**,718-738 (2007).
- 180. Çelebi, E., Fırat, S. & Çankaya, İ., The evaluation of impedance functions in the analysis of foundations vibrations using boundary element method. *Applied Mathematics and Computation*, **173(1)**,636-667 (2006).
- López-Mendoza, D., Romero, A., Connolly, D.P. & Galvín, P., Scoping assessment of building vibration induced by railway traffic. Soil Dynamics and Earthquake Engineering, 93,147-161 (2017).
- 182. Peng, B., Xu, L., Connolly, D.P., Li, Z., He, X., Xiao, Y. & Guo, Y., Railway bridge dynamics considering piled foundations in soft soil. *Soil Dynamics and Earthquake Engineering*, **184**,108844 (2024).
- 183. López-Mendoza, D., Connolly, D.P., Romero, A., Kouroussis, G. & Galvín, P., A transfer function method to predict building vibration and its application to railway defects. *Construction and Building Materials*, **232**,117217 (2020).
- 184. Lopes, P., Costa, P.A., Calçada, R. & Cardoso, A.S., Influence of soil stiffness on building vibrations due to railway traffic in tunnels: Numerical study. *Computers and Geotechnics*, **61**,277-291 (2014).
- 185. Colaço, A., Alves Costa, P., Amado-Mendes, P. & Calçada, R., Vibrations induced by railway traffic in buildings: Experimental validation of a sub-structuring methodology based on 2.5D FEM-MFS and 3D FEM. *Engineering Structures*, **240**,112381 (2021).
- 186. Colaço, A., Alves Costa, P., Castanheira-Pinto, A., Amado-Mendes, P. & Calçada, R., Experimental validation of a simplified soil-structure interaction approach for the prediction of vibrations in buildings due to railway traffic. *Soil Dynamics and Earthquake Engineering*, **141**,106499 (2021).

- 187. Colaço, A., Barbosa, D. & Costa, P.A., Hybrid soil-structure interaction approach for the assessment of vibrations in buildings due to railway traffic. *Transportation Geotechnics*, **32**,100691 (2022).
- 188. Arcos, R., Soares, P.J., Costa, P.A. & Godinho, L., An experimental/numerical hybrid methodology for the prediction of railway-induced ground-borne vibration on buildings to be constructed close to existing railway infrastructures: Numerical validation and parametric study. *Soil Dynamics and Earthquake Engineering*, **150**,106888 (2021).
- 189. Nelson, J.T. & Saurenman, H.J., A Prediction Procedure for Rail Transportation Groundborne Noise and Vibration. *Transportation Research Record*, **1143**,26-35 (1987).
- 190. Kuo, K., Lombaert, G. & Degrande, G., Quantifying dynamic soil-structure interaction for railway induced vibrations. *Procedia engineering*, **199**,2372-2377 (2017).
- 191. Richart, F.E., Hall, J.R. & Woods, R.D., Vibrations of soils and foundations. (1970).
- 192. Avilés, J. & Sánchez-Sesma, F.J., Piles as barriers for elastic waves. *Journal of Geotechnical Engineering*, **109(9)**,1133-1146 (1983).
- 193. Avilés, J. & Sánchez-Sesma, F.J., Foundation isolation from vibrations using piles as barriers. *Journal of Engineering Mechanics*, **114(11)**,1854-1870 (1988).
- 194. Tsai, P.-h., Feng, Z.-y. & Jen, T.-l., Three-dimensional analysis of the screening effectiveness of hollow pile barriers for foundation-induced vertical vibration. *Computers and Geotechnics*, **35(3)**,489-499 (2008).
- 195. Biot, M.A., Theory of propagation of elastic waves in a fluid saturated porous solid. II. Higher frequency range. *The Journal of the acoustical Society of america*, **28(2)**,179-191 (1956).
- 196. Cai, Y.Q., Ding, G.Y. & Xu, C.J., Amplitude reduction of elastic waves by a row of piles in poroelastic soil. *Computers and Geotechnics*, **36(3)**,463-473 (2009).
- 197. Cai, Y.Q., Ding, G.Y., Xu, C.J. & Wang, J., Vertical amplitude reduction of Rayleigh waves by a row of piles in a poroelastic half space. *International Journal for Numerical and Analytical Methods in Geomechanics*, **33(16)**,1799-1821 (2009).
- 198. Gao, G., Li, Z., Qiu, C. & Yue, Z., Three-dimensional analysis of rows of piles as passive barriers for ground vibration isolation. *Soil Dynamics and Earthquake Engineering*, **26(11)**,1015-1027 (2006).
- 199. Zhang, X. & Lu, J.-F., A wavenumber domain boundary element method model for the simulation of vibration isolation by periodic pile rows. *Engineering Analysis with Boundary Elements*, **37(7-8)**,1059-1073 (2013).
- 200. Xu, B., Lu, J.-F. & Wang, J.-H., Numerical analysis of the isolation of the vibration due to Rayleigh waves by using pile rows in the poroelastic medium. *Archive of Applied Mechanics*, **80**,123-142 (2010).
- 201. Lu, J.-F., Xu, B. & Wang, J.-H., A numerical model for the isolation of moving-load induced vibrations by pile rows embedded in layered porous media. *International Journal of Solids and Structures*, **46(21)**,3771-3781 (2009).
- 202. Lu, J., Jeng, D., Wan, J. & Zhang, J., A new model for the vibration isolation via pile rows consisting of infinite number of piles. *International Journal for Numerical and Analytical Methods in Geomechanics*, **37(15)**,2394-2426 (2013).

- 203. Huang, J. & Shi, Z., Attenuation zones of periodic pile barriers and its application in vibration reduction for plane waves. *Journal of Sound and Vibration*, **332(19)**,4423-4439 (2013).
- 204. Huang, J. & Shi, Z., Application of periodic theory to rows of piles for horizontal vibration attenuation. *International Journal of Geomechanics*, **13(2)**,132-142 (2013).
- 205. Huang, J. & Shi, Z., Vibration reduction of plane waves using periodic in-filled pile barriers. Journal of Geotechnical and Geoenvironmental Engineering, **141(6)**,04015018 (2015).
- 206. Pu, X. & Shi, Z., Surface-wave attenuation by periodic pile barriers in layered soils. *Construction and Building Materials*, **180**,177-187 (2018).
- 207. Pu, X. & Shi, Z., A novel method for identifying surface waves in periodic structures. *Soil Dynamics and Earthquake Engineering*, **98**,67-71 (2017).
- 208. Pu, X. & Shi, Z., Periodic pile barriers for Rayleigh wave isolation in a poroelastic half-space. *Soil Dynamics and Earthquake Engineering*, **121**,75-86 (2019).
- 209. Ma, M., Jiang, B., Gao, J. & Liu, W., Experimental study on attenuation zone of soil-periodic piles system. *Soil Dynamics and Earthquake Engineering*, **126**,105738 (2019).
- 210. Li, T., Su, Q. & Kaewunruen, S., Seismic metamaterial barriers for ground vibration mitigation in railways considering the train-track-soil dynamic interactions. *Construction and Building Materials*, **260**,119936 (2020).
- 211. Castanheira-Pinto, A., Alves-Costa, P., Godinho, L. & Amado-Mendes, P., On the application of continuous buried periodic inclusions on the filtering of traffic vibrations: A numerical study. *Soil Dynamics and Earthquake Engineering*, **113**,391-405 (2018).
- 212. Jiang, Y., Meng, F., Chen, Y., Zheng, Y., Chen, X., Zhang, J. & Huang, X., Vibration attenuation analysis of periodic underground barriers using complex band diagrams. *Computers and Geotechnics*, **128**,103821 (2020).
- 213. He, C., Zhou, S. & Guo, P., Mitigation of railway-induced vibrations by using periodic wave impeding barriers. *Applied Mathematical Modelling*, **105**,496-513 (2022).
- 214. Li, Z., Ma, M., Liu, K. & Jiang, B., Performance of rubber-concrete composite periodic barriers applied in attenuating ground vibrations induced by metro trains. *Engineering Structures*, **285**,116027 (2023).
- 215. Pu, X., Shi, Z. & Xiang, H., Feasibility of ambient vibration screening by periodic geofoam-filled trenches. *Soil Dynamics and Earthquake Engineering*, **104**,228-235 (2018).
- 216. Gao, L., Cai, C., Mak, C.M., He, X., Zou, Y. & Wu, D., Surface wave attenuation by periodic hollow steel trenches with Bragg band gap and local resonance band gap. *Construction and Building Materials*, **356**,129289 (2022).
- 217. Cai, C., Gao, L., He, X., Zou, Y., Yu, K. & Wu, D., The surface wave attenuation zone of periodic composite in-filled trenches and its isolation performance in train-induced ground vibration isolation. *Computers and Geotechnics*, **139**,104421 (2021).
- 218. Brûlé, S., Enoch, S. & Guenneau, S., Emergence of seismic metamaterials: Current state and future perspectives. *Physics Letters A*, **384(1)**,126034 (2020).
- 219. Cao, Y., Xia, H. & Lombaert, G., Solution of moving-load-induced soil vibrations based on the Betti–Rayleigh Dynamic Reciprocal Theorem. *Soil Dynamics and Earthquake Engineering*, **30(6)**,470-480 (2010).

- 220. Wolf, J.P., Foundation vibration analysis using simple physical models. Pearson Education (1994).
- 221. Rikse, L. Modelling of subway induced vibrations using the Pipe-in-Pipe model. MSc thesis, Katholieke Universiteit Leuven & University of Cambridge (2007).
- 222. Kuo, K.A. Vibration from underground railways: considering piled foundations and twin tunnels. (2011).
- 223. Newland, D.E., *Mechanical vibration analysis and computation*. Courier Corporation (2006).
- 224. Leung, A.Y.T., An accurate method of dynamic condensation in structural analysis. *International Journal for Numerical Methods in Engineering*, **12(11)**,1705-1715 (1978).
- 225. François, S., Schevenels, M., Dooms, D., Jansen, M., Wambacq, J., Lombaert, G., Degrande, G. & De Roeck, G., Stabil: An educational Matlab toolbox for static and dynamic structural analysis. *Computer Applications in Engineering Education*, **29(5)**,1372-1389 (2021).
- 226. Jeyachandrabose, C. & Kirkhope, J., Construction of new efficient three-node triangular thin plate bending elements. *Computers & Structures*, **23(5)**,587-603 (1986).
- 227. Hussein, M.F.M., François, S., Schevenels, M., Hunt, H.E.M., Talbot, J.P. & Degrande, G., The fictitious force method for efficient calculation of vibration from a tunnel embedded in a multi-layered half-space. *Journal of Sound and Vibration*, **333(25)**,6996-7018 (2014).
- 228. Coulier, P., Lombaert, G. & Degrande, G., The influence of source–receiver interaction on the numerical prediction of railway induced vibrations. *Journal of Sound and Vibration*, **333(12)**,2520-2538 (2014).
- 229. Sheng, X., Jones, C. & Thompson, D., A theoretical model for ground vibration from trains generated by vertical track irregularities. *Journal of sound and vibration*, **272(3-5)**,937-965 (2004).
- 230. Graff, K.F., Wave motion in elastic solids. London: Oxford University Press (1975).
- 231. Thompson, D., Ntotsios, E., Degrande, G., Lombaert, G., Herremans, G., Nélain, B., Bouvet, P., Fröhling, B. & Nuber, A., Database for vibration emission, ground transmission and building transfer functions. . *SILVARSTAR project GA 101015442, Deliverable D2. 1, Report to the EC*, (2022).
- 232. Lurcock, D. Predicting groundborne noise and vibration in buildings from railway. University of Southampton (2018).
- 233. Ntotsios, E., Thompson, D.J. & Hussein, M.F.M., A comparison of ground vibration due to ballasted and slab tracks. *Transportation Geotechnics*, **21** (2019).
- 234. Ntotsios, E., Thompson, D.J., Reumers, P., Degrande, G., Bouvet, P. & Nélain, B., A track-independent vehicle indicator for ground-borne noise and vibration emission classification. *Transportation Geotechnics*, **45** (2024).
- 235. Felippa, C.A., Introduction to finite element methods. University of Colorado (2004).